Cronfa
Swansea University's Research Repository

The Performance of Novel Cr(III) Based Coatings for Packaging Steel

By

Ellen Christine Bluett

A Thesis

Presented to Swansea University

In fulfilment of the requirements for the degree of
Engineering Doctorate (EngD) in Materials Engineering

Swansea University
Prifysgol Abertawe

College of Engineering, Swansea University, 2023

© Ellen C. Bluett 2023

Distributed under the terms of a Creative Commons Attribution Non Commercial 4.0 License (CC BY-NC 4.0).

Author Declarations

STATEMENT 1

This work has not previously been accepted in substance for any degree and is not being concurrently submitted in candidature for any degree.

Signed: E.Bluett

Date: 09/05/23

STATEMENT 2

This thesis is the result of my own investigations, except where otherwise stated. Other sources are acknowledged by footnotes giving explicit references and a bibliography is appended.

Signed: E.Bluett

Date: 09/05/23

STATEMENT 3

I hereby give consent for my thesis, if accepted, to be available for photocopying and for inter-library loan, and for the title and summary to be made available to outside organisations.

Signed: E.Bluett

Date: 09/05/23

STATEMENT 4

I confirm that the University's ethical procedures have been followed and, where appropriate, that ethical approval has been granted.

Signed: E.Bluett

Date: 09/05/23

Abstract

The main driver for this thesis was the understanding of the mechanisms involved in the corrosion of novel trivalent chromium coatings for packaging steels and comparison with traditional materials, namely electro chromium coated steel (ECCS).

Tata Steel are currently developing trivalent chromium coated technology steel (TCCT) as a replacement for ECCS in steel packaging applications. ECCS offers excellent corrosion resistance when used in conjunction with a polymer overcoat. The understanding of corrosion performance of the novel TCCT when overcoated with an organic coating is currently limited. Thus, this work utilised experimental procedures to help understand the mechanism behind two forms of corrosion-driven organic coating failure; filiform corrosion and corrosion-driven cathodic delamination. In turn, this work also aimed to identify, and supply the steel industry with evidence of the TCCT coating weights that are important for optimum resistance to organic coating failure.

Increasing the Cr (III) oxide coating weight led to an improvement in corrosion performance with regards to both filiform corrosion and cathodic delamination, with a Cr (III) oxide coating weight of approximately 7 $mg.m^{-2}$ providing impressive corrosion resistance, comparable to that of the current standard, ECCS. The increased presence of defects on TCCT samples with lower Cr (III) oxide coating weights, as well as the impressive insulating properties of Cr (III) oxide, were thought to be contributing factors to the improved corrosion resistance observed with increasing coating weight.

Furthermore, a lab-scale TCCT electroplating line was successfully replicated in the Swansea labs. Varying parameters including current density and temperature had a profound effect on the amount of Cr deposited. Hydrogen evolution was proposed to be one of the reasons for this variance in deposit.

Table of Contents

Acknowledgements

Firstly, I would like to thank the M2A, Tata Steel and the various other funders (UKRI, EPSRC, European Social Fund and the Welsh Government) that allowed me to carry out this work. I would also like to say thanks to the whole M2A team for their guidance, humour, and generosity throughout.

I seem to have gone through numerous supervisors (hopefully that's not a reflection on myself) but I would like to thank each and every one of them for their support over the years. In particular, I would like to thank Dr Natalie Wint for her enthusiasm, guidance, knowledge and general chats throughout this project. A special thank you also to Professor Neil McMurray and Dr Arnoud de Vooys for their wisdom, wit and input throughout the project.

I would also like to thank all of my fellow EngDs for the laughs over the years, as well as my friends and family for their continued support. A final thank you goes to Gethin Thomas the milk man!

List of Figures

List of Tables

List of Symbols/Abbreviations

Symbols/Abbreviations

ECCS	Electro chromium coated steel
TCCT®	Trivalent chromium coated technology
ΔG	Gibbs Energy Change
ΔG*	Gibbs Activation Energy
E	Electrode Potential
E^0	Standard Electrode Potential
EIS	Electrochemical Impedance Spectroscopy
SVET	Scanning Vibrating Electrode Technique
PVB	Poly-Vinyl Butyral
E_{corr}	Free corrosion potential
I_{corr}	Corrosion current
OCP	Open-circuit potential
SEM	Scanning electron microscopy
SKP	Scanning Kelvin Probe

List of Publications

Performance assessment of chrome coated packaging steel manufactured via a Cr (III) processing route

M.Dodd, E.Holding, C.Griffiths, E.Bluett, A.Mescall, K.Lammers, A.de Vooys, N.Wint, E.Jewell

Submitted - in review Journal:*International Journal of Adhesion and Adhesives*
Manuscript Number: IJAAD-D-22-00470

The influence of chromium oxide coating weight on filiform corrosion of trivalent chromium coatings for packaging

E. Bluett, M. Dodd, J.Edy, A. Mescall, A. C. A. de Vooys, N. Wint, E. Jewell, H. N. McMurray.

(Yet to be submitted)

1 Literature Review

1.1 Aims and Objectives

Due to its impressive mechanical properties and cost efficiency, steel is one of the most widely used materials across the world. However, steel is susceptible to corrosion, which can lead to disastrous consequences with regards to the strength of metals, and therefore structural integrity. Also, corrosion that affects the aesthetic appearance of the metal can cause a potential for loss of value of the product. Globally the cost of corrosion is estimated to be US$2.5 trillion, which is 3.4% of the global gross domestic product GDP (2013) (1). Corrosion damage results in significant costs associated with both additional material, labour and equipment, and loss of revenue as well as loss of reputation, tax, the local economy and the environment (1). To avoid large financial losses, it is vital that metals, which require corrosion resistance, are designed suitably for this task.

One application of steel is within the food packaging industry where it accounts for 10 % of all beverage cans (2). Food and beverage cans may hold substances with various properties, including high acidity as well as high salinity. Food quality and safety are major sources of concern in the food packaging industry. It is vital that there is a sufficient barrier to stop the can and its contents from reacting. A metallic coating is often used and acts as a barrier to the underlying steel to prevent such reactions from occurring. The coating must possess several properties; it must be non-toxic as well as adhesive and offer corrosion protection, even if subject to accidental deformation (3). This layer is often used in conjunction with an organic coating as additional protection.

Electro chromium coated steel (ECCS) is a packaging material that is often used for food applications. Hexavalent chromium (Cr (VI)) based chromic acid electrolyte baths are used for the electrodeposition process. However, in recent years REACH legislation has imposed a restriction on the use of Cr (VI), due to health and environmental concerns and a sunset date for the use of ECCS is in the horizon. This has resulted in the drive of the steel packaging industry to find a suitable, non-toxic replacement (4, 5).

Developed by Tata Steel, TCCT (Trivalent Chromium Coating Technology) involves the use of a trivalent chromium (Cr(III)) salt based electrolyte A two-step process is used to deposit a Cr-Cr oxide bilayer onto a steel substrate.

It is important that the mechanisms of corrosion of the novel material are understood so they can be compared to existing products. Two mechanisms of corrosion are of primary concern. These are wet corrosion, which may take place internally where the substrate is in contact with the contents, and atmospheric corrosion of the external surface.

Previous literature has studied TCCT made via a one-step deposition process. However, the TCCT samples that are studied in this thesis are novel as they are produced using a two-step process, which is described in more depth in section 1.13. Like ECCS, TCCT is used in conjunction with a polymer overcoat. Hence, chapters 3 and 4 examine the resistance of TCCT to organic coating failure mechanisms, and whether it performs as well as, if not better than the current standard, ECCS. Moreover, chapter 3 concentrates on the kinetics and mechanism of corrosion driven cathodic disbondment. A Scanning Kelvin Probe (SKP) is employed to measure the corrosion potential under the organic coating as a function of distance and time. Chapter 4 focuses on the kinetics and mechanism of filiform corrosion, a type of atmospheric corrosion that commonly occurs on packaging materials in storage conditions. Chapter 5 employs the use of a lab scale plating line and looks at the effect of varying electroplating parameters on the amount of Cr deposited. The parameters that were altered could also be feasibly altered in the plant, hence the results of this study are very beneficial to industry. Chapter 6 looks at the use of heat treatment as a way to alter the Cr (III) oxide layer. Packaging materials are subjected to sterilisation, and hence, high temperatures during the manufacturing process. The impact of heat treatment on the chemical make-up of the coating is therefore of interest. Chapter 7 focuses on the use of amino acids as green, chromate-free corrosion inhibitors of iron. Whilst, corrosion inhibitors are not considered suitable for packaging applications, they may be used for automotive and construction applications where food safety does not apply and so have industrial relevance here to the steel industry.

1.2 Electrochemistry of Corrosion

Corrosion is an electrochemical process whereby material reacts with its environment resulting in its subsequent attack (6). The process involves returning the metal back into its original 'ore' form, or a compound of similar chemical make-up due to it being lower in energy and more stable.

A metal's most stable state is in the form of its ore. Thus, when a metal is manufactured into its metallic form it is not in its preferential state and holds a significant amount of free energy (G). To revert to their most preferential state, metals will often return to a state similar to their ore such as in the form as oxides. This takes place during corrosion. This can be explained by means of an energy profile.

When the value of Gibbs free energy is negative, between a pure metal and compounds of the metal, the reaction to form the corrosion product occurs spontaneously. The equation of ΔG for the corrosion of two metals is given by:

$$G = \Delta G1 - \Delta G2 \qquad (1.1)$$

where ΔG_1 is the reduction value for free energy change and ΔG_2 is the free energy change for oxidation.

The rate at which corrosion occurs is determined by Gibbs free activation energy, ΔG^*.

A graphic demonstration of the energy profile for this reaction can be seen in Figure 1.1.

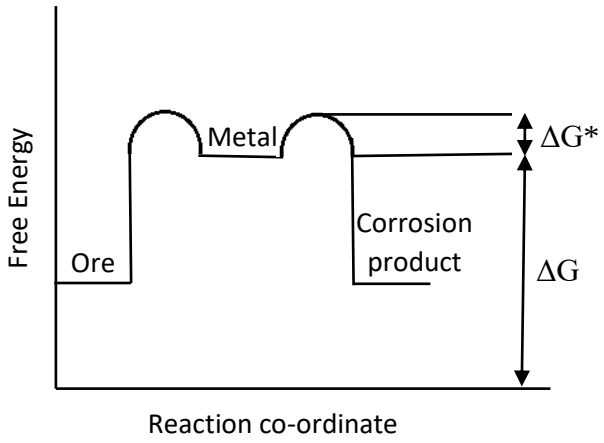

Figure 1.1: Energy profile diagram for the formation of a metal and its subsequent corrosion.

An electrochemical reaction is a chemical reaction during which electrons are accepted or received to bring about chemical change. During an electrochemical reaction, electrons are donated from a reducing agent and accepted by an oxidizing agent. The reducing agent itself is oxidized whilst the oxidizing agent is reduced. In the case of metal corrosion, the oxidation reaction (Equation 1.2), which involves formation of ions and at which electrons are released, takes place at the anode:

$$Me \rightarrow Me^{n+} + ne^{-} \qquad (1.2)$$

The metal ions formed go into solution whilst the electrons travel through the metal to a place where they can be used up in a reduction reaction at the cathode. Oxygen dissolved in water is often used as an oxidising agent during the reduction reaction.

If the reaction is taking place in a solution containing neutral/alkaline substances the following oxygen reduction reaction may occur:

$$O_2 + 2H_2O + 4e^{-} \rightarrow 4OH^{-} \qquad (1.3)$$

If the reaction is taking place in a solution containing an acidic substance, and hence an abundance of H^+, the following oxygen reduction reaction may occur:

$$O_2 + 4H^{+} + 4e^{-} \rightarrow 2H_2O \qquad (1.4)$$

Other cathodic reduction reactions that can occur include hydrogen evolution, metal ion reduction and metal deposition which are demonstrated by the following equations respectively.

$$2H^{+} + 2e^{-} \rightarrow H_2 \qquad (1.5)$$

$$Fe^{3+} + e^{-} \rightarrow Fe^{2+} \qquad (1.6)$$

$$Cu^{2+} + 2e^{-} \rightarrow Cu \qquad (1.7)$$

An electrochemical cell (Figure 1.2) therefore consists of four components: an anode, cathode, electrolyte, an electrically conductive solution, and the electrical connection provides a means of connecting the anode and cathode for free electron flow. Disruption of any one of these four components will cause corrosion to come to a halt.

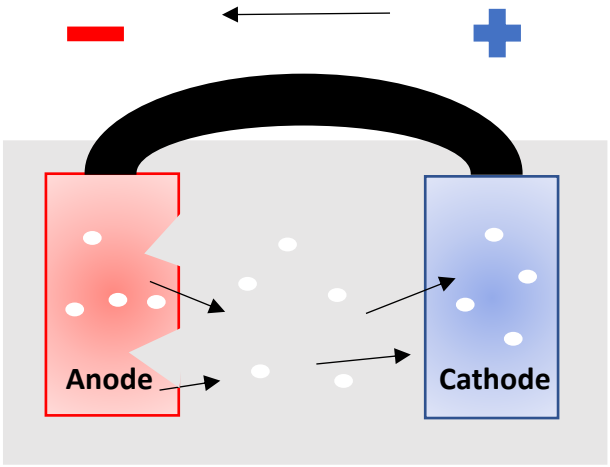

Figure 1.2: The current flow between an anode and cathode in a corrosion cell. The arrows indicate the flow of current.

In the case of iron corrosion, water hydroxide ions, formed during the reduction reaction at the cathode, migrate through the electrolyte and combine with ferrous ions, produced at the anode, to form iron(III) hydroxide (equation 1.8).

$$4Fe + 6H_2O + 3O_2 \rightarrow 4Fe(OH)_3 \qquad (1.8)$$

Iron(III) hydroxide is insoluble and red-brown in colour. During drying, dehydration occurs leading to the formation of ferric oxide (equation 1.9).

$$2Fe(OH)_3 \rightarrow Fe_2O_3 + 3H_2O \qquad (1.9)$$

The reaction products are referred to as the corrosion products, which may be insoluble or soluble.

Commonly, anodic and cathodic half reactions occur on the same material's surface and the distance between the anode and cathode may vary. General corrosion occurs when there are numerous, small anodes and cathodes located close together. Localised corrosion, on the other hand, occurs when the anodes and cathodes are located further apart. Localised corrosion often occurs at a more prominent rate and can rapidly cause detrimental damage.

1.3 Electrode potentials

In an electrochemical cell the corrosion of one of the metals will be accelerated, and the other decelerated. This is determined by the electrical potential difference between

them, with each electrode having an electrode potential. Electrode potentials are always quoted for the reduction of a chemical species relative to a defined standard reference point, commonly the standard hydrogen electrode (SHE). Differences in electrode potentials between the anode and cathode determine the likelihood of any chemical reaction occurring. The electrode which has the more positive reduction electrode potential will draw electrons and act as the cathode. If the reduction electrode potential is negative this is indicative that the reduction reaction is thermodynamically unfavourable. The electrochemical series arranges reactions in order of their standard electrode potentials (Figure 1.3).

Element	*Electrode rection*	*E°(V)*
Li	$Li + e^- \rightarrow Li$	−3.045
K	$K^+ + e^- \rightarrow K$	−2.925
Cs	$Cs^+ + e^- \rightarrow Cs$	−2.923
Ba	$Ba^{2+} + 2e^- \rightarrow Ba$	−2.906
Ca	$Ca^{2+} + 2e^- \rightarrow Ca$	−2.866
Na	$Na^+ + e^- \rightarrow Na$	−2.714
Mg	$Mg^{2+} + 2e^- \rightarrow Mg$	−2.363
Al	$Al^{3+} + 3e^- \rightarrow Al$	−1.662
H_2	$H_2O + 2e^- \rightarrow H_2 + 2OH^-$	−0.829
Zn	$Zn^{2+} + 2e^- \rightarrow Zn$	−0.763
Fe	$Fe^{2+} + 2e^- \rightarrow Fe$	−0.440
Cd	$Cd^2 + 2e^- \rightarrow Cd$	−0.403
Pb	$PbSO_4 + 2e^- \rightarrow Pb + SO_4^{2-}$	−0.310
Co	$Co^{2+} + 2e^- \rightarrow Co$	−0.280
Ni	$Ni^{2+} + 2e^- \rightarrow Ni$	−0.250
Sn	$Sn^{2+} + 2e^- \rightarrow Sn$	−0.136
Pb	$Pb^{2+} + 2e^- \rightarrow Pb$	−0.126
Fe	$Fe^{3+} + 3e^- \rightarrow Fe$	−0.036
H_2	$2H^+ + 2e^- \rightarrow H_2(SHE)$	0
Cu	$Cu^{2+} + e^- \rightarrow Cu^+$	+0.153
S	$S_4O_6^{2-} + 2e^- \rightarrow 2S_2O_3^{2-}$	+0.170
Cu	$Cu^{2+} + 2e^- \rightarrow Cu$	+0.337
I_2	$I_2 + 2e^- \rightarrow 2I^-$	+0.534
Fe	$Fe^{3+} + e^- \rightarrow Fe^{2+}$	+0.77
Ag	$Ag^+ + e^- \rightarrow Ag$	+0.799
Hg	$Hg^{2+} + 2e^- \rightarrow Hg$	+0.854
Br_2	$Br_2 + 2e^- \rightarrow 2Br^-$	+1.066
O_2	$O_2 + 4H^+ + 2e^- \rightarrow 2H_2O$	+1.230
Cr	$Cr_2O_7^{2-} + 14H^+ + 6e^- \rightarrow 2Cr^{3+} + 7H_2O$	+1.330
Cl_2	$Cl_2 + 2e^- \rightarrow 2Cl^-$	+1.359
Au	$Au^{3+} + 3e^- \rightarrow Au$	+1.498
Mn	$MnO_4^- + 8H^+ + 5e^- \rightarrow Mn^2 + 4H_2O$	+1.510
F_2	$F_2 + 2e^- \rightarrow 2F^-$	+2.870

Figure 1.3. Electrochemical series (7).

An example of some typical reference electrodes and potential with respect to the standard hydrogen electrode are as follows:

- Standard hydrogen electrode (SHE) (E = 0.000 V)
- Saturated calomel electrode (SCE) (E = +0.241 V)
- Copper-copper(II) sulphate electrode (CSE) (E = +0.314 V)

1.4 Faraday's Law

Differences in the electrode potential are related thermodynamically to Gibbs Free Energy (ΔG) (equation 1.10).

$$\Delta G = -nFE^{o} \qquad (1.10)$$

where n is the number of electrons transferred, F the Faraday constant and E^{o}, the cell potential.

In the case of a corroding metal, the anodic and cathodic current densities are not at equilibrium and are said to be polarised with respect to its equilibrium by an overpotential. This variation on the polarised overpotential (E) will be related to corrosion rate (given by current density, i) following an exponential relationship. Moreover, plotting anodic and cathodic current density against the polarisation gives rise to the graph observed in Figure 1.4.

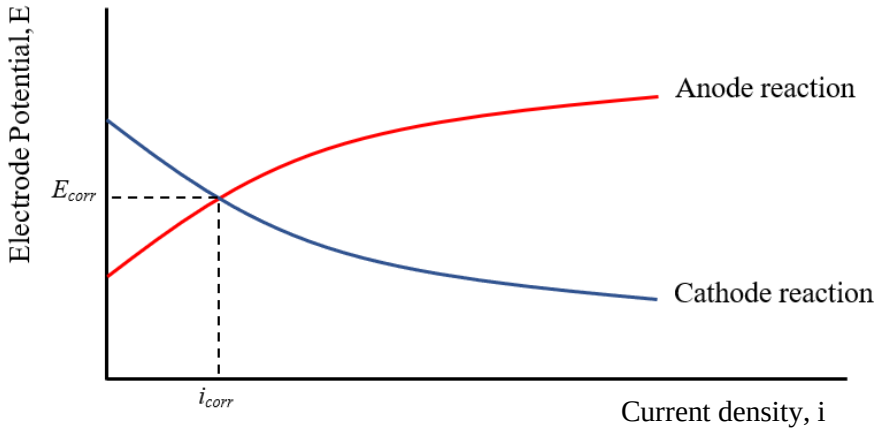

Figure 1.4: An Evans diagram identifying the corrosion current and free corrosion potential.

The current density becomes linear by arranging the data into a log plot, known as a Tafel plot, as shown in Figure 1.5. The cathodic and anodic reaction rate are equal at

the point that they intersect, and this is known as the free corrosion potential, E_{corr} (Figure 1.5). The current density associated with the E_{corr} is known as the corrosion current density, i_{corr}. i_{corr} is a useful measure of corrosion as it is proportional to the corrosion rate.

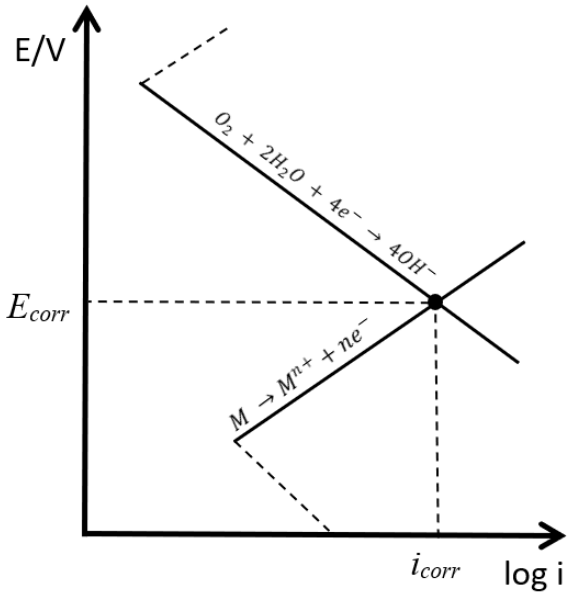

Figure 1.5: Simplified Tafel plot for a metal immersed in aerated electrolyte identifying the free corrosion potential and the free corrosion current.

1.5 Concentration effects

Electrode potentials are established in standard conditions of temperature, pressure and concentration, i.e. 25°C, 1 atm pressure and 1 moldm^{-3}. Under non-standard conditions i.e. varying concentrations, the likelihood of a metal to corrode may be different and the relationship is given by the Nernst equation (equation 1.11):

$$E = E^0 + \frac{RT}{nF} ln \frac{[products]}{[reactants]} \qquad (1.11)$$

where E is the cell potential (V), E^0 the standard electrode potential (V), R the universal gas constant (JK^{-1}mol^{-1}), T the temperature (K), n the number of electrons (C) and F the Faraday constant (Cmol^{-1}). The term [products] refers to the concentration (M) of the aqueous products from the oxidation reaction and [reactants]

corresponds to the concentration (M) of aqueous reactants of the reduction reaction of the electrode.

Using the Nernst equation and knowledge of the important reactions that will occur, along with their electrode potentials, it is possible to predict the performance of a metal subject to various conditions.

1.6 Pourbaix Diagrams

The Pourbaix diagram can be used to show the equilibrium phases of a metal and its various oxidised species as a function of pH and potential, and is a useful tool when predicting how a material will behave under certain environments.

The three states include when the metal is in its active form (it is corroding), when it is immune and when it is passive (protected by an insoluble layer e.g. iron oxide). The metal is said to be corroding when the amount of its ions in solution is greater than 10^{-6} $moldm^{-3}$ (8). Below this threshold the metal is described as immune. The two parallel dotted lines present on the Pourbaix diagram represent the potential reactions of water on the surface of an immersed electrode; hydrogen evolution and oxygen evolution.

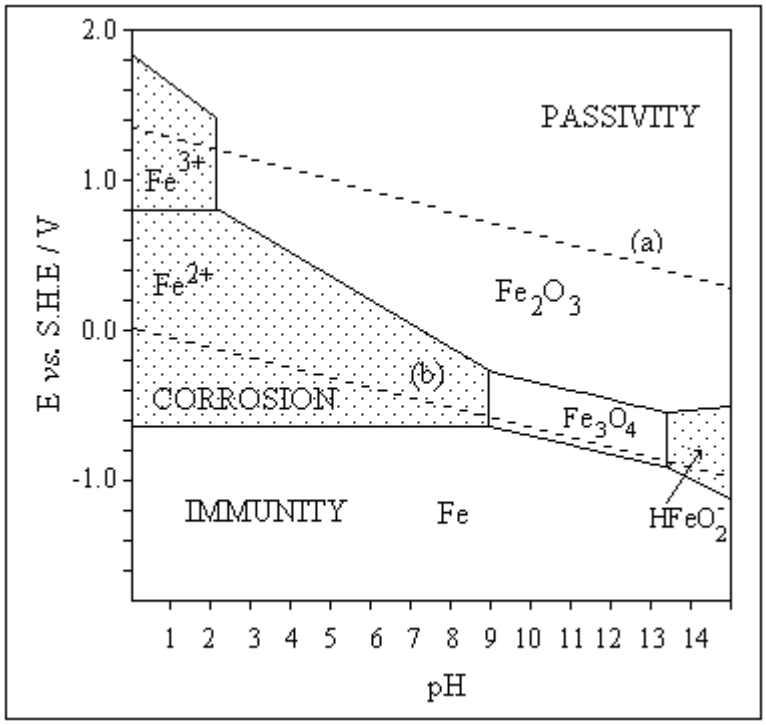

Figure 1.6: The Pourbaix diagram for iron in water at 25°C. (a) oxygen evolution line. (b) hydrogen evolution line (8).

The Pourbaix diagram for Fe is shown in Figure 1.6. It is in its most stable form from pH 9 to pH 13, existing as Fe_3O_4. Commonly, iron is oxidised to Fe^{2+}, which in turn reacts with dissolved oxygen to form Fe^{3+}. The Fe^{3+} ions react with hydroxide ions to form iron hydroxides, and rust is formed. It is shown in Figure 1.6 that Fe^{2+} is formed between pH 0 and 9.

Pourbaix diagrams do, however, have several limitations. The chemical reactions used to construct the Pourbaix diagram in the first place are obtained under conditions of thermodynamic equilibrium and ignore any unstable and metastable compounds that might form. Furthermore, they do not offer information about the kinetics of the reactions or more specifically the rate of corrosion.

1.7 Differential aeration and Evans droplet

An aqueous corrosion cell of a metal corroding in a droplet of water, commonly known as an Evans droplet, is shown in Figure 1.7. The differential aeration conditions, caused by different oxygen supplies, leads to the formation of a focal anode in the

middle of the droplet, and cathodes on the droplet borders. Moreover, the metal substrate undergoes anodic dissolution releasing Fe^{2+}, in the case of iron. These ions diffuse away into solution whilst the hydroxide ions diffuse into the centre of the droplet. At the point they meet, the product of corrosion develops, e.g. rust. These local conditions displace the oxygen supply to a point where corrosion is still occurring. Ultimately, an oxygen-deficient zone is established which becomes the point of anodic dissolution whilst cathodic oxygen reduction occurs in the surrounding oxygen rich areas.

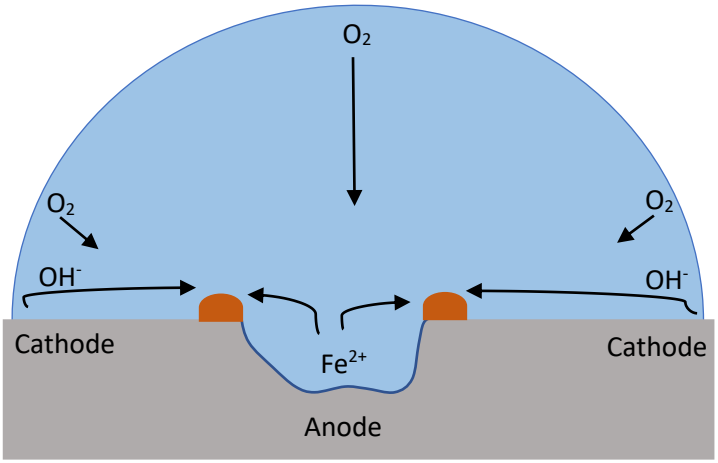

Figure 1.7: Differential aeration corrosion as an Evans droplet.

1.8 Protective Coatings

As shown, metals are susceptible to corrosion. Thus, the need for artificial coatings to protect the underlying metal is of utmost importance (9).

There are various ways in which a coating can work in order to decrease the chance of corrosion attack. Common ways of protection include forming an impervious barrier to moisture and corrosive species, using corrosion inhibitors, as well as cathodic protection (9). Some examples of coatings that are based on some of these techniques include sacrificial coatings and noble (or barrier) coatings.

Sacrificial coatings protect the metal underneath as they have a more negative electrode potential and are thus themselves ‘sacrificed’. A common example of a sacrificial coating in action is galvanized steel, whereby a zinc coating is applied to

steel. The zinc will corrode first, and even if the underlying metal becomes exposed, if the two metals are electrically coupled the steel will stay undamaged (9).

A noble coating involves a thin metallic layer being placed on top of the metal substrate in order to protect it from moisture and corrosive species; it provides a physical barrier between the underlying metal and the atmosphere (9).

Coatings such as these are often used as protection for packaging materials.

1.9 Organic coatings

Packaging materials including ECCS and tinplate are usually used in conjunction with an organic coating, the most commonly used corrosion protection application for metals (10). Organic coatings not only enhance corrosion resistance they also often add to the aesthetic appearance of the product too. The organic coatings used for tinplate and ECCS are usually a lacquer and a polymer such as Protact® respectively. TCCT® will also be used in conjunction with a lacquer such as epoxy-phenolic.

The coating is expected to withstand various environmental conditions depending on its application. As cans are often stored for long periods of time and often in contact with extreme environments, such as strong acidity or salinity, they must be designed to withstand failure.

However, coatings can fail for a large number of reasons, including unsatisfactory film coating weight, as well as inadequate surface preparation (11). Delamination and flaking are types of adhesion failures caused by detachment of the coating from the substrate or underlying layers. They can be caused due to internal stress sometimes alongside other contributing factors including formulation or an inadequate surface profile (11). The chemical make-up and application of the coating may also be causes of adhesion problems (12).

Various types of corrosion mechanisms have been researched and are known to occur on the surface of cans. Thus, it is important that the coating acts to resist all these forms of corrosion. If a can is found to be faulty it is vital that the problem is recognised quickly and resolved so that it does not happen again.

1.10 Failure mechanisms

The formation of a differential aeration cell, where there is an uneven supply of oxygen on the same metal, can lead to several corrosion mechanisms taking place, including cathodic delamination and filiform corrosion (FFC). Both of these failure mechanisms occur in the presence of an organic coating, such as that present on packaging materials.

1.11 Filiform Corrosion

First correctly defined in 1944 by Sharman (13), filiform corrosion (FFC) is a form of localised, atmospheric corrosion that commonly occurs at scratch defects on a material, as here the electrolyte comes into contact with the underlying substrate. It leads to the production of unsightly, worm-like defects on the surface of the material, disrupting its aesthetic look. A high relative humidity (commonly 65 – 95 %) (14) is also required for FFC to propagate as it enables the salt ions to be dissolved (15). FFC travels from the scratch, along the metal under the surface of the coating. An example of a differential aeration cell in the case of FFC is shown in Figure 1.8.

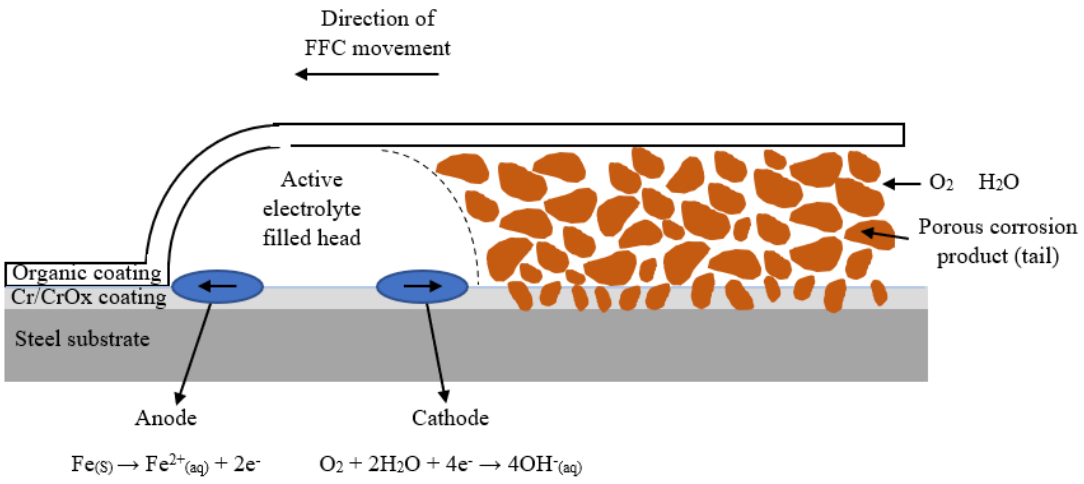

Figure 1.8. Electrochemical processes occurring during the propagation of filiform corrosion.

Metal dissolution occurs at the anode whilst hydrolysis occurs at the cathode. Metal oxidation leads to the formation of the corrosion product, ferric hydroxide ($Fe(OH)_3$). The driving force for FFC is differential aeration, caused by facile oxygen diffusion in the filament tail.

It is widely agreed that during FFC a differential aeration cell is made and conserved in the head electrolyte. Although there is some dispute as to which end the head and tail lie; in general it is thought that cathodic oxygen reduction occurs at the back end of the filament head whilst anodic metal dissolution leads at the front (16). The corresponding reactions are as follows:

Cathodic oxygen reduction

$$O_2 + 2H_2O + 4e^- \rightarrow 4OH^- \quad (1.13)$$

Anodic metal dissolution

$$Fe \rightarrow Fe^{2+} + 2e^- \quad (1.14)$$

In essence, water, supplied due to the high concentration of dissolved ferrous ions on the surface of substrate, diffuses under the coating. Ferric hydroxide is left behind as the corrosion product in the inactive tail.

Oxygen reduction occurs at the active head and a differential aeration cell is made. The acidified anode is located at the front of the head whilst the alkaline cathode is located towards the tail end of the head. Metal oxidation gives rise to the corrosion product and the pH is lowered to 1 due to hydrolysis and acidification (17).

Research by Charbonneau showed FFC occurring on Tin Free Steel (TFS) cans filled with tuna in water (12). Due to the thin material of a can a more detrimental effect is caused by FFC as there is more chance of the base layer being exposed, a site prone to corrosion. The chances of FFC occurring can be reduced by decreasing the chances of scratches occurring as well as by complete washing and drying of the can (12). On organically coated iron, FFC leads to the formation of electrolyte rich filament heads, comprising of iron cations and aggressive anions, such as Cl^-.

There is still, however, widespread dispute about FFC on iron with regards to the involvement of cathodic oxygen reduction in relation to coating disbondment (16). Some authors suggest that the delamination behaviour is in concordance with a previous corrosion driven cathodic disbondment mechanism shown to occur on organic-coated iron when underfilm corrosion is initiated by a group (I) chloride electrolyte. Others believe that cathodic oxygen reduction occurs at a distant site

significantly ahead of the filament-head and some think that cathodic disbondment takes place in a narrow region at the border of the leading filament-head (16).

It is important to ensure that alternatives to ECCS are equivalent or better in terms of their performance. As such, previous work has compared the performance of TCCT® to ECCS, with respect to FFC. Whilst there was no evidence of FFC on ECCS after 5 weeks, it was observed on TCCT®, albeit at a lower rate than that observed on uncoated steel (18). This finding was attributed to differences in chemical composition of the coatings. For example, the TCCT® possessed increased levels of surface metallic iron, as well as fewer outer OH^- groups compared to ECCS (18). Pores in the Cr (III) coating were also believed to contribute to the enhanced FFC corroded area. However, the TCCT® used during these pieces of work was produced using the one step electroplating process (19) whereby a mixed Cr metal – Cr oxide single layer is applied to the steel substrate. Since then, due to the positive effect provided by Cr (III) oxide on corrosion resistance, newer TCCT® samples, as previously mentioned, are made by overcoating the existing Cr layer with a Cr (III) oxide rich layer. Very limited work has been conducted into the corrosion resistance properties of bilayer TCCT®, and the work that has been done primarily focuses on cathodic delamination.

1.12 Cathodic Delamination

Another form of organic coating failure is referred to as cathodic delamination. Unlike FFC, where the separation of the organic coating from the substrate is linked to the anodic reaction, in the case of cathodic delamination, separation of the coating from the substrate is linked to the cathodic reaction (16, 9). Anodic metal dissolution located in the defect is coupled with the cathodic delamination front by a thin electrolyte which ingresses underneath the coating (16).

Moreover cathodic reactions (commonly oxygen reduction) often occur on metals, such as those in the packaging industry, leading to delamination of the coating from the metal by means of the cathodic disbondment mechanism (18).

The hydroxyl ions, or a reaction intermediate, disturb the bonds between the substrate and coating leading to adhesion failure, and delamination of the coating. Without external polarization, the anodic reaction is again the metal dissolution of the substrate

at the place of corrosion damage. This region of disbondment enlarges with time. Alkaline electrolyte, present under the coating, can have a pH as high as 14 (20).

During cathodic delamination a differential aeration cell is set up, due to the ease of oxygen transport through the thin polymer coating, in comparison to the thick electrolyte later, which in turn results in delamination of the coating. Delamination may occur as a result of a coating defect such as a scratch or indentation. Such defects in the coating lead to completion of the corrosion cell as they allow the electrolyte (and thus ions) to be in contact with the metal surface, enabling dissolution to take place at the anode. This anodic dissolution can be coupled with cathodic oxygen reduction at the cathode. This can be observed in Figure 1.9.

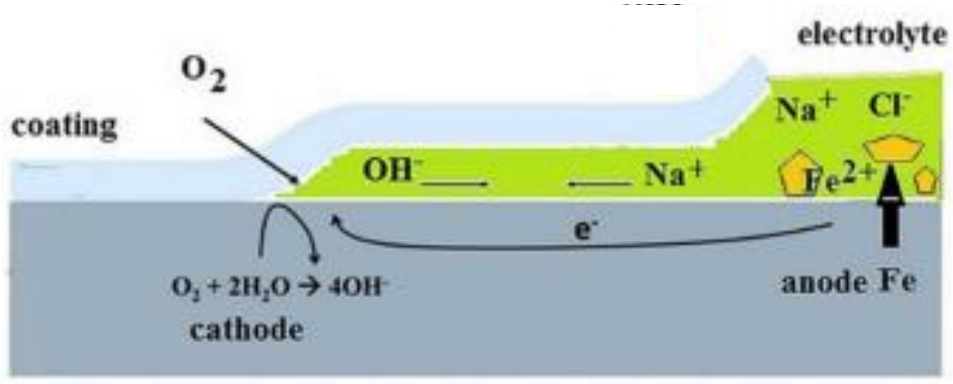

Figure 1.9. Schematic of a cathodic delamination cell and the relevant reactions that occur (21).

In the case of the delamination of a simple organic model coating from pure iron, a thin layer of electrolyte penetrates under the region of coating that has delaminated, and couples Fe metal dissolution at the defect, with cathodic oxygen reduction at the cathode. In this example, the hydroxide ions lead to the disruption of bonds between the coating and metal leading to loss of adhesion, and ultimately delamination of the coating. Water and oxygen transport occur predominantly through the coating, whilst cation transport occurs primarily thought migration along the interface. In turn, the migration of cations from the defect to the intact interface is generally the rate-determining step (16).

Previous research on chromium coated steel has shown a link between thicker chromium oxide layers and increased corrosion resistance; an area of interest with regards to TCCT®. Furthermore, Warren et al. showed that more specifically increasing the thickness of a chromium oxide layer, deposited onto (chromium metal

coated) low carbon steel, can stop disbondment from taking place at all, thus drastically improving the performance of the coating (22).

Previous research on ECCS cans by Boelen et al. investigated the effect of various parameters on the performance of the can (23). It was found that without oxygen present, cathodic delamination did not occur in the presence of artificial defects. What's more, a threshold level was determined for both chromium metal and chromium oxide that must be exceeded for the can to withstand initiation and propagation of corrosion, respectively (23). It was shown that too little chromium metal led to the material being more prone to iron exposure after deformation. These points are bad as they have weaker adhesion and can help with the initiation and propagation of corrosion (23).

Whiteside et al. (2021) showed that ECCS was resistant to cathodic delamination in non-deformed and deformed states. In comparison, deformation of the TCCT® significantly increased the extent of cathodic delamination (24).

It is the cation diffusion constant which is important not the size. Li+ is slow because it has a large charge density and so has a relatively large sphere of water molecules around each solvated Li+ cation.

Cation type and concentration influences the rate of delamination. It has been shown that the cation diffusion constant is important, with rate increasing in the order $Li^+ < Na^+ < K^+ < Cs^+$ (16). It is of note that the type of anion does not significantly alter the delamination rate. A greater concentration of cations at the defect also increases the rate of delamination. Furthermore, a threshold concentration must be surpassed in order to galvanically couple the intact interface with the defect and enable oxygen reduction just in front of the delaminated zone, ultimately leading to adhesion failure (16).

Oxygen partial pressure also impacts delamination rate (25). The delamination front is the site of oxygen reduction and the potential difference between the delamination front and the defect is given by the ohmic potential drop caused by the galvanic current along the already delaminated interface. The ohmic potential drop is given by the difference of the open circuit potential at the defect and the intact interface and the ionic conductivity between the two sites. The oxygen partial pressure controls the potential of the local cathode at the metal/polymer interface (25).

Stratmann et al. researched the atmospheric corrosion properties of iron for several wet/dry transitions. The results showed that the corrosion of iron during drying was determined by an acceleration of the rate of oxygen reduction (diffusion limited) as the thickness of the electrolyte decreased. The surface of the metal was passivated at the iron/electrolyte interface due to a thick layer of corrosion product. Also, during the last stage of drying there was enough oxygen activity inside the oxide layer to re-oxidise Fe^{2+} species. Thus, there was a strong retardation in the rate of oxygen reduction as this electron transfer reaction takes place at the interface oxide/electrolyte (26).

1.13 Corrosion of Packaging Materials

This thesis focuses on the development of a new packaging material; TCCT®. It is essential that packaging materials serve their purpose in terms of ensuring the produce inside reaches the customer in a satisfactory condition.

Traditionally there are two types of coated steel used to make cans; tinplate and electro ECCS also known as tin-free steel (TFS) (12).

As an alternative to tinplate, ECCS was first used in 1965 for cans containing carbonated drinks (27) due to its economically advantageous price in comparison to tinplate (28).

Electrodeposited chromium is commonly used during the coating of the surface of many industrial materials including cans made using tinplate and ECCS. This is due to its impressive corrosion and wear resistance properties as well as its aesthetically pleasing finish (29). The production of both tinplate and ECCS, however, involve the use of Cr(VI) (19). The composition of ECCS can be seen in Figure 1.10, where blackplate is the name given to low carbon steel used for such applications.

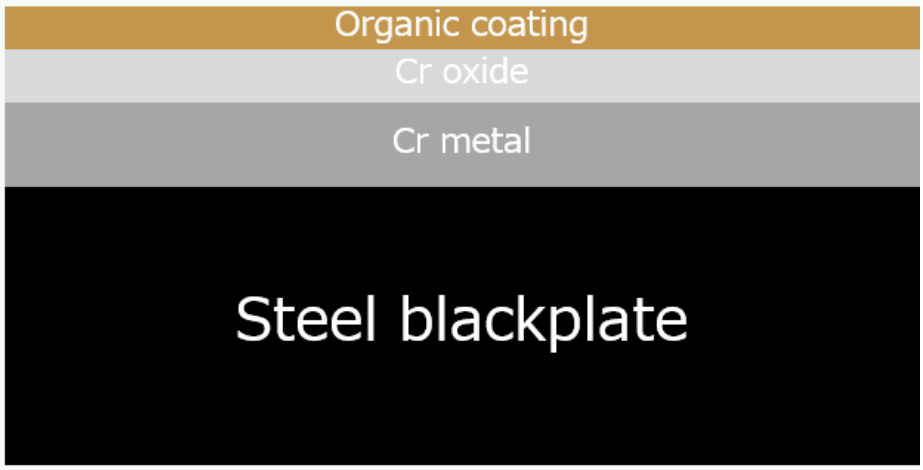

Figure 1.10. Composition of ECCS.

ECCS is typically produced as part of a continuous electrodeposition process whereby the low carbon steel strip is polarised in such a way that it becomes the cathode as it passes through baths of chromic acid electrolyte. The final product comprises of two distinct layers; a Cr metal layer and a native Cr (hydr)oxide layer is formed on top. The oxide arises as a result of the strong oxidizing ability of Cr(VI) (30). Hexavalent chromium is not however, present in the final product of ECCS. ECCS offers high levels of corrosion resistance against both cathodic delamination and filiform corrosion. As previously mentioned, ECCS is used in conjunction with Protact, an organic coating, and provides impressive adhesion properties.

The coating weights of ECCS can vary from 20 - 110 mg/m^2 for metallic chromium and 2 - 20 mg/m^2 for the oxide (19). Autoreduction of the outer chromium oxide is prevented as it will not be oxidised to a lower state.

The coating line for ECCS involves various stations including cleaning, pickling, plating and rinsing. A schematic of the production line can be seen in Figure 1.11 below.

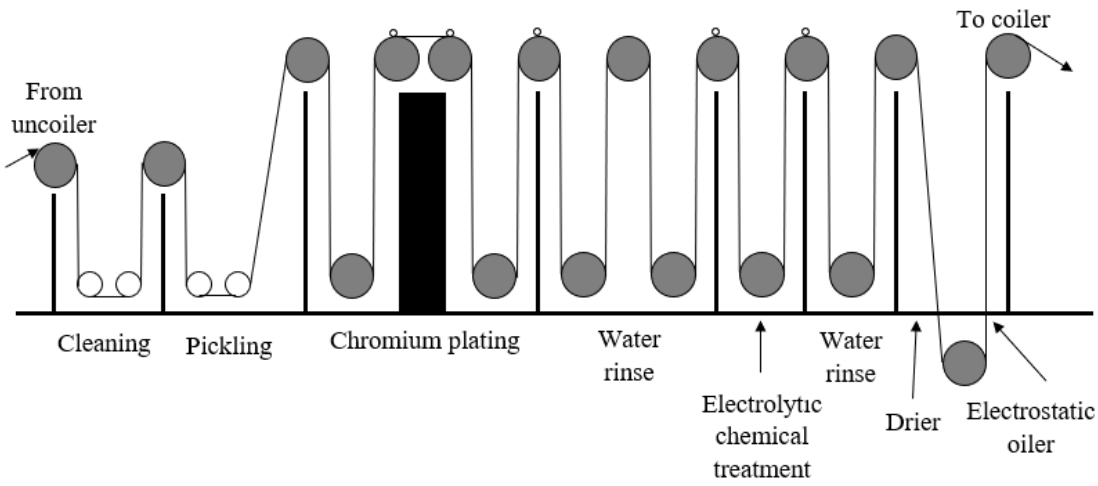

Figure 1.11. The various stages in the ECCS coating line.

TCCT® is also produced via electrodeposition and involves similar steps to the ECCS coating line; cleaning, pickling, plating and rinsing. The process of manufacturing TCCT® has undergone numerous iterations in order to create a product that performs as well as and if not better than ECCS. An initial one-step process, depositing a single Cr-Cr oxide layer, developed into a two-step process involving the application of a bilayer coating (31). The process involves a steel strip being passed through the electrolyte bath where it is polarised in such a way that it becomes the cathode. During the first stage a ~100 $mg.m^{-2}$ layer comprised primarily of Cr metal is deposited. Chromium carbide (Cr_3C_2) is also present due to the use of formate in the electrolyte (32). During the second stage a ~10 $mg.m^{-2}$ layer consisting primarily of Cr (III) oxide (Cr_2O_3) is applied. The first step used a bath consisting of Cr (III) sulphate, sodium sulphate, sodium formate and sulphuric acid. Sodium formate was excluded from the second bath. The amount of Cr (III) oxide deposited can be varied by adjusting numerous parameters including the line speed, the number of anodes as well as the applied plating current (32).

Work by Wijenberg et al. involved the electrodeposition of a trivalent chromium coating containing the chromium metal, carbide and oxide onto blackplate using a trivalent chromium-formate electrolyte. It was found that at equilibrium (pH 2.3), chromium primarily existed in the form of $[Cr(HCOO)(H_2O)_5]^{2+}$. Hydrogen evolution was shown to cause the pH to increase and thus, water ligands to deprotonate. Furthermore, the applied current density altered the amount of hydrogen evolution and

it was found that three different regimes existed at various current densities and mass fluxes as follows (see Figure 1.12) (32);

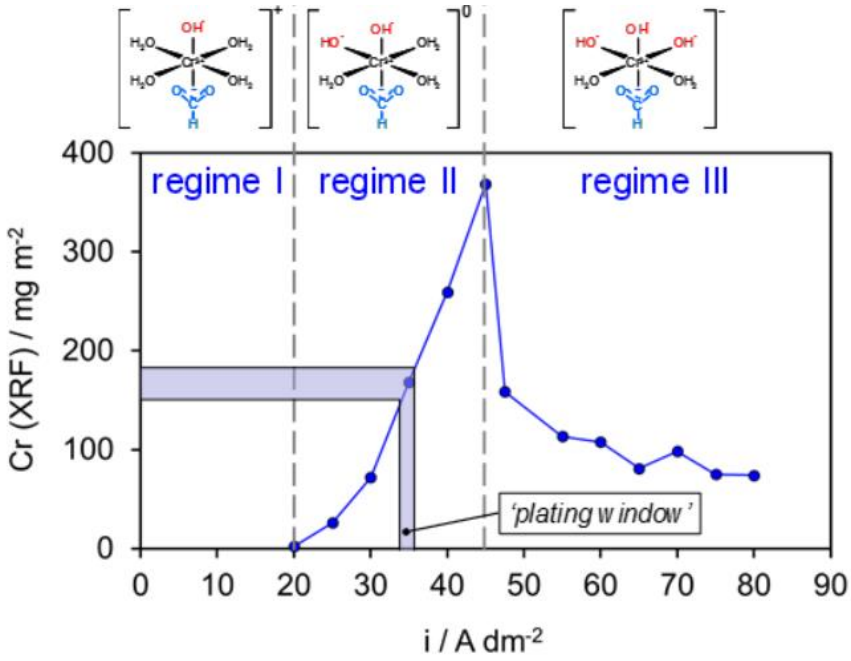

Figure 1.12. The effect of current density on Cr-Cr oxide deposition of a one-step Cr electrolyte. Three regimes and the respective chrome species present are proposed.

Regime I: no deposit is formed on the electrode as soluble $[Cr(HCOO)(OH)(H_2O)_4]^+$ is formed at the electrode at low current densities.

Regime II: $Cr(HCOO)(OH)_2(H_2O)_3$ is deposited at the electrode above a certain current density.

Regime III: a shift to $[Cr(HCOO)(OH)_3(H_2O)_2]^-$ at high current densities causes a deposition mainly composed of Cr-oxide on the electrode

The amount and composition of regime II largely corresponds to the applied current density, mass flux and electrolysis time whilst for regime III this has an insignificant effect (32). Figure 1.13 shows the composition of the coating at various current densities.

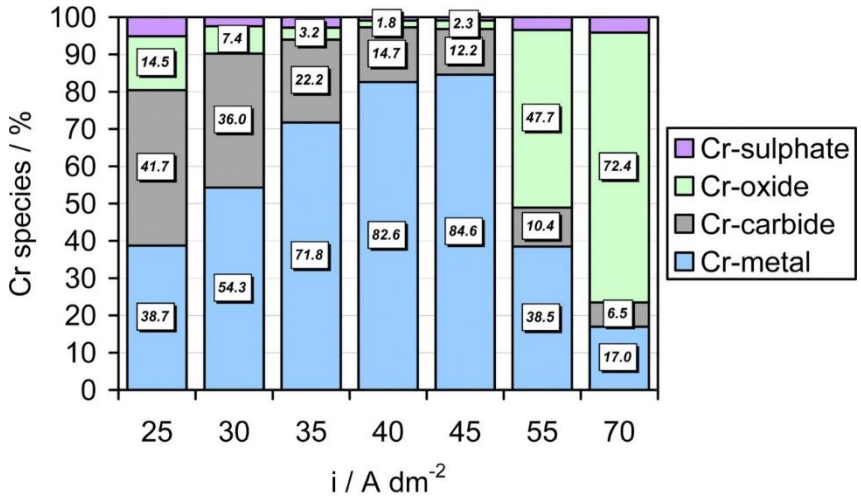

Figure 1.13: The change in coating composition due to current density (32).

During electroplating the current density must overcome a certain value (regime I) for chromium to successfully be electro-deposited. On reaching this value, the coating weight increases linearly with current density up until reaching regime III where the species that is majority plated is chromium oxide (32).

Research by (33) involved looking at the electrochemical reduction of Cr^{3+} by formic acid. Ultraviolet–visible absorption spectroscopy (UV–Vis) was used to identify the Cr complexes present in the electrolyte and XPS was used to was used to determine the products at the cathode. Usually Cr^{3+} would exist as $[Cr(H_2O)_6]^{3+}$ in solution, however, in the presence of formic acid from its regular-octahedron structure to the irregular-octahedron structure of $[Cr(H_2O)_4CHOO]^{2+}$ (via an intermediate of $[Cr(H_2O)_5CHOO]^{2+}$). This change in structure enables the Cr^{3+} ion to come into contact with the cathode enabling it to readily accept electrons to become $[Cr(H_2O)_4CHOO]^{+}$. From here removal of the H_2O molecules is relatively easy and the Cr^{2+} can readily be reduced.

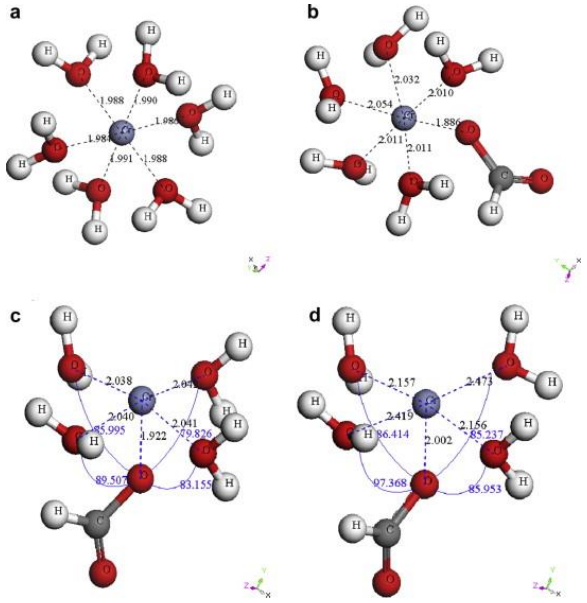

Figure 1.14: The structural formulas of (a) $[Cr(H_2O)_6]^{3+}$, (b) $[Cr(H_2O)_5CHOO]^{2+}$, (c) $[Cr(H_2O)_4CHOO]^{2+}$ and (d) $[Cr(H_2O)_4CHOO]^{+}$ (33).

1.14 Corrosion inhibitors

Corrosion inhibitors act to suppress the rate of corrosion and often, only a small concentration is needed to be effective. There are various types, some of which include cathodic, anodic and mixed type inhibitors which hinder the cathodic, anodic or both processes respectively.

Anodic inhibitors can react with metal ions to form low-solubility precipitates as a means of controlling metal dissolution. The precipitates block the anodic site thus reducing the rate of the anodic reaction and lowering the current with respect to the Evans diagram (Figure 1.15).

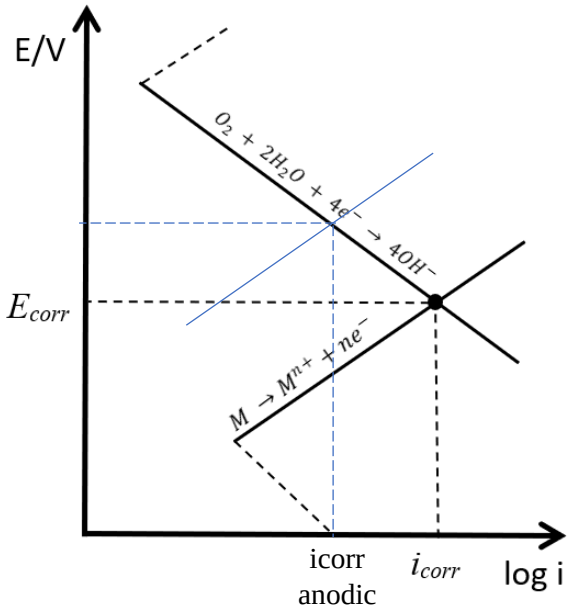

Figure 1.15. Evans diagram corresponding to anodic inhibition.

Like anodic inhibitors, cathodic inhibitors can precipitate insoluble layers, but this occurs at the site of cathodic activity. Often the additions form oxides or hydroxides at the cathodic site, in turn limiting the amount of oxygen reaching the surface, thus retarding the rate of corrosion. Although less effective than anodic inhibitors, cathodic inhibitors do offer the advantage of lowering the free corrosion potential as well as the corrosion current, as demonstrated in Figure 1.16.

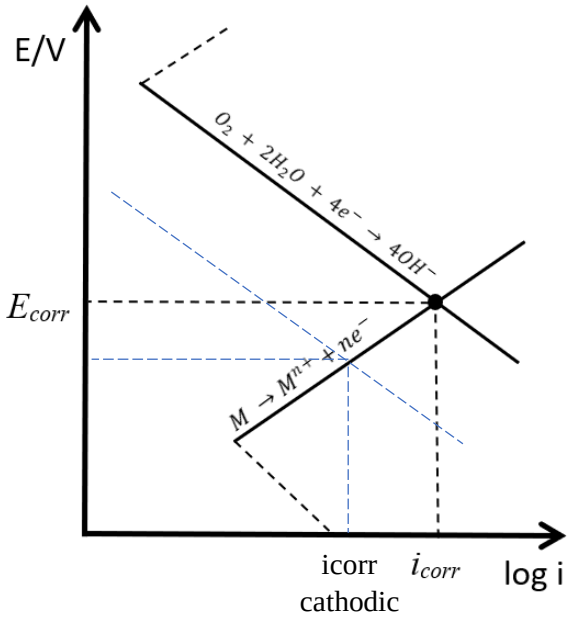

Figure 1.16. Evans diagram corresponding to cathodic inhibition.

Within industry corrosion inhibitors offer a great means of corrosion protection. Chromates (CrO_4^{2-}) are renowned corrosion inhibitors which are used for a wide range of applications. They function as both anodic and cathodic inhibitors and thus, can retard the rate of both metal dissolution and cathodic reduction reactions in various environments. They have been successfully incorporated into coating systems due to their impressive ability to work at a variety of pHs. For example, at a scratch defect the chromate ion is able to leach into the electrolyte and undergo cathodic reduction to create a protective Cr (III) oxide film which is insoluble in a wide range of pHs (equation 1.12) (34).

$$2CrO_4^{2-} + 5H_2O + 6e^- \rightarrow Cr_2O_3 + 10OH^- \qquad (1.12)$$

However, due to toxicity issues associated with chromate compounds, as previously mentioned, environmentally friendly corrosion inhibition systems have become of significant interest across numerous industrial sectors in recent years.

Hence, a range of research has been done on the effect of amino acids as corrosion inhibitors. These organic compounds offer many advantages as they are non-toxic, biodegradable and economically viable (35). Amino acids may act as anodic or

cathodic inhibitors, depending on experimental conditions. This is due to changes in adsorption behaviour, however, it has been commonly reported that amino acids act as mixed type inhibitors (36). It is well known that organic inhibitors can adsorb onto metallic surfaces via nitrogen and oxygen atoms (37), and the same can be considered in the case of amino acids. Research into the inhibitory effect of amino acids on steel in acidic conditions found, by means of polarisation measurements, that they were indeed effective inhibitors (38). They worked to inhibit corrosion by adsorption onto the steel surface. The extent of inhibition was determined by the type and concentration of amino acid used. Work by Dai et al. reported that glutamic acid and aspartic acid could inhibit corrosion on copper by adsorption onto the surface through their polar sites (39). Furthermore, glutamic acid has been shown to coordinate with metals by means of its two carboxyl groups and in turn, inhibit corrosion on steel. Numerous techniques including weight loss, electrochemical measurements and microscopy were used to investigate the inhibition efficiency of glutamic acid and to characterise the protective film formed on the metal surface (40).

A different study evaluated the inhibitory effect of glutamic acid, leucine, methionine, and alanine on carbon steel using techniques including weight loss, and microscopy. Again, their inhibitory effects were due to their adsorption on the metal surface. It was found that alanine provided the most impressive inhibition efficiency (40).

Alanine ($C_3H_7NO_2$) is a very common amino acid present in many proteins and enzymes. Due to the presence of amino and carboxyl functional groups, alanine may have a negative or positive charge, pH dependant. At a pH of 6.04 (the isoelectric point of alanine), the molecule will have a net charge of 0. The pKa values of alanine are 2.34 and 9.69, meaning it is predominantly in its zwitterion form in between this environment (41). Below and above these pH values alanine will be cationic or anionic, respectively. In the protonated form, alanine will be highly attracted to cathodic areas of metal.

Computer modelling has previously been used to investigate the use of alanine as a corrosion inhibitor on iron as well as its mechanism of action. Density functional theory (DFT) calculations were used to investigate the minimum energy structures of alanine molecules on iron and potential adsorption configurations, and preferred adsorption sites were generated computationally. The results indicated that alanine

could adsorb on the surface of iron by means of its nitrogen/oxygen atoms with the lone pair electrons in its molecule (42). Alanine has been looked into as a corrosion inhibitor for 5083 AA in 0.1 mol.dm^{-3} NaOH. In an alkaline environment, potentiodynamic polarisation showed that alanine acted as a functional inhibitor, with inhibition efficiency increasing with increasing inhibitor concentration. It was revealed alanine behaved as a mixed-type inhibitor that worked through chemical and physical adsorption onto the surface of the metal, retarding the dissolution of the metal into solution.

Little work experimental work on the inhibitory effects of alanine on iron has been conducted and hence, this will be examined late on in this thesis.

1.15 Types of can and their manufacture

There are two main types of can; two-piece and three-piece cans. A 2-piece can consists of a main cylindrical body attached to the bottom lid and a top lid (with an opening for food and drink cans). The three-piece can consists of a main cylindrical body as well as a separate bottom and top lid (43). Double seaming is used to connect the body of the can to the lids and stops the contents from being in contact with the outside.

The can ends are punched out of the coated steel, thus the coating must be flexible. Also, the coating should not be affected by heat treatment, an important property due to the nature of the sterilisation process. Moreover, food cans are subjected to a sterilisation temperature of up to 121 °C during the food filling process in order to ensure the safety of the food (44). Food cans must be provided with an easy opening mechanism and should also be made from a widely recycled material (e.g. steel) (45).

Steel is commonly used as a packaging material, such as that for cans, for several reasons. These include its great strength and ductility; allowing it to be moulded into various desired shapes as well as its high melting temperature so that it will not be affected by the increase in temperature during sterilisation.

A range of high strain rates, temperatures and pressures are used during can production. Adhesion of the organic coating must be sufficient to withstand mechanical deformation of the steel during the can making process as well as the

conditions used during sterilisation. The adhesion of the coating to ECCS is impressive and sufficiently withstands significant mechanical deformation. The food and beverage industry states that the material must not exhibit any visible, or invisible damage after production and during the prolonged shelf-life, as this compromises the quality of the canned content (23). Hence, it is important that TCCT® offers similar properties, with regards to mechanical deformation, as ECCS.

1.16 Scanning Kelvin Probe (SKP)

Corrosion rate correlates to corrosion potential and this is useful when utilising various electrochemical techniques including the scanning kelvin probe (SKP).

First founded by Lord Kelvin and later developed by Stratmann et al. in the mid-1980s, the SKP is a non-invasive technique used to measure the surface electrical potential of a material, thus allowing for electrochemical mapping of localized corrosion. Stratmann focused the application of the SKP towards examining the effect of atmospheric corrosion on metallic surfaces (46). It has been demonstrated that the SKP can be used to investigate atmospheric corrosion as well as cathodic delamination.

The SKP will be a useful technique with regards to research into TCCT®. Cathodic disbondment, as described earlier, is a detrimental defect that is known to occur on this type of material. The SKP will enable the monitoring of under-coating corrosion phenomena originating from coating defects; in this case delamination of the coating from the metal by means of the cathodic disbondment mechanism. The delamination front will produce a positive value, differing from the usual large negative value. The SKP was used in research by Wint et al. to investigate cathodic disbondment rates (18). ECCS was studied over 96 hours but cathodic disbondment did not occur in this period. Alternatively, the Cr^{3+} coating did display cathodic disbondment.
In the research presented here, the Scanning Kelvin probe was used to measure and analyse the kinetics of corrosion-driven cathodic disbondment of organic polymer films adhered to TCCT® steel.

1.17 Scanning Vibrating Electrode Technique (SVET)

In essence, the scanning vibrating electrode technique (SVET) spatially resolves areas of dissimilar electrochemical activity on the surface of a metallic sample under

immersion conditions. The technique provides a way of gaining a mechanistic understanding of surface corrosion events as well as the prediction of corrosion behaviour, in aqueous conditions. The SVET gives values for anodic current density which in turn can be used to provide a semi quantitative value for metal loss. The monitoring of corrosion behaviour using the SVET offers similar predictions to long-term, alternative weathering techniques (47).

1.18 Electrochemical techniques

Potentiodynamic polarisation, open circuit potential (OCP) as well as EIS measurements are ways of monitoring the corrosion behaviour of a material.

OCP measurements determine the free corrosion potential in a set environment. The setup is found in the experimental chapter and makes use of a working electrode and a reference electrode, in this case a KCl saturated calomel electrode (SCE). The time dependent potential is measured with respect to the reference electrode. The measurements are useful for providing information on the substrate's relative thermodynamic susceptibility to corrosion.

The setup for potentiodynamic polarisation is found in the experimental chapter and consists of a three-electrode set up, submerged in electrolyte. Potentiodynamic polarisation is useful for characterising the relative performance of substrates in similar conditions. The initiation and propagation of corrosion, as well as the breakdown and reestablishment of passive films can also be ascertained. The working electrode is polarised away from its free corrosion potential to cathodic or anodic over potentials and the change in current (reaction rate) is measured. The results are plotted on an Evans style axis of E vs log*i*.

EIS is an electrochemical technique that measures the impedance of a system. It can be used to understand the mechanism of corrosion processes. In short, it utilizes an alternating current signal over a wide range of frequencies in order to create an impedance spectrum of the electrochemical cell being tested.

To measure the impedance, a potential wave is applied to the working electrode and the resultant current wave is recorded. Z, Φ, $Z_{real,}$ and Z_{imag} are extracted from these waves and a spectrum is produced by recording these parameters for potential waves at varying frequencies (48).

In a conventional electrochemical cell, numerous electrochemical processes occur at the electrolyte/interface, including charge, transfer, mass transfer from the bulk solution to the electrode as well as resistance of the electrolyte. These features can be simulated by an electrical circuit using resistors, capacitors or constant phase elements, connected in parallel or series to create an equivalent circuit. This equivalent circuit can be used to understand and evaluate the individual components of the EIS system (48).

1.19 Fourier-Transform Infrared (FTIR) Spectroscopy

FTIR Spectroscopy involves passing an infrared beam through an Attenuated Total Reflectance (ATR) crystal, which has a high refractive index, where it reflects numerous times off the sample under investigation. The internal reflectance creates an evanescent wave which extends beyond the surface of the crystal. The evanescent wave is attenuated in regions of the IR spectrum that the sample absorbs energy. The detector measures the attenuated IR beam in the form of an interferogram signal which is then converted into an IR spectrum (49). Moreover, molecular bonds will oscillate differently and at different wavelengths which enables the characterisation of absorption wavelengths for specific functional groups. The absorption peaks can be compared to known peak locations for different functional groups which enable the functional groups present in a sample to be identified.

1.20 X-ray photoelectron spectroscopy (XPS)

Surface characterisation of a material is important as it provides information as to why a material is behaving in a certain way with regards to properties such as corrosion rate, adhesion and failure mechanisms. XPS is a quantitative technique that is used for determining the surface chemistry of a material; it can provide information about elemental composition, empirical formula, chemical state and electronic state of the elements within a material in a relatively short time frame (50). It has a sampling depth of 10nm and involves firing a beam of x-rays at a sample of interest. Consequently, electrons are emitted and their kinetic energy measured (50). A schematic of how XPS works can be seen in Figure 1.17.

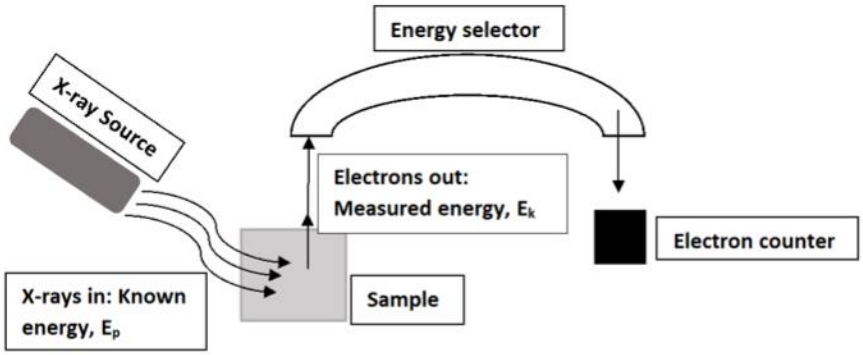

Figure 1.17 Schematic of the main principles of the XPS.

A spectrum of the elemental composition of the material is then produced, similar to the one seen in Figure 1.18Figure 1.18. It can be seen which atom as well as which shell the electron was emitted from (50).

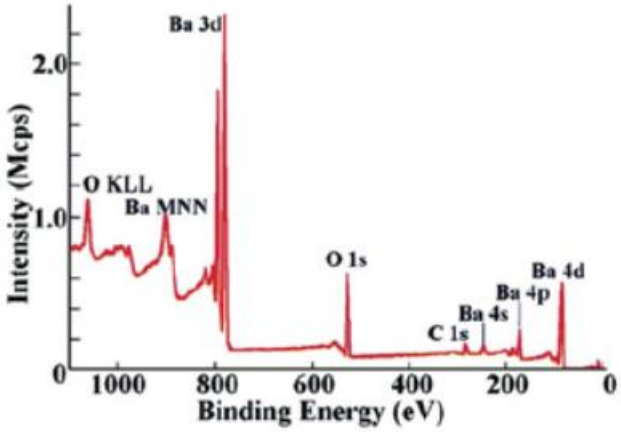

Figure 1.18: An example of a spectra produced from XPS for barium oxide (40).

As it is the surface of the material that is being analysed, impurities can easily be picked up from this technique. For example, improper handling of the sample can lead to carbon from your fingers contaminating the sample.

XPS will be a useful technique with regards this work. It will help to determine the surface composition of TCCT®. Knowing the surface composition of TCCT® will also provide insights as to why certain properties (e.g. corrosion resistance) of TCCT® are different to ECCS.

Analysis of the spectrum of TCCT® was expected to show the presence of the metal, oxide and carbide of chromium as well as some iron. More iron would be expected to

be present in TCCT® than ECCS. Changing the composition of the TCCT® coating would potentially alter the amount of iron present. Conclusions may be drawn with regards to the amount of iron present on the surface and the respective corrosion resistance. It was expected that the more iron present, the lower the corrosion resistance the sample will have.

1.21 Summary

The literature showed that various research has been undertaken with regards to relevant chromium oxides or similar. The findings of this work can be summarised as follows.

Due to changes in legislation, regarding the use of hexavalent chromium, the need for a new packaging material to replace ECCS is a necessity. It is important that the replacement performs as well as, if not better than ECCS. There are several properties that are important within packaging materials some of which include corrosion resistance, good adhesion of the coating to the substrate as well as the product being aesthetically pleasing. If the material does not provide the right properties for its job it could lead to drastic consequences and end up costing the company a lot financially.

The need for corrosion protection in canned produce is of utmost importance with regards to the health and safety of the consumer. The aesthetics of the can may also be affected by corrosion, again reinforcing the importance of a reliable coating. Failure of the product to offer a reliable coating may result in the shortening of the shelf-life of the product, customer rejection or even worse a health and safety risk. Ultimately this could cause damage to the company financially as well as to its reputation.

Previous research has given insights as to where and why certain coatings fail as well as what is the strongest proposal for a replacement thus far. It appears that the two-electrolyte process, which deposits two separate layers consisting of mainly chromium metal and chromium oxide respectively, seems to be the most promising approach for an ECCS replacement.

Research thus far has shown that variants of TCCT®/Cr^{3+} coatings possess some promising properties suggesting that TCCT® will become a replacement for ECCS in

the not-too-distant future. There are still, however, some properties where TCCT® is outperformed by ECCS.

This literature review has highlighted some of the issues that can arise on packaging materials such as FFC and cathodic delamination. It has also enlightened some of the differences in the chemical make-up of TCCT® and ECCS and thus some reasons why, as of yet, TCCT® does not outperform ECCS in every domain.

It has been hypothesized that an increased coating weight of oxide layer can offer a better resistance against some types of corrosion, and this is something that will be investigated.

Furthermore, although there is limited literature available with regards to TCCT®, it has been demonstrated that FFC has previously been shown to occur on Cr^{3+} based coatings (18).

Filiform experiments will thus be conducted on the most recent version of TCCT®. Its performance will be compared against the leading product, ECCS. Depending on the outcome of this experiment, the mechanism, kinetics and rates of FFC on TCCT® may be investigated. For example, differences in the optical appearance of the surface as well as surface chemistries may be looked into in order to identify why performance may be hindered in comparison to ECCS.

TCCT® and similar Cr^{3+} coatings have also showed evidence of cathodic delamination. This has been reduced, however, with the increase in the thickness of the oxide layer.

Experimenting with the amount of oxide or even other species plated could lead to another avenue of research in terms of getting closer to the best chemical make up in order to protect against corrosion.

Potentiodynamic polarisation measurements will enable the corrosion rates of samples with varying parameters to be established. Identifying why certain samples are more resistant against anodic or cathodic polarisation than others will establish what changes could be made to improve TCCT®.

Moreover, electrochemical techniques will be used to give an understanding on how corrosion effects coating integrity and if changes can be made to reduce the risk of

corrosion. The corrosion resistant properties of TCCT® must be investigated under various conditions in order to represent the various environments that the can will be subject to whilst filled with food or drink. The SKP and SVET will be useful techniques for comparing the corrosion resistance of different substrates. However, such research will not necessarily uncover all the potential faults of TCCT® and only long term use of the product will draw attention to any features that still need improving (11).

1.22 References

1. Koch G. 1 - Cost of corrosion. El-Sherik A., editor. Trends in Oil and Gas Corrosion Research and Technologies. Elsevier Ltd; 2017. 3-30 p.
2. Birgit G. Can coatings [Internet]. 2016 [cited 2019 Jan 18]. Available from: https://www.foodpackagingforum.org/food-packaging-health/can-coatings
3. Oldring PKT, Nehring U. Packaging Materials 7 . Metal Packaging. 2007.
4. Deng Y, Wang M, Tian T, Lin S, Xu P, Zhou L. The Effect of Hexavalent Chromium on the Incidence and Mortality of Human Cancers : A Meta-Analysis Based on Published Epidemiological. 2019;9.
5. Petry T, Knowles R, Meads R. An analysis of the proposed REACH regulation. 2007;44(2006):24–32.
6. Bardal E, editor. Introduction. In: Corrosion and Protection. London: Springer London; 2004. p. 1–4.
7. Electrochemical Series - Study Page [Internet]. [cited 2023 Feb 1]. Available from: https://www.studypage.in/chemistry/electrochemical-series
8. Pourbaix M. Atlas of Electrochemical Equilibria in Aqueous Solutions. Oxford: Pergamon Press; 1966.
9. Hihara LH. Chapter 1 Electrochemical. In: Intelligent Coatings for Corrosion Control. Elsevier Inc.; 2015. p. 1–15.
10. Lyon S., Bingham A., Mills D. Advances in corrosion protection by organic coatings: What we know and what we would like to know. Prog Org Coatings.

2017;102:2–7.

11. Fitzsimons B, Parry T. Paint and Coating Failures and Defects. In: Shreir's Corrosion. 2010. p. 2728–45.

12. Charbonneau J. Recent Case Histories of Food Product – Metal Container Interactions Using Scanning Electron Microscopy – X-Ray Microanalysis. 1997;19:512–8.

13. Sharman CF. Filiform Underfilm Corrosion of Lacquered Steel Surfaces. Nature. 1944;153:621.

14. Figueira RB, Sousa R, Silva CJR. Multifunctional and smart organic–inorganic hybrid sol–gel coatings for corrosion protection applications. Adv Smart Coatings Thin Film Futur Ind Biomed Eng Appl. 2020;57–97.

15. Watson TM, Coleman AJ, Williams G, Mcmurray HN. The effect of oxygen partial pressure on the filiform corrosion of organic coated iron. Corros Sci. 2014;89:46–58.

16. Mcmurray HN, Williams G. 2.14 -Under Film / Coating Corrosion. Shreir's Corros. 2010;2:988–1004.

17. Popov BN. Chapter 7 - Pitting and Crevice Corrosion. In: Popov BNBT-CE, editor. Amsterdam: Elsevier; 2015. p. 289–325.

18. Wint N, de Vooys ACA, McMurray HN. The corrosion of chromium based coatings for packaging steel. Electrochim Acta. 2016;203:326–36.

19. Wijenberg J, Steegh M, Penning JP, Portegies Zwart I. Wo 2014/079909. 2014.

20. Øystein O, Knudsen AF. Corrosion Control Through Organic Coatings. Second. Schweitzer PA, editor. New York: Taylor & Francis; 2017.

21. Nazarov A, Thierry D. Application of Scanning Kelvin Probe in the Study of Protective Paints. 2019;6:1–17.

22. Warren DJ, McMurray H, de Vooys ACA. Localised SKP Studies of Cathodic Disbondment on Chromium/Chromium Oxide Coated Steel. Electrochem Soc Trans. 2013;50:67–78.

23. Boelen B, Hartog H Den, Weijde H Van Der. Product performance of polymer coated packaging steel , study of the mechanism of defect growth in cans. 2004;50:40–6.

24. Whiteside J, de Vooys ACA, Sackett E, McMurray HN. Influence of uniaxial deformation on surface morphology and corrosion performance of chromium-based coatings for packaging steel. Corros Sci. 2021;190:109662.

25. Leng A, Streckel H, Hofmann K, Stratmann M. The delamination of polymeric coatings from steel Part 3: Effect of the oxygen partial pressure on the delamination reaction and current distribution at the metal/polymer interface. Corros Sci. 1998;41(3):599–620.

26. Stratmann M, Streckel H. On the atmospheric corrosion of metals which are covered with thin electrolyte layers-II. Experimental results. Corros Sci. 1990;30(6–7):697–714.

27. Kamm GG, Willey AR, Linde NJ. Surface and Corrosion Characteristics of Tin-Free SteelmChromium Type for Beverage Containers. :1299–305.

28. Wijenberg J. Method for electrodeposition of chromium containing coatings from trivalent chromium based electrolytes. WO 2014/079911 A2, 2014.

29. Liang A, Ni L, Liu Q, Zhang J. Structure characterization and tribological properties of thick chromium coating electrodeposited from a cr(III) electrolyte. Surf Coatings Technol. 2013;218(1):23–9.

30. Martyak NM. Deposition of chromium oxides from a trivalent chromium solution containing a complexing agent for a buffer. United States Patent; 6,004,448, 1999.

31. Wijenberg J, Hubert J. Oversættelse af europæisk patentskrift. WO2014202316, 2017.

32. Wijenberg JHOJ, Steegh M, Aarnts MP, Lammers KR, Mol JMC. Electrodeposition of mixed chromium metal-carbide-oxide coatings from a trivalent chromium-formate electrolyte without a buffering agent. Electrochim Acta. 2015;173:819–26.

33. Zeng Z, Sun Y, Zhang J. The electrochemical reduction mechanism of

trivalent chromium in the presence of formic acid. Electrochem commun. 2009;11(2):331–4.

34. Kloet J Vander, Schmidt W, Hassel AW, Stratmann M. The role of chromate in filiform corrosion inhibition. Electrochim Acta. 2003;48(9):1211–22.

35. Mobin M, Zehra S, Parveen M. l-Cysteine as corrosion inhibitor for mild steel in 1 M HCl and synergistic effect of anionic, cationic and non-ionic surfactants. J Mol Liq. 2016;216:598–607.

36. Khaled KF. Corrosion control of copper in nitric acid solutions using some amino acids - A combined experimental and theoretical study. Corros Sci. 2010;52(10):3225–34.

37. Nady H. Tricine [N-(Tri(hydroxymethyl)methyl)glycine] – A novel green inhibitor for the corrosion inhibition of zinc in neutral aerated sodium chloride solution. Egypt J Pet. 2017;26(4):905–13.

38. Ashassi-Sorkhabi H, Majidi MR, Seyyedi K. Investigation of inhibition effect of some amino acids against steel corrosion in HCl solution. Appl Surf Sci. 2004;225(1–4):176–85.

39. Dai W, Zhang Y. Molecular dynamics simulation of the adsorption behavior of amino acid corrosion inhibitor on Cu (001) surface. Appl Mech Mater. 2012;121–126:226–30.

40. Hamadi L, Mansouri S, Oulmi K, Kareche A. The use of amino acids as corrosion inhibitors for metals: A review. Egypt J Pet. 2018;27(4):1157–65.

41. PubChem. Alanine [Internet]. Available from: https://pubchem.ncbi.nlm.nih.gov/compound/Alanine#section=Dissociation-Constants

42. Khaled K., Abdelshafi N., El-Maghraby A., Aouniti A, Al-Mobarak N, Hammouti B. Alanine as Corrosion Inhibitor in Acid Medium: A Molecular Level Study. Electrochem Sci. 2012;7:12706–19.

43. Nayar SK, Munn BJ. EXPANDED CANS. Vol. 1. WO99/39981, 2001.

44. Abdul Ghani AG, Farid MM, Chen XD. Numerical simulation of transient

temperature and velocity profiles in a horizontal can during sterilization using computational fluid dynamics. J Food Eng. 2002;51(1):77–83.

45. Page B, Edwards M, May N. Metal cans. In: Coles R, McDowell D, Kirwan M, editors. Food Packaging Technology. Blackwell publishing; 2003. p. 120–1.

46. Stratmann M, Leng A, Fiirbeth W, Streckel H, Gehmecker HI. The scanning Kelvin probe; a new technique for the in situ analysis of the delamination of organic coatings. Org Coatings. 1996;27(1–4):161–267.

47. Worsley DA, McMurray HN, Sullivan JH, Williams IP. Quantitative Assessment of Localized Corrosion Occurring on Galvanized Steel Samples Using the Scanning Vibrating Electrode Technique. Corrosion. 2004;60(5):437–47.

48. Magar H., Hassan RY., A M. Electrochemical Impedance Spectroscopy (EIS): Principles, Construction, and Biosensing Applications. Sensors. 2021;19(6578).

49. ThermoFisher. FTIR Sample Techniques: Attenuated Total Reflection (ATR) [Internet]. [cited 2022 Feb 1]. Available from: https://www.thermofisher.com/us/en/home/industrial/spectroscopy-elemental-isotope-analysis/spectroscopy-elemental-isotope-analysis-learning-center/molecular-spectroscopy-information/ftir-information/ftir-sample-handling-techniques/ftir-sample-handling-tec

50. Scientific Thermo Fisher. Learn XPS [Internet]. 2019. Available from: https://xpssimplified.com/whatisxps.php

2 Experimental methods

The work carried out during this research involves the characterization of novel coatings for packaging steels and compares them to traditional, commercialized products. This section outlines the materials and chemicals used, alongside the experimental techniques followed.

2.1 Materials

The majority of work conducted in this thesis has focussed on investigating a variety of chromium coated steel substrates, ECCS and TCCT®.

TCCT® samples consisted of electroplated low carbon steel coated and were obtained from Tata Steel Packaging IJmuiden. A two-stage electroplating process was used to apply a bilayer coating to the steel substrate and the coating weights were as supplied from Tata Steel. In the first stage a 100 $mg.m^{-2}$ Cr metal layer was applied to all samples. A Cr oxide layer of varying coating weight (2 $mg.m^{-2}$ to 23.5 $mg.m^{-2}$) was applied during the second step. The coatings were produced using bath chemistries described in section 1.11. The variation in the amount of Cr (III) oxide deposited was achieved by varying numerous parameters including the line speed, the number of anodes as well as the applied plating current.

ECCS, produced on the pilot coating line using Cr (VI) electrolyte, had an as received Cr oxide coating weight of 9 $mg.m^{-2}$.

Low carbon steel (blackplate – the substrate metal of TCCT) of 0.2 mm was sourced from Tata Steel, Trostre UK

A model organic coating, poly(vinyl) butyral co-acetate (PVB) was used as an overcoat for certain experiments. PVB with a molecular weight of 70,000 – 100,000 was made into a 15.5% (w/w) ethanolic solutions of PVB. The PVB solutions were placed in an ultrasound bath to remove trapped gas bubbles from the solution. Although PVB does not represent the fully formulated product, its solubility in non-toxic solvents such as ethanol allows for ease of safe formulation within a lab environment. It dries at room temperature and allows for comparisons to be made easily between samples. The coating produced dries at room temperature and offers

good adhesion to the substrate, this being made possible by the presence of both hydrophobic and hydrophilic monomers. (1)(2).

The chemicals used, and their respective supplier and purity can be seen in Table 1.

To make up stock solution the following equations were used.

$$n = C\ x\ V \qquad (2.1)$$

Where n is the number of moles, C the concentration, and V the volume of solution.

$$n = \frac{M}{Mr} \qquad (2.2)$$

Where n is the number of moles, M is the mass and Mr the molar mass.

Table 1: List of the chemicals used throughout this thesis.

Chemical	**Supplier**	**Purity, Grade**
PVB	Sigma-Aldrich	Analytical grade
De-ionised water, H_2O	*In situ*	Analytical grade
Isopropanol	Sigma-Aldrich	Analytical grade
Sodium chloride, NaCl	Sigma-Aldrich	Analytical grade
$FeCl_2$	Sigma-Aldrich	Analytical grade
Non-corrosive silicone sealant	RS components Ltd	Analytical grade
Sodium hydroxide, NaOH	Sigma-Aldrich	Analytical grade
Sulfuric acid, H_2SO_4	Sigma-Aldrich	Analytical grade
Phenolphthalein	Sigma-Aldrich	Analytical grade
Chromium(III) sulfate hydrate	Fisher Scientific	Analytical grade
Sodium sulfate	Fisher Scientific	Analytical grade
Sodium formate	Sigma-Aldrich	Analytical grade
Alanine	Sigma-Aldrich	Analytical grade
Phenylalanine	Sigma-Aldrich	Analytical grade

2.2 Electrochemical techniques overview

2.2.1 Filiform corrosion (FFC)

Details of the methodology adopted during FFC experiments follows that described elsewhere (3). In brief, 5 cm x 5 cm coupons were cut from a larger sheet of either TCCT® or ECCS and degreased with isopropanol (IPA). Electrical tape, with a known thickness, was applied to two parallel edges of the sample and acted as a height guide during coating of PVB. A glass rod was used to bar-cast the samples with PVB, in line with the rolling direction, resulting in an air-dried thickness of 30 µm as measured using a micrometer screw gauge.

Once the PVB was dry, three 1 cm long artificial scribe defects were made in the PVB coatings, perpendicular to the rolling direction, using a scalpel, as shown in Figure 2.1. The direction of filiform propagation often aligns with the rolling direction (4), thus it was proposed that kinetic data would be more easily obtained if the filaments were predominantly travelling in a straight line. To compare results accurately between samples it was also important that the scribe direction was kept consistent. A syringe was used to introduce 2 µl of 0.005 M $FeCl_2$ electrolyte into the scribe which has been shown to initiate FFC on iron and Cr (III) coated steel elsewhere (5)(1).

Samples were then placed in a chamber where the temperature and relative humidity were kept constant at 20°C and 75 % R.H. respectively (6). The humid atmosphere was maintained using a saturated NaCl solution and measured using a ThermoPro TP50 digital humidity sensor inside the chamber.

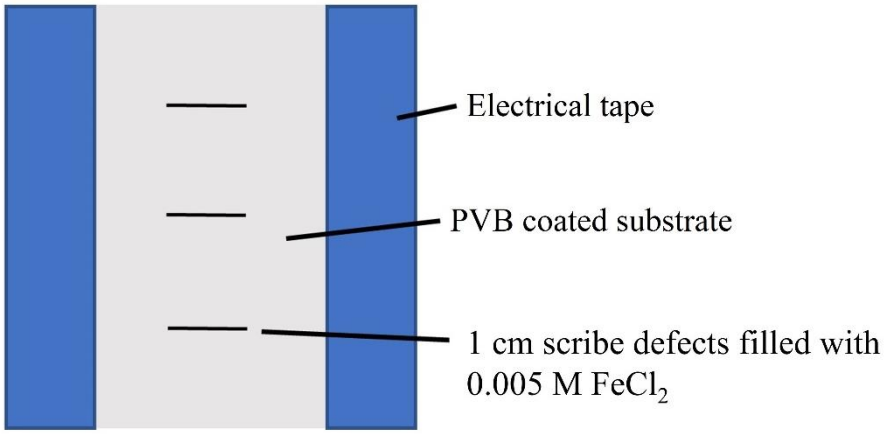

Figure 2.1. Schematic of a filiform specimen with three artificial scribe defects filled with 2 µl of 0.005 M FeCl2 electrolyte.

Samples were removed from the chamber at weekly time intervals over a period of 4 weeks to obtain photographs. Image analysis was carried out to calculate the area of FFC. The images were loaded into GIMP image analysis software which was calibrated by specifying a pre-measured distance between two points and inputting the actual distance. The surface discoloration of the corroded parts of the samples enabled surface area measurement to be recorded. 6 measurements were recorded for each different coating type.

2.2.2 Cathodic delamination preparation

Stratmann cells (7) were used to study cathodic delamination. Stratmann cells were made following the method of Stratmann et al. (7). In brief, 5cm x 5cm samples were cleaned with isopropanol (IPA). Following this, a strip of clear, adhesive tape was placed across the top of the sample, perpendicular to the rolling direction. Two strips of electrical tape were applied to opposite edges (perpendicular to the adhesive tape) of the sample to ensure an air-dried thickness of 30µm. A glass rod was used to bar-cast the samples with PVB to imitate an organic coating. The casting direction was parallel with the rolling direction (see Figure 2.3a).

Once the PVB was dry (1 hour) the adhesive tape and PVB was peeled back to create a lip, exposing the underlying substrate as shown in Figure 2.2. Non-corrosive silicon

sealant was applied around the edges of the exposed area to create a well to which 1 ml of 5 wt. % NaCl was added (see Figure 2.3c).

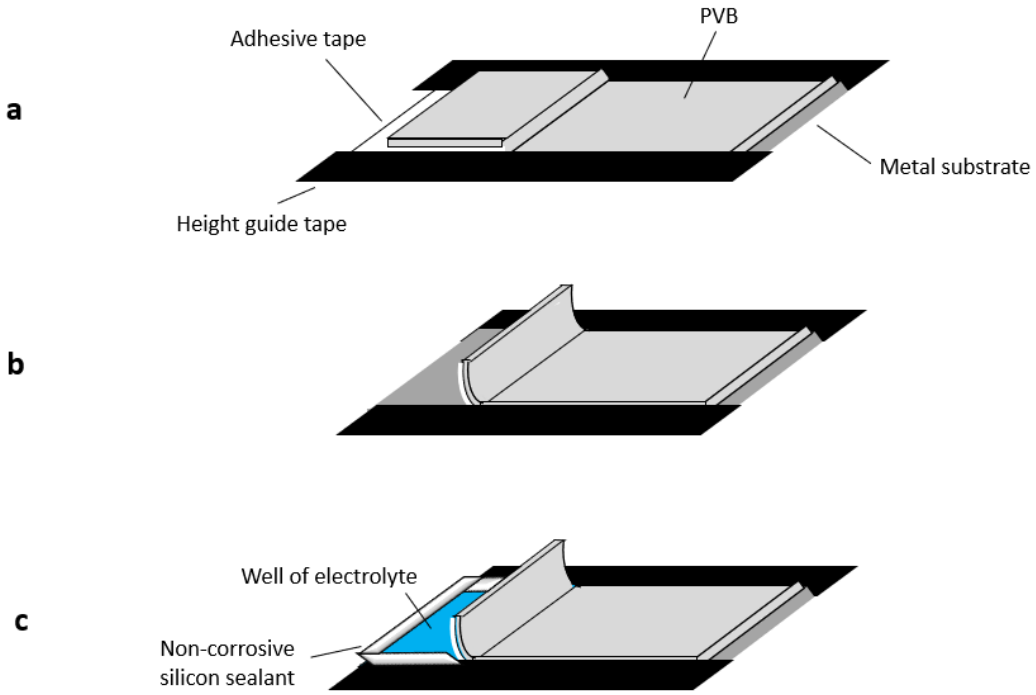

Figure 2.2. A schematic showing the making of a Stratmann cell.

Two types of experiment were conducted using Stratmann cells. For both studies Stratmann cells were placed in a humidity chamber which was maintained at 95 % R.H using 5 wt. % NaCl reservoirs. The humidity was monitored using a ThermoPro TP50 digital humidity sensor inside the chamber.

Firstly, for optical studies, 6 wt. % phenolphthalein was dissolved into the ethanolic PVB solution for pH indication (8). This ensured the change in colour could be visualised distinctly. It is also of note that phenolphthalein does not affect the rate of delamination (8). In acidic conditions (below pH 7) phenolphthalein is colourless whilst in alkaline conditions above pH 8.2 it begins to turn pink and above pH 10 it reaches a bright magenta colour (9).

The main driving force for cathodic delamination is the cathodic reaction (10):

$$O_2 + 2H_2O + 4e^- \rightarrow 4OH^- \quad (2.3)$$

The cathodic reaction causes a build-up of hydroxyl ions underneath the organic coating. Thus, an alkaline environment (over pH 10) will be present in the electrolyte underneath the delaminated part of the coating causing the phenolphthalein dissolved in the PVB to change from colourless to a bright magenta (11). The distance between the defect and the interface between the coloured and uncoloured coating is therefore the delaminated distance and can be recorded as a function of time to provide a delamination rate. An average of 3 measurements across the interface of the delamination distance was taken along the width of the sample. This optical approach is appropriate for iron but not necessarily all materials as it is easy to see the delamination front on iron, due to the colour and nature of the substrate. 3 measurements were taken for each sample type and a mean and standard deviation calculated.

The second type of study made use of the SKP which is able to record the corrosion potential underneath an organic coating as a function of distance and time. The probe tip is situated just above the sample generating the two plates of a parallel plate capacitor. Vs, as seen in Figure 2.3, is the potential difference between the two plates and this creates a charge on the probe tip. The tip oscillates which in turn generates a current which is used to calculate Vs (12). Vs is directly related to the corrosion potential of the test subject thus allowing for a map of corrosion to be made.

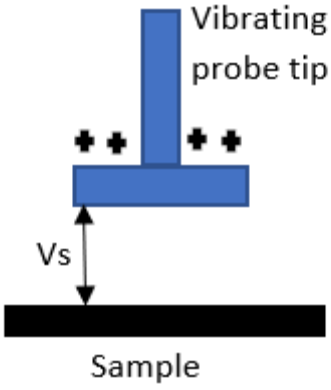

Figure 2.3. Schematic of the probe tip of the SKP.

SKP experiments are normally carried out in a humid atmosphere as in these conditions a thin layer of water forms on the surface of the sample of interest. The

water is able to take up ions from salts that are present either naturally or placed intentionally to form an electrolyte film. This then enables metal surface electrochemical reactions to become possible and the electrode potential of the surface to be measured. Under operation the metal surface and the vibrating probe tip form a parallel plate capacitor. The capacitance (C) of a parallel plate capacitor is given by,

$$C = \frac{\varepsilon\varepsilon_0 A}{d} \qquad (2.4)$$

where $\varepsilon\varepsilon$ is the dielectric constant of the capacitor dielectric, ε_0 the permittivity of vacuum, A the plate area and d the distance between plates.

The SKP can be calibrated by means of a known metal/aqueous ion redox couple, in this case a Cu/Cu^{2+} cylindrical well was used. A copper (II) sulphate solution was placed in this well and Volta potential difference values were obtained by vibrating the reference probe close to the meniscus of the well. The electrode potential was measured versus SCE using a Solartron 1280 potentiostat.

The standard reduction potential (E_{corr}) for copper is known to be 298 mV vs SHE and the value of the Cu/Cu^{2+} redox couple was measured during calibration so the SKP Volta potential for the calibration sample can be measured using the equation below:

$$E_{corr} = E_{KP} + \text{constant} \qquad (2.5)$$

The value of the constant in this calculation is for a metal-electrolyte system only and does not consider any other factors, such as the presence of a polymer film. The PVB film was determined to cause an offset of -220 mV. The value of the offset was added to the value of the constant to give the E_{corr} of the metal/polymer/electrolyte system.

As mentioned, the SKP measures the free corrosion potential (E_{corr}) against distance from the defect site (x). As cathodic delamination proceeds, $E_{corr}(x)$ profiles develop, and these have distinct regions. The intact region has the highest value for E_{corr} (often referred to as E_{intact}) as this is the region where delamination has yet to occur as no electrolyte is present for corrosion to occur. If delamination does occur, a sharp decrease in E_{corr} is observed corresponding to the delamination front at which

delamination of the coating is occurring. An E_{corr} gradient is observed between the delamination front and defect due to the ohmic resistance to ionic current flow in the underfilm electrolyte layer. Immediately adjacent to the defect the value for E_{corr} is low, relative to the intact region and ultimately becomes like that of the freely corroding metal.

To study cathodic delamination, Stratmann cells were placed in an SKP chamber which was maintained at 95 % R.H using 5 wt. % NaCl reservoirs. Scans took place every hour for 48 hours and 3 measurements were taken for each sample type.

Figure 2.4 shows an example of time dependant E_{corr} profile and the associated delamination cell that would give this profile.

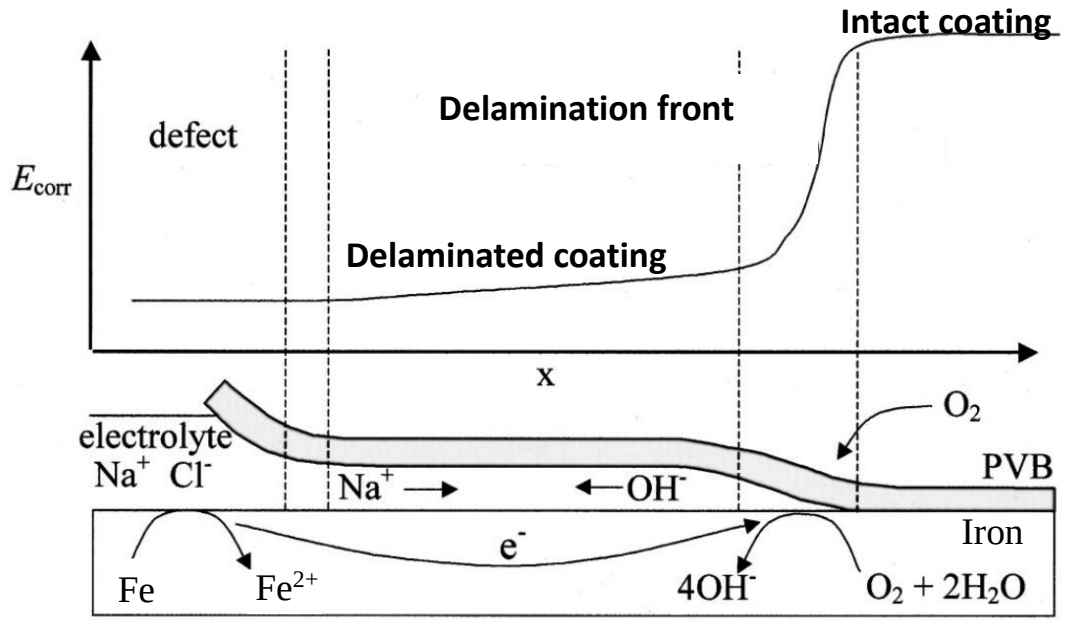

Figure 2.4. Schematic representation of the corrosion-driven delamination cell in correspondence with the relevant time-dependant E_{corr} profile. Adapted from (16).

SKP settings were constant throughout all experiments with a sensitivity of 10mV, a time constant of 50 ms and an oscillating frequency of 280 Hz.

Calibration of the SKP was performed using a Cu/Cu^{2+} redox couple. A copper (II) sulphate solution was placed into a pre-made cylindrical well and Volta potential difference values were obtained by vibrating the reference probe close to the meniscus of the copper calibration well. The electrode potential was measured versus SCE using a Solartron 1280 potentiostat. The standard reduction potential (Ecorr) for copper is a

known to be 298 mV vs SHE and the value of the Cu/Cu^{2+} redox couple was measured during calibration so the SKP Volta potential for the calibration sample can be calculated.

After calibration, the Stratmann cell was placed on the sample stage of the SKP chamber. The tip was lowered to 100 µm above the surface of the sample by raising the stage towards the probe tip, in increments of 10µm until an overload signal was recorded on the lock-in amplifier, indicating that the probe was at the sample's surface. The probe was raised to 100 µm above the sample surface and positioned at a set distance (12 mm) from the defect. Scans were taken with the SKP chamber closed, immediately following addition of the electrolyte to initiate corrosion. Scans took place every hour for 48 hours and 3 measurements were taken for each sample type.

2.2.3 Electrochemical measurements

Sample preparation

In all cases, samples of size 2.5 x 2.5cm were cut from a larger sheet and cleaned using isopropanol (IPA). The sample was held in place using an in-house manufactured sample holder. This enabled, by means of a circular gasket, a known size ($0.8cm^2$) of metal surface to be exposed to the electrolyte. A contact at the back of the sample enabled an electrical connection with the WE.

Open circuit potential

Open circuit potential (OCP) values were recorded at 20°C using a Gamry interface 1000. A 2-electrode set up was used consisting of the working electrode and reference electrode. The sample acted as the working electrode (WE), and a saturated calomel electrode (SCE) for the reference electrode. These were submerged in 250 ml of an aqueous electrolyte (NaCl). A sample period of 1s was used and a the OCP was recorded over a variety of times were used, experiment dependent.

Potentiodynamic polarisation

For recording potentiodynamic polarisation a standard three-electrode cell set up was used and experiments were conducted at 20°C, using a Gamry interface 1000. In addition to the WE and SCE, platinum was used as the counter electrode. These were

all submerged in 250 ml of an aqueous electrolyte (NaCl). This set up is shown in Figure 2.5.

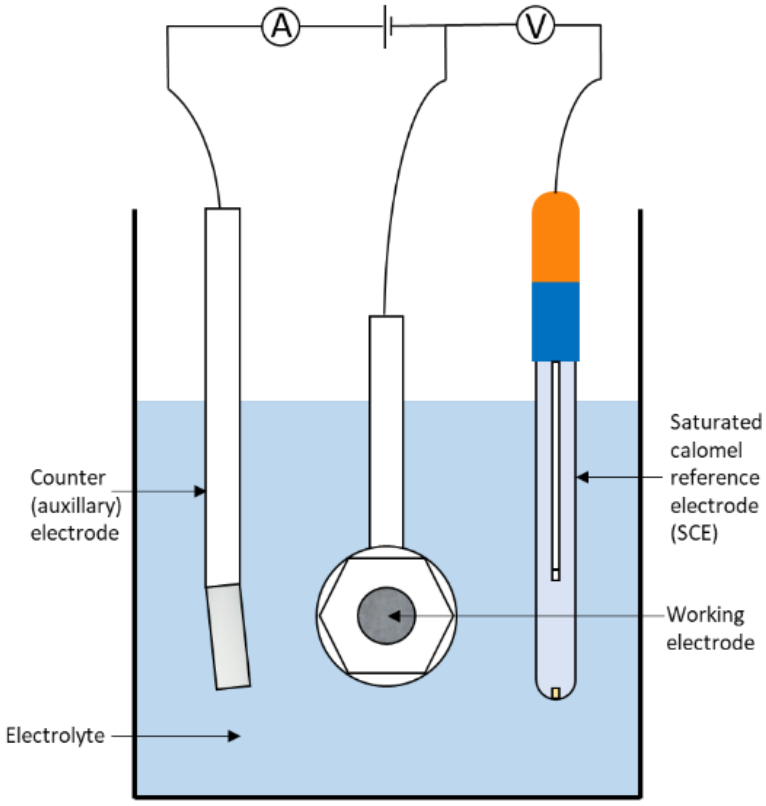

Figure 2.5: Three-electrode cell set up.

For the majority of experiments, anodic and cathodic branches of the potentiodynamic curve were acquired separately.

The cathodic polarisation sweep was conducted between 5 mV above OCP to 80 mV below OCP. The anodic polarisation sweep was conducted between 5 mV below OCP and 80 mV above OCP. A sweep rate of 0.1667 $mV.s^{-1}$ was used, the ASTM standard scan rate (13). For cathodic delamination studies, the cathodic branch of the experiment as repeated under deaerated conditions to investigate the rate that corrosion may occur on the inside of cans. Measurements were taken after sparging the electrolyte with nitrogen for 20 minutes to produce deaeration. A polyurethane film lid was placed over the beaker to keep the solution deaerated.

Electrochemical impedance spectroscopy (EIS)

A 3-electrode cell, composed of a working electrode, counter electrode and SCE reference electrode, was used for EIS. EIS measurements were carried out in the frequency range of 1 mHz to 100 kHz with 10 points per decade. The amplitude of the excitation signal was set to 10 mV relative to the OCP. Measurements were performed every 2.5 hours. The impedance data were fitted with an equivalent circuit model using Gamry Echem Analyst.

2.2.4 The Scanning Vibrating Electrode Technique (SVET)

In essence, the SVET technique spatially resolves areas of dissimilar electrochemical activity on the surface of a metallic sample under immersion conditions. The technique provides a way of gaining a mechanistic understanding of surface corrosion events as well as the prediction of corrosion behaviour in aqueous conditions. The SVET gives values for anodic current density which in turn can be used to provide a semi quantitative value for metal loss.

To utilise the SVET, the surface of the sample to be analysed is isolated using PTFE tape. The SVET uses a 125 µm platinum wire microtip encapsulated in glass. The probe tip is situated 100 µm above the surface of the sample, immersed in electrolyte. The microtip vibrates at constant amplitude, frequency and height above the immersed sample. The SVET detects alternating potential at the frequency of vibration, and this is proportional to the vertical component of the potential gradient in solution. The lock-in amplifier controls the frequency of vibration as well as measures the signal received at the microtip. Anodic and cathodic regions on the surface of the sample can be resolved at known locations and intensities. Ionic current flux that originates at any anode on the sample's surface passes through the electrolyte and causes potential fields in solution. The SVET records an alternating potential when crossing these lines of current flux, directly proportional to the vertical component of ionic current density.

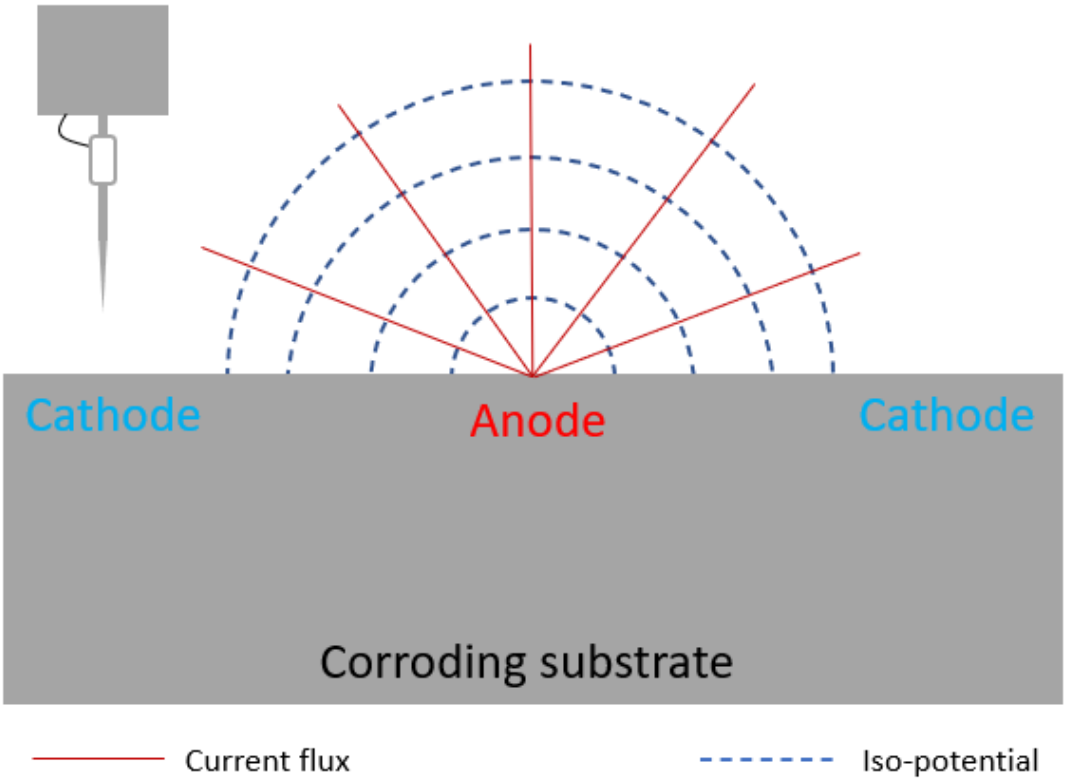

Figure 2.6. SVET operation principles above a point anodic site.

The SVET does, however, have limitations in terms of resolution. The spatial resolution of the SVET is the ability of the probe to distinguish the distance separating two localised corrosion features. Due to the Gaussian distribution of the normal electrical field strength from the point source origin, the theoretical spatial resolution of the SVET can be determined by means of the full-width half-maximum (*whm*) of the signal peak. Considering a scan height of 100 µm, used throughout this thesis, a theoretical resolution of 153 µm would result, as considered in other work (14). However, the observed *whm* value in practice is typically realised to be 0.27 mm, providing a spatial resolution of approximately 250 µm. This is partly due to the dimensions of the SVET microtip. This spatial limit means that the SVET is unable to detect localised corrosion features that are separated by a distance smaller than that stated. Hence, this highlights the ability of the SVET to view localised corrosion activity rather than generalised activity, as during the latter, potential gradients in solution terminate prior to SVET probe intersection.

Calibration of the SVET is undertaken prior to experimental procedure. The SVET records potentials in solution in nV. In order to obtain more useful data these values

must be converted into current density values ($A.m^{-2}$) by means of calibration. One method of calibration is through the use of a point current source. Under conditions that abide to Ohm's law, the current flux in the direction of vibration (jz) is correlated with the peak-to-peak voltage signal measured by the SVET (Vpp). At a point current source, current disperses from the centre evenly with a hemispherical profile Therefore, the current density in the plane of the scan (jz) can be calculated by dividing the applied current by the hemispherical surface area (equation 2.6)

$$j_z = \frac{i}{2\pi z^2} \tag{2.6}$$

Calibration involves the use of a two-compartment cell, linked by a glass tube, where each compartment contains a 1 cm^2 platinum electrode. The calibration cell is filled with the electrolyte to be used for experimentation. A range of known currents are applied using a galvanostat. The known area of the glass tube allows the current densities to be calculated for each known current. The voltage measured by the SVET for each current density leads to the formation of a linear line. From that, a gradient is obtained which can be used as the calibration factor between potential and current density. This calibration factor enables the SVET to produce results in the form of current density values.

For each map of current density distribution (j_z), a corresponding value of anodic-going current (Ia_t) can be produced by means of numerical area integration (equation 2.7).

$$Ia_t = \int_0^X \int_0^Y [j_{z(x,y)}] dxdy \tag{2.7}$$

Where ia_t is the anodic current, j_z the SVET derived current density and x,y the length and width of the SVET scan.

The resulting value for each scan is considered the total anodic current present on the scanned surface. This can be divided by the scanned sample area to give the area averaged anodic current density, Ja_t. In turn a semi quantitative value for metal loss, by the application of Faraday's law, can be produced. It is a semi quantitative value as it considers that corrosion activity remains constant between scans and the fact that the SVET measures a normal component of ionic current flux rather than direct surface

current density. To establish a value for charge, the anodic current for an individual scan is multiplied by scan time (equation 2.8).

$$Q = I \times t \tag{2.8}$$

Where Q corresponds to charge, I current and t time.

The value determined for charge can then be applied to Faraday's law to produce a value for the approximate mass loss. In the case of Fe, the total Fe lost could be determined by equation 2.9.

$$\text{Total Fe lost} = \frac{Q}{2F} \times M_{(Fe)} \tag{2.9}$$

Where Q corresponds to charge, F Faraday's constant and M_{Fe} the molar mass of iron.

Experiments that utilised the SVET were performed using 1 wt. % NaCl. The samples were allowed to freely corrode over a time period of 24 hours. Scans took place from the onset of the experiment and scanned hourly for the duration of the experiment. Calibration of the SVET was performed prior to each experiment using the two-compartment cell.

A sample size of 6 x 6 mm was isolated using PTFE tape. 61 x 61 points were recorded per scan with a distance of 0.1 mm between points.

The surface modelling software package, Surfer 10 was used for mapping the calibrated data. A false colour was imposed on the maps and defined the locations and relative intensities of the anodic and cathodic activities. Red was used for anodic regions and blue cathodic.

2.2.5 Scanning electron microscopy (SEM) / Energy Dispersive X-Ray Spectroscopy (EDS)

SEM is a widely used characterisation technique that can be used to obtain high quality images of the surface of a material. It can be used to analyse defects, such as micropores on a metal's surface. SEM works by using a focused beam of primary electrons to scan the surface of the material. On reaching the surface secondary electrons are knocked out from the material and detected by a secondary electron

detector and used to build up an image. SEM was beneficially used by Charbonneau to analyse defects, and thus causes of corrosion on food packaging. It will be used in this research in a similar way (15).

Various types of SEM at various levels of magnification were used in this research.

- Hitachi TM3000 Tabletop Microscope with a15 kV accelerating voltage for imaging of samples.
- Zeiss axio observer Z1M inverted optical microscope was used to determine the width and length of filiform filaments. Images of individual filament were captured and measuring tools on the microscope's software allowed distances across the width and length of the filaments to be measured accurately.
- Zeiss EVO SEM with a 15 kV accelerating voltage and a probe current of 250 pA for imaging samples and analysing defects.

EDS is a technique which can be used in conjunction with SEM. It identifies the elemental composition of the sample utilising an electron beam. It works by focussing a high energy electron beam on the sample which causes an electron to be ejected from the inner shell of an atom. A higher energy electron fills the hole and an x-ray, of corresponding energy difference between the higher and lower energy shell, is emitted. This energy difference is characteristic to a specific atomic element, and thus the composition can be determined. EDS was performed using the Bruker Quantax70 EDS apparatus integrated into the SEM suite.

2.2.6 X-ray photoelectron spectroscopy (XPS)

Samples of TCCT® or ECCS were cut to 1 cm x 1 cm coupons, cleaned and mounted into the machine. The sample was handled as little as possible (using tweezers) to avoid contamination which may hinder results.

XPS spectra were recorded on a Kratos Axis Ultra using monochromated Al Kα X-rays of 1486.8 eV. The measured spot size was 700 μm x 300 μm. The XPS spectra was subsequently analysed in CasaXPS software with Shirley backgrounds. Binding energies were calibrated to the main hydrocarbon peak at 284.8 eV (1).

2.2.7 Time-of-flight Secondary Ion Mass Spectrometry (ToF-SIMS)

Time of flight secondary ion mass spectrometry (ToF-SIMS) is a surface sensitive technique often used to determine what elements are present on the surface of a material. ToF-SIMS analysis was conducted using a Scientific Analysis Instruments (SAI) MiniSIMS-ToF. A gallium source was used to obtain secondary ion spectra to give elemental maps of the substrate surface. A lateral resolution of 10 µm and a mass resolution of +/- 0.1 Daltons were used. SIMS is used within this research project for:

- Analysis of surface species.
- Image mapping of corrosion phenomenon.

Chemical images and spectrums were obtained and analysed using MiniSIMS software. Chemical imaging enabled a macro scale overview of the surface chemistry present on the samples. The software was able to convert the mass spectrometry data into an image so that each pixel represented an individual mass spectrum. Different elements were assigned colours to offer a visual representation of the surface chemistry on the substrate. A dwell time of 5 ms per pixel was used and images were obtained with the detector in both positive and negative polarity to portray the positive and negative ions emitted from the surface. It is a semi quantitative technique so the data analysed must be viewed with caution. A scan size of 1024 x 1024 was used.

Some of the applications of the ToF-SIMS required removal of the organic polymer layer. This was achieved by mechanically peeling away the organic layer from the surface of the substrate. Acetone was used as a solvent to loosen the organic polymer and remove any residue.

2.2.8 Fourier-Transform Infrared Spectroscopy (FTIR)

FTIR was used to obtain infrared spectrums of transmission for blackplate immersed in NaCl in both the presence and absence of alanine. A Perkin Elmer FTIR 100 was used with a Universal Attenuated Total Reflectance (UATR) attachment. Samples were removed from their respective solution and dried. A background scan was taken for reference. FTIR scans were carried out with a resolution of 4 cm^{-1} for 8 scans over the sample.

2.2.9 X-ray fluorescence (XRF)

An Oxford instruments X-MET7500 series XRF gun was used as a means to characterise the amount of Cr that was deposited on in-house electroplated TCCT® at Swansea. XRF is a powerful but non-destructive technique for measuring elemental composition of a substrate. The XRF measured counts of Cr in ppm. Thus, a calibration factor was determined in order to obtain results in $mg.m^{-2}$. This was achieved by using known Cr amounts in $mg.m^{-2}$ and measuring their counts in ppm and creating a line of best fit. 4 measurements were taken per sample and an average recorded. Mining high S mode was used and the measurement was recorded for 3 seconds.

2.2.10 Lab scale electroplating of TCCT®

To produce TCCT® samples in Swansea a lab scale electroplating line was set up. Numerous pre-treatment steps were necessary prior to electroplating. Blackplate samples were cut to the appropriate size using a guillotine and cleaned via an acetone rub. Following this they were places in an alkaline cleaning bath where an anodic current was applied to provide scrubbing action. To avoid contamination of the next bath samples were rinsed with deionized water. Following this they were placed in an acid bath and then rinsed with deionized water. The blackplate substrate was then placed in the respective electroplating bath for Cr or Cr (III) oxide deposition. The compositions of the two baths are shown in Table 2. Sodium formate is used as a complexing agent to destabilise the very stable $Cr(H_2O)_6^{3+}$ complex and sodium sulphate aids in the electrolyte conductivity.

Table 2. Composition of TCCT® electrolytes.

TCCT®	**Chemistry**	**pH**	**Temp / ºC**
Step 1 – Cr metal	$(CrOHSO_4)_2 \times Na_2SO_4$ Na_2SO_4 HCOONa	2.3	37
Step 2 – Cr(III) oxide	$(CrOHSO_4)_2 \times Na_2SO_4$ Na_2SO_4	3.2	55

An Inkbird digital temperature controller enabled the temperature of the respective bath to be maintained to ±1 °C. Following electrodeposition of the relevant Cr species, samples were dried and stored.

2.3 References

1. Wint N, de Vooys ACA, McMurray HN. The corrosion of chromium based coatings for packaging steel. Electrochim Acta. 2016;203:326–36.

2. Williams G, Kousis C, McMurray N, Keil P. A mechanistic investigation of corrosion-driven organic coating failure on magnesium and its alloys. npj Mater Degrad. 2019;3(1).

3. Williams G, Mcmurray HN, Lett ES, Williams G, Mcmurray HN. Anion-Exchange Inhibition of Filiform Corrosion on Organic Coated AA2024-T3 Aluminum Alloy by Hydrotalcite-Like Pigments Anion-Exchange Inhibition of Filiform Corrosion on Organic Coated AA2024-T3 Aluminum Alloy by Hydrotalcite-Like Pigments. 2003;9–12.

4. Campbell J. Properties of Castings. Complet Cast Handb. 2015 Jan 1;447–528.

5. Williams G, McMurray HN. The mechanism of group (I) chloride initiated filiformcorrosion on iron. Electrochem commun. 2003;5:871–7.

6. Li SX, Hihara LH. Atmospheric corrosion initiation on steel from predeposited NaCl salt particles in high humidity atmospheres. Corros Eng Sci Technol. 2013;45(1):49–56.

7. Stratmann M, Streckel H, Feser R. A new technique able to measure directly the delamination of organic polymer films. Corros Sci. 1991;32(4):467–70.

8. Hagen CHM, Knudsen O, Zavieh AH, Pfleging W. Effect of laser structured micro patterns on the polyvinyl butyral/oxide/steel interface stability. Prog Org Coatings. 2020;147:105766.

9. Kozlowski R. Sciencing [Internet]. Why Does Phenolphthalein Change

Color? 2020 [cited 2021 Jul 9]. Available from: https://sciencing.com/phenolphthalein-change-color-5271431.html

10. Leidheiser H, Wang W, Igetoft L. The mechanism for the cathodic delamination of organic coatings from a metal surface. Prog Org Coatings. 1983;11:19–40.

11. Fürbeth W, Stratmann M. Scanning Kelvinprobe investigations on the delamination of polymeric coatings from metallic surfaces. Prog Org Coatings. 2000;39(1).

12. Grimnes S, Martinsen Ø. Bioimpedance and Bioelectricity Basics (Third Edition). Academic Press; 2015. p. 179–254.

13. Potentiodynamic Scan/Cyclic Polarization Gamry Instruments [Internet]. [cited 2023 Mar 9]. Available from: https://www.gamry.com/application-notes/corrosion-coatings/potentiodynamic-cyclic-polarization/

14. McMurray H., Worsley DA. Research in Chemical Kinetics. Compton R., Hancock G, editors. Vol. 4. Oxford: Blackwell Science; 1997. 149–202 p.

15. Charbonneau J. Recent Case Histories of Food Product – Metal Container Interactions Using Scanning Electron Microscopy – X-Ray Microanalysis. 1997;19:512–8.

16. Mcmurray HN, Williams G. 2.14 -Under Film / Coating Corrosion. Shreir's Corros. 2010;2:988–1004.

3 The atmospheric corrosion of trivalent Cr metal / Cr oxide coatings for packaging steels

3.1 Introduction

One of the primary functions of ECCS is to provide corrosion resistance to protect whatever contents may be inside. TCCT® must also be suitable for use commercially and thus, it is important to investigate its corrosion resistance properties.

Like ECCS, TCCT® is commonly used in conjunction with an organic overcoat to improve corrosion resistance. TCCT® is susceptible to certain organic coating failure mechanisms such as cathodic delamination. Corrosion-driven organic coating delamination, whereby a coating becomes physically separated from the underlying substrate, is a key failure process that affects organically coated metal products (1) and occurs in humid conditions where oxygen is present, such as the outside of a can wall in storage conditions. In the case of cathodic disbondment, this corrosion mechanism is linked to the cathodic reaction. In the case that there is a defect in the coating, iron is exposed and anodic iron dissolution occurs (2). This anodic activity is constrained to the defect and coupled to the cathodic oxygen reduction reaction, which takes place at the cathode in the region of the delamination front. Cations are charge carriers which migrate from the defect to the delamination front to balance out the charge, enabling the reduction of oxygen at the steel surface.

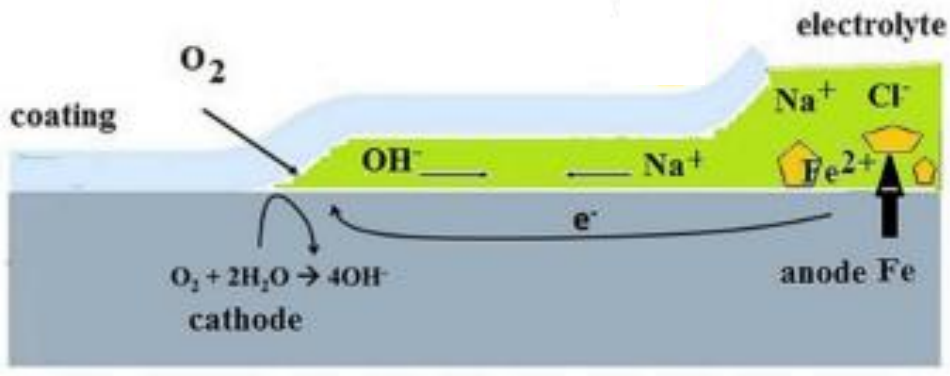

Figure 3.1. Schematic of a cathodic delamination cell and the relevant reactions that occur.

Full details of the mechanism of corrosion-driven disbondment can be found in section 1.9. Exposure of the underlying metal surface that occurs during organic coating delamination can lead to contamination and loss of quality of canned foods (3). The resistance of novel packaging materials to corrosion driven organic coating delamination is therefore of interest. Previous work has focused on the extent of cathodic delamination on ECCS and TCCT® made using the one step deposition process.

For example, Whiteside et al. (2021) showed that ECCS was resistant to cathodic delamination in non-deformed and deformed states. In comparison, deformation of the TCCT® significantly increased the extent of cathodic delamination (4). Edy et al. demonstrated the ability of TCCT® to resist cathodic delamination once the chemical composition consisted of a Cr oxide coating weight of 20 $mg.m^{-2}$ (where the composition of Cr remained at 122 $mg.m^{-2}$) (5). However, the TCCT® used during this piece of work was produced using the one step electroplating process (6) and there is a lack of work focusing on cathodic delamination as it occurs on TCCT produced using a two-step process, whereby the Cr metal and Cr (III) oxide layer are deposited using separate electrolytes to create a bilayer coating.

The research that has been undertaken demonstrated that increasing the Cr (III) oxide thickness from 8 to 63 $mg.m^{-2}$ (in the case that the Cr metal layer was kept a constant thickness at approximately 70 $mg.m^{-2}$) resulted in decreased rates of cathodic delamination. Significantly, the delamination behaviour of the coating with a Cr (III) oxide thickness of 30 $mg.m^{-2}$ was found to be similar to that of traditional ECCS, with delamination not occurring (7). Comparing these values to Edy's work on TCCT® produced via the one-step method, this coating weight corresponded to a reduced amount of total Cr for the inhibition of cathodic delamination.

In this chapter a systematic study into the effect of Cr (III) oxide coating weight on the initiation and propagation of cathodic delamination is described. Cathodic delamination was studied both optically (using phenolphthalein, an indicator dye which in acidic conditions (below pH 7) is colourless whilst in alkaline conditions (above pH 8.2) it begins to turn pink (8)) and using the SKP, which is able to measure corrosion potentials underneath polymer coatings and which has been used on

numerous occasions to study cathodic delamination of PVB metal substrates (9)(5)(4). Potentiodynamic polarisation experiments were used to provide complimentary data regarding the kinetics of the ORR as it occurs on TCCT® of varying Cr (III) oxide coating weights.

3.2 Materials and methods

3.2.1 Materials

The samples used were the same as those described in Chapter 2.1.

Blackplate (the low carbon steel substrate of uncoated TCCT® and ECCS), 0.2 mm thick, was obtained from Tata Steel Packaging, Trostre.

TCCT® was obtained from the pilot coating line from Tata Steel Packaging Ijmuiden and consisted of a low carbon substrate with a Cr (III) based electroplated coating. Electroplating had taken place in two stages to create a bilayer coating with an as received underlayer of Cr metal (100 $mg.m^{-2}$) and varying amounts of overlaying Cr (III) oxide as shown in Table 3.1

Table 3.1. Cr (III) oxide coating weights of TCCT® samples with an underlayer of 100 $mg.m^{-2}$ of Cr metal.

	Cr (III) oxide coating weight						
2	2.5	3	4	6.5	7.5	21.5	23.5

ECCS obtained from Tata Steel, produced using Cr (VI) electrolyte, had an as received Cr (hydr)oxide coating weight of 9 $mg.m^{-2}$.

A 15 % w/w ethanolic solution of polyvinyl butyral (PVB), molecular weight 70,000-100,000, was used as the organic coating during experiments. Although PVB does not represent the fully formulated product, it dries at room temperature and allows for comparisons to be made easily between samples (10)(11).

3.2.2 Methods

3.2.2.1 Electrochemical measurements

Samples of size 2.5 x 2.5cm were cut from a larger sheet and cleaned using isopropanol (IPA). A 0.8 cm^2 area of the TCCT® samples was exposed to a NaCl electrolyte, pH 7.

Potentiodynamic polarisation was conducted on these samples in aerated and deaerated conditions to determine the rate that corrosion may occur on both the outside and inside of cans.

3.2.2.2 Time-of-Flight Secondary Ion Mass Spectrometry (ToF-SIMS)

ToF-SIMS was used to analyse the chemical composition of the surface of TCCT® and how the relative ratio of species varied with changes in Cr (III) oxide coating weight. ToF-SIMS analysis was conducted using a Scientific Analysis Instruments (SAI) MiniSIMS-ToF. Chemical images and spectrums were obtained and analysed using MiniSIMS software. A scan size of 1024 x 1024 was used. To allow a better signal to noise ratio and a greater number of counts, a dwell time of 5 ms per pixel was used (12).

3.2.2.3 Cathodic delamination studies

To understand the effect of Cr (III) oxide coating weight on the extent of cathodic delamination and how it compares to the current standard, ECCS Stratmann cells were utilized. Stratmann cells were constructed as described in section 2.2.2. Cathodic delamination was then studied using two methods, optically using phenolphthalein and, to get more of an insight into the kinetics, using a scanning Kelvin probe (SKP). Both of these methods are outlined in more detail in section 2.2.2.

3.3 Results

3.3.1 Physical characterisation

Due to the electrochemical availability of iron in comparison with chromium, any defects present in the coating will expose the underlying steel and thus, increase the rate of corrosion.

XPS and ToF-SIMS was used to investigate the presence of iron on the surface of the samples.

The depth profiles of a relative high (21.5 mg.m^{-2}) and low (2 mg.m^{-2}) Cr (III) oxide coating weight are shown below in Figure 3.2 and Figure 3.3, respectively. Iron is present within a few nm depth of the lower oxide sample, suggesting the Cr coating was providing less coverage to the underlying substrate.

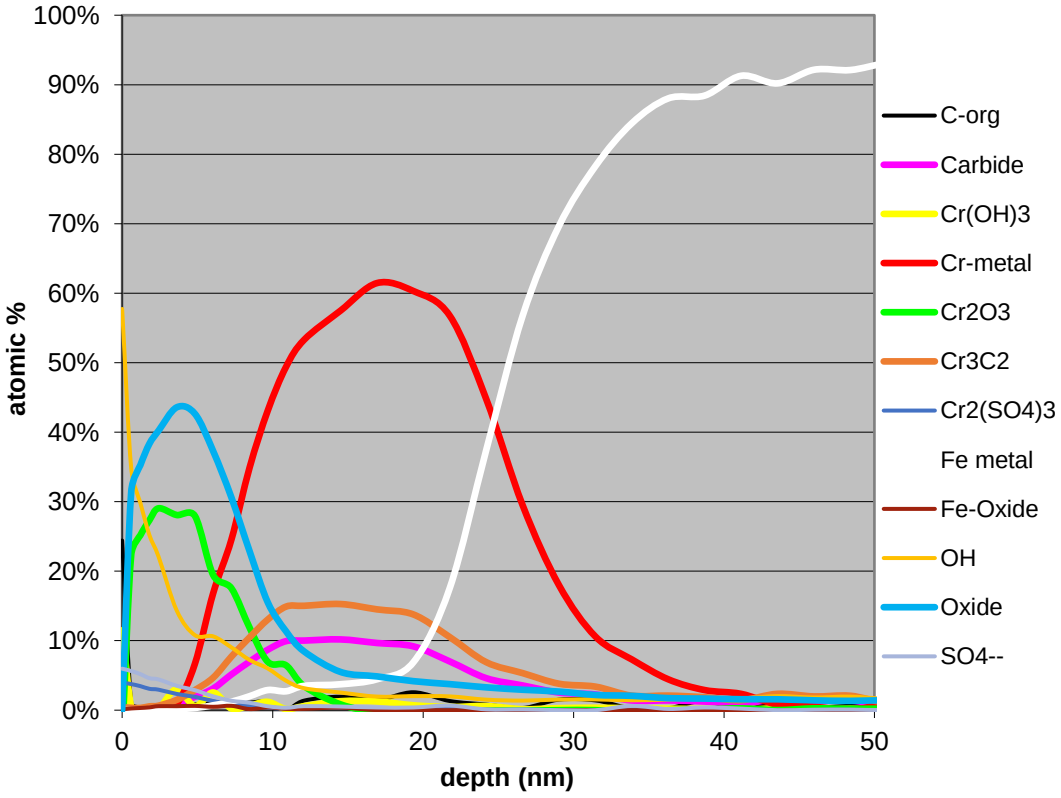

Figure 3.2. XPS depth profile for a TCCT sample with a Cr (III) oxide coating weight of 21.5 mg.m^{-2}.

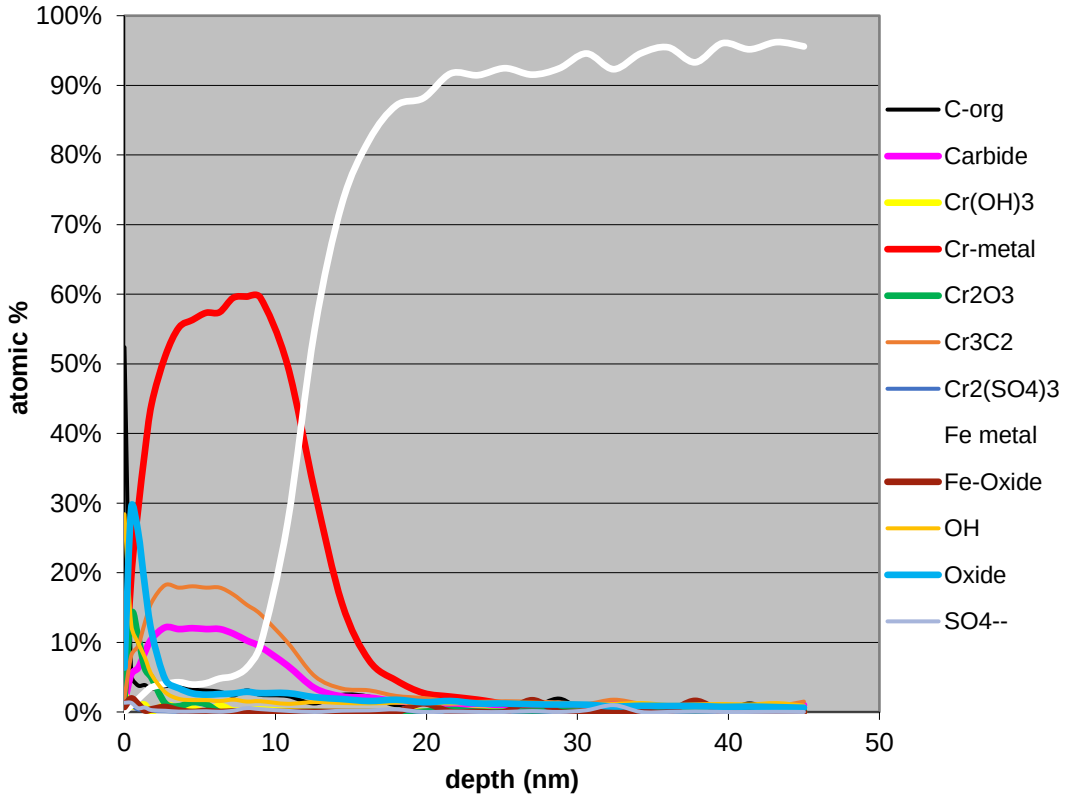

Figure 3.3. XPS depth profile for a TCCT sample with a Cr (III) oxide coating weight of 2 mg.m^{-2}.

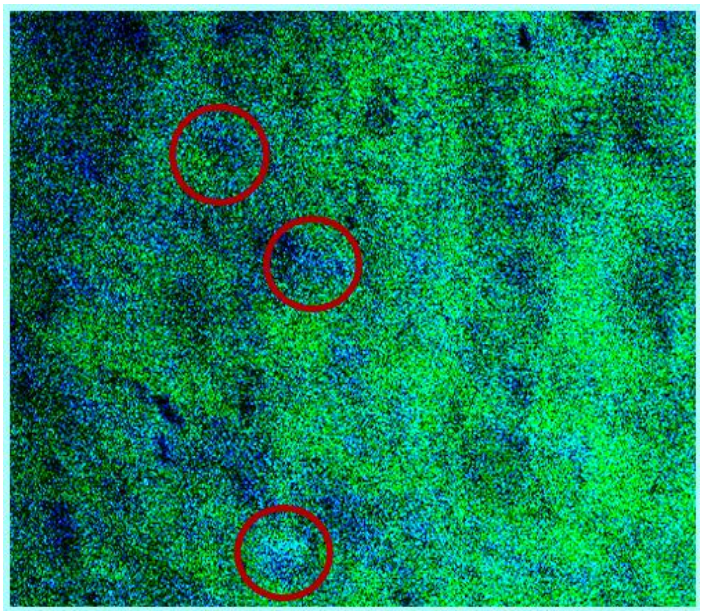

Figure 3.4: ToF SIMS chemical image map of a sample with an Cr(III) oxide coating weight of 2 mg.m^{-2} oxide. Green represents Cr and Blue, Fe. The red circles are highlighting some of the areas of blackplate that have not been sufficiently coated with Cr and thus appear blue on the chemical image.

Figure 3.4 shows a chemical image map obtained using ToF-SIMS where patches of iron appear amongst the general chromium coverage. As ToF-SIMS has a very low penetration depth, this could suggest a couple of things; the coverage of chromium may not be uniform across the whole sample and thus the underlying iron is detected in some regions. Alternatively, during the electroplating process some iron from the substrate may go into the bath and subsequently be plated again amongst the chromium on the surface. A mixture of the two suggestions is also a possibility.

Table 3.2. Ratio of Fe to Cr on the surface of TCCT® with varying Cr (III) oxide coating weight. Calculated from a chemical image map with a sample size of 1024 x 1024 pixels.

Cr (III) oxide / mg.m^{-2}	**Ratio Fe:Cr**	
23.5	1	16.7
7.5	1	11.2
2	1	7.6

Table 3.2 shows the ratio of Fe to Cr on the surface of TCCT® with varying Cr (III) oxide coating weights. This was calculated using the ratio of pixels of the respective chemical species. It was shown that a greater Cr (III) oxide coating weight has a lower Fe to Cr ratio. As more iron is detected on samples with a lower Cr (III) oxide coating weight it suggests these samples have a greater number of defected areas in the Cr coating where iron is exposed.

3.3.2 Polarisation studies

Initially potentiodynamic scans were conducted on blackplate, ECCS and TCCT® with a Cr (III) oxide coating weight of 4 mg.m^{-2} to provide a comparison in corrosion resistance between the relative performance of traditional and novel materials in similar conditions. Figure 3.5 shows the polarisation curves for blackplate, ECCS and TCCT®.

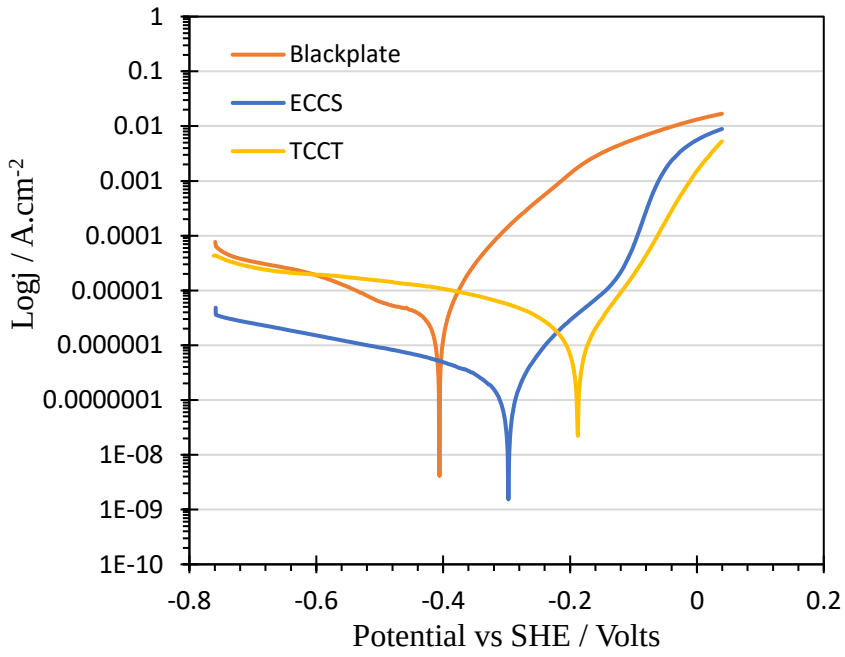

Figure 3.5. Current density as a function of potential for blackplate, ECCS and TCCT® with a Cr (III) oxide coating weight of 4 mg.m^{-2} measured in 1 wt. % NaCl with a potential sweep rate of 0.1667 mV.s^{-1}.

As shown in Figure 3.5, the cathodic current density values recorded in the case of ECCS were significantly smaller (~10 times) than those for TCCT® and blackplate.

The OCP values for TCCT® and ECCS were more positive in comparison with blackplate. The more positive OCP may be linked a reduction in the rate of the anodic process on these materials compared to blackplate.

The anodic currents of ECCS and TCCT® were very similar and significantly lower than those of blackplate. The Cr (III) oxide may provide a partial barrier to the anodic reaction. In the case of the blackplate substrate, higher anodic currents were recorded (~100 times), consistent with the uncoated nature of the substrate and thus exposure of iron.

These initial polarisation experiments showed it was clear that the cathodic branches varied significantly between ECCS and TCCT®. Hence, it was then decided to characterise cathodic activity for oxygen reduction on TCCT® substrates as this is directly relevant to cathodic disbondment.

Potentiodynamic scans were conducted on samples of TCCT® with a high, medium, and low (21.5 $mg.m^{-2}$, 7.5 $mg.m^{-2}$ and 2 $mg.m^{-2}$ respectively) Cr (III) oxide coating weight. To replicate the conditions used to initiate cathodic delamination, a 5 wt. % NaCl solution was used as the electrolyte in which the following polarisation experiments were conducted.

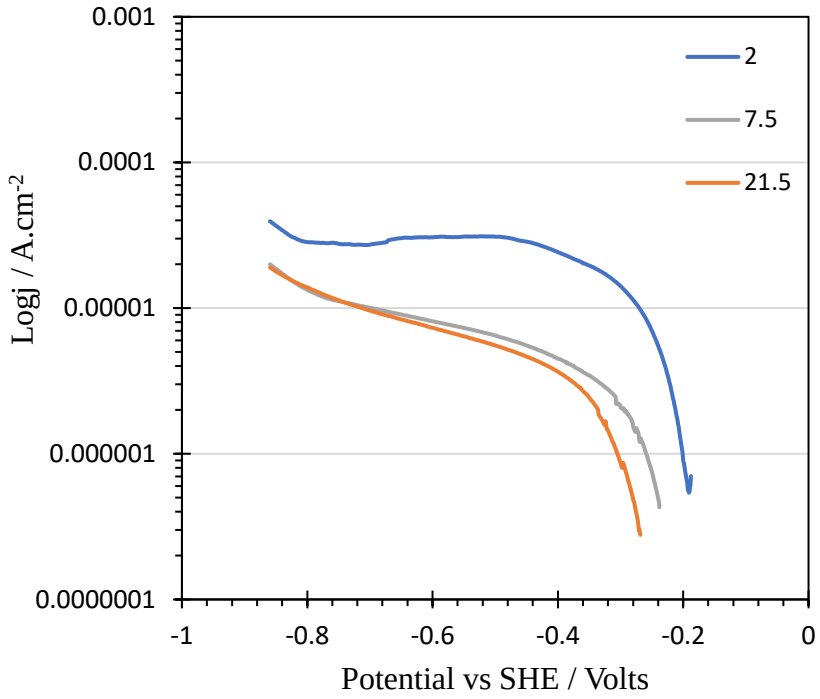

Figure 3.6. Current density as a function of potential for a relative high, medium and low (21.5, 7.5 and 2 mg.m^{-2}) Cr (III) oxide coating weight measured in 5 wt. % NaCl with a potential sweep rate of 0.1667 mV.s^{-1}.

Figure 3.6 shows the cathodic polarisation curve for samples with a relative high (21.5 mg.m^{-2}), medium (7.5 mg.m^{-2}) and low (2 mg.m^{-2}) Cr (III) oxide coating weight. The samples with a relative high Cr (III) oxide coating weight were associated with lower current densities (~10 times). Thus, a trend was seen that linked higher oxide coating weights to lower cathodic currents. As the Cr (III) oxide coating weight was increased, the value of the OCP became more negative suggesting they were acting to suppress the cathodic reaction. 2 measurements were conducted for each sample type.

Deaerated potentiodynamic scans were then conducted on a high, medium and low oxide coating weight of TCCT®; 21.5 mg.m^{-2}, 7.5 mg.m^{-2} and 2 mg.m^{-2} respectively. The results are displayed in Figure 3.7.

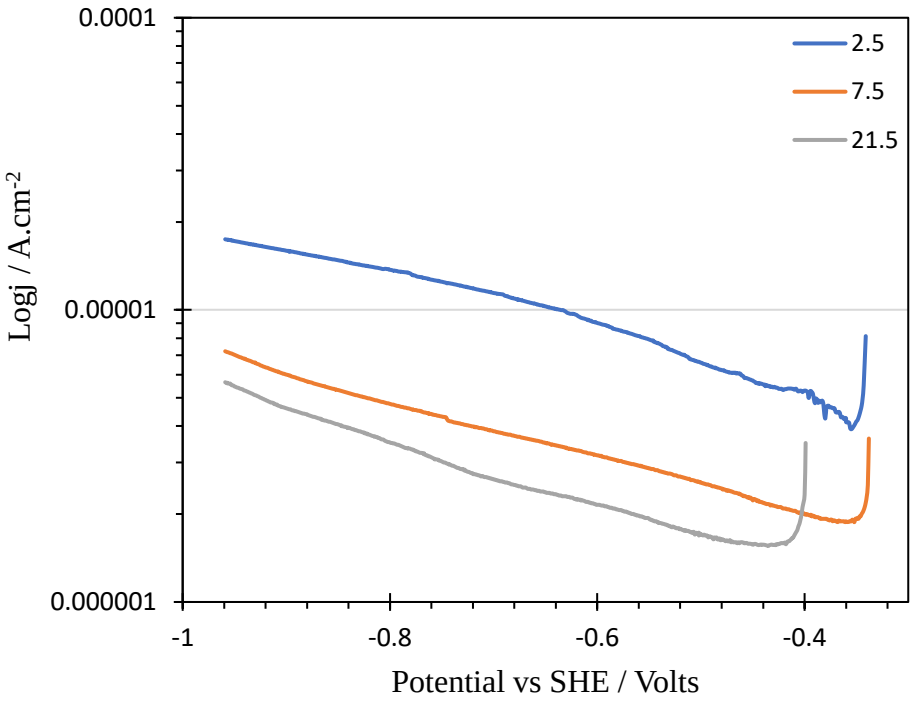

Figure 3.7. Current density as a function of potential for TCCT® with a variety of different Cr (III) oxide coating weights immersed in 1 wt. % NaCl with a potential sweep rate of 0.1667 mV.s^{-1}.

The OCP values were more negative in deaerated conditions in comparison to aerated conditions. Under deaerated conditions, the major cathodic reaction will be the evolution of hydrogen, the reaction potential of which is more negative in comparison to the ORR.

As shown in Figure 3.7, a similar trend was observed as with the oxygen reduction reaction in aerated conditions; the samples with a higher oxide coating weight displayed lower cathodic currents. The samples with a relative high Cr (III) oxide coating weight were associated with lower current densities (~5 times). Thus, a trend was seen that linked higher oxide coating weights to lower cathodic currents. Again, the higher Cr (III) oxide coating weights had more negative OCP values suggesting they were acting to suppress the cathodic reaction.

3.3.3 Cathodic delamination studies

From the potentiodynamic studies, it was clear that the coating weight had an effect on the amount of cathodic activity occurring on the surface of the substrate. This has

implications for corrosion-driven coating disbondment. Hence, cathodic disbondment was highlighted as an area for a more in-depth study.

An initial experiment into the kinetics of disbondment of the PVB overcoat from blackplate was investigated to establish baseline characteristics in the absence of a chromium coating (Figure 3.8). The point of maximum gradient in the E_{corr} profiles is considered to be the position of the delamination front and the rate of change of this position with respect to time is used to determine the rate of delamination of the organic coating (13).

After initiation with 5 wt. % NaCl, the time dependent $E_{corr}(x)$ profiles (where x is distance from the defect edge) became established within 180 minutes. E_{corr} values over the intact coating surface where no anodic partial reaction has occurred, commonly referred to as E_{intact}, remained constant at approximately 0.15 V vs. SHE. This value corresponds to the typical free corrosion potential of at the active metal and is common for that of pure iron (14). The more negative the potential of the E_{intact}, the more oxygen reduction is being slowed down (15). A potential difference exists between the defect and the intact interface. E_{corr} values dropped for the delaminated parts of the coating to that of the bare metal in contact with the electrolyte in the defect. In this case it dropped to approximately −0.3 V vs. SHE, this being common for anodically active iron (2). The location of the delamination front can be determined from the point of maximum gradient in the time dependent $E_{corr}(x)$ profiles. The time-dependent SKP profiles are produced due to the ionic current flux in the thin electrolyte layer that penetrates beneath the delaminated coating which leads to an ohmic potential gradient. The delamination front is therefore easily identifiable on the graph.

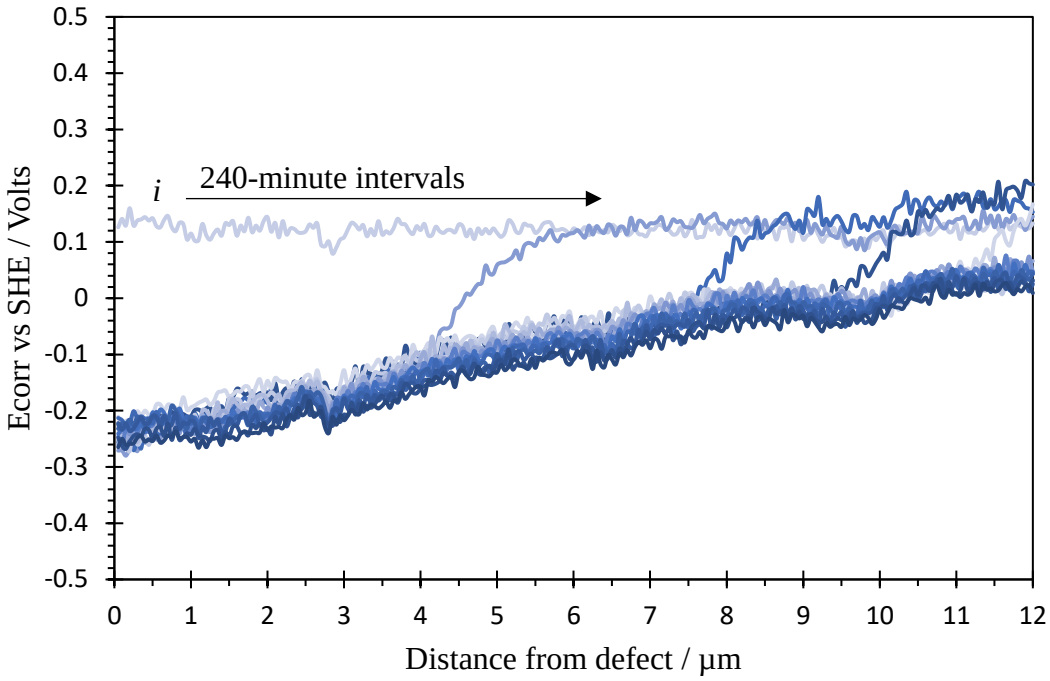

Figure 3.8. Time-dependent SKP derived E_{corr} vs. distance (x) from the defect edge profiles recorded for unpigmented 30 mm PVB coatings on blackplate. Electrolyte in contact with the defect is 5 wt. % NaCl. Scan times = (i) 60 minutes and 240 minute intervals thereafter.

Cathodic delamination was not observed on ECCS, this being made evident by the potential plateau shown in Figure 3.9.

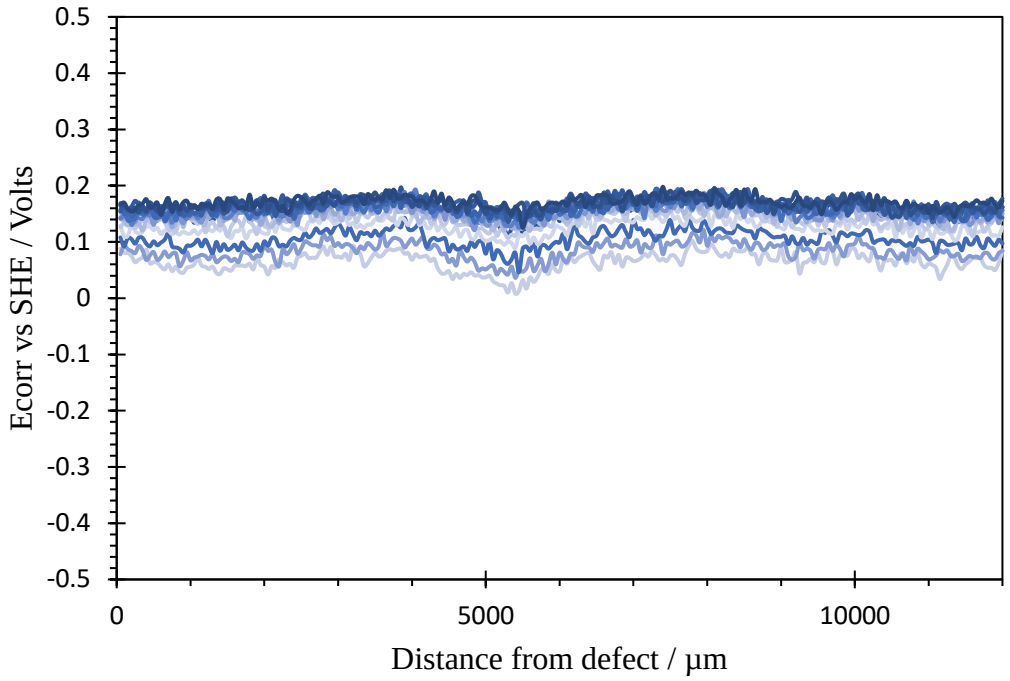

Figure 3.9. Time-dependent SKP E_{corr} vs. distance from defect (x) profiles recorded for unpigmented 30 mm PVB coatings on ECCS. Electrolyte in contact with the defect is 5 wt. % NaCl. Scan ran for 4320 minutes with no evidence of delamination.

Following baseline cathodic delamination studies on blackplate and the current standard, ECCS, the susceptibility of TCCT® to cathodic delamination was investigated. Initially cathodic delamination was studied optically to determine, firstly, whether it would occur on the latest version of TCCT® and secondly, if there was a link between the extent of delamination and Cr (III) oxide coating weight. This was done using phenolphthalein as an indicator, dissolved in the PVB, and enabled the delamination distance to be determined visually by a colour change from colourless to pink, initiated by the alkaline environment under the delaminated part of the coating. This optical method was chosen over the SKP as numerous samples could be studied at once to gauge an idea of which samples, if any, to investigate using the SKP.

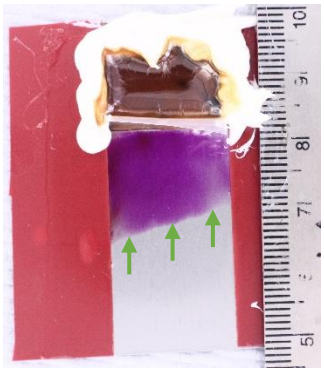

Figure 3.10. A cathodically delaminating sample with a Cr (III) oxide coating weight of 4 mg.m^{-2}. The pink colour shows how far the coating has delaminated and the green arrows represent where the delaminated distance measurements were taken.

Figure 3.10 shows an example of a cathodically delaminating sample, with the extent of delamination being represented by the pink colour, due to the presence of phenolphthalein in the coating. It is of note that although the extent of delamination differs from one side of the sample to the other, the angle remains consistent and so the distance travelled and thus, rates are similar from one side of the film to the other.

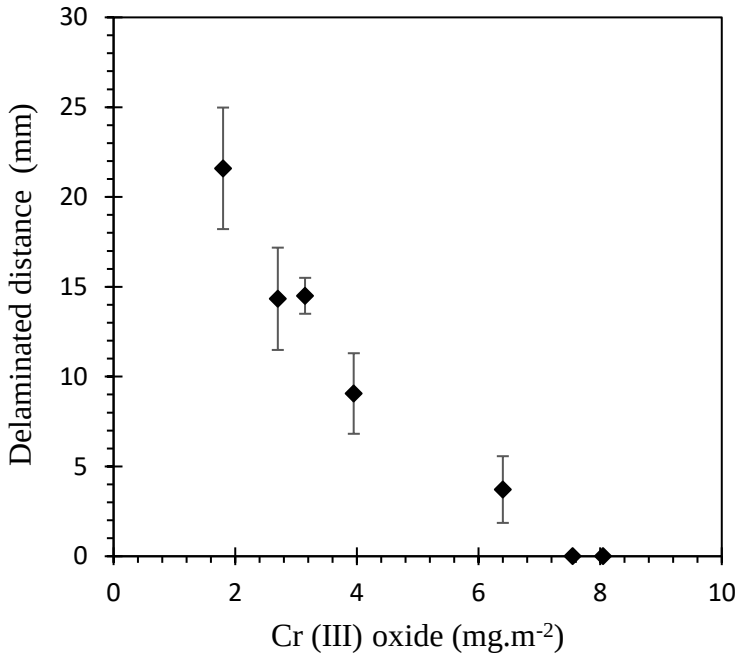

Figure 3.11. Effect of Cr (III) oxide coating weight on delamination distance after 4 days. Delamination was initiated using 5 wt. % NaCl and the delamination distance was determined optically using phenolphthalein as an indicator.

Unlike ECCS, cathodic disbondment was observed on TCCT®. Figure 3.11 shows the delamination distance, measured using phenolphthalein as an indicator, as a function of Cr (III) oxide coating weight over a period of 4 days. There was a clear correlation between Cr (III) oxide coating weight and delamination distance with a greater Cr (III) oxide coating weight leading to a decrease in delamination distance. The distance over which PVB delaminated the greatest was with the lowest Cr (III) oxide coating weight, of 2 $mg.m^{-2}$. The distance decreased with increasing oxide coating weight and delamination was not observed on samples with a Cr (III) oxide coating weight of 7.5 $mg.m^{-2}$ or more.

Once a trend was established between increased Cr (III) oxide coating weight and decreased delamination distance, the SKP was used to obtain a better understanding of the kinetics involved. The SKP can provide values of potential for a metal that is underneath an intact and delaminated coating in situ.

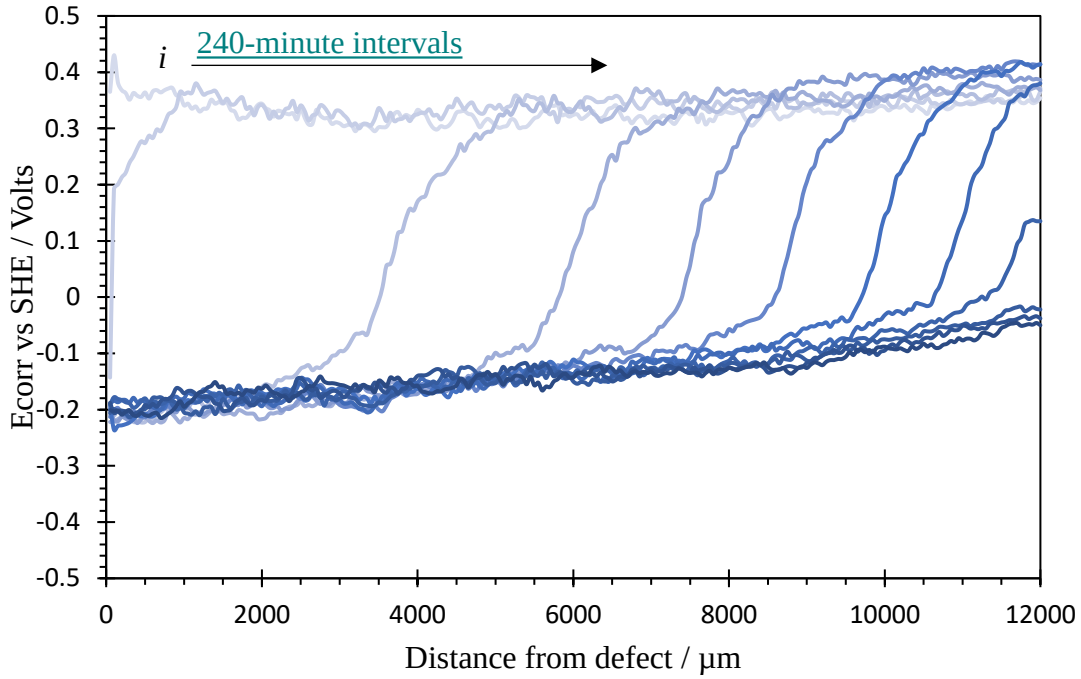

Figure 3.12. Time-dependent SKP derived E_{corr} vs. distance (x) from the defect edge profiles recorded for unpigmented 30 mm PVB coatings on TCCT® with a Cr (III) oxide coating weight of 2 $mg.m^{-2}$. Electrolyte in contact with the defect is 5 wt. % NaCl. Scan times = (i) 60 minutes and 240 minute intervals thereafter.

Figure 3.12 shows that that delamination has occurred on the sample with a relative low Cr (III) oxide (2 mg.m^{-2}) coating weight. The initial steep drop in the voltage, indicative of the delamination front, eventually reaches a shallower gradient indicating the change from the delamination front to the region next to the coating defect. After 60 minutes (the scan indicated by *i*), there was no obvious drop in voltage, this being indicative of delamination not having occurred. Delamination had started to occur once a time of 240 mins had passed. The delamination front moves further away from the defect edge with time as delamination continues to occur on the substrate. The steepness of the delamination front observed is also indicative of inhibited cation migration (16).

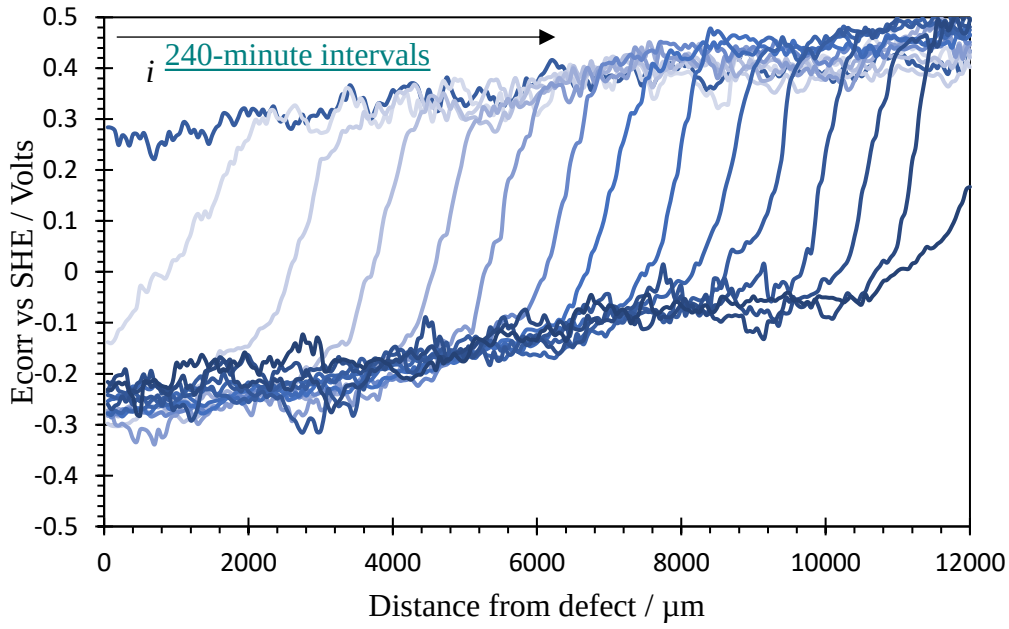

Figure 3.13. Time-dependent SKP derived E_{corr} vs. distance (x) from the defect edge profiles recorded for unpigmented 30 mm PVB coatings on TCCT® with a Cr(III) oxide coating weight of 2.5 mg.m^{-2}. Electrolyte in contact with the defect is 5 wt. % NaCl. Scan times = (i) 540 minutes and 240 minute intervals thereafter.

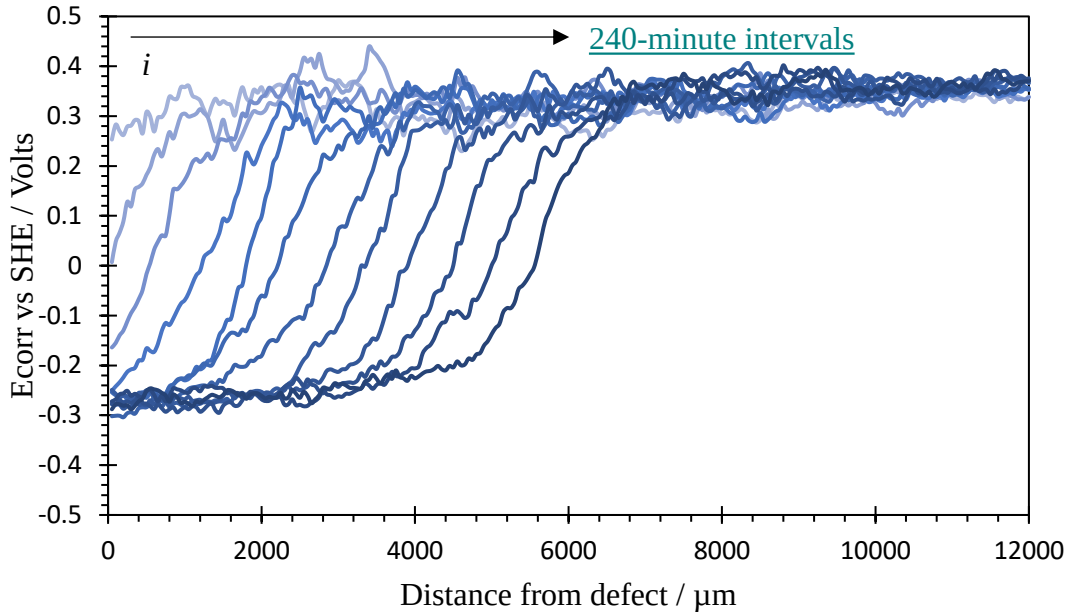

Figure 3.14. Time-dependent SKP derived E_{corr} vs. distance (x) from the defect edge profiles recorded for unpigmented 30 mm PVB coatings on TCCT® with a Cr(III) oxide coating weight of 3 mg.m^{-2}. Electrolyte in contact with the defect is 5 wt. % NaCl. Scan times= (i) 1500 minutes and 240 minute intervals thereafter.

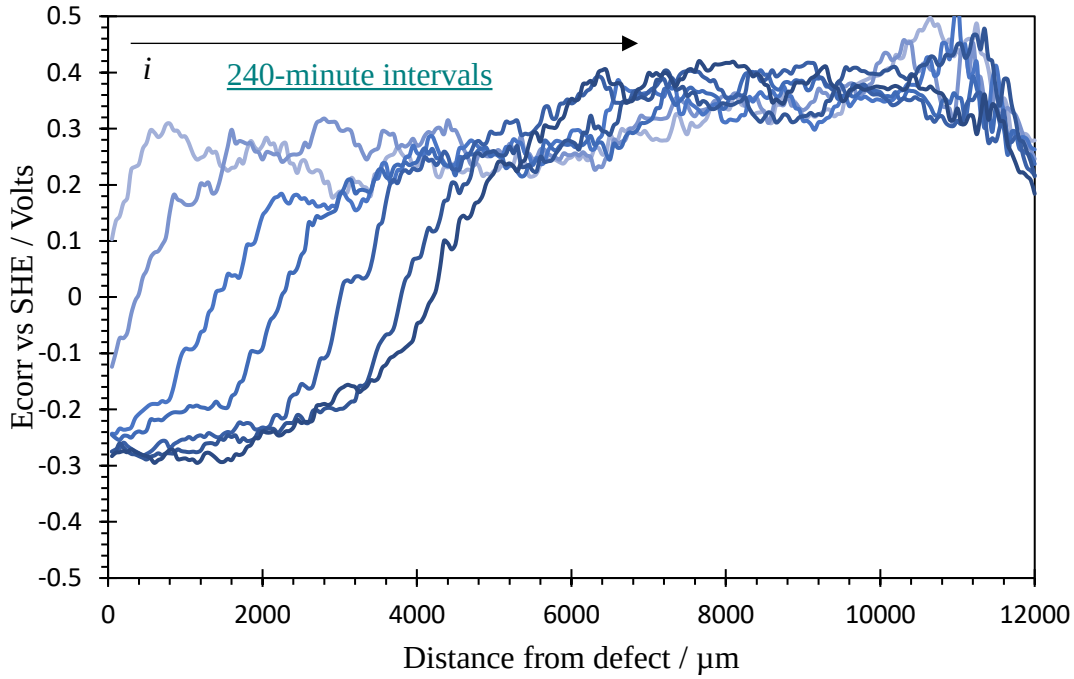

Figure 3.15. Time-dependent SKP derived E_{corr} vs. distance (x) from the defect edge profiles recorded for unpigmented 30 mm PVB coatings on TCCT® with a Cr(III) oxide coating weight of 4 mg.m-2. Electrolyte in contact with the defect is 5 wt. % NaCl. Scan times = (i) 1260 minutes and 240 minute intervals thereafter.

It can be seen in Figure 3.13,Figure 3.14 and Figure 3.15, that cathodic delamination also occurs relatively quickly in samples of TCCT® with a coating weight of up to 4 $mg.m^{-2}$. The time for cathodic delamination to initiate on the TCCT® samples with oxide coating weights of 2.5, 3 and 4 $mg.m^{-2}$ was 720, 1740 and 1260 minutes respectively. The time taken for delamination to initiate on the three samples was longer than the 240 minutes it took for delamination to occur on the sample with 2 $mg.m^{-2}$ coating weight. The extent of delamination was also less in the samples with higher oxide coating weights especially for the samples with coating weights over 3 $mg.m^{-2}$ oxide. E_{corr} values over the intact surface (E_{intact}) became slightly less positive as the coating weight was increased. These findings suggest that the Cr (III) oxide provides a degree of protection against cathodic delamination.

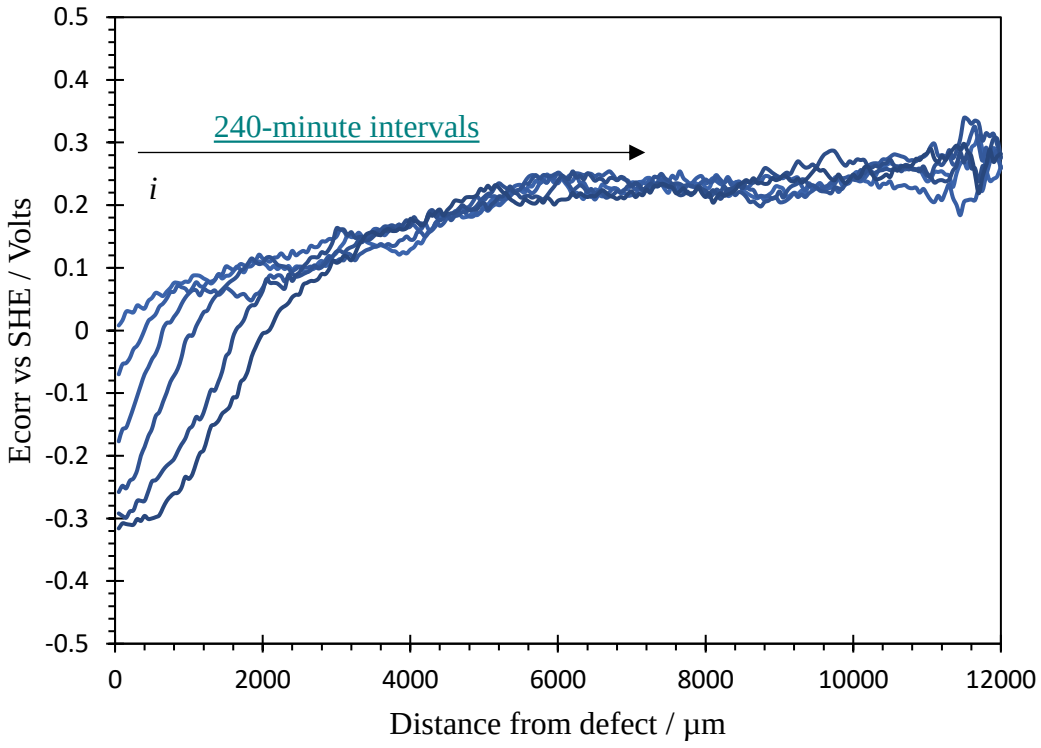

Figure 3.16. Time-dependent SKP derived E_{corr} vs. distance (x) from the defect edge profiles recorded for unpigmented 30 mm PVB coatings on TCCT® with a Cr(III) oxide coating weight of 6.5 mg.m-2. Electrolyte in contact with the defect is 5 wt. % NaCl. Scan times = (i) 2940 minutes and 240 minute intervals thereafter.

It is shown in Figure 3.16 that the increase in coating weight to 6.5 $mg.m^{-2}$ of Cr(III) oxide has acted to provide a degree of cathodic disbondment inhibition as the delamination rate has slowed from approximately 12 $\mu m.min^{-1}$ (with a coating weight

of 2 mg.m^{-2}) to approximately 1.5 µm.min^{-1}. Furthermore, the time for delamination to initiate was a lot longer at 3120 minutes in comparison to the lower oxide samples.

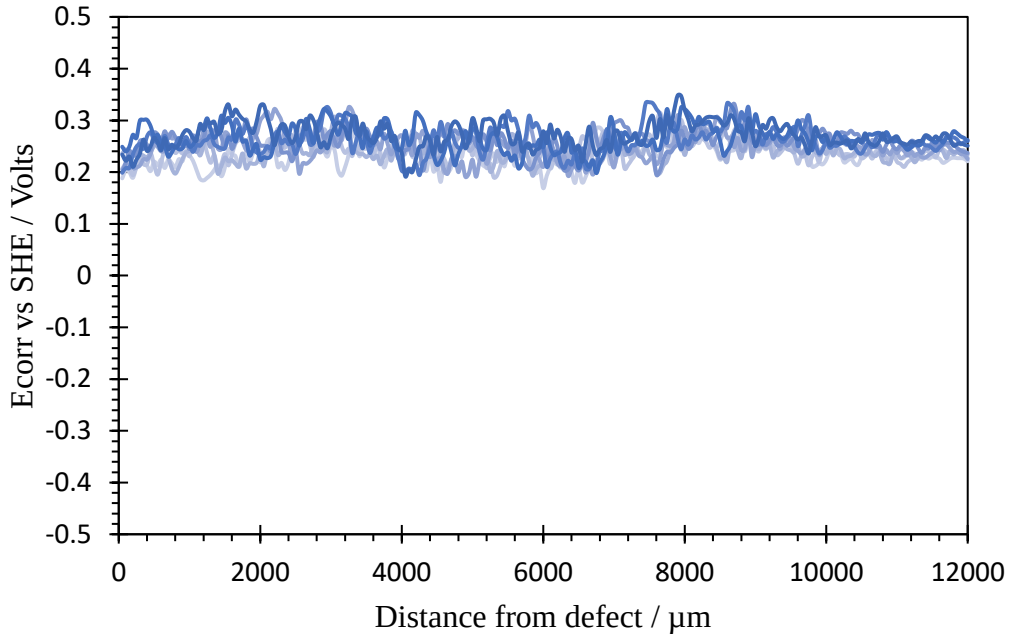

Figure 3.17. Time-dependent SKP E_{corr} vs. distance from defect (x) profiles recorded for unpigmented 30 mm PVB coatings on TCCT® with a Cr (III) oxide coating weight of 7.5 mg.m^{-2}. Electrolyte in contact with the defect is 5 wt. % NaCl. Scan ran for 4320 minutes with no evidence of delamination.

After 4320 minutes cathodic delamination was still not observed on the sample with a coating weight of 7.5 mg.m^{-2} as shown in Figure 3.17. Thus, it is plausible that a threshold value for Cr (III) oxide coating weight in terms of preventing cathodic delamination exists between 6.5 and 7.5 mg.m^{-2}.

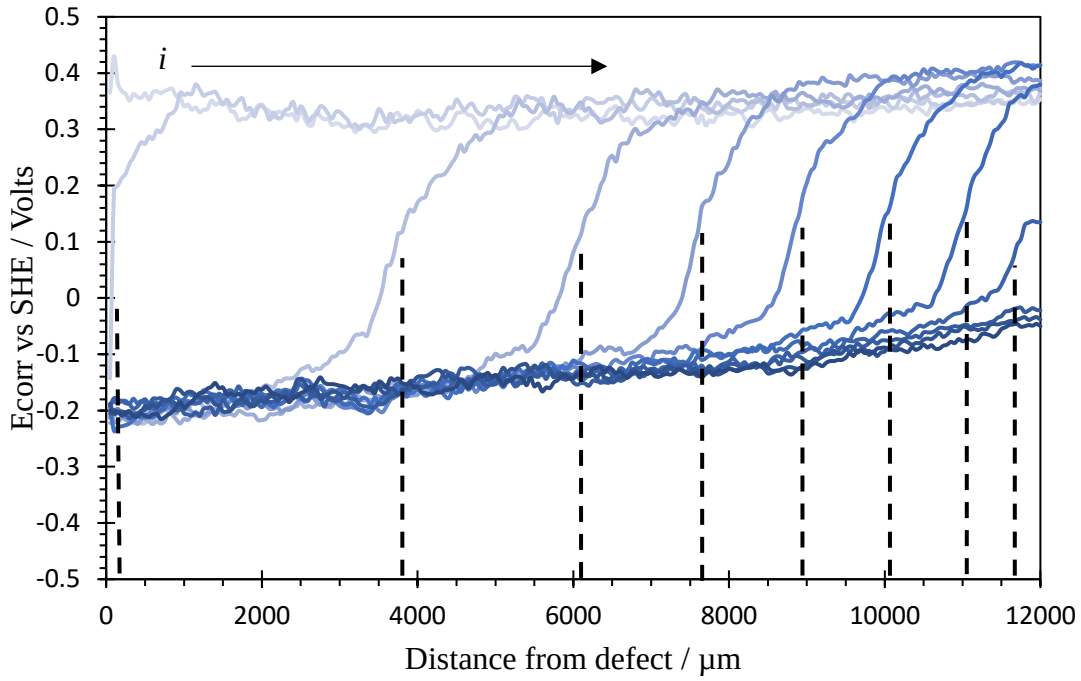

Figure 3.18. Schematic of how the position of the delamination front was measured on the Time-dependent SKP E_{corr} vs. distance from defect (x) profiles.

As demonstrated in Figure 3.18, the position of the cathodic delamination front was taken as the midpoint of the maximum gradient in potential from the intact coating region. This value was plotted against the respective time minus the time taken for cathodic delamination to initiate.

Parabolic kinetics is indicative of cation migration between the anode and cathode being rate determining. It is the migration of electrolyte cations (in this case Na^+) in the underfilm electrolyte, which typically controls the delamination rate (13).

In contrast, linear kinetics generally suggest that surface reactions occurring at the interface can be considered in some cases to be slow and therefore rate determining. These include processes such as electron transfer associated with cathodic oxygen reduction at the delamination front (13).

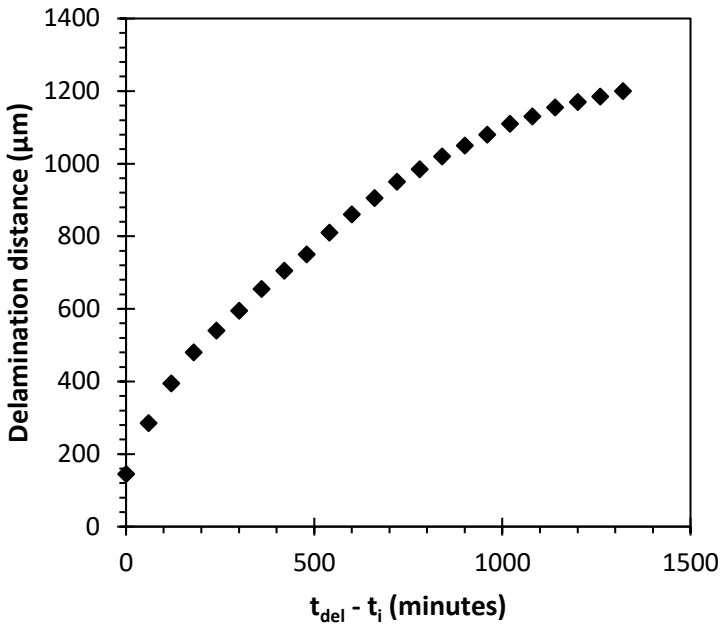

Figure 3.19. Delamination distance as a function of $t_{del} - t_i$ obtained for blackplate overcoated with a 30 µm PVB film where corrosion was initiated using a 5 wt. % NaCl electrolyte.

Figure 3.19 shows plots of delamination distance as a function of $t_{del} - t_i$ obtained from time dependent E_{corr} profiles for blackplate. The plot shows a curved line, consistent with parabolic kinetics, and thus indicative of cation migration control.

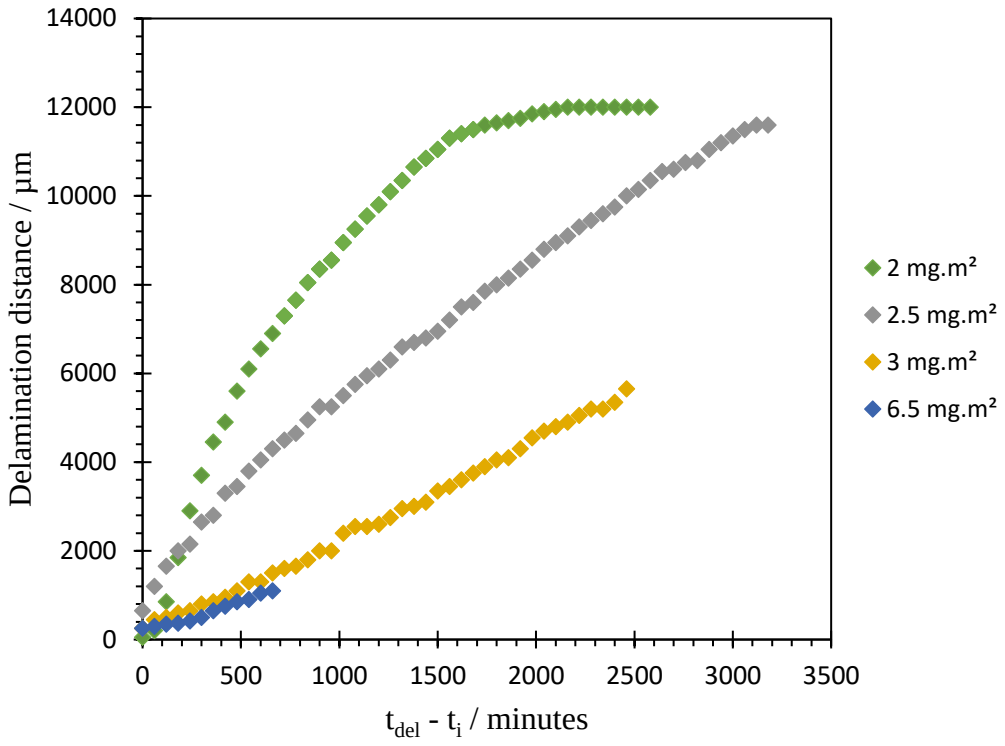

Figure 3.20. Plots of delamination distance vs. time for the cathodic delamination of PVB from TCCT® with varying Cr (III) oxide coating weights, where corrosion was initiated using a 5 wt. % NaCl electrolyte.

Figure 3.20 shows plots of delamination distance vs. time for TCCT® samples with varying Cr (III) oxide coating weights. The rate of delamination decreased with time for the lower Cr (III) oxide coating weights and the delamination kinetics were parabolic in nature indicating that cation migration from the coating defect is rate determining (13). As the coating weight increased the kinetics changed from parabolic to linear and the rate of delamination becomes proportional to time.

Since the delamination kinetics varied from parabolic for low Cr (III) oxide coating weights to linear for the higher coating weights, the initial gradient of the delamination vs. time graphs were used to compare delamination rates. A tangent was used to estimate the initial delamination rates. These values were plotted as a function of Cr (III) oxide coating weight, and it can be seen in Figure 3.21 that delamination rate decreased with increasing Cr (III) oxide coating weight.

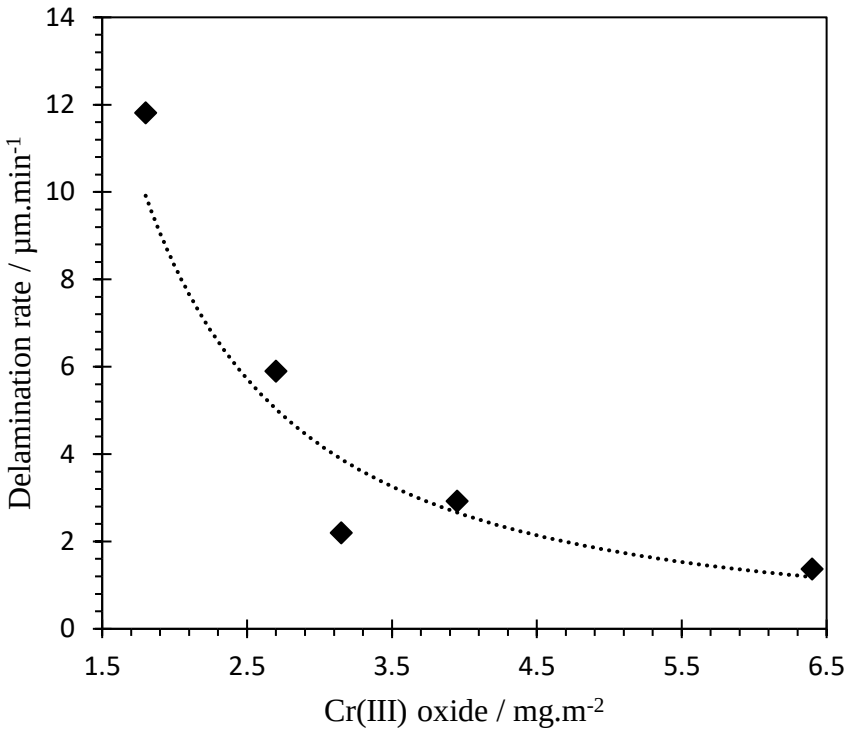

Figure 3.21. Cathodic delamination rate (µm.min^{-1}) as a function of Cr (III) oxide coating weight (mg.m^{-2}) for TCCT® samples coated with PVB.

It is shown in Figure 3.21 that the initial rate of cathodic delamination of PVB from the TCCT® substrate decreases with increasing Cr (III) oxide coating weight.

If delamination rate is controlled by the migration of cations form the defect to the delamination front then the distance (x_{del}) over which delamination has occurred is related to the time since electrolyte contact (t_{del}) by the following equation:

$$x_{del} = k_d (t_{del} - t_i)^{1/2} \qquad (3.1)$$

where k_d is the delamination rate constant and t_i the initiation period.

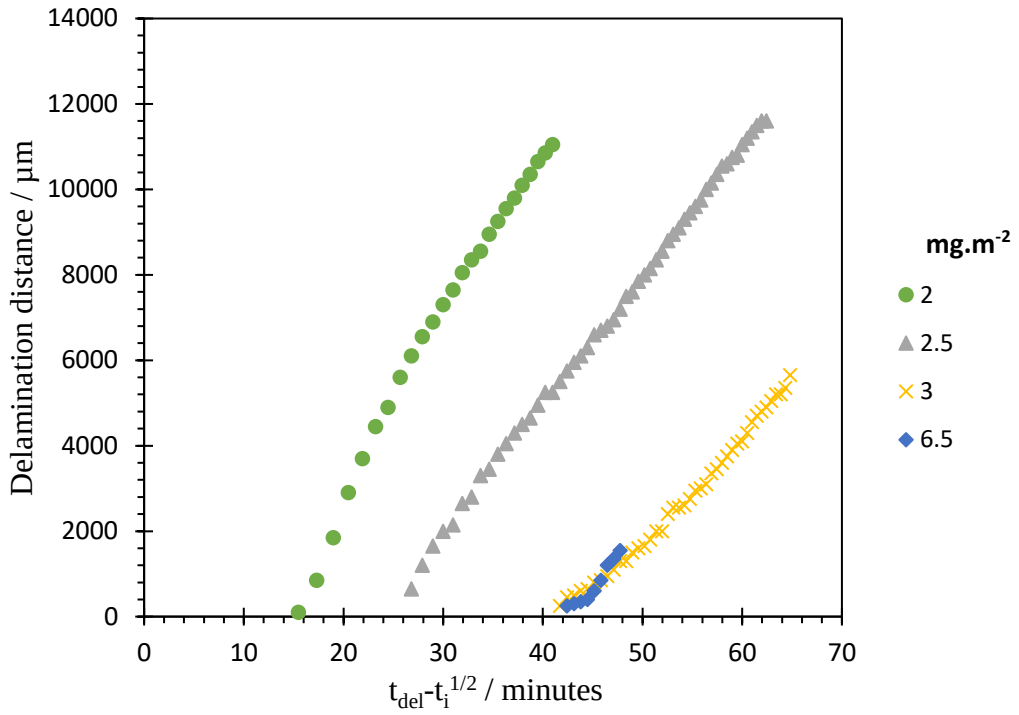

Figure 3.22. Plots of delamination distance vs. $t_{del} - t_i^{1/2}$ for the cathodic delamination of PVB from TCCT® with varying Cr (III) oxide coating weights, where corrosion was initiated using a 5 wt. % NaCl electrolyte.

Figure 3.22 shows plots of delamination distance vs. $(t_{del} - t_i)^{1/2}$ obtained from time dependent E_{corr} profiles for various TCCT substrates. The lower oxide curves show a good straight line consistent with migration control and thus parabolic kinetics.

3.4 Discussion

A greater Cr (III) oxide coating weight provided a greater degree of inhibition with regards to cathodic delamination. A Cr (III) oxide coating weight of approximately 7.5 mg.m^{-2} proved significant with regards to completely stopping cathodic delamination. It was also observed that cathodic delamination did not occur on ECCS, the current industry standard.

The difference in corrosion resistance of the coatings may exist due to a number of factors. Potentiodynamic measurements showed that ECCS displayed lower cathodic currents in comparison to TCCT® and blackplate. Furthermore, the TCCT® samples with higher Cr (III) oxide coating weights displayed lower cathodic currents in comparison with the lower oxide coatings. During electroplating Cr (VI) is rapidly

reduced to Cr (III) when in contact with iron, which is considered to be relatively noble. Consequently, there is very little iron exposed in the final product (ECCS). In comparison, the electrodeposition involved in the production of TCCT® occurs as a result of a local change in pH at the substrate surface which occurs due to the hydrogen evolution reaction (17). Consequently, it has been reported that this causes incomplete coating coverage and thus defects in the coating, exposing underlying iron (17). Wint et al. has previously shown the cathodic activity of iron to be large compared with other Cr (III) coated steels (10). Thus, this presence of iron in the final product may be a cause of the enlarged cathodic currents and thus, cathodic delamination rates in comparison to ECCS. ToF-SIMS analysis and well as XPS profiles showed that the lower Cr (III) oxide coating weights had a less even coating coverage, leading to patches where the underlying iron was present. This could act as a weak spot with regards to corrosion protection. For cathodic delamination to propagate, a continuous cathode is required. Hence, increased porosity observed on the lower coating weights may provide an easier means for oxygen to penetrate and for cathodic delamination to occur, in comparison to the higher oxide coating weights.

Another cause of the lower cathodic currents measured for the samples with higher Cr (III) oxide coating weights could be due to the poor electrical conductivity of Cr (III) oxide. Cr (III) oxide is a wide band gap insulator (E_g = 3.4 eV) (18). It is proposed that the Cr (III) oxide is acting as a protective barrier and as a means of limiting the cathodic reaction. This property can also explain the change in kinetics from parabolic to linear in nature. In the lower Cr (III) oxide coating weights the insulating properties were not great enough for the interfacial electron transfer between the anode and cathode to be rate limiting. Instead, the migration of cations was the rate determining factor. However, on increasing the Cr (III) oxide coating weight, the insulating properties that Cr (III) oxide offers became great enough to hinder the cathodic reaction by blocking electron transfer.

Potentiodynamic scans in deaerated conditions showed how lower cathodic current values for hydrogen evolution were observed on higher Cr (III) oxide coating weights. It is proposed that this is related to an increase in the exposure of underlying iron.

From these observations, it is reasonable to assume that both oxygen reduction and hydrogen evolution will occur on the surface of the steel substrate, where it is exposed

through defects in the Cr (III) coating. Thus, the observed currents for both the ORR and HER may serve as a measure of the portion of the sample surface which is electrochemically available to support cathodic activity. A greater Cr (III) oxide coating weight is expected to decrease cathodic activity. Hence, it is unsurprising that the greater Cr (III) oxide coating weights were less susceptible to cathodic delamination.

3.5 Conclusions

Cathodic delamination was studied optically using phenolphthalein, as well as using the SKP. Both of the methods used showed that TCCT® samples with a lower Cr (III) oxide coating weight were more susceptible to cathodic delamination. There were several proposed reasons for this being the case. Firstly, a greater Cr (III) oxide coating weight was important in order for the coating to have sufficient coverage of, and act as a barrier to, the underlying (electrochemically active) steel substrate. Secondly, a threshold value in the amount of Cr (III) oxide coating weight was also needed to sufficiently hinder interfacial electron transfer between the anode, (the defect) and cathode (the delamination front) and to stifle oxygen reduction at the under-film cathode and thus, resist propagation of the delamination front. It was also proposed that the mechanism of Cr deposition, used for the production of TCCT®, led to an increase of heterogeneities in the coating and hence, an increase in the presence of iron. It is believed that this played a role in the increased cathodic currents observed on the samples with a reduced level of Cr (III) oxide and hence, increased cathodic delamination rates. TCCT samples with a sufficiently high Cr (III) oxide coating weight (7.5 $mg.m^{-2}$) were found to resist corrosion-driven organic coating delamination, such that they offered similar performance to that of ECCS.

Furthermore, the cathodic delamination kinetics on blackplate, and samples with a lower Cr (III) oxide coating weight were primarily parabolic and rate-limited by the migration of cations. As the coating weight increased the kinetics changed from parabolic to linear in nature, most likely caused by the insulating properties that Cr (III) oxide offers which hinder the cathodic reaction by blocking electron transfer.

It is proposed that the lower Cr (III) oxide coatings do not provide sufficient protection for the insulating properties of Cr (III) oxide to take effect. Thus, the rate determining

factor is the migration of cations between the anode and cathode. Increasing the Cr (III) oxide weight means that the insulating properties of Cr (III) oxide hinder electron transfer processes at the delamination front, to the point it would become the rate determining process.

The results here conclude that TCCT®, of sufficient Cr (III) oxide coating weight, displays similar properties to ECCS with respect to their resistance to cathodic disbondment. This is promising with regards to the use of TCCT® commercially in the near future.

3.6 References

1. Mcmurray HN, Williams G. 2.14 -Under Film / Coating Corrosion. Shreir's Corros. 2010;2:988–1004.

2. Leng A, Streckel H, Stratmann M. The delamination of polymeric coatings from steel. Part 1: Calibration of the Kelvinprobe and basic delamination mechanism. Corros Sci. 1999;41:547–78.

3. Boelen B, Hartog H Den, Weijde H Van Der. Product performance of polymer coated packaging steel , study of the mechanism of defect growth in cans. 2004;50:40–6.

4. Whiteside J, de Vooys ACA, Sackett E, McMurray HN. Influence of uniaxial deformation on surface morphology and corrosion performance of chromium-based coatings for packaging steel. Corros Sci. 2021;190:109662.

5. Edy J, McMurray N, de Vooys A. In situ scanning Kelvin Probe study of cathodic disbondment on trivalent chromium coated steel. In: Corrosion and Prevention. 2017. p. 134213.

6. Wijenberg J, Steegh M, Penning JP, Portegies Zwart I. Wo 2014/079909. 2014.

7. Prabhakara M, Varanasi RS, Corrêa da Silva C, De Vooys A, Erbe A, Rohwerder M. Chromium coatings from trivalent chromium plating baths: Characterization and cathodic delamination behaviour. Corros Sci. 2021;187.

8. Kozlowski R. Sciencing [Internet]. Why Does Phenolphthalein Change Color? 2020 [cited 2021 Jul 9]. Available from: https://sciencing.com/phenolphthalein-change-color-5271431.html

9. Wint N, Geary S, Mcmurray HN, Williams G, Vooys ACA De. The Kinetics and Mechanism of Atmospheric Corrosion Occurring on Tin and Iron-Tin Intermetallic Coated Steels The Kinetics and Mechanism of Atmospheric Corrosion Occurring on Tin and Iron-Tin Intermetallic Coated Steels. Electrochem Soc. 2015;162.

10. Wint N, de Vooys ACA, McMurray HN. The corrosion of chromium based coatings for packaging steel. Electrochim Acta. 2016;203:326–36.

11. Williams G, Kousis C, McMurray N, Keil P. A mechanistic investigation of corrosion-driven organic coating failure on magnesium and its alloys. npj Mater Degrad. 2019;3(1).

12. Introduction to mass analyzers : SHIMADZU (Shimadzu Corporation) [Internet]. [cited 2022 Jul 22]. Available from: https://www.shimadzu.com/an/service-support/technical-support/analysis-basics/fundamental/mass_analyzers.html

13. Stratmann M, Streckel H, Feser R. A new technique able to measure directly the delamination of organic polymer films. Corros Sci. 1991;32(4):467–70.

14. Holness RJ, Williams G, Worsley DA, McMurray HN. Polyaniline Inhibition of Corrosion-Driven Organic Coating Cathodic Delamination on Iron. J Electrochem Soc. 2005;152(2):B73.

15. Fürbeth W, Stratmann M. The delamination of polymeric coatings from electrogalvanised steel – a mechanistic approach.: Part 1: delamination from a defect with intact zinc layer. Corros Sci. 2001;43(2):207–27.

16. Leng A, Streckel H, Stratmann M. The delamination of polymeric coatings from steel. Part 2: First stage of delamination, effect of type and concentration of cations on delamination, chemical analysis of the interface. Corros Sci. 1998;41(3):579–97.

17. Wijenberg JHOJ, Steegh M, Aarnts MP, Lammers KR, Mol JMC.

Electrodeposition of mixed chromium metal-carbide-oxide coatings from a trivalent chromium-formate electrolyte without a buffering agent. Electrochim Acta. 2015;173:819–26.

18. Arca E, Fleischer K, Krasnikov SA, Shvets I. Effect of chemical precursors on the optical and electrical properties of p-Type transparent conducting Cr2O3:(Mg,N). J Phys Chem C. 2013;117(42):21901–7.

4 The Role of Chromium Oxide in Suppressing Filiform Corrosion on Cr metal / Cr oxide coatings for steel used in packaging applications

4.1 Introduction

Chapter 3 covered one example of corrosion driven coating disbondment, namely cathodic delamination. Another form of organic coating failure is referred to as filiform corrosion (FFC). Unlike cathodic delamination, where the separation of the organic coating from the substrate is linked to the cathodic reaction (usually oxygen reduction), in the case of FFC, separation of the coating from the substrate is linked to the anodic reaction (1)(2). Full details of the mechanism of filiform corrosion can be found in section 1.8.

FFC occurs at high relative humidity (commonly 65 – 95 %) (3) and is known to occur on packaging materials in storage conditions. It is important to ensure that alternatives to ECCS are equivalent or better in terms of their performance. They should also be non-toxic, acceptable to the food industry, and capable of application under similar tinning line conditions. As such, previous work has compared the performance of TCCT® to ECCS, with respect to both cathodic delamination and FFC, Whilst there was no evidence of FFC on ECCS after 5 weeks, it was observed on TCCT®, albeit at a lower propagation rate than that observed on uncoated steel (4). This finding was attributed to differences in chemical composition of the coatings. For example, the TCCT® possessed increased levels of surface metallic iron as well as fewer outer OH^- groups compared to ECCS (4). Pores in the Cr (III) coating were also believed to contribute to the enhanced FFC corroded area. Later work demonstrated the ability of TCCT® to resist cathodic delamination once the Cr oxide coating weight had reached 20 $mg.m^{-2}$ (where the Cr layer remained at 122 $mg.m^{-2}$) (5).

However, the TCCT® used during these pieces of work was produced using a one step electroplating process (6) whereby a mixed Cr metal – Cr oxide single layer is applied to the steel substrate. In comparison, very limited work has been conducted into the corrosion resistance properties of bilayer TCCT®, when the Cr metal and Cr oxide are

deposited in two separate stages, and the work that has been done primarily focuses on cathodic delamination.

As such, this chapter presents an optical study into the initiation and propagation of FFC as it occurs on dual layer trivalent chromium based, Cr metal-Cr oxide coatings applied to packaging steels, as a function of Cr (III) oxide coating weight. The time dependant extent of FFC is investigated optically and an explanation of the findings is given in terms of the effect of Cr (III) oxide coating weight. The results are also compared to ECCS, the current standard, as well as the older style TCCT® produced via a one-step electroplating process.

A combination of scanning electron microscope (SEM) and time of flight secondary ion mass spectroscopy (ToF-SIMS) is used to determine the differences in surface chemistry and appearance of the various oxide coating weights. This sample characterisation allowed hypothesises with regards to the mechanism of FFC to be formed. In this instance, ToF-SIMS us used to observe the elemental composition of the filaments after filiform had been initiated and propagated. SEM imaging allows for investigation of differences in the number of defects observed between samples of varying Cr (III) oxide coating weights.

4.2 Materials and methods

4.2.1 Materials

The samples used were the same as those described in Chapter 2.1.

Electroplated low carbon steel, produced on the pilot coating line using Cr (III) electrolyte, was obtained from Tata Steel Packaging Ijmuiden. For the Cr (III) based substrates, electroplating had taken place in two stages to create a bilayer coating with an underlayer of Cr metal (100 $mg.m^{-2}$) and varying amounts of overlaying Cr (III) oxide as shown in Table 4.1 below.

Table 4.1. The varying Cr (III) oxide coating weights overlaying the 100 $mg.m^{-2}$ Cr metal.

Cr (III) oxide coating weights / $mg.m^{-2}$										
2	3	5.5	6.5	8	9	13	13.5	16.5	21.5	23.5

In all cases the coating weight values quoted are those corresponding to the above values.

TCCT® produced via a one-step cathodic electrodeposition process on an industrial electroplating line were obtained from TATA Steel. Samples had comparable levels of Cr metal (~100 $mg.m^{-2}$), and Cr (III) oxide coating weights of 7 and 24 $mg.m^{-2}$.

ECCS, obtained from Tata Steel, had an as received Cr oxide coating weight of 9 $mg.m^{-2}$. All chemicals, including polyvinyl butyral-co-vinyl alcohol-co-vinyl acetate (PVB), molecular weight 70,000-100,000, were obtained from Sigma-Aldrich Chemical Co. and of analytical grade purity. A 15% w/w ethanolic solution of PVB was made by slowly dissolving PVB in ethanol and used as the organic coating during experiments. Although PVB does not represent the fully formulated product, it dries at room temperature and allows for comparisons to be made easily between samples (4)(7).

2.2. Methods

2.2.1. Filiform corrosion studies

To understand the effect of Cr (III) oxide coating weight on the extent of FFC and how it compares to the current standard, ECCS, FFC studies were conducted as described in section 2.2.1.

2.2.2. Electrochemical measurements

Samples of size 2.5 x 2.5 cm were cut from a larger sheet and cleaned using isopropanol (IPA). A 0.8 cm^2 area of the TCCT samples was exposed to NaCl electrolyte, pH 2. Open circuit potential (OCP) values were recorded to help determine whether the coating would anodically dissolve when coupled to the iron substrate.

2.2.3. Microscopy

At the end of the 4-week period a Zeiss axio observer Z1M inverted optical microscope was used to determine the width and length of the filaments. Images of individual filament were captured and measuring tools on the microscope's software allowed distances across the width and length of the filaments to be measured accurately.

2.2.4. ToF-SIMS

ToF-SIMS was used to analyse the chemical composition of the FFC filaments. ToF-SIMS analysis was conducted using a Scientific Analysis Instruments (SAI) MiniSIMS-ToF. Chemical images and spectrums were obtained and analysed using MiniSIMS software. To allow a better signal to noise ratio and a greater number of counts, a dwell time of 5 ms per pixel was used (8). Images were obtained with the detector in negative polarity to portray the negative ions emitted from the surface such that the presence of chloride could be identified (8).

2.2.5 X-ray photoelectron spectroscopy (XPS)

XPS spectra were recorded on a Kratos Axis Ultra using monochromated Al Kα X-rays of 1486.8 eV. The measured spot size was 700 μm x 300 μm. The XPS spectra was subsequently analysed in CasaXPS software with Shirley backgrounds. Binding energies were calibrated to the main hydrocarbon peak at 284.8 eV (1)

4.3 Results

4.3.1 Materials Characterisation

SEM images of the surface of the TCCT® substrates with a relative high (21.5 $mg.m^{-2}$) and low (2 $mg.m^{-2}$) Cr (III) oxide coating weight were obtained prior to any other experimental procedures. These samples were chosen to quickly determine whether there was likely to be any changes in surface appearance of the coating as the coating weight was increased. The SEM images of the high Cr oxide (21.5 $mg.m^{-2}$) and low (2 $mg.m^{-2}$) TCCT® substrates, as well as ECCS, are shown in Figure 4.1.

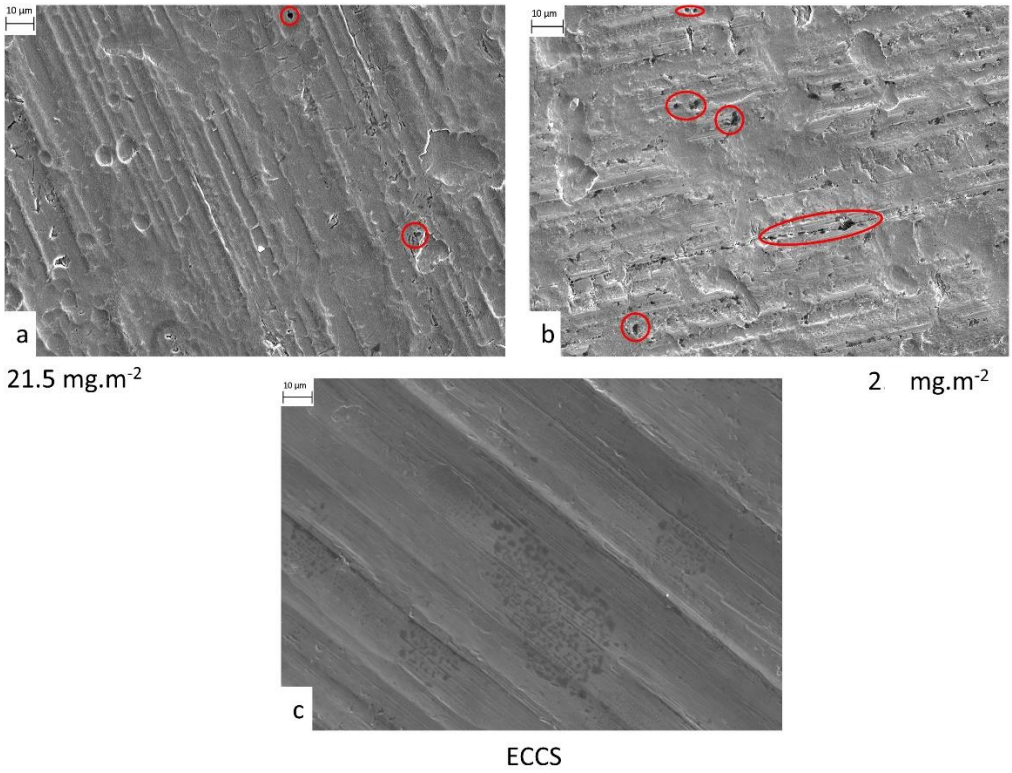

Figure 4.1. SEM images of TCCT® substrates with a relative high (21.5 mg.m^{-2}) and low (2 mg.m^{-2}) Cr (III) oxide coating weight, as well as ECCS for comparison.

The SEM images of the TCCT® substrates show that the steel substrate is heterogenous with evidence of varying rolling roughness. It was also observed that the Cr coating follows the structure of the substrate. Defects, approximately 1–2 µm in diameter, as highlighted by the red circles, were observed on the surface of both the Cr (III) coated samples. Features higher above the surface appear lighter. Hence, the defects were identified as small, darker areas and explained as holes in the Cr coating allowing underlying iron to be exposed. However, the number of defects present was far greater for the sample with the lower, Cr (III) oxide coating weight (2 mg.m^{-2}) as shown in Figure 4.1. Similarly, the steel substate of ECCS exhibited heterogeneities, like many industrial substrates, and the coating followed the structure of the substrate. However, the presence of defects on ECCS was minimal.

To quantify the number defects and how these varied between coating weights, a copper sulphate test was conducted. Samples of TCCT® and ECCS were dipped in a

copper sulphate solution, the composition of which can be found in Table 4.2 and left for 60 s before being rinsed under a stream of DI water and left to drip dry.

Table 4.2. Composition of copper sulphate solution used to visualise defects in chrome oxide layer on chrome oxide coated substrate materials.

Constituent	**Weight / Volume**
Copper Sulphate Pentahydrate	8 g
Sulphuric Acid	2 ml
DI Water	500 ml

In this basic reaction, iron displaces copper ions from an aqueous solution of copper sulphate. It is a single displacement reaction of one metal by another metal which is realised through iron placing above copper in the reactivity series of materials; this therefore makes iron more reactive. Metallic iron is converted into ferrous ion (Fe^{2+}), and cupric ions (Cu^{2+}) are converted into metallic copper (equation 4.1).

$$Fe(s) + Cu^{2+}(aq) \rightarrow Fe^{2+}(aq) + Cu(s) \quad (4.1)$$

Due to this being a quick displacement reaction, and not copper plating, the copper formed is a precipitate and so is not formally adhered to the surface of the substrate. For this reason, it is important not to wipe the samples dry after the $CuSO_4$ dip and instead let them drip dry as the deposited nodules are easily removed mechanically. SEM imagery of precipitated copper on substrates surfaces and optical imagery of these copper nodules and their relative sizes is shown in Figure 4.

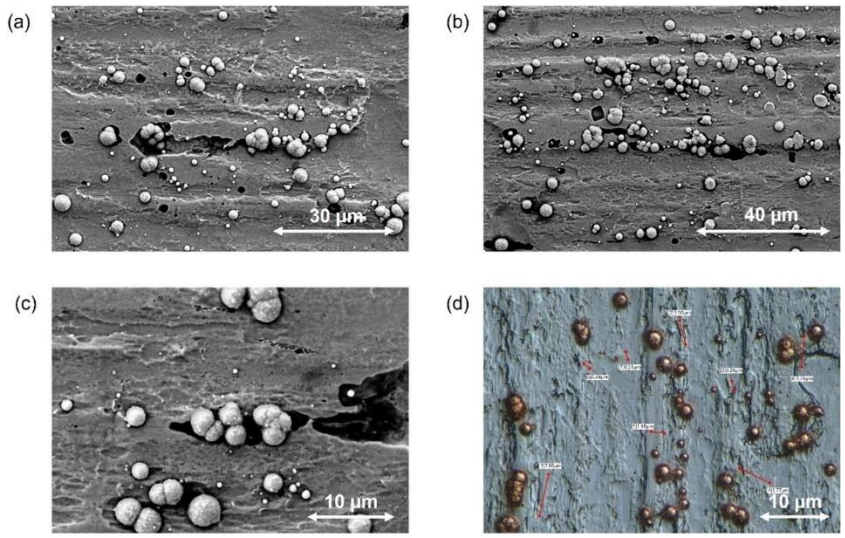

Figure 4.2. SEM and optical imagery of a TCCT® substrate with a Cr (III) oxide coating weight of 3 mg.m^{-2} showing copper on its surface after a $CuSO_4$ dip.

As seen in Figure 4.2, the copper nodules have a characteristic 'mushroom' shape, being circular in most cases, with a significant height profile from the substrates surface. SEM imagery has shown that the shape of these defects is not consistent, so it is noted that this shape of copper precipitation is independent of the defect or iron it may precipitated in or on. In order to ensure that the nodules witnessed on the surface of these substrates were in fact copper, XRF measurements and EDX mapping were conducted.

By varying the light settings and contrast on the Keyence optical microscope, it is possible to define these copper nodules more clearly in order to use a colour contrast tool to calculate the area average of copper on a given sample, as shown in Figure 4.3.

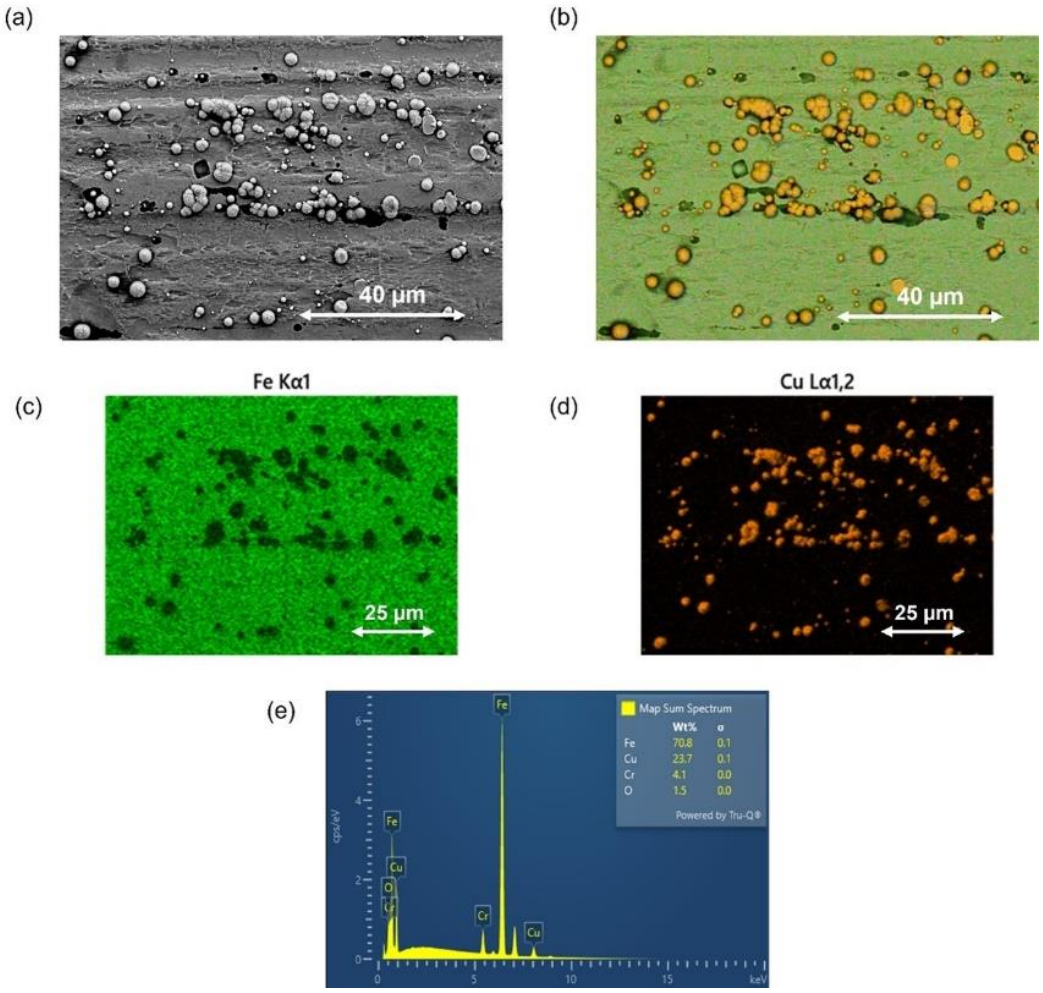

Figure 4.3. a) SEM image b) EDS map c) EDS of iron d) EDS of copper and e) the map spectrum for a TCCT® sample with a Cr (III) oxide coating weight of 3 mg.m^{-2}, highlighting copper on the surface of the substrate.

Using this method, the area of copper present on the surface, and hence an estimate of the area populated with defects was quantified. The results are shown in Figure 4.4.

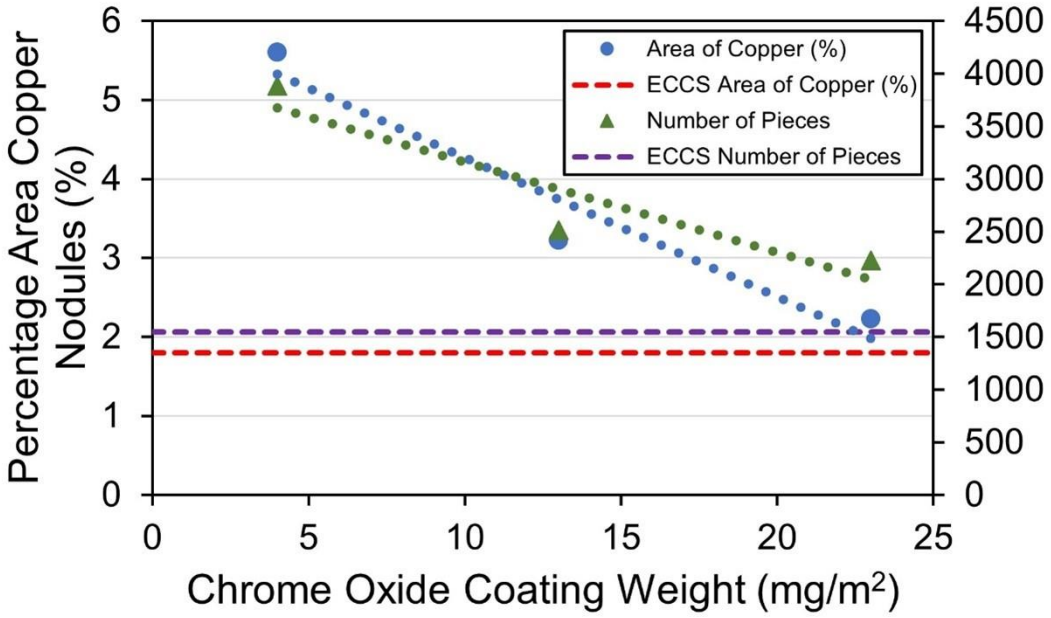

Figure 4.4. Area ratio of copper on the surface of TCCT® and ECCS substrate materials plotted with their respective site densities.

Increasing the Cr (III) oxide coating weight caused a decrease in the area ratio of copper, and hence a decrease in the amount of defects present on the surface of the substrate. TCCT® with a Cr (III) oxide coating weight of 3 $mg.m^{-2}$ had a copper area ratio of 5.6 %. This decreased to a copper area ratio of 2.2 % when the coating weight was increased to 23.5 $mg.m^{-2}$. ECCS exhibited the lowest copper area ratio of approximately 1.8 %, confirming that minimal defects, and thus underlying iron were present.

4.3.2 Electrochemical characterisation

All materials were characterised in terms of their OCP in 1 wt.% NaCl, pH 2 (made by the addition of HCl) solution, typical of that found inside a filament head, due to the high concentration of chloride ions (1). This would help determine whether the coating would anodically dissolve when coupled to the iron substrate. The OCP measurements enabled the corrosion potentials associated with varying TCCT® samples to be determined. the TCCT® samples were immersed in solution for 2 hours where they were free to corrode. This allowed enough time for the OCP to stabilise (the voltage was negligibly changing).

OCP measurements as a function of Cr (III) oxide coating weight are shown in figure 7 where the errors relate to ±one unit of standard deviation, on the basis of 2 consecutive measurements. The OCP measurements of blackplate and ECCS are also shown for comparison as the red and green point, respectively. The OCP measured for ECCS was more anodic relative to blackplate and TCCT. The OCP value for blackplate was similar to the samples of TCCT®, thus suggesting that the exposed iron, as a result of defects in the coating, dominates the potential reading. Similarly, OCP values observed on TCCT® electrodeposited via the one step method were also found to be similar to iron.

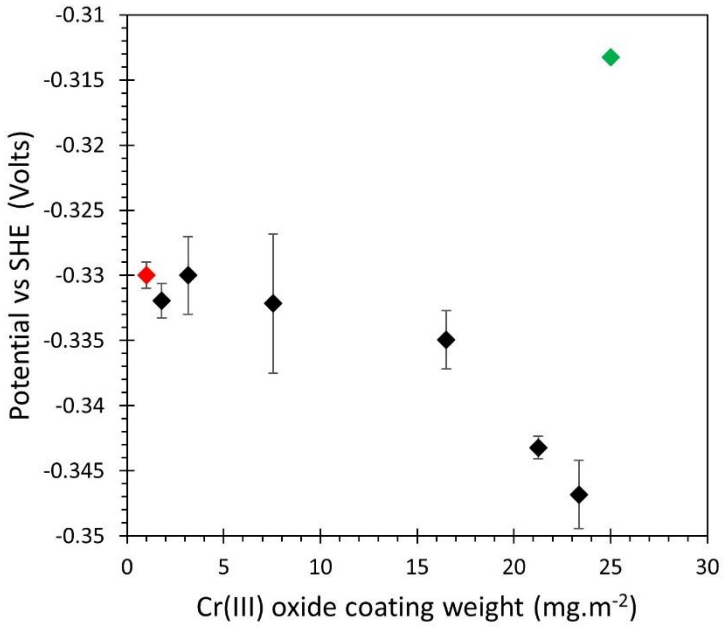

Figure 4.5. OCP values as a function of Cr (III) oxide coating weight. OCP measurements of blackplate and ECCS are also shown for comparison as the red and green point, respectively.

4.3.3 Surface characterisation

XPS was used to determine and quantify the surface chemistry of the outermost layer (5 nm) of both a relative low and high Cr (III) oxide coating weight (2 and 21.5 $mg.m^{-2}$ respectively) in the view that this outermost layer will dictate to what extent FFC propagates. ECCS was also analysed for comparison purposes. Figure 4.6 shows the XPS wide scans and chemical compositions of the outermost layer of these coatings. There were similarities between the surface scans for both the low and high coating weight as well as ECCS, with chromium peaks being present at 575 eV and 584 eV as

well as the oxygen peak at 530 eV (9). . The iron peak is also present at 708 – 711 eV (10) but is larger for the lower Cr (III) oxide sample, suggesting more iron is present at the surface, most likely due to the reduced coating weight and presence of more defects. It is shown in the bar charts that the chemical constituents of the outermost layer vary between the two Cr (III) oxide coating weights. Approximately 90x more $Cr(OH)_3$ was observed in the case of the sample with 21.5 $mg.m^{-2}$ oxide compared with that of the sample with 2 $mg.m^{-2}$. Also, a significant quantity of iron is present on the surface of the 2 $mg.m^{-2}$ sample in comparison to the 21.5 $mg.m^{-2}$ sample. The chemical constituents of the outermost layer of ECCS comprise of a mixture of Cr_2O_3, Cr metal and $Cr(OH)_3$ with very little iron present.

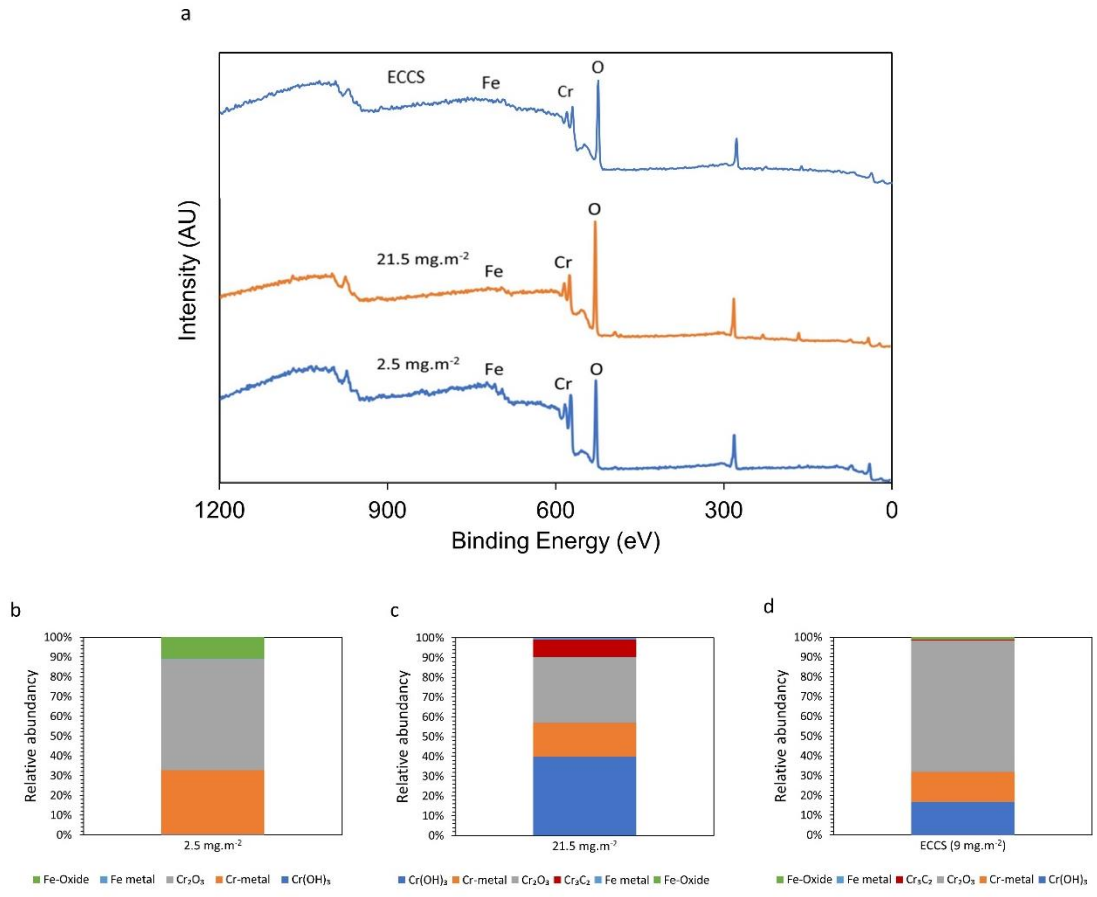

Figure 4.6. XPS wide scans and chemical compositions of the outermost layer of TCCT with a Cr (III) coating weight of 2.5 and 21.5 $mg.m^{-2}$. ECCS is also shown for comparison purposes.

4.3.4 FFC Experiments

A systematic study into the influence of Cr (III) oxide coating weight on the initiation and propagation of FFC was then completed. Figure 4.7 shows images at weekly intervals after FFC was initiated from a scribe defect using $FeCl_{2,}$ of a sample with a relative low and high Cr (III) oxide coating weight. It can be noted that FFC initiated on both samples within the first week and continued to propagate during the following weeks, albeit at a greater rate for the sample with a lower Cr (III) oxide coating weight. The filaments projected perpendicular to the scribe defect, typically seen with this substrate (22). Some of the filaments appeared to be made up of a series of 'dots' or blisters, and the filiform appeared to 'jump' to the next propagation site. These filaments also appeared to cross over one another. This was more noticeable in the samples with lower Cr (III) oxide coating weights. Filiform propagated in a similar manner to the lower Cr (III) oxide coating weights for TCCT® electrodeposited via the one step method. Filaments propagated in a perpendicular direction, away from the scribe. The filaments were made up of interconnected pit like circular features.

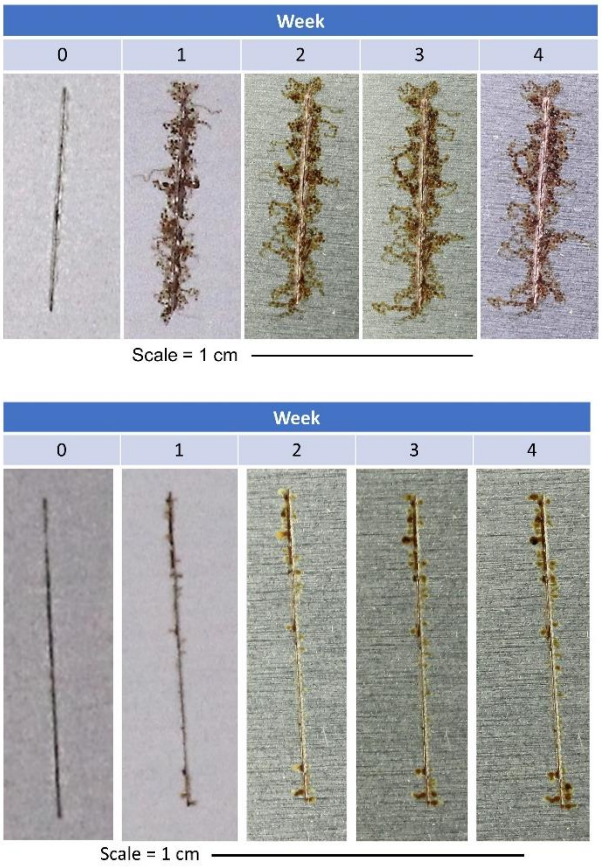

Figure 4.7. Images at weekly intervals after FFC was initiated from a scribe defect using $FeCl_2$, of TCCT® samples with a relative low and high Cr (III) oxide coating weight.

It is of note that FFC did not occur on ECCS, 4 weeks after initiation with $FeCl_2$ as shown in Figure 4.8.

Figure 4.8. Appearance of ECCS 4 weeks after initiation with $FeCl_2$.

Figure 4.9 shows samples of varying Cr (III) oxide coating weight (21.5 $mg.m^{-2}$, 13.5 $mg.m^{-2}$, 8 $mg.m^{-2}$ and 3 $mg.m^{-2}$ respectively), 4 weeks after FFC was initiated using 2 µl $FeCl_2$. Visually, it appeared that the area of FFC significantly increased

from approximately 2 to 21 mm^2 when the Cr (III) oxide coating weight was decreased from 21.5 $mg.m^{-2}$ to 3 $mg.m^{-2}$. Again, some of the filaments, most notably on samples with lower Cr (III) oxide coating weights, were made up of a series of 'dots' or blisters.

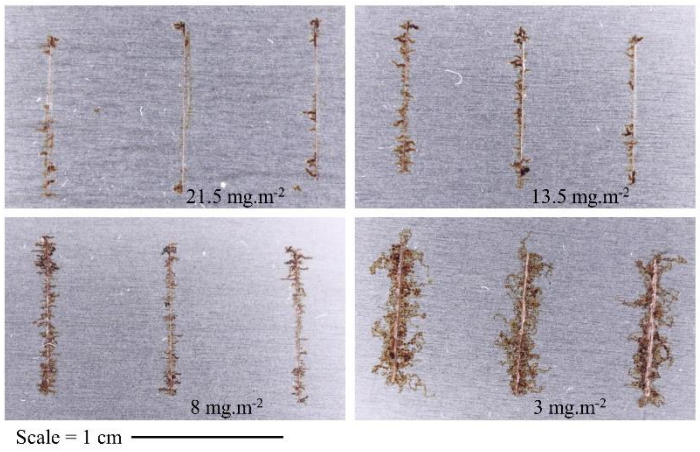

Figure 4.9. Samples of varying Cr (III) oxide coating weight (21.5 $mg.m^{-2}$, 13.5 $mg.m^{-2}$, 8 $mg.m^{-2}$ and 3 $mg.m^{-2}$ respectively), 4 weeks after FFC was initiated using 2 µl $FeCl_2$.

Figure 4.10 show SEM images of a sample 4 weeks after FFC was initiated, where blisters in the coating were observed due to the propagation of FFC. At these blisters, cracks in the coating were seen along some of the filaments. These blisters in the Cr (III) coating were more prevalent on the samples with a relative lower Cr (III) oxide coating weight.

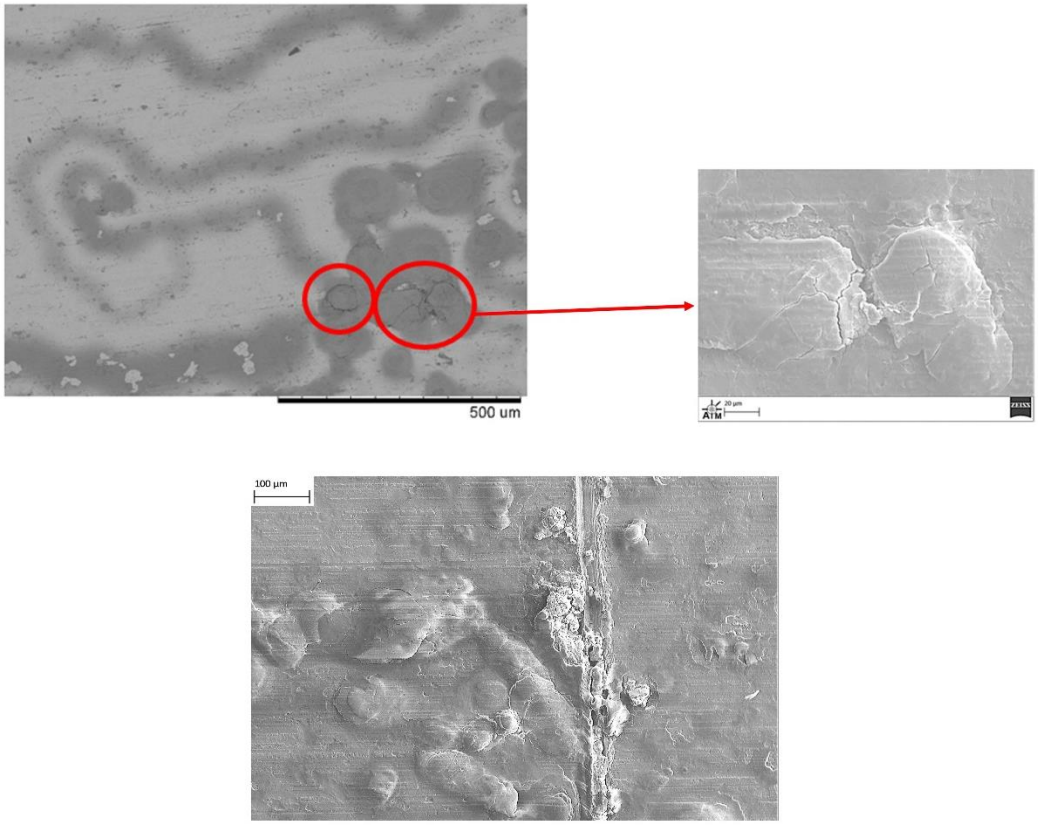

Figure 4.10. SEM images of the surface of TCCT®, 4 weeks after FFC was initiated, where blisters in the coating were observed due to the propagation of FFC.

Computerized image analysis was performed to calculate the area of FFC present on each sample. Figure 4.11 shows the total FFC corroded area, 4 weeks after FFC initiation, as a function of Cr (III) oxide coating weight. The error corresponds to ± one standard deviation on the mean of six measurements.

From Figure 4.11 it is clear that the FFC corroded area is larger for samples with smaller Cr (III) oxide coating weight. The three samples with the lowest Cr (III) oxide coating weight (2 - 5.5 $mg.m^{-2}$) appeared to be significantly more susceptible to FFC than those with higher coating weights. These lower coating weights had an average FFC corroded area of 18.3±2.7 mm^2. A Cr (III) oxide coating weight between 6.5 and 16.5 $mg.m^{-2}$ significantly reduced the FFC corroded area to an average of 6.4±1mm^2. The highest coating weights of 21.5 and 23.5 $mg.m^{-2}$ exhibited the greatest resistance to FFC with an average FFC corroded area of 2.4±0.05 mm^2. A comparatively low area of FFC is hence recorded at coating weights greater than 6.5 $mg.m^{-2}$ suggesting

that a threshold value of approximately 6.5 mg.m^{-2} exists with regards to inhibiting FFC.

In comparison with the one step process of producing TCCT®, a Cr (III) oxide coating weight of 7 mg.m^{-2} exhibited a FFC corroded area of approximately 17.5 mm^2, over double that observed on a comparable sample made via the two-step deposition process. A coating weight of 24 mg.m^{-2} had a FFC corroded area of 8 mm^2, over 3x more than that observed on a comparable sample deposited via the two-step process. Thus, highlighting the improvements that the two-step process offers with regards to inhibiting FFC.

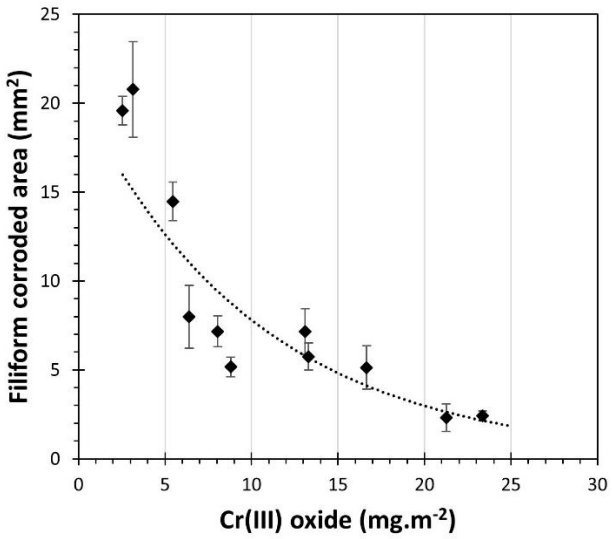

Figure 4.11. FFC corroded area, 4 weeks after FFC initiation, as a function of Cr (III) oxide coating weight. The error corresponds to ± one standard deviation on the mean of six measurements.

Figure 4.12 shows the FFC corroded area as a function of time for each of the Cr (III) oxide coating weights. The rate of FFC was relatively linear during the first two weeks of growth, but beyond this the change in FFC corroded area was somewhat stifled and the rate of FFC appeared to have reduced. The error bars correspond to ± one standard deviation on the mean of six measurements. It is of note that this decrease in rate of FFC was also observed on the samples produced via the one-step deposition process.

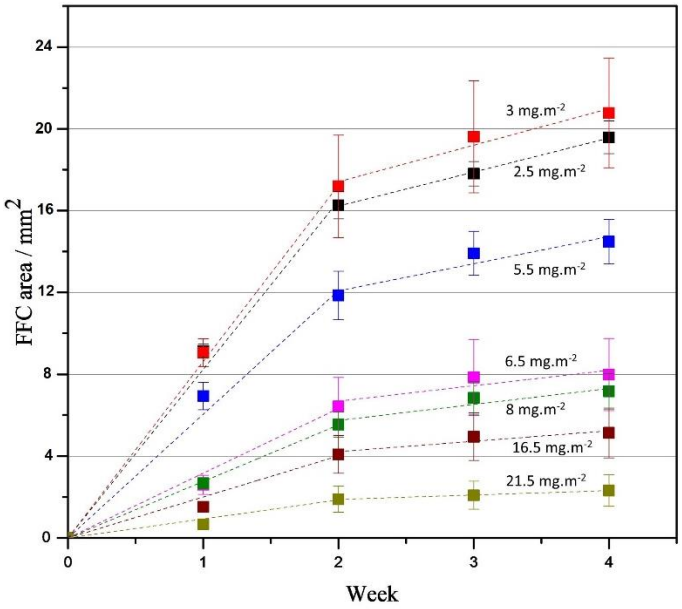

Figure 4.12. FFC corroded area as a function of time for varying Cr (III) oxide coating weights.

Table 4.3 shows the average corroded area for the different Cr (III) oxide coating weight samples as a function of time. The rate of FFC decreased as the Cr (III) oxide coating weight increased. Moreover, the rate of FFC for the sample with a Cr (III) oxide coating weight of 2mg.m^{-2} was 16.5mm^2 for weeks 0-2 and 3.4mm^2 for weeks 2-4. This decreased to 1.8mm^2 for weeks 0-2 and 0.4mm^2 for weeks 2-4 on a sample with 21.5 mg.m^{-2} Cr (III) oxide. On average the reduction in FFC rate from weeks 0-2 to weeks 2-4 was 4.3x less. The reduction in FFC rate between weeks 0-2 and 2-4 was greater in the samples with lower Cr (III) oxide coating weights.

Table 4.3. Average corroded area in the case that FFC is initiated using $FeCl_2$ on TCCT® samples of varying Cr (III) oxide coating weight.

	FFC corroded area / mm^2						
Time / weeks	**2mg.m^{-2}**	**3 mg.m^{-2}**	**5.5 mg.m^{-2}**	**6.5 mg.m^{-2}**	**8 mg.m^{-2}**	**16.5 mg.m^{-2}**	**21.5 mg.m^{-2}**
0-2	16.5 ± 0.6	17.3 ± 0.2	12.1 ± 0.7	6.3 ± 0.3	5.5 ± 0.1	4.0 ± 0.3	1.8 ± 0.1
2-4	3.4 ± 0.1	3.2 ± 0.7	2.6 ± 0.8	1.5 ± 0.8	1.60 ± 0.6	1.0 ± 0.4	0.40 ± 0.02

4.3.5 Post Corrosion analysis

After FFC had been initiated with $FeCl_2$ and left to propagate for 4 weeks, optical microscope images were taken to look at the individual FFC filaments. The width of

the filaments was observed to decrease with distance from the scribe defect, producing a tapered effect. Figure 4.13 shows an example of the tapering filaments that were observed.

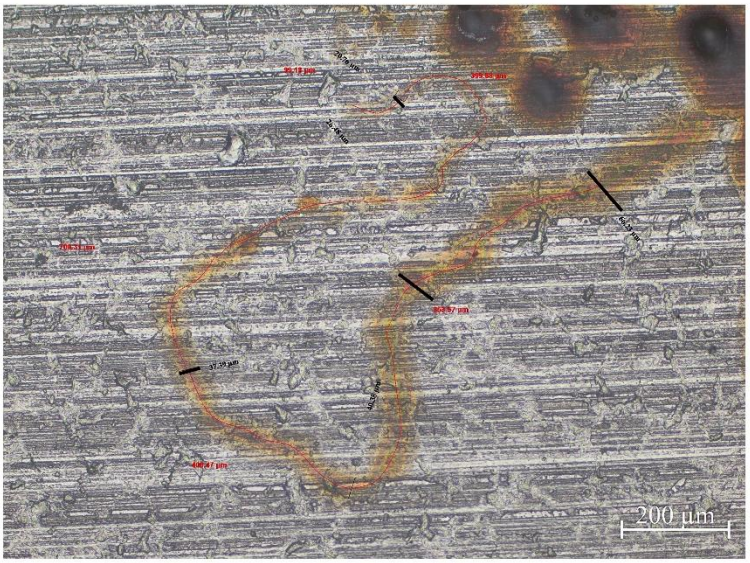

Figure 4.13. An example of the tapering filaments observed on the surface of TCCT® substrates.

Images of individual filaments were taken and measurements of their width at various distances from the filiform head were recorded using measuring tools on the microscope's software. Figure 4.14 shows an example of the width of the filaments as a function of length from the active head. The width of the filament decreases as the length of the active head from the scribe increased, confirming the assumption that the filaments were tapering.

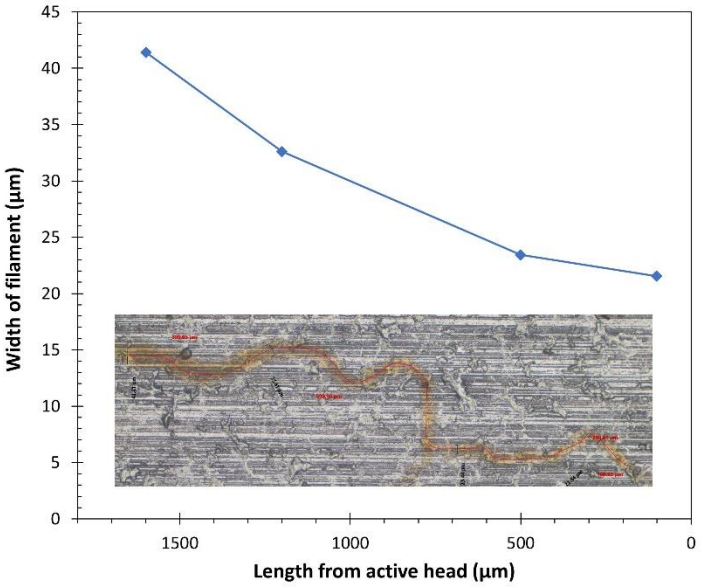

Figure 4.14. An example of the width of the filaments as a function of length from the active head.

Table 4.4 shows the average rate of change of the width of the filaments. The width of the filament is shown to decrease as it gets closer to the active head and thus end of the filament. Tapering of the filaments was more prominent on the samples with lower Cr (III) oxide coating weights.

Table 4.4. The average rate of change of the width of the FFC filaments

Length from active head (µm)	***1600***	***1200***	***500***	***100***
Percentage loss in width of filament relative to starting point at 1600 µm (%)	N/A	27±4.8	60±8.4	68±10.9

Filament tapering has previously been associated with chloride entrapment, whereby chloride ions are left behind in the filament meaning less electrolyte is available for FFC to propagate (23). There would thus, be a change in the activity of the head electrolyte and halting of the rate of FFC propagation. ToF-SIMS was used to determine the likelihood of this hypothesis.

ToF-SIMS was used to create a chemical image which provided a macro scale overview of the surface chemistry present on the samples. More specifically, it was used to analyse the chemical composition of the filaments and determine the distribution of certain elements including Cl^-. Figure 4.15 shows a chemical image of one of the TCCT® samples where FFC had propagated. The scribe can be seen towards the bottom of the image with the filaments protruding perpendicular to the scribe. The pink colour denotes Cl^- and is present throughout the filaments. Oxygen was also present across a large proportion of the surface, indicative of corrosion product.

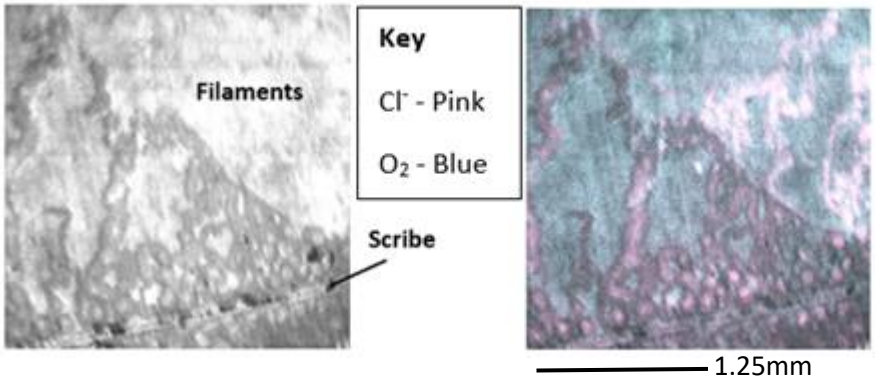

Figure 4.15. A chemical image of one of the TCCT® samples where FFC had propagated.

4.4 Discussion

The results show that, in comparison to ECCS, on which FFC was not observed, FFC was shown to initiate and propagate on TCCT®, with the FFC corroded area being smaller at higher Cr (III) oxide coating weights. It is also of note that the FFC corroded area was significantly less for equivalent TCCT® samples produced via the two-step method in comparison to the one-step process. The rate of FFC remained linear during the first 2 weeks of FFC propagation. After 2 weeks had passed there was a decrease in the rate of FFC propagation and the rate of FFC plateaued.

The difference in corrosion resistance of the various coatings may exist due to numerous factors. SEM images of the TCCT® coatings, both one and two-step, are relatively imperfect with the presence of numerous penetrative defects relative to the surface of ECCS. During the production of ECCS, the electroplating process involves the rapid reduction of Cr (VI) to Cr (III) onto iron, which is relatively noble. Thus, little iron is exposed through the coating. In comparison the electrodeposition of Cr

(III) based coatings is caused by a local change in pH at the cathode surface (15). This lack of spontaneous deposition may be the cause of the increased porosity. Furthermore, the number of defects was greater for samples with lower Cr (III) oxide coating weights as shown by SEM and copper sulphate testing. The samples with lower Cr (III) oxide coating weights had numerous filaments made up of blisters. It is proposed that these filaments were advancing via a successive pitting-mechanism whereby the majority of the surface was unaffected by corrosion, but individual pits were observed between these uncorroded areas (27). Figure 4.16 shows a schematic displaying the propagation of FFC beneath the Cr coating, such that it appears to stay intact, as shown by SEM images.

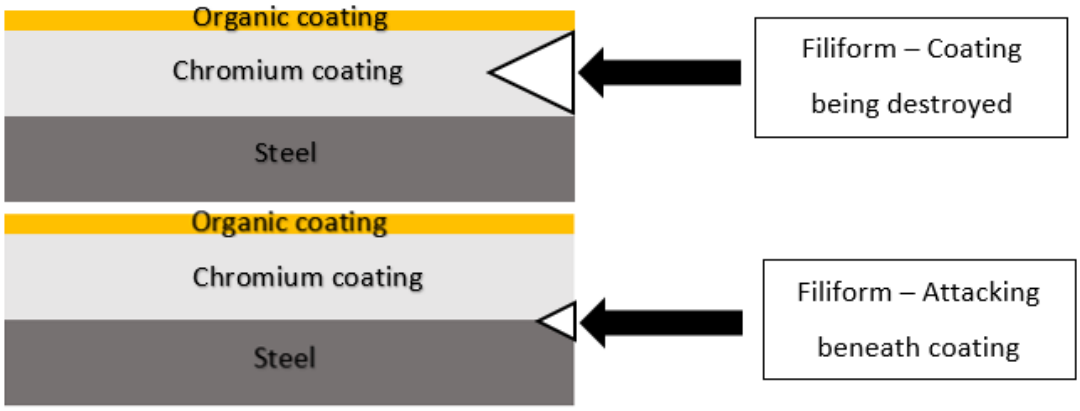

Figure 4.16. Schematic of filiform propagating beneath the Cr coating as opposed to the Cr coating being destroyed.

It is thought that these filaments were able to advance forward by 'jumping' to the next available defect or area of exposed iron in the coating. It is envisaged that after corrosion has been initiated at the artificial scribe in the coating, some of these propagate further, lifting the coating in doing so. This allows the corrosive environment to progress under the coating. It is proposed that at defects and areas of weakness in the coating, corrosion pits are formed that penetrate the Cr coating. This penetrative pressure, will again lift the coating, allowing the propagation of the filament. Hence, due to the increased amount of defects, as well as thinner nature of the coatings with lower Cr (III) oxide coating weights, the filaments would be able to propagate more easily.

It was proposed that the presence of these defects was the cause of the OCP values being the same as iron. The presence of iron, shown by XPS data on the surface of the

TCCT® substrates, and thus increase in anodic processes, may explain the more negative OCP values in comparison to ECCS (Figure 7). These defected areas would be more susceptible to anodic dissolution than the chromium layer itself.

What's more, the increased FFC corroded area observed for lower Cr(III) oxide coating weights suggests that Cr(III) oxide was acting to resist FFC. Cr_2O_3, of rhombohedral structure, offers insulating characteristics due to its semiconductor properties; it has a wide band gap of around 3 eV indicating more energy is required to excite an electron compared with most transition metal-oxides (11). Electron transfer is associated with the cathodic oxygen reduction reaction towards the back of the FFC filament head as seen in Figure 1. It is thus plausible that Cr (III) oxide blocks electron transfer during cathodic oxygen reduction, thus reducing the rate of the cathodic reaction. Hence, a greater coating weight of Cr (III) oxide would further reduce the rate of the cathodic reaction. FFC propagation rates may be surface controlled (by processes occurring at the electrolyte-substrate interface such as electron transfer) or controlled by mass transport in the electrolyte. Previous studies by McMurray et al. have shown that when FFC propagation rates are surface controlled (i.e. electron transfer limited), the rate is strongly dependent on the quantity of electrolyte in the head. The rate is shown to be proportional to the interfacial area present between the filament-head electrolyte droplet and the metal substrate. This is in resemblance to the results found in this study, where the substrates with a greater Cr (III) oxide coating weight, and thus larger interfacial area, exhibited a lower rate of FFC.

A second finding of the FFC results was the decrease in the rate of FFC over the 4 week time period. There could be several reasons for the rate of FFC growth slowing down. Initially two potential mechanisms were proposed. Firstly, being, the cathode may form in the defect, where iron, an active oxygen cathode (12) is exposed. If this were the case the distance between anode and cathode, over which they couple, would increase as the filament length increased over time. This would cause a greater ohmic resistance of the electrolyte and would result in a reduction in corrosion rate.

Secondly, it is possible that the tapering occurs as a result of the change in head electrolyte composition. As discussed, the presence of chloride ions is needed for the propagation of FFC on iron. In the case that Cl^- becomes entrained in the corrosion

product (13)(14). the head electrolyte would become depleted as it moved forward. This phenomenon would lead to tapering, and eventually termination of individual filaments as fewer Cl^- ions would be available as the electrolyte-filled head moved forward. This theory is supported by TOF-SIMS results (figure 11) which shows presence of chloride ions (denoted by the pink colour) throughout the filament tails.

In summary, this work establishes that variations in the Cr (III) oxide coating weight can have significant impacts on the susceptibility of TCCT® to FFC. Most notably, increasing the Cr (III) oxide coating weight improves the ability of TCCT® to withstand FFC. It is proposed that a higher Cr (III) oxide coating weight provides improved insulating properties and better surface coverage, ultimately protecting the underlying substrate.

4.5 Conclusion

This paper describes a systematic study into the effect of Cr (III) oxide coating weight on the kinetics and mechanism of FFC as it occurs on Cr (III) based coatings for packaging steels.

Cr (III) oxide was shown to provide some resistance with regards to inhibiting the extent of FFC and an improvement in FFC resistance was seen compared to samples produced via then one-step deposition process. The results suggest that the samples with lower Cr (III) oxide coating weights are more susceptible to FFC than the relative higher oxide coating weights. After 4 weeks of FFC propagation the sample with a Cr (III) oxide coating weight of 2 $mg.m^{-2}$ had a FFC corroded area of approximately 20 mm^2. In comparison, the sample with a Cr (III) oxide coating weight of 23.5 $mg.m^{-2}$ had a FFC corroded area of approximately 2.5 mm^2. This is proposed to occur for two reasons. Firstly, 1.) lower oxide coatings are shown to contain a greater number of defects, this allowing for the ingress of electrolyte to the substrate beneath which would mean that the coating would be broken down at a more rapid rate due to ingress of the electrolyte through the micropores in the coating to substrate iron and/or 2.) Secondly, the insulating properties that Cr (III) oxide offers would allow samples with greater coating weights to block the electron transfer reaction even more, thus slowing the rate of the cathodic reaction.

It was also found that the linear growth rate of FFC decreased with time. This is proposed to be a result of chloride entrapment in the tail of the filament such that the volume of chloride ions in the head reduced with time. As the conservation of chloride ions is required for continued FFC propagation the implication is a reduced rate of FFC, ultimately leading to the termination of FFC propagation. .

The present work displayed how FFC was initiated and propagated on novel, bilayer TCCT® composed of two distinct layers in comparison to the current standard, ECCS. Industrially scaled TCCT® would need to surpass a Cr (III) oxide coating weight of 6.5 $mg.m^{-2}$ (whilst the Cr layer remains at $100mg.m^{-2}$) to have a FFC corroded area less than 8 mm^{-2} over a 4-week time period. If the Cr (III) oxide coating weight is too low the coating coverage will not be good enough to provide sufficient corrosion protection.

4.6 References

1. Mcmurray HN, Williams G. 2.14 -Under Film / Coating Corrosion. Shreir's Corros. 2010;2:988–1004.

2. Sharman CF. Filiform Underfilm Corrosion of Lacquered Steel Surfaces. Nature. 1944;153:621.

3. Figueira RB, Sousa R, Silva CJR. Multifunctional and smart organic–inorganic hybrid sol–gel coatings for corrosion protection applications. Adv Smart Coatings Thin Film Futur Ind Biomed Eng Appl. 2020;57–97.

4. Wint N, de Vooys ACA, McMurray HN. The corrosion of chromium based coatings for packaging steel. Electrochim Acta. 2016;203:326–36.

5. Edy J, McMurray N, de Vooys A. In situ scanning Kelvin Probe study of cathodic disbondment on trivalent chromium coated steel. In: Corrosion and Prevention. 2017. p. 134213.

6. Wijenberg J, Steegh M, Penning JP, Portegies Zwart I. Wo 2014/079909. 2014.

7. Williams G, Kousis C, McMurray N, Keil P. A mechanistic investigation of corrosion-driven organic coating failure on magnesium and its alloys. npj

Mater Degrad. 2019;3(1).

8. Introduction to mass analyzers : SHIMADZU (Shimadzu Corporation) [Internet]. [cited 2022 Jul 22]. Available from: https://www.shimadzu.com/an/service-support/technical-support/analysis-basics/fundamental/mass_analyzers.html

9. Wijenberg JHOJ, Steegh M, Aarnts MP, Lammers KR, Mol JMC. Electrodeposition of mixed chromium metal-carbide-oxide coatings from a trivalent chromium-formate electrolyte without a buffering agent. Electrochim Acta. 2015;173:819–26.

10. Wang J-C, Ren J, Zhang L, Wang J-S, Zang S-Q, Han L-F, et al. Synergistic photocatalysis of Cr(VI) reduction and 4-Chlorophenol degradation over hydroxylated α-Fe2O3 under visible light irradiation. J Hazard Mater. 2016;311:11–9.

11. Abdullah MM, Rajab FM, Al-abbas SM. Structural and optical characterization of Cr 2 O 3 nanostructures : Evaluation of its dielectric properties. 2014;027121:1–11.

12. Wint N, Geary S, Mcmurray HN, Williams G, Vooys ACA De. The Kinetics and Mechanism of Atmospheric Corrosion Occurring on Tin and Iron-Tin Intermetallic Coated Steels The Kinetics and Mechanism of Atmospheric Corrosion Occurring on Tin and Iron-Tin Intermetallic Coated Steels. Electrochem Soc. 2015;162.

13. Williams G, McMurray HN. The mechanism of group (I) chloride initiated filiformcorrosion on iron. Electrochem commun. 2003;5:871–7.

14. Wint N, Eaves D, Michailidou E, Bennett A, Searle JR, Williams G, et al. The kinetics and mechanism of filiform corrosion occurring on zinc- aluminium-magnesium coated steel. Corros Sci. 2019;158:108073.

5. Electrodeposition of chromium metal and chromium oxide coatings from a trivalent chromium electrolyte

5.1. Introduction

The majority of the experimental work outlined in this thesis has involved investigation of TCCT® made using an industrial-scale electroplating line at Tata Ijmuiden. In order to be able to systematically change the Cr metal and Cr (III) oxide coating weights and in turn allow for a more efficient means of identifying trends in terms of samples produced, the process of electroplating a Cr (III) metal/oxide bilayer coating onto blackplate was learnt in Ijmuiden Tata steel works. This was achieved using a lab scale electroplating set up. Following this, a lab scale electroplating line was established in Swansea with the initial intention of validating the effect of current density on Cr metal and Cr (III) oxide coating weight. From here it was the aim to investigate the effect of various parameters, such as electrolyte temperature, on the coating weight of Cr metal and Cr (III) oxide using the latest TCCT® electrolyte composition. The parameters were chosen on the basis it was also feasible to alter these parameters industrially.

SEM and electrochemical characterisation of the lab made samples are compared with those obtained for pilot coating line TCCT® samples produced at TATA Steel in Ijmuiden.

5.2. Materials and methods

5.1.1. Substrate acquisition

Low carbon steel (blackplate) of 0.2 mm was obtained from Tata Steel, Trostre UK and used as the substrate material for the electrodeposition of Cr.

5.3.1. Electrolyte compositions

Two electrolyte baths were made up for both the electrodeposition of Cr metal and Cr (III) oxide onto blackplate. Their respective compositions can be seen in Table 5.1 below. In electrolyte 1 formate is used as a complexing agent to destabilise the very stable hexa-aqua complex $[Cr(H_2O)_6]^{3+}$, which is formed when Cr (III) ions are in the presence of water, and is difficult to reduce to Cr metal. The formate ion replaces one of the H_2O ligands to form a much weaker $[Cr(HCOO)(H2O)_5]^{2+}$ complex (1). Heating was applied during the making of the electrolyte to aid in the dissolution of the sodium sulphate. The pH of the electrolyte was adjusted using dilute sulphuric acid or dilute sodium hydroxide appropriately.

Table 5.1. Composition of TCCT electrolytes.

TCCT®	**Chemistry**	**pH**	**Temp / ºC**
Step 1 – Cr metal	$(CrOHSO_4)_2$ Na_2SO_4 HCOONa	2.3	37
Step 2 – Cr (III) oxide	$(CrOHSO_4)_2$ Na_2SO_4	3.2	55

5.3.2. Pre-treatment steps

Prior to the electrodeposition of the relevant Cr species, numerous pre-treatment steps were conducted as detailed in Table 5.2. Initially the steel substrate was cut to the acquired size using the guillotine. Following this, the steel substrate was pre-cleaned with acetone to remove oil and fingerprints. To remove other surface contaminants the steel substrate was then placed in an alkaline solution containing unisurfa KB35 additive and Sodium Hydroxide at a temperature of 60 ˚C (2). An anodic current of 1.5 $A.dm^{-2}$ was applied to provide scrubbing action. Samples were then rinsed in a bath of deionised water followed by a stream of deionised water. This allowed for removal of sodium hydroxide and prevented contamination of the solution used for the next pre-treatment step. The steel sample was then dipped in sulphuric acid at 25 ˚C for to remove the oxide film and activate the surface (2). The deionised water

rinsing process was repeated and the samples were placed in the relevant electroplating bath where a specified current density was applied.

Table 5.2. Pre-treatment steps prior to the electrodeposition of Cr.

Pre-treatment step	**Chemicals involved**	**Temperature / ºC**
Acetone clean	Acetone	Room temperature
Alkaline clean	Unisurfa KB35 additive and NaOH	60
Bath / rinse	Deionized water	Room temperature
Pickling	50 $g.L^{-1}$ H_2SO_4	Room temperature
Bath / rinse	Deionized water	Room temperature

5.3.3. Electroplating equipment set-up

As per the afore mentioned electroplating method Figure 5.1 and Figure 5.2 illustrate the equipment used. During the electrodeposition process the steel substrate acted as the cathode. A titanium plate electrode with iridium / tantalum mixed metal oxide (MMO) coating, sourced from MAGNETO special anodes, acted as the anode. This anode has very high catalytic activity and provides a high throwing power, and better plating distribution, whilst also reducing or eliminating the oxidation of Cr^{3+} ions to Cr^{6+} ions (2).

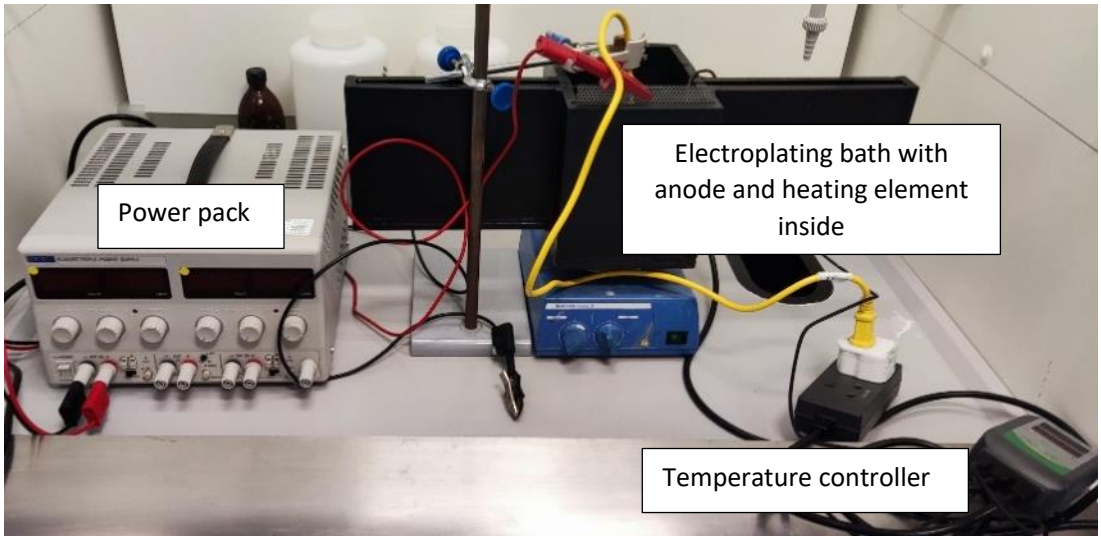

Figure 5.1 Electroplating equipment setup showing the custom-made electrolyte bath with external heating supply.

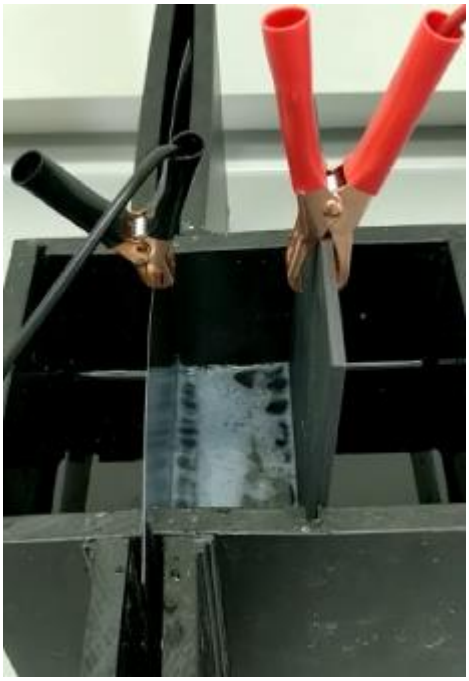

Figure 5.2. The anode and cathode (blackplate sample) immersed in electrolyte.

When Cr^{3+} are in aqueous solution, a very stable hexa-aqua complex known as $[Cr(H_2O)_6]^{3+}$ forms, where six ligands coordinate the central Cr ion.

The reduction reaction of Cr^{3+} to Cr is characterized by a standard reduction potential.

$$Cr^{3+} + 3e^- \rightarrow Cr \qquad E° = -0.74\ \text{V vs SHE} \qquad (5.1)$$

This is more negative than the standard reduction potential of hydrogen.

$$2H^+ + 2e^- \rightarrow H_2 \qquad E° = 0\ \text{V vs SHE} \qquad (5.2)$$

Thus, a significant amount of hydrogen evolution (equation 5.2) will be generated during the electrodeposition process which can be observe in Figure 5.2 (3). A large amount of current is also used for this reaction, and hence the process has a low current efficiency.

Hydrogen gas is evolved at the surface of the cathode and causes a large pH increase near the electrode surface. At pH values greater than 4.5 the $[Cr(H_2O)_6]^{3+}$ complex hydrolyses and olation reactions occur leading to the formation of precipitate that block the cathode surface for the desired Cr^{3+} reduction reaction. Olation refers to the process by which metal ions form polymeric oxides in aqueous solution (3).

The oxidation of water to oxygen is the principal reaction occurring at the anode.

Numerous Cr complexes are known to exist, which are predominantly hexacoordinate in nature, and hence, there are a number of possible reaction steps and mechanisms that could occur during plating of the coating (4).

A custom-made electroplating bath constructed from a polymer, resistant to the chemicals in the bath, was used. The anode and cathode were placed parallel to one another with a gap of 4 cm, pre-determined by Tata Steel Ijmuiden, between them. The temperature of the bath was maintained by a heating element attached to an Inkbird digital temperature controller, accurate to ±1 °C. A magnetic flea was used to agitate the electrolytes throughout the electroplating process, to imitate the turbulence caused by the fast movement of the steel strip in industrial conditions (4). The current was controlled using a power pack connected to an Arduino relay system. The applied currents required were calculated by multiplying the area of submerged cathode by the current density required.

Once the substrate had been electroplated with Cr, it was subjected to a final rinse under a stream of deionised water and dried, prior to storing. Samples were characterised by the use of a handheld XRF and SEM.

5.3.4. X-ray fluorescence (*XRF)*

The total quantity of Cr was measured using a handheld XRF gun. The reported XRF values were corrected for the contribution of the steel substrate to the Cr signal. Four measurements were recorded per sample.

5.3.5. Scanning electron microscopy (SEM)

SEM allowed any differences between the surfaces of the lab made electroplated samples as well as the line samples to be observed.

5.3.6. Cyclic Voltammetry

Cyclic voltammetry was used to investigate the presence of sulphite in the electrolyte. Repetitive potential scans between the onset of hydrogen evolution on the cathodic side and oxygen evolution on the anodic side were run until a stable cyclic voltammogram (CV) was acquired. The potential was controlled by a Metrohm Autolab PGSTAT302N potentiostat. All potentials were reported vs. a Hg / Hg_2Cl_2 / KCl (sat'd) electrode. The working electrode was a mirror polished platinum electrode. A platinum electrode served as the counter electrode. All cyclic voltammograms were recorded with a scan rate of 100 $mV.S^{-1}$.

5.3.7. Scanning vibrating electrode technique (SVET)

The SVET was used to visualise the electrochemical processes occurring on the surface of the sample and see how this differs between line produced and lab-made samples. The SVET is able to spatially resolve areas of dissimilar electrochemical activity. Spatially resolved maps were produced on Golden Software's Surfer 10, a contouring and surface modelling software platform. TCCT samples were immersed in 1 wt. % NaCl over a 24-hour period. Samples were scanned immediately after the addition of electrolyte and every hour onwards until the end of the 24-hour period.

5.3.Results and discussion

5.3.8. Initial results

Once the Swansea electroplating lab scale rig was successfully established, an initial study to determine whether Cr was successfully deposited was undertaken. The plating bath was filled with electrolyte one at a pH of 2.3 and temperature of 37 °C. A sample of blackplate was subjected to the pre-plating regime and then electroplated for 800 ms at a current density of 20 $A.dm^{-2}$. For this initial experiment the current, and time it was applied for, was controlled using a potentiostat. However, it was confirmed by XPS that no Cr had been deposited.

The explanation for this could be due to a too low current density being applied, thus the plating window (regime II in Figure 5.3) was not reached. Figure 5.3 shows the three regimes that were determined during the plating of TCCT using a one step process and a single electrolyte, containing formate.

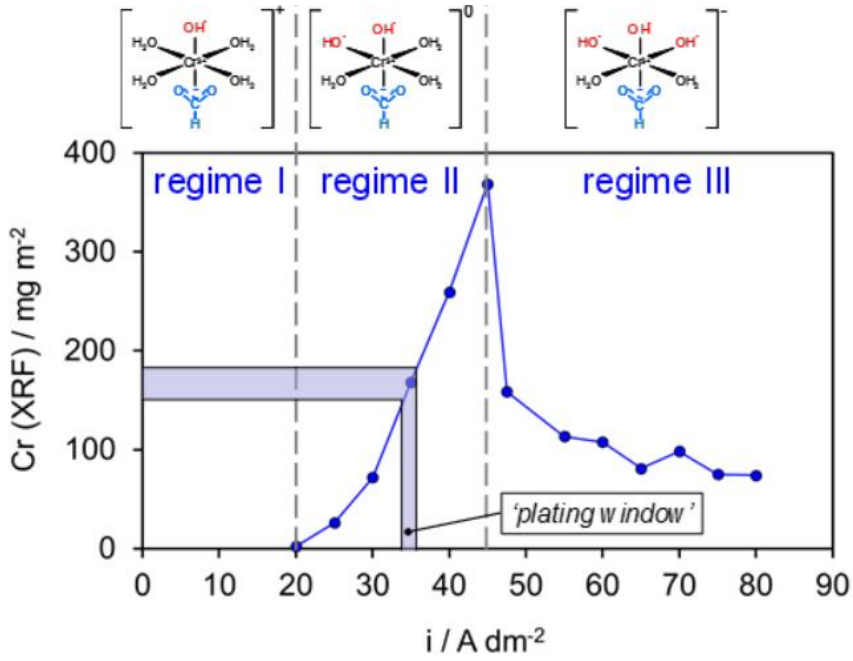

Figure 5.3. The effect of current density on Cr-Cr oxide deposition of a one-step Cr electrolyte. Three regimes and the respective chrome species present are proposed.

The complex formed in regime I is soluble and thus Cr will not be deposited. The current density must overcome a certain value (regime I) for Cr to successfully be electro-deposited. It is proposed that the current density that was applied was in the region of regime I thus explaining why little to no Cr was deposited. To overcome this issue, power packs with higher current output were used. An Arduino was used to control the time that current was applied for.

Alternatively, it was proposed that sulphite may be present in the electrolyte, in turn hindering the deposition of Cr.

5.3.9. Removing sulphite from the electrolyte

Previous work found the presence of sulphite in the basic chromium sulphate chemistries used as the electroplating solution (5). Basic chromium salt is industrially

prepared via the reduction of Cr (VI) (in the form of sodium dichromate) to Cr(III) with sulphur dioxide (SO_2) (5). An excess of SO_2 is used to fully reduce Cr to the +3 oxidation state. If the excess sulphur dioxide is not sufficiently removed, sulphurous acid will be formed which may form sulphite anions (see equation 5.3) (5). The equation for the formation of sulphite is as follows:

$$SO_2 + H_2O \rightarrow H_2SO_3 \leftrightarrow 2H^+ + SO_3^{2-} \quad (5.3)$$

Sulphite can adsorb onto the surface of a metal, in turn blocking binding sites for Cr deposition as seen in Figure 5.4 (5). The presence of sulphite inhibits oxidation of formate to CO_2 at the electrode (equation 5.4) and in turn Cr is not successfully deposited.

$$HCOO^+ \rightarrow CO_2 + H^+ \quad (5.4)$$

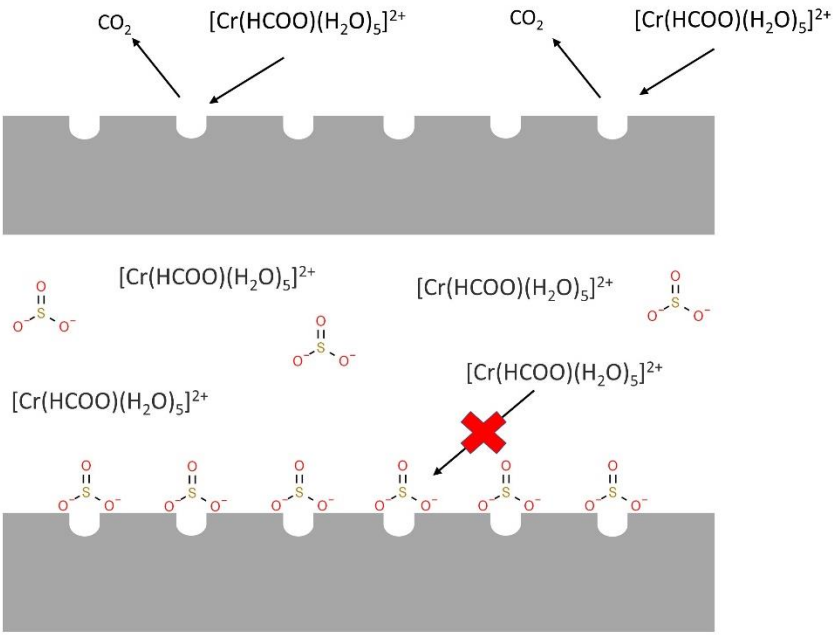

Figure 5.4. Schematic showing how sulphite can adsorb to the surface of the metal, in turn blocking binding sites for the formate complex.

Formate is used as a complexing agent in electrolyte 1. Cyclic voltammetry can be used as a means to monitor the presence of sulphite when formate is present in the electrolyte (electrolyte 1) (5).

If the electrolyte is free from sulphite a characteristic CO_2 'surface explosion' peak, caused by a very high activity towards CO_2 formation, will be observed during cyclic

voltammetry, as formate will successfully be oxidised to CO_2. If the peak is not observed and formate has not been successfully oxidised to CO_2, indicating sulphite is present, a prolonged reductive current may be used as a way to remove the sulphite (5).

Cyclic voltammetry was used as a means to monitor sulphite removal when formate was present in the electrolyte. The cyclic voltammogram (CV) of a freshly prepared Cr (III) electrolyte is given in Figure 5.5.

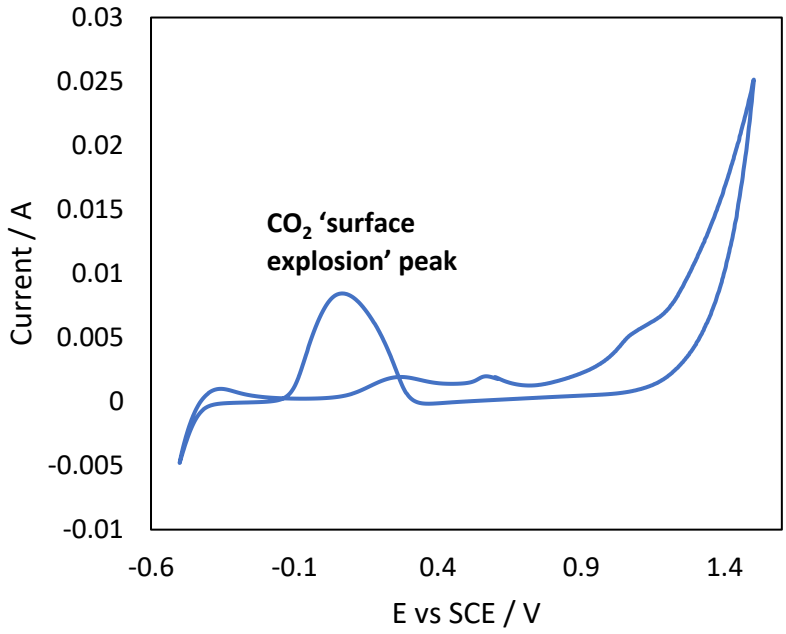

Figure 5.5. Cyclic Voltammogram of electrolyte 1.

Hydrogen and oxygen evolution can be observed to the far left and right of the cyclic voltammogram, respectively. The characteristic CO_2 'surface explosion' peak was observed at approximately 0.2 V vs. SCE in the CV for electrolyte 1 indicating that sulphite was not present in the electrolyte and formate was oxidised to CO_2, thus the deposition of Cr would not be hindered (5).

Once the issues of the electroplating process had been overcome, the effect of various plating parameters on the deposition of both Cr and Cr (III) oxide were investigated.

5.3.10. Effect of applied current density on coating weight

The applied current is the driving force for the reaction and thus is expected to have an important role in the amount of respective Cr species deposited. Thus, a systematic study into the effect of current density on the amount of Cr and Cr (III) oxide deposited onto blackplate in $mg.m^{-2}$ as measured by XRF was undertaken. All samples were subjected to the pre-plating regime described earlier and were electroplated for 0.8 s at current densities ranging from 10 to 40 $A.dm^{-2}$.

This study was conducted on blackplate samples and was undertaken separately for both the first and second electrolyte. The results of the study can be seen in Figure 5.6 and Figure 5.7 for electrolyte 1 and 2 respectively.

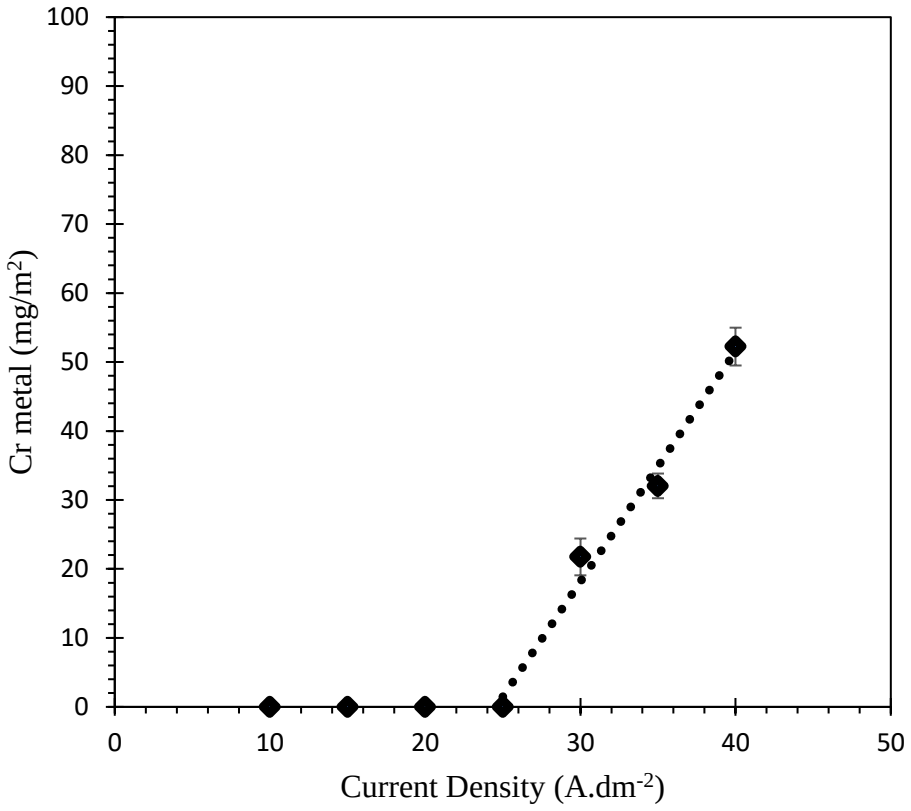

Figure 5.6. Coating weight for Cr metal deposited onto blackplate as a function of current density. The respective current was applied for a time of 0.8 s.

Cr metal was not successfully deposited onto blackplate until a threshold current density of 30 $A.dm^{-2}$ was applied. It was proposed that below this current density, an insufficient amount of H^+ had been reduced to H_2 in order to increase the surface pH at the cathode for Cr to be deposited. The chrome species present were thought to be those present in regime I of Figure 5.3. Between 30 and 40 $A.dm^{-2}$ the amount of Cr metal deposited increased with increasing current density. An increase in current

density of 10 A.dm^{-2} (from 30 to 40 A.dm^{-2}) caused an increase in Cr metal deposit of approximately 30 mg.m^{-2}. It is proposed at these greater current densities, a greater amount of hydrogen was produced, thus altering the surface pH enough such that reactions such as those occurring in regime II (see equation 5.5) were able to occur, and Cr be successfully deposited.

$$[Cr(HCOO)(OH)(H_2O)_4]^+ + OH^- \rightarrow Cr(HCOO)(OH)_2(H_2O)_3 + H_2O \qquad (5.5)$$

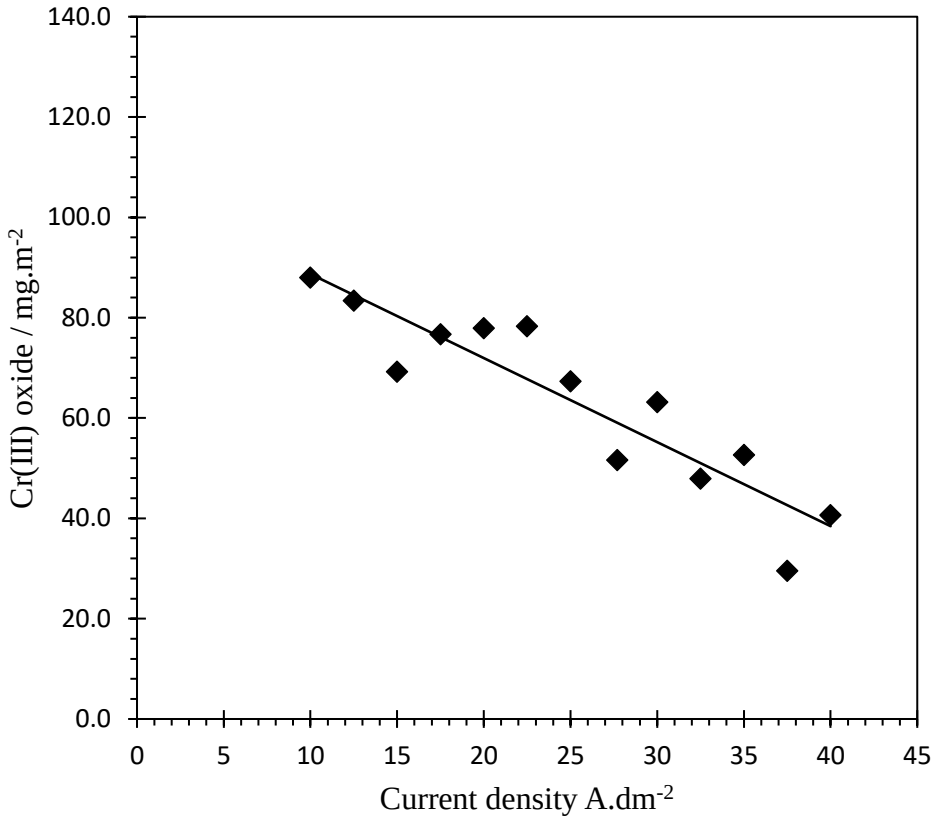

Figure 5.7. Coating weight for Cr (III) oxide deposited onto blackplate as a function of current density. A consistent electroplating time of 0.8 s was used.

In Figure 5.7 the effect of current density of the coating weight of Cr (III) oxide deposited onto blackplate can be seen. It appears that increasing the current density decreases the amount of Cr (III) oxide deposited. When a current of 10 A.dm^{-2} was applied the resultant Cr (III) oxide deposit was approximately 90 mg.m^{-2}. This decreased to approximately 40 mg.m^{-2} at an applied current density of 40 A.dm^{-2}. It was proposed that this trend was linked to changes in the chrome species present in

the electrolyte. Greater amounts of hydrogen evolution at higher current densities may have driven the following reaction (equation 5.6).

$$[Cr(H_2O)_6]^{3+} + 3OH^- \rightarrow [Cr(H_2O)_3(OH)_3] + 3H_2O \quad (5.6)$$

In turn, Cr complexes such as $[Cr(OH)_3(H_2O)_3]$ may have been present, blocking the electrode surface, thus hindering the amount of Cr (III) oxide that was deposited (4).

Figure 5.8 shows the surface appearance of blackplate samples electroplated using the second electrolyte at 20 (a) and 40 A.dm^{-2} (b) respectively. The surfaces appear relatively similar, and the underlying rolling direction was obvious through the coating. More pinholes were observed on the surface of the sample electroplated using a current density of 40 A.dm^{-2}, concurring the enhanced rate of hydrogen evolution which produces this pinhole effect.

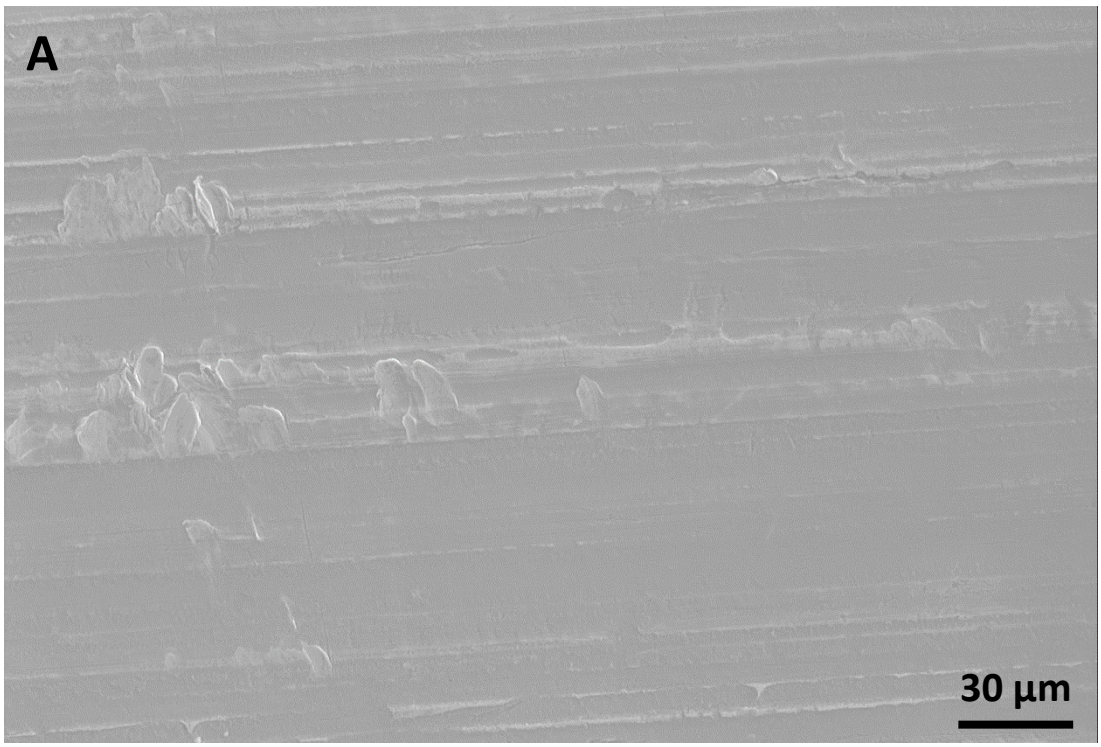

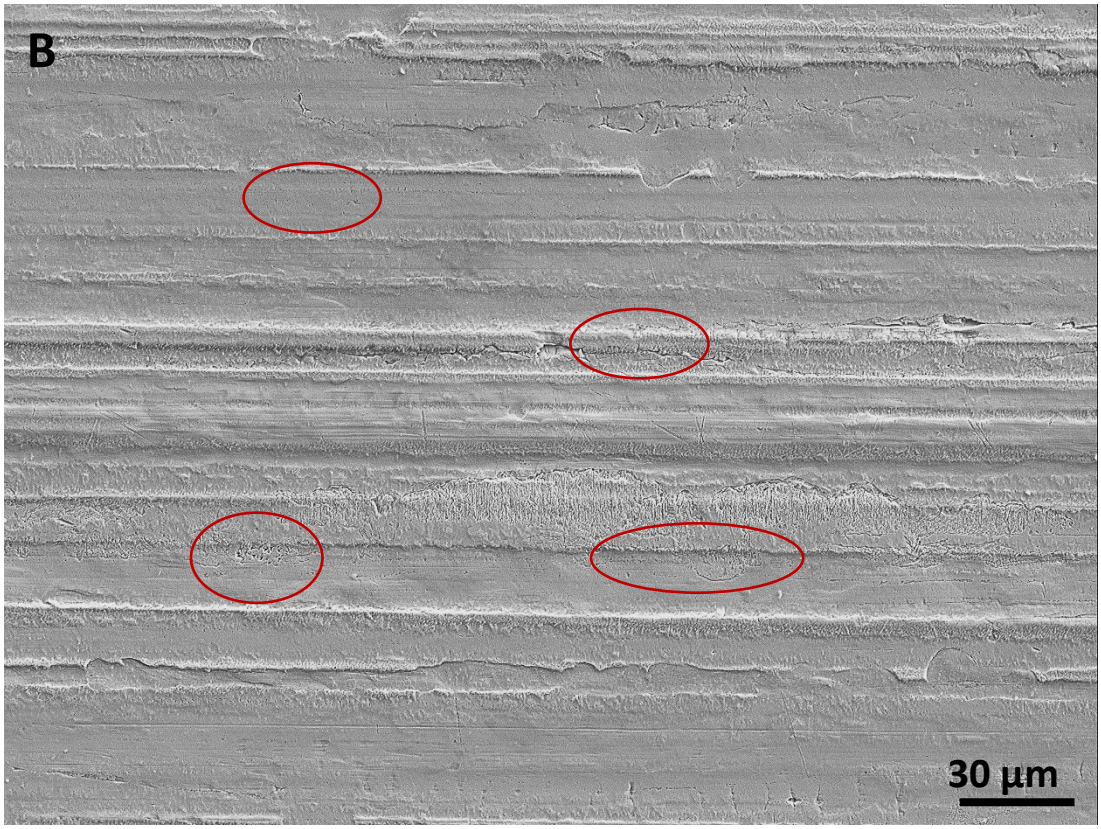

Figure 5.8. SEM images of the surface of blackplate samples electroplated using the second electrolyte at A) 20 A.dm^{-2} and B) 40 A.dm^{-2}.

5.3.11. Effect of electrolysis time on coating weight

The time current is applied for is another parameter that could feasibly be altered on-line conditions. Hence, the effect of the time of current application on the quantity of deposit was then investigated. Figure 5.9, shows Cr metal coating weight, as measured with XRF, plotted as a function of current density for 3 different electrolysis times, 0.8, 3 and 5 s. Irrespective of electrolysis time, no Cr metal was deposited onto blackplate until a threshold current density of 30 A.dm^{-2} was applied. Again, this was proposed to be due to the lack of surface pH increase needed for Cr deposition to occur.

Although increasing the electrolysis time to 3 seconds caused an increase in Cr metal deposit in comparison to an electrolysis time of 0.8 s, it also caused the amount of Cr metal deposited to decrease with increasing current density. The same trend was seen when the electrolysis time was increased again to 5 s. It was proposed that hydrogen evolution played a key role in explaining this trend. Longer electrolysis times will

mean that hydrogen evolution is occurring over a longer period of time. In turn, the production of hydrogen evolution may be so great that it leads to a decrease in efficiency of the deposition process as well as a large increase in pH at the surface of the cathode. This increase in pH leads to precipitation of soluble Cr (III) hydroxides, which block the electrode surface (6)(7). Moreover, this restricts the Cr^{3+}ion electro reduction to metal Cr and in turn, decreases the deposition rate (6). Also, the increased time that hydrogen evolution is occurring will shift in acid-base equilibrium may cause an increase in reaction 6, thus leading to a decrease in deposition.

$$Cr(HCOO)(OH)_2(H_2O)_3 + OH^- \rightarrow [Cr(HCOO)(OH)_3(H_2O)_2]^- + H_2O \qquad (7)$$

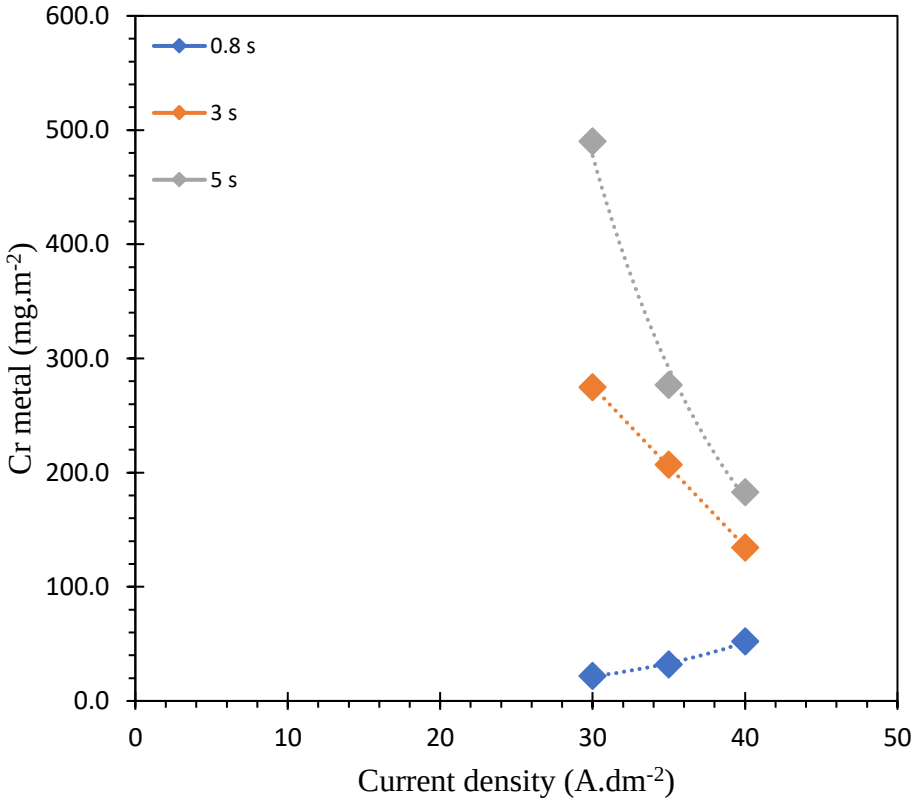

Figure 5.9. The effect of electrolysis time on the coating weight for Cr deposited onto blackplate at varying current densities.

The same study was then conducted on the second electrolyte which deposits Cr (III) oxide. Figure 5.10 shows Cr (III) oxide coating weight as measured with XRF as a function of current density for varying electrolysis times of 0.8, 3 and 5 s, respectively.

An increase in applied current density caused a decrease in Cr (III) oxide deposition, irrespective of electrolysis time. However, a longer electrolysis time caused this rate of decrease in Cr (III) oxide deposition to be greater, as the current density was increased. Moreover, at an electrolysis time of 0.8 s and an applied current density of 10 $A.dm^{-2}$, approximately 90 $mg.m^{-2}$ was deposited. This decreased to approximately 40 $mg.m^{-2}$ at 40 $A.dm^{-2}$. In contrast, at an electrolysis time of 5 s and a current density of 10 $A.dm^{-2}$ approximately 120 $mg.m^{-2}$ was deposited. At 40 $A.dm^{-2}$, however, Cr (III) oxide was not deposited in the case of the higher electrolysis times (3 and 5 s).

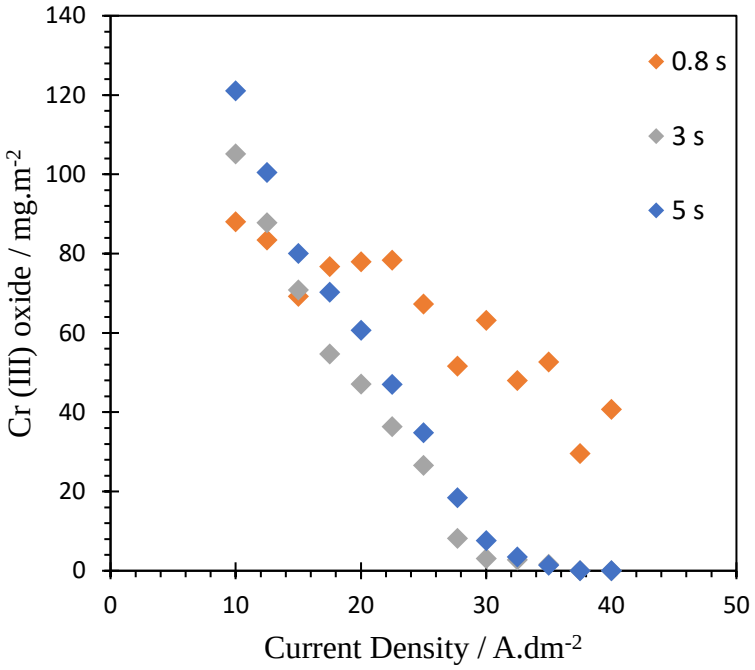

Figure 5.10. The effect of electrolysis time on the coating weight for Cr (III) oxide deposited onto blackplate at varying current densities.

Furthermore, at low current densities (10 – 15 $A.dm^{-2}$) a longer electroplating time increased the amount of Cr (III) oxide deposition. It was also proposed that as the reaction that drives hydrogen evolution is controlled by the applied current density, less hydrogen evolution was occurring at lower current densities. Hence, at these lower current densities, the increased time that the current was applied for, was not as greatly impacted by the hydroxide precipitates, such as $[Cr(OH)_3(H_2O)_3]$, that impede deposition.

When a current density of 30 A.dm^{-2} and above was applied a significant amount of Cr (III) oxide was only deposited when the electroplating time was 0.8 s. At 3 and 5 s little to no Cr (III) oxide was deposited at these higher current densities. It is thought at higher current densities the increased electroplating time was impacted by the hydroxide precipitates that impede deposition.

5.3.12. Effect of number of electroplating pulses on coating weight

Steel substrates such as ECCS are often subjected to 'pulsing' when manufactured industrially as they pass through multiple sets of anodes. This is advantageous as the number of active anodes in which the steel strip passes through (at a fixed line speed and applied current density) enables the desired chromium coating thickness and composition to be achieved. The effect of pulsing on coating weight deposition was therefore investigated on samples produced using the Cr (III) electrolyte. Figure 5.11 and Figure 5.12 show the Cr and Cr (III) oxide coating weight as measured with XRF plotted as a function of electroplating pulses, respectively. Each pulse corresponds to a specific applied current density for a time of 0.8 s. To allow for replenishment of Cr ions near to the cathode, electroplating pulses were applied within 10 s of each other in the case where 2 or 3 pulses were applied. Unsurprisingly, there was a threshold applied current density of 30 and 10 A.dm^{-2} for deposition of Cr and Cr (III) oxide to occur, respectively. Irrespective of current density, increasing the number of electroplating pulses led to an increase in both Cr and Cr (III) oxide deposition.

For the deposition of Cr metal, the greatest increase in Cr deposition was seen when 2 pulses were applied. For example, at a current density of 30 A.dm^{-2} the application of one pulse led to a deposition of approximately 25 mg.m^{-2}, an increase of 25 mg.m^{-2}. After two pulses approximately 90 mg.m^{-2} was deposited, an increase of 65 mg.m^{-2} and after the application of 3 pulses 100 mg.m^{-2} was deposited, an increase of 10 mg.m^{-2}.

Hence, it appeared that the optimal number of pulses for electrolyte 1 was 2. Above this value (3 pulses), there was not a significant amount more of Cr metal deposited. It was proposed that the once the layer of Cr metal deposited onto blackplate became of a certain coating weight, further deposition of Cr metal onto the substrate became more difficult.

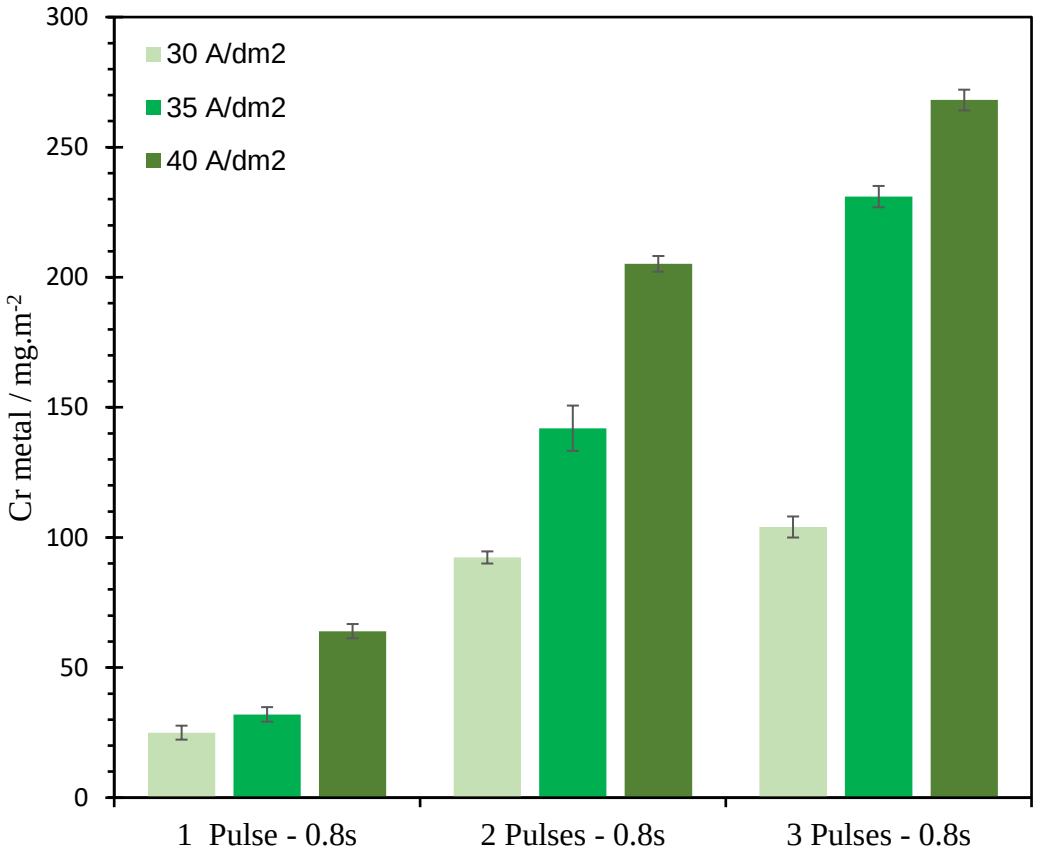

Figure 5.11. Coating weight as a function of electroplating pulses for Cr deposited onto blackplate for various current densities. The figure legend corresponds to the applied current density in A.dm^{-2}.

For electrolyte 2, the greatest increase in the deposition of Cr (III) oxide was seen when just 1 pulse was applied. For example, at a current density of 10 A.dm^{-2} the application of one pulse led to a deposition of approximately 95 mg.m^{-2}, an increase of 95 mg.m^{-2}. After two pulses approximately 115 mg.m^{-2} of Cr (III) oxide was deposited, an increase of 20 mg.m^{-2}. Finally, after the application of 3 pulses 130 mg.m^{-2} of Cr (III) oxide was deposited, an increase of 15 mg.m^{-2}.

The optimal number of pulses observed for the deposition of Cr (III) oxide was 1 (no additional pulses). Above this value there was little extra Cr (III) oxide deposited. It was proposed that Cr (III) oxide preferentially deposits onto blackplate. Thus, the increase in the amount of deposit decreases after 1 pulse. Furthermore, some time will

be needed to build up a concentration gradient to result in a surface pH increase, making it more difficult to deposit Cr (III) oxide during the next 'pulse' (4).

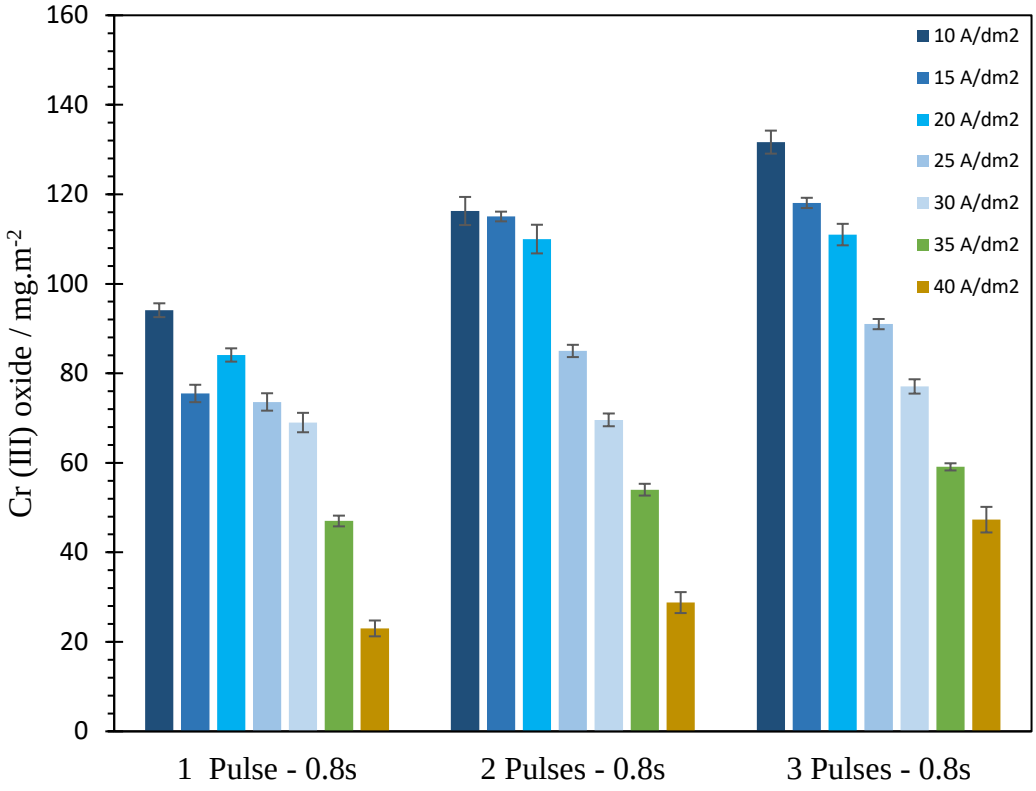

Figure 5.12. Coating weight as a function of electroplating pulses for Cr (III) oxide deposited onto blackplate for various current densities. The figure legend corresponds to the applied current density in A.dm^{-2}.

Introducing pulsing of the electrolyte also resulted in changes to the appearance of the sample, most notably at greater current densities. An example of these changes in appearance is shown in Figure 5.13, whereby the samples subjected to 2 or 3 pulses were considerably darker and more 'scarred' in appearance than the one subjected to just the one pulse. Due to the commercial use of these substrates, appearance is an important factor and must be considered when industrially manufacturing on a large scale.

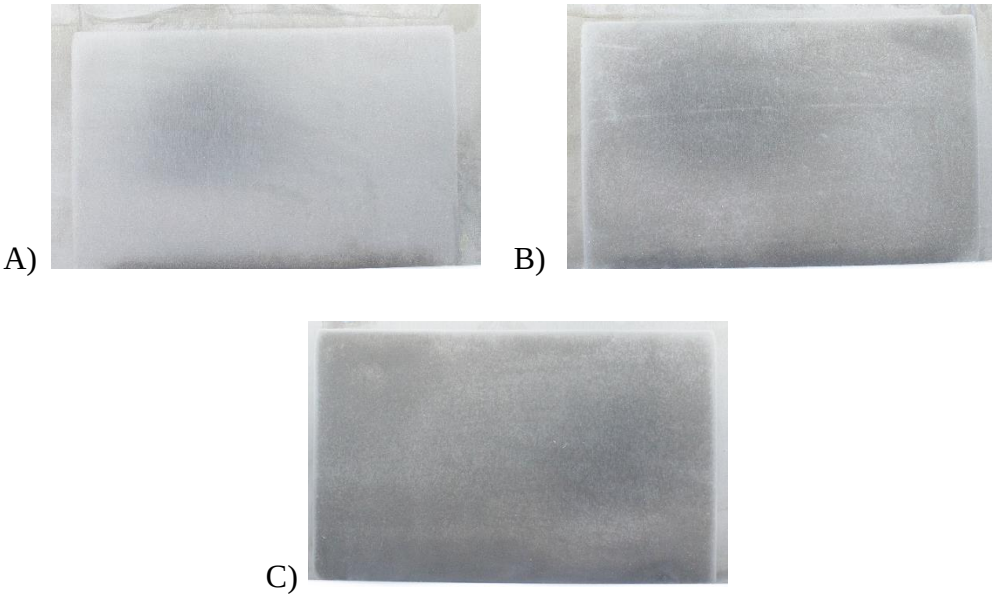

Figure 5.13. Appearance of a blackplate substrate electroplated with electrolyte one (to deposit Cr) at an applied current density of 40 A.dm^{-2}. A) shows the appearance of the substrate after one pulse, B) the appearance of the substrate after 2 pulses and C) the appearance of the substrate after 3 pulses.

The amount of deposit formed from the application of three pulses (combining to a total of 2.4 s) with the application of a continuous time of 3 s was compared. The results are shown in Figure 5.14 and Figure 5.15. It appeared that pulsing provided a greater deposit in comparison to the application of a continuous current for similar time durations. The impact of this was far more significant for the second electrolyte, and the deposition of Cr (III) oxide. The breaks in current, during pulsing of the electrolyte, may allow for replenishment of Cr complexes near to the cathode surface, thus enhancing deposition. Furthermore, the effects of hydrogen evolution and formation of hydroxide complexes may be less prominent during pulsing.

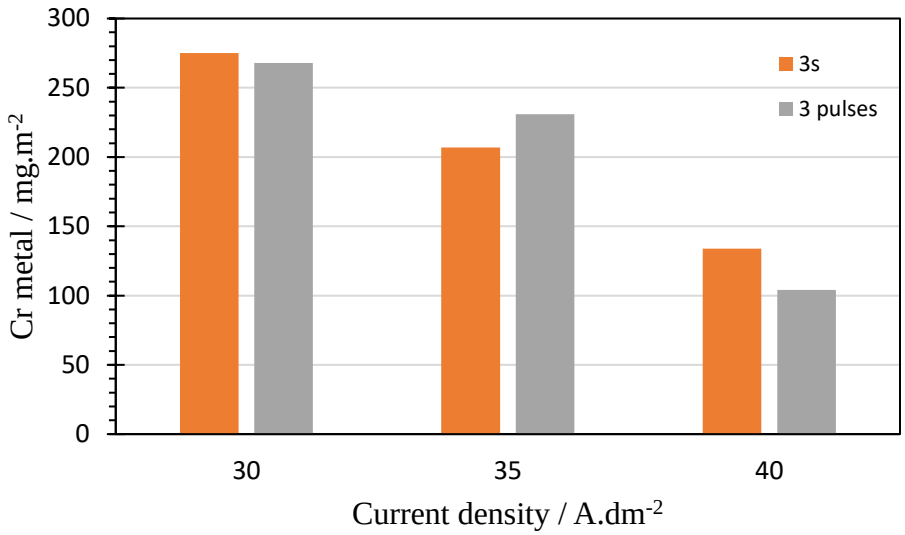

Figure 5.14. Comparison of the amount of Cr metal deposited via the application of a continuous current for 3 s and the application of 3 separate 0.8 s pulses totalling 2.4 s.

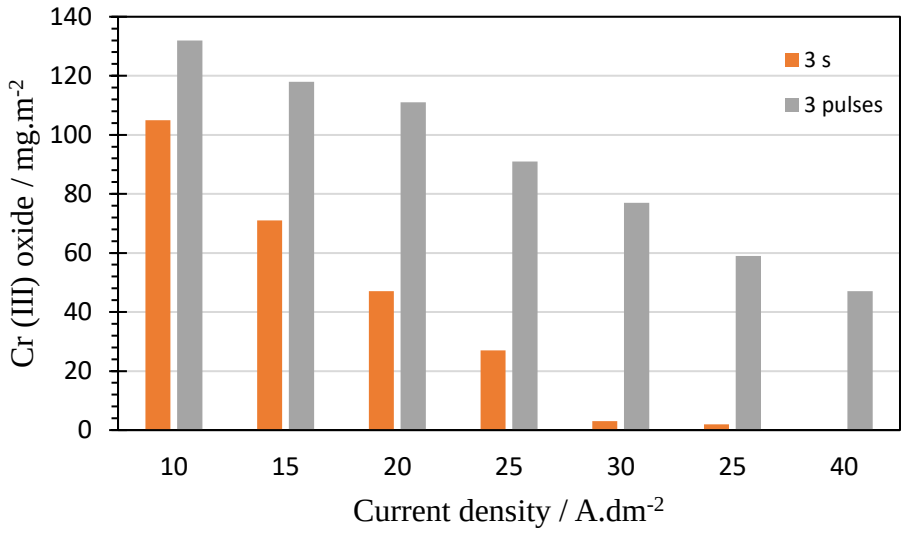

Figure 5.15. Comparison of the amount of Cr (III) oxide deposited via the application of a continuous current for 3 s and the application of 3 separate 0.8 s pulses totalling 2.4 s.

5.3.13. Effect of electrolyte temperature on coating weight

Up to now the temperature of the electrolytes were kept constant at 37 and 55 °C for electrolyte 1 and 2 respectively. The effect of altering electrolyte temperature on Cr deposition was then investigated. In Figure 5.16, Cr metal coating weight as measured with XRF is plotted as a function of electrolyte temperature. Cr metal was not

deposited until a current of 30 A.dm^{-2} was applied, irrespective of temperature. When a current of 30 A.dm^{-2} was applied, Cr metal was deposited at temperatures between 37 and 45 °C. At this current density, no Cr metal was deposited when the electrolyte bath was at a temperature of 50 °C. Moreover, at this current density the lower temperature of the electrolyte bath (down to a temperature of 37 °C) appeared to be preferential in terms of the amount of Cr metal deposited. It was proposed that when the temperature was decreased below 50 °C, the onset of regime II was shifted to a lower current density. This can be explained as, at a lower temperature there will be a higher kinematic viscosity of the electrolyte and a smaller diffusion coefficient of the hydrogen ion (8). This will cause the replenishment of H^+ ions to the electrode surface to slow down. For industry this is very beneficial, not only due to economic reasons, but this would allow the use of lower current densities and thus, also help reduce hydrogen evolution. Although the cost of heating the bath will also have to be taken into consideration. On applying a current density of 40 A.dm^{-2}, however, the optimal temperature for Cr metal deposition was 40 – 45 °C. At this applied current density, an electrolyte bath below or above this temperature window caused a decrease in the amount of Cr metal deposited.

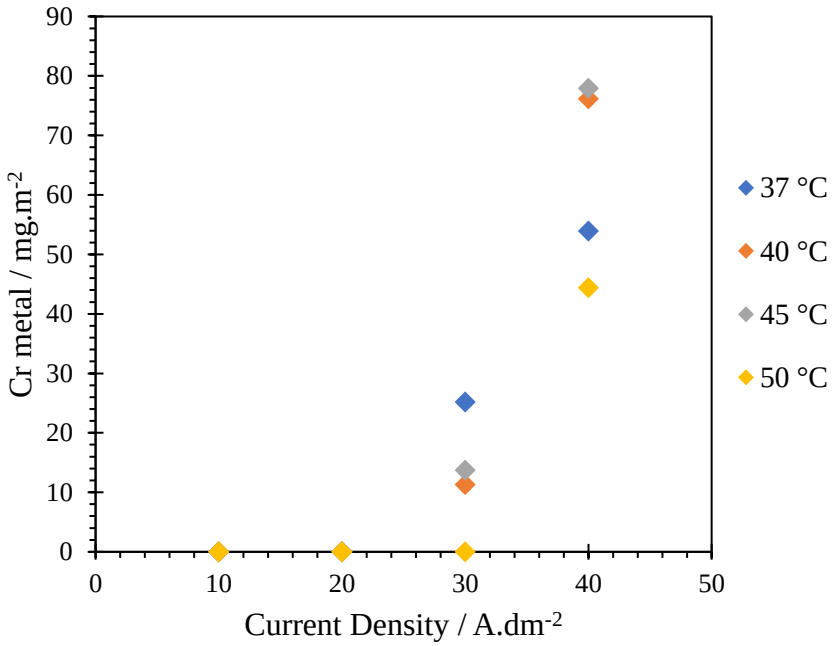

Figure 5.16. The effect of temperature for Cr metal deposited onto blackplate at various current densities. The figure legend corresponds to the temperature of the electrolyte bath.

In Figure 5.17 Cr (III) oxide coating weight as measured with XRF is plotted as a function of electrolyte temperature. Cr (III) oxide was successfully deposited at 10 A.dm^{-2} irrespective of temperature. Generally, the amount of Cr (III) oxide deposited increased with increasing temperature. A higher temperature widened the plating window, with Cr (III) oxide successfully being deposited at 40 A.dm^{-2} when the temperature of the electrolyte was kept at 55 and 60 °C. In comparison when the temperature of the bath was between 30 and 50 °C, there was no deposit at an applied current density of 40 A.dm^{-2}. A temperature of 55 °C seemed optimal with regards to the amount of Cr (III) oxide deposit, irrespective of current density. It was proposed that the conductivity of the electrolyte increased with increasing temperature, in turn improving ion mobility and the current efficiency, thus increasing the amount of deposit (9). Furthermore, it is not uncommon for there to be an optimum plating temperature as different metal complexes may arise at different temperatures (9).

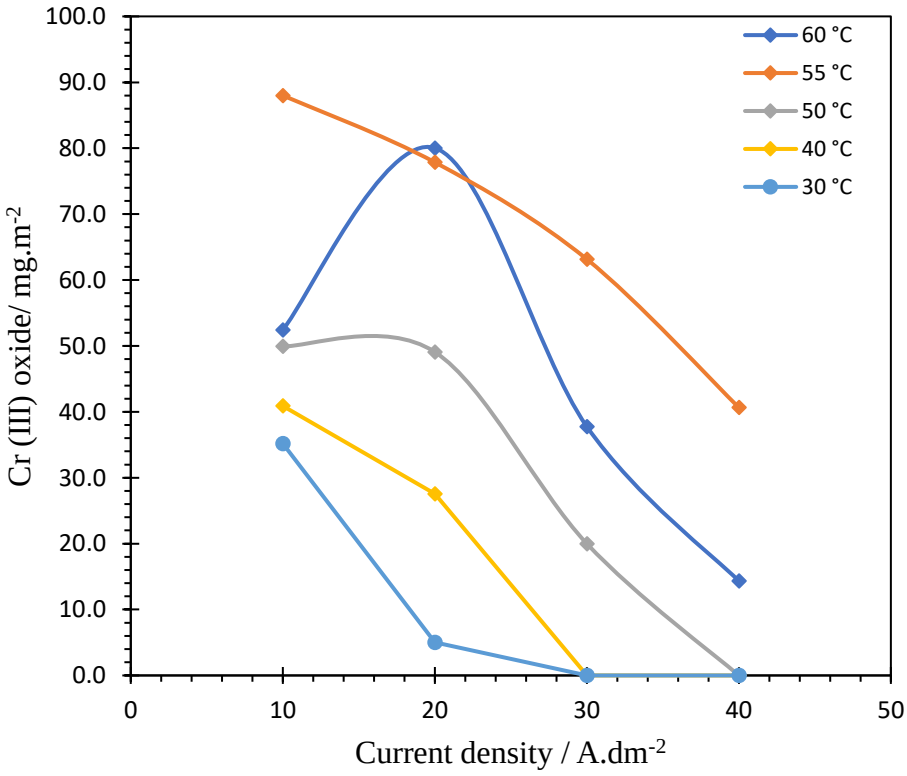

Figure 5.17. The effect of temperature for Cr (III) oxide deposited onto blackplate at various current densities. The figure legend corresponds to the temperature of the electrolyte bath.

5.3.14. Effect of electrolyte pH on coating weight

The pH of the electrolyte will alter the type and ratio of complexes that are present in the electrolyte and is another parameter that could easily be altered in an industrial setting. In Figure 5.18 Cr metal coating weight as measured with XRF is plotted as a function of pH. Irrespective of pH, no Cr metal was deposited until a current density of 20 $A.dm^{-2}$ was applied. At an applied current density of 20 $A.dm^{-2}$ Cr was only deposited when the electrolyte bath was at pH of 3.2. It was proposed that due to the greater pH of the electrolyte, less current was needed to obtain the same surface pH, thus regime II was shifted to lower current densities. Furthermore, at a lower pH, hydrogen evolution would dominate over the reduction of chromium ions which would also result in a decrease in plating efficiency. At an applied current density of 30 $A.dm^{-2}$, increasing the pH had a positive effect on the amount of Cr metal deposited. It was proposed that at lower pHs a greater proportion of complexes existed in the form of $[Cr(H_2O)_6]^{3+}$. Increasing the pH leads to a greater concentration of $[Cr(H_2O)_n(HCOO)_m]^{3-}$, thus making the deposition of Cr easier to occur. At an applied current density of 40 $A.dm^{-2}$, the greatest deposition of Cr metal was seen when the electrolyte bath was at a pH of 2.8.

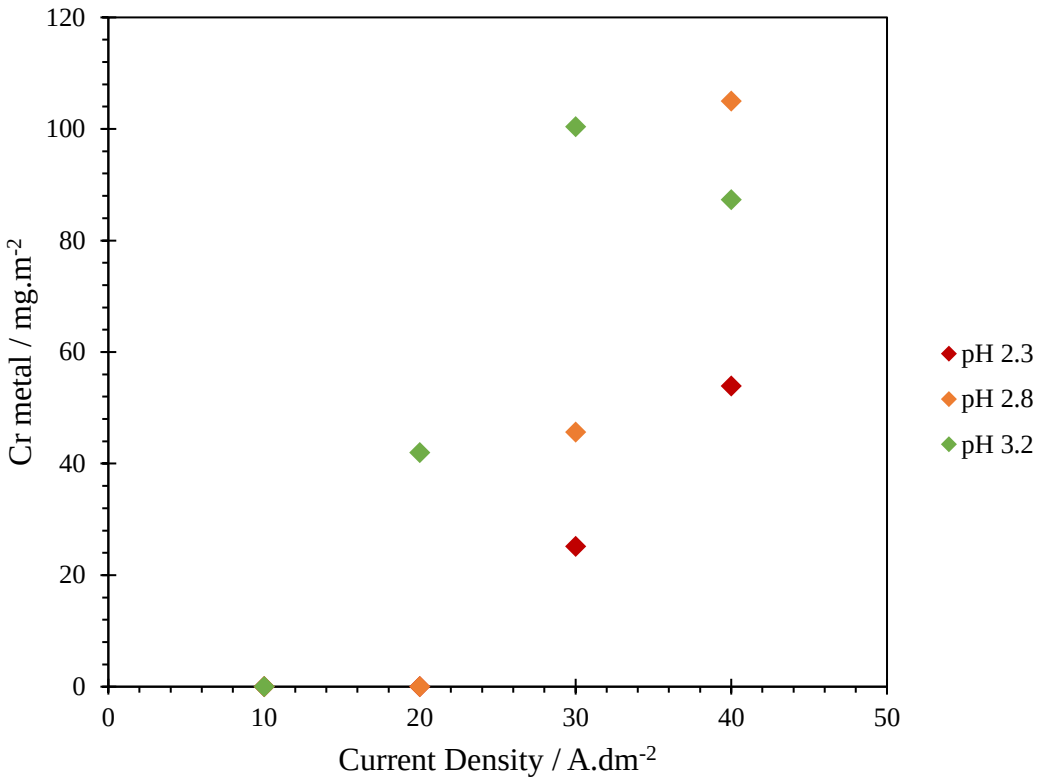

Figure 5.18. Coating weight as a function of current density for Cr metal deposited onto blackplate at various pHs.

When a current density of 30 A.dm^{-2} or 40 A.dm^{-2} was applied, a higher pH of electrolyte caused a greater amount of Cr metal to be deposited. Again, it is thought that this was caused by the shift in regime II to lower current densities and thus, greater deposition.

In Figure 5.19 Cr (III) oxide coating weight as measured with XRF is plotted as a function of pH. Deposition of Cr (III) oxide started at an applied current density of 10 A.dm^{-2} providing that the pH of the electrolyte bath was greater than pH 2. When a current of 20 A.dm^{-2} was applied, increasing the pH led to an increase in Cr (III) oxide deposition, up to a pH of 2.8. Above this electrolyte pH, a decrease in Cr (III) oxide deposit was observed. At an applied current density of 30 and 40 A.dm^{-2}, the least amount of Cr (III) oxide deposit was seen when the electrolyte bath was at the highest pH (pH 3.6), whilst the greatest deposit was seen when the pH of the bath was at pH 2.4 and pH 2, respectively.

Increasing current density led to a decrease in Cr (III) oxide deposit at higher pHs (pH 3.2 and 3.6). A peak in deposition of Cr (III) oxide was seen at 20 A.dm^{-2} for the electrolytes at lower pHs.

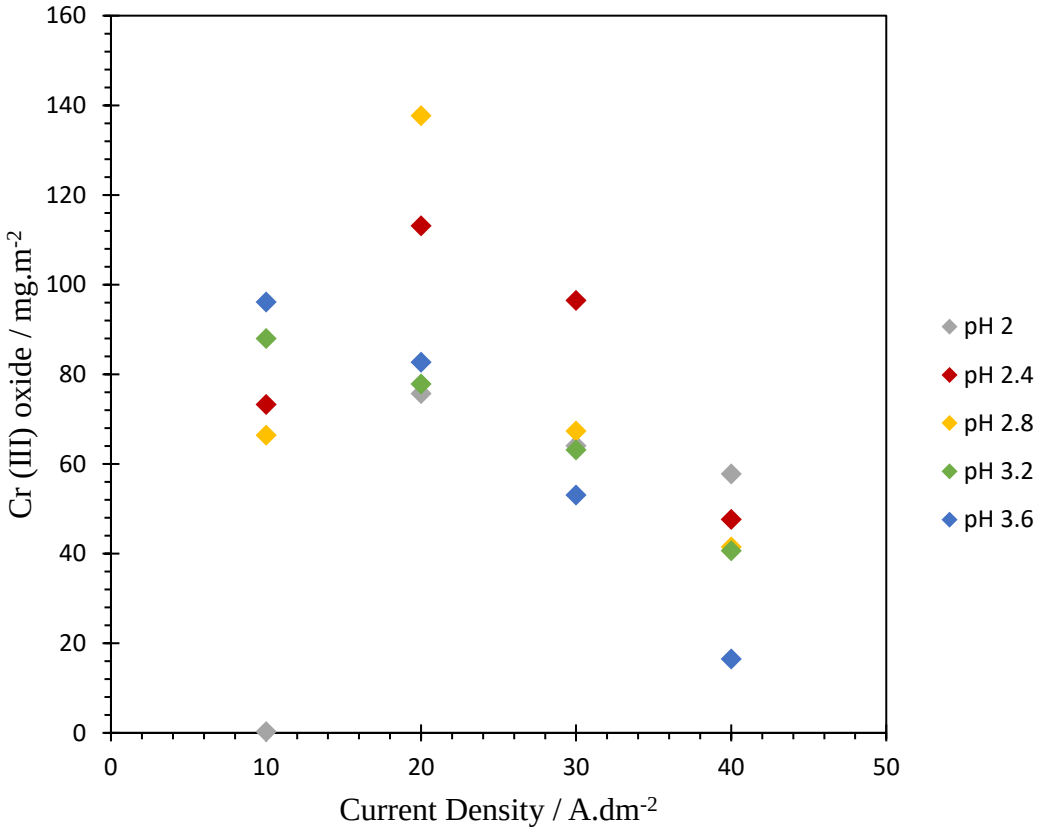

Figure 5.19. Coating weight as a function of current density for Cr (III) oxide deposited onto blackplate at various pHs.

At a current density of 10 A.dm^{-2} a higher pH caused more Cr (III) oxide to be deposited. This can be explained as a smaller pH increase would be needed to arrive at the same final pH. Moreover, less current is needed to obtain the same surface pH, thus regimes II and III are shifted to lower current densities. It is proposed that no Cr (III) oxide was deposited at a pH of 2 and a current density of 10 A.dm^{-2} as not enough H^+ had been reduced to H_2 in order to increase the surface pH at the cathode such that Cr (III) oxide will be deposited. When the pH of the electrolyte is increased it allows deposition of Cr (III) oxide at lower applied current densities which is beneficial industrially as this will result in less hydrogen evolution.

The decrease in deposition with increasing pH observed at a current density of 40 $A.dm^{-2}$ may be linked to the formation of hydroxide complexes which may block Cr (III) oxide deposition.

A clear peak in Cr (III) oxide deposition was observed at 20 $A.dm^{-2}$ at lower pHs (below pH 3.2). It is proposed that this current density is optimum in terms of hydrogen evolution. There is enough hydrogen evolution for a sufficient surface pH increase but not too great that the formation of hydroxide complexes may block Cr (III) oxide deposition.

5.3.15. Corrosion studies

In order to determine whether the samples made in lab scale conditions were comparable to those manufactured industrially, samples with the same coatings weights as those used earlier in this thesis were recreated. Lab made samples were created using blackplate electroplated with an initial layer of 100 $mg.m^{-2}$ of Cr metal followed by a layer of Cr (III) oxide with coating weights of 5, 10, 15, 20 and 25 $mg.m^{-2}$.

An example of the surface appearance is shown in Figure 5.20 below. The surface appears very similar to that of the line made samples.

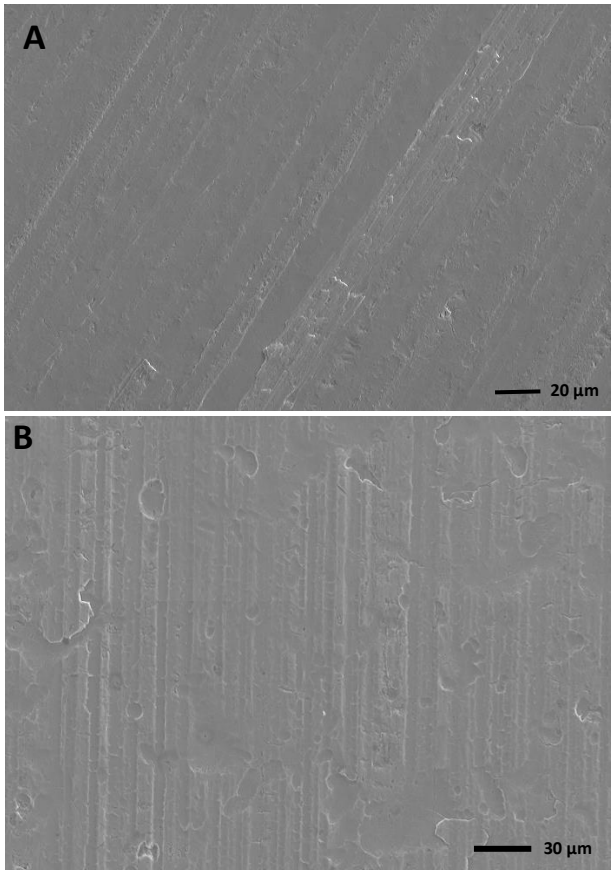

Figure 5.20. A shows an SEM image of the surface appearance of a lab made TCCT sample with a Cr (III) oxide coating weight of 15 mg.m^{-2}. For reference, B shows an SEM image of the surface of a line produced TCCT sample with a Cr (III) oxide coating weight of 21.5 mg.m^{-2}.

To compare the aqueous corrosion behaviour of the lab made samples to that of the line produced samples, SVET studies were performed. Samples were left to freely corrode in 1 wt. % NaCl for 24 hours and the SVET current density maps for the 5 different Cr (III) oxide coating weights (5, 10, 15, 20, and 25 mg.m^{-2}) can be seen below in Figure 5.21.

5 mg.m^{-2} Cr (III) oxide

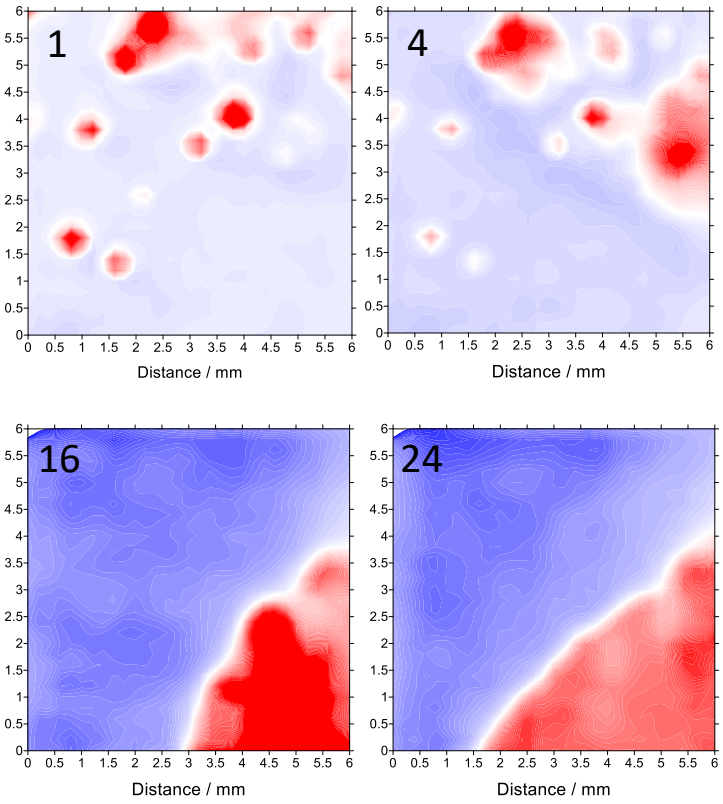

10 mg.m^{-2} Cr (III) oxide

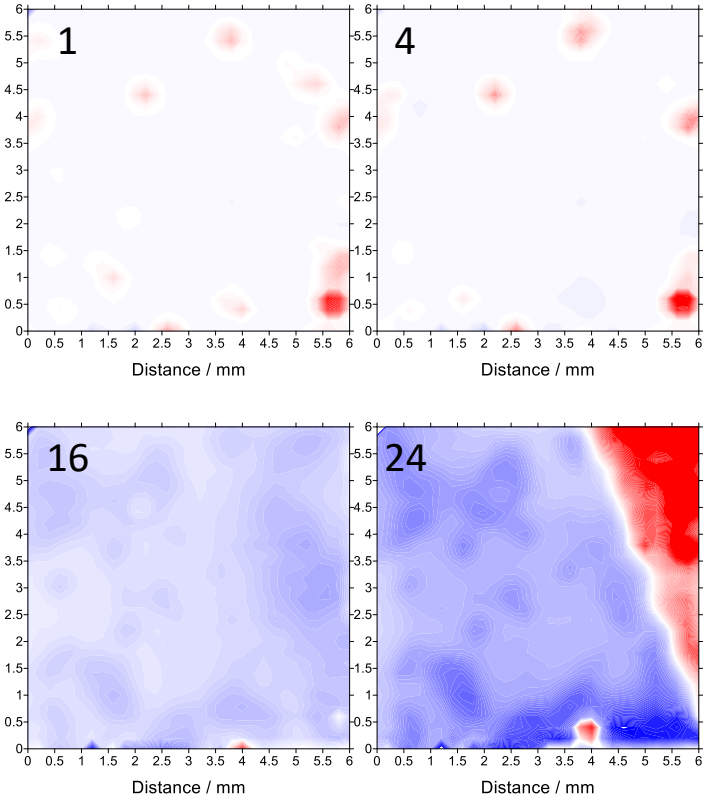

15 mg.m^{-2} Cr (III) oxide

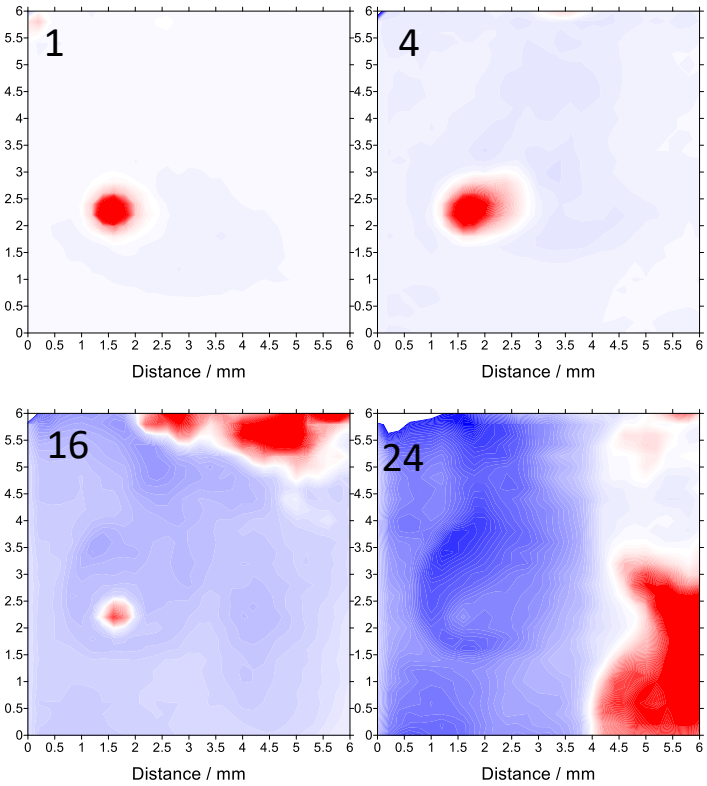

20 mg.m^{-2} Cr (III) oxide

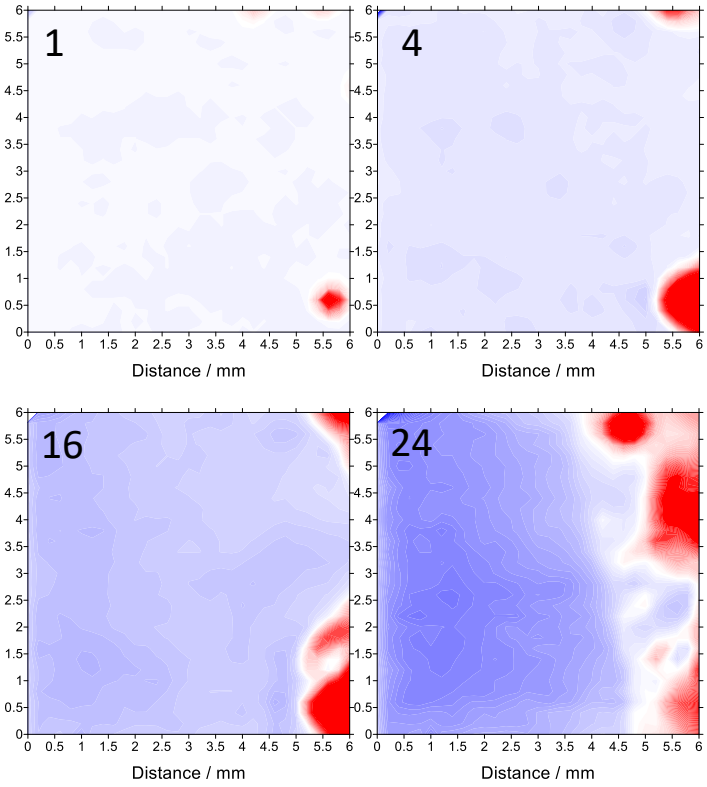

25 mg.m^{-2} Cr (III) oxide

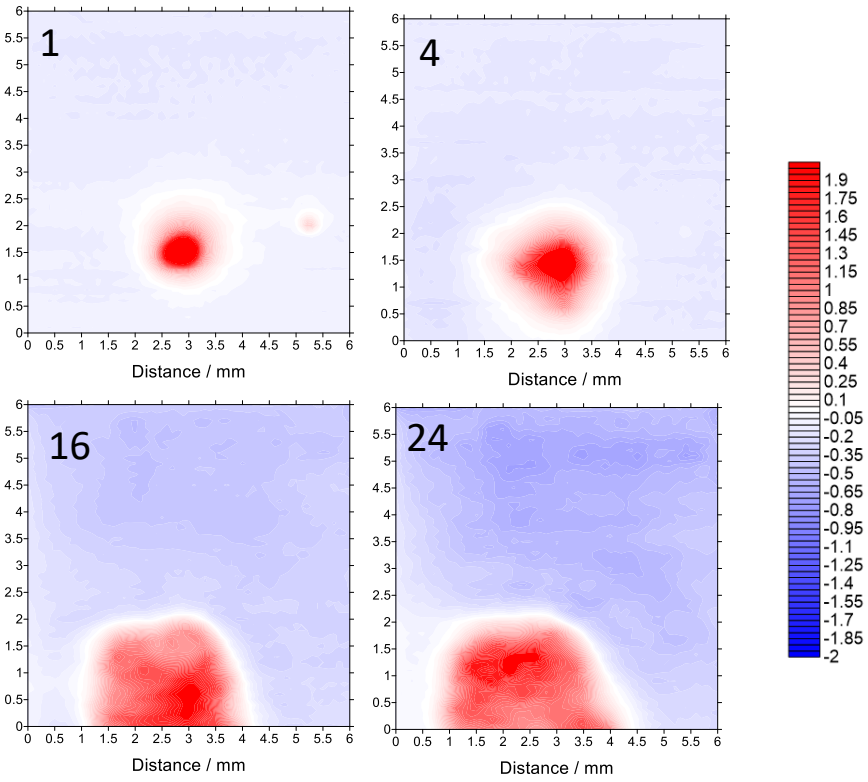

Figure 5.21. SVET current density maps for lab made samples with varying Cr (III) oxide coating weights (5, 10, 15, 20, and 25 mg.m^{-2}). Scans shown display hours 1, 4, 16 and 24.

There were clear differences in the corrosion behaviour of the samples with relative lower Cr (III) oxide coating weights compared with those with higher coating weights. Multiple anodes were formed within the first hour of the experiment for samples with lower Cr (III) oxide coating weights (5 and 10 mg.m^{-2}). Over time these individual anodes were no longer present and instead a large focal anode gradually swept its way across the surface. The samples with a Cr (III) oxide coating weight greater than 10 mg.m^{-2} showed slightly different behaviours. One or two anodes were present on the surface at start of the experiment, and these tended to grow with time. Overall, the samples with a greater Cr (III) oxide coating weight tended to have a decrease in anodic activity present on the surface. The anodic current density values recorded were greater on the lower Cr (III) oxide coating weights suggesting that corrosion activity on the surface was more prominent.

Similar observations were seen on line-produced samples as seen in Figure 5.22. Multiple anodes were seen on the samples with lower Cr (III) oxide coating weights within the first hour. Overtime, these decreased in number and a larger more focal anode seemed to sweep across the surface. Less anodic activity was observed on samples with greater coating weights and the sample with a Cr (III) oxide coating weight of 21.5 mg.m^{-2} displayed very little anodic activity indeed.

2.5 mg.m^{-2} Cr (III) oxide

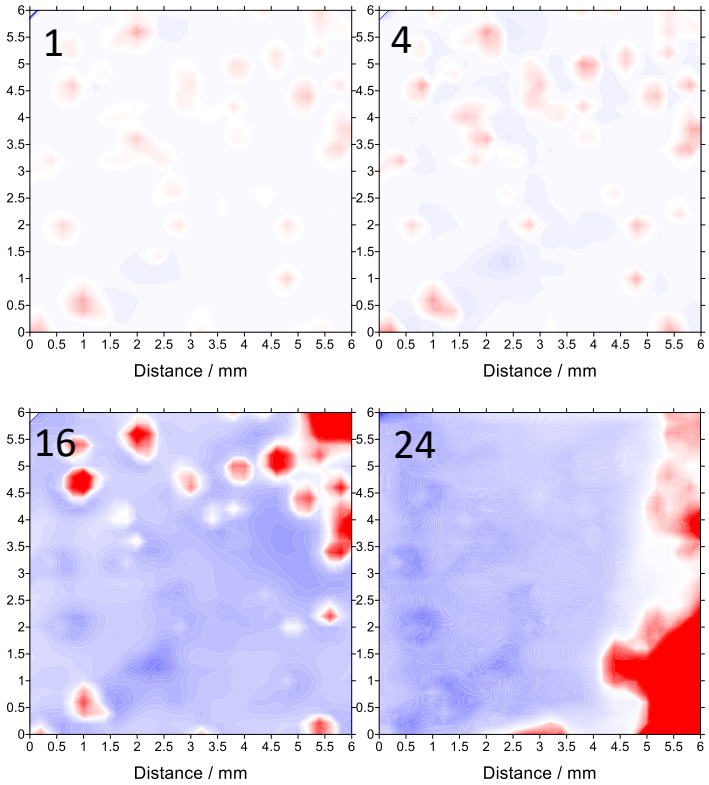

7.5 mg.m^{-2} Cr (III) oxide

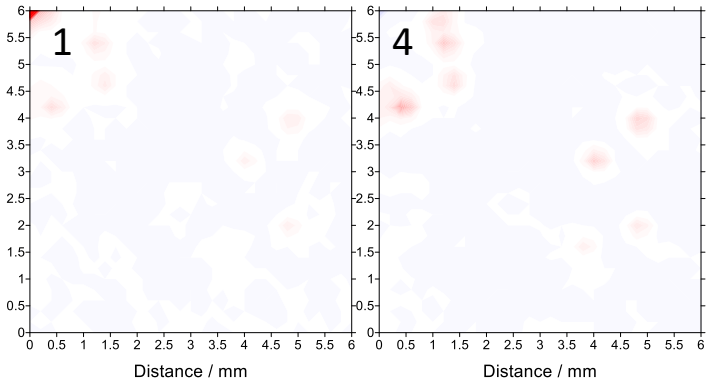

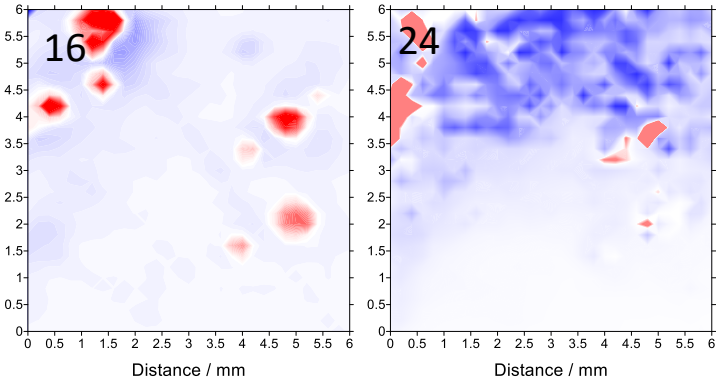

21.5 mg.m^{-2} Cr (III) oxide

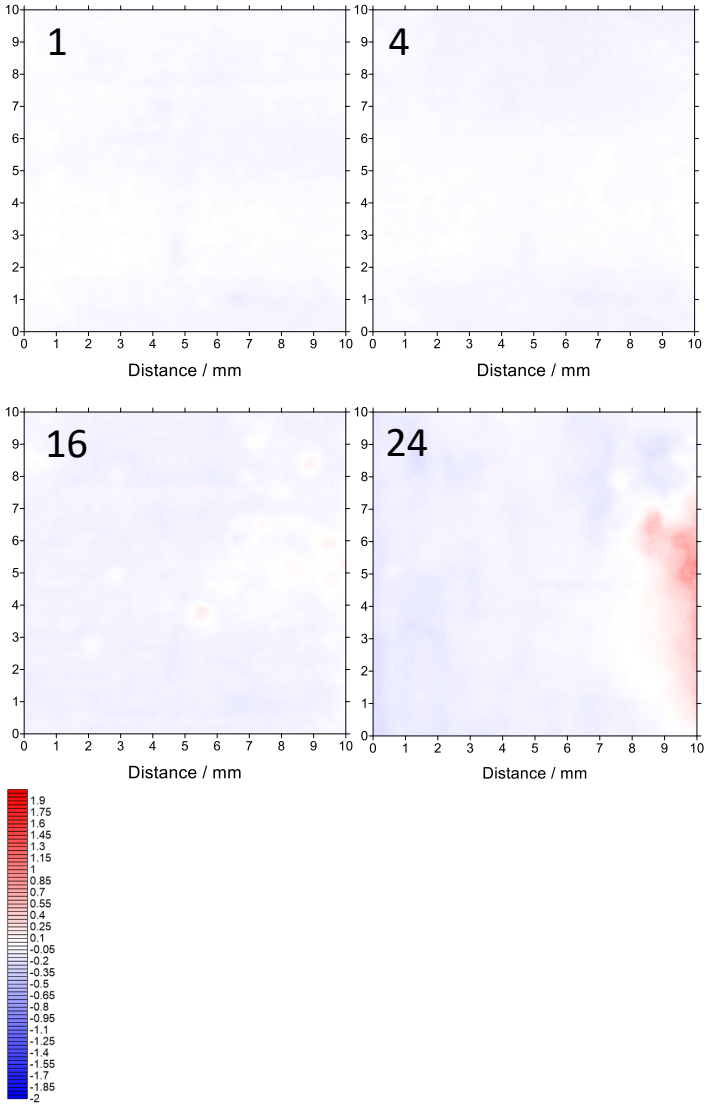

Figure 5.22. SVET current density maps for line-produced samples with varying Cr (III) oxide coating weights. Scans shown display hours 1, 4, 8, 16, 20 and 24.

The SVET derived mass loss measurements, as described in section 2.2.4, for both the lab made and line-produced samples can be seen in Figure 5.23 and Figure 5.24.

Generally, the trend for the lab based and line produced samples as individual sets showed that a greater Cr (III) oxide coating weight caused a decrease in SVET derived mass loss. The performance of the line-produced samples was significantly better with much lower values of mass loss in comparison to lab-made samples.

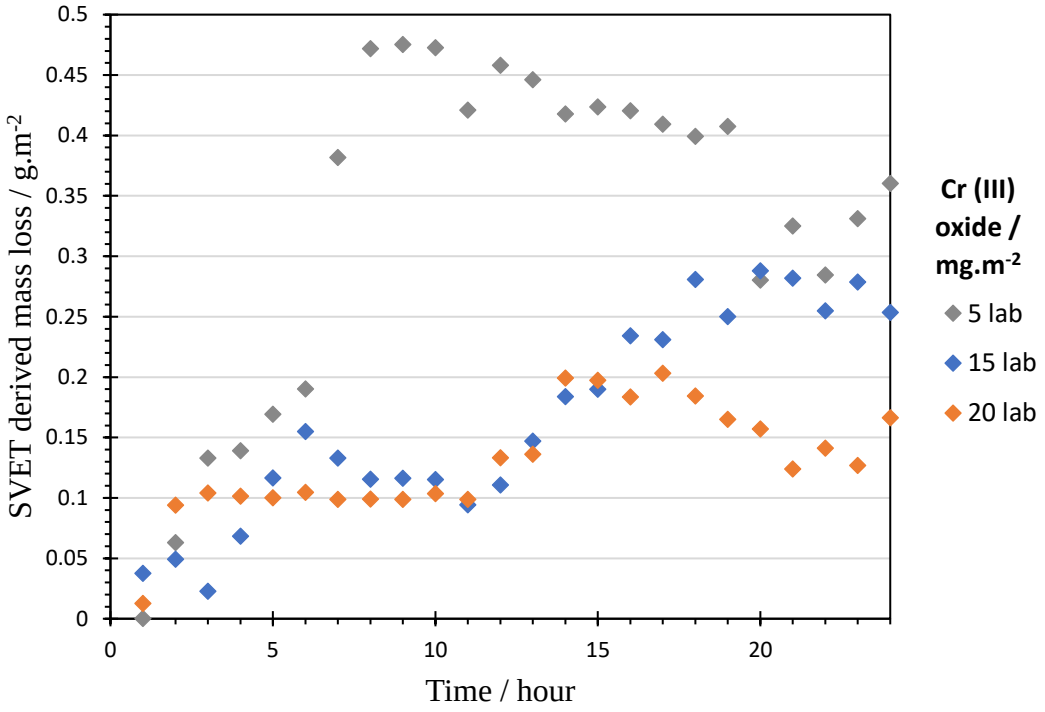

Figure 5.23. SVET derived mass loss as a function of time for a selection of lab-made samples.

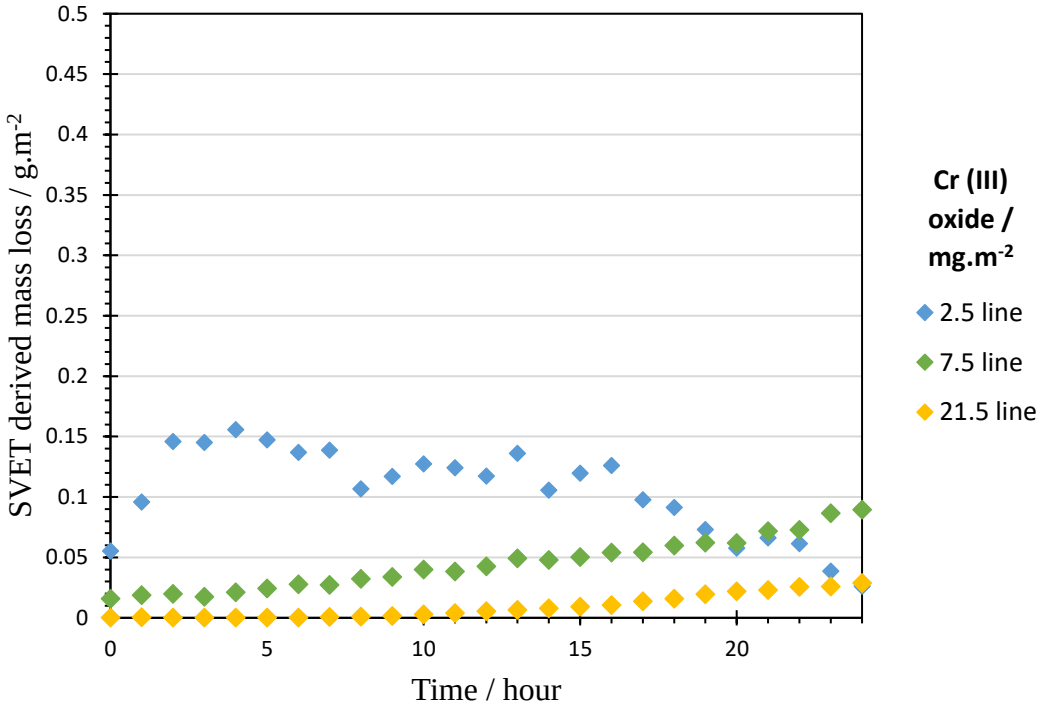

Figure 5.24. SVET derived mass loss as a function of time for a selection of line-produced samples.

Lab made TCCT with the same coating weights as line-produced samples were successfully produced. To compare the corrosion behaviour of line-produced and lab made samples, lab made samples with comparable Cr metal and Cr (III) oxide coating weights were produced. SVET studies showed how both sample types showed similar corrosion behaviour with numerous anodes being present on the lower coating weights and this changing to a decreased proportion of anodic sites on the higher coating weights. This result is very positive as it suggests that comparable observations can be made on lab produced samples to those of line-produced. This in turn, removes the requirement to be reliant on samples from industry and allows specific coating weights or parameters to be achieved quickly.

The reason for the greater number of anodes and increased anodic current density values on the lower Cr (III) oxide coating weights was proposed to be due to a greater number of defects and decreased coverage of the underlying steel. The presence of these defects would allow corrosion of the underlying steel at various points across the surface of the substrate, giving rise to numerous anodes. This in turn would also cause the increase in mass loss observed on the lower oxide samples.

Although it is of note that overall, the corrosion performance of the line-produced samples was better than that of the lab made samples. There were several potential reasons for this. Firstly, there are several variables involved in lab-based work and the samples may be less homogenous than that of the line-produced variants. Also due to the nature of the Cr complexes, the chemistry of the bath may vary to that of the line produced samples. Further work is required to determine how to resolve this issue.

5.4. Conclusion

The electrodeposition of Cr metal and Cr (III) oxide coatings on low carbon mild steel from a trivalent chromium electrolyte was investigated. The amount of the deposit strongly depended on the applied current density, electrolysis time, temperature and pH. At low current densities no deposit was formed on the electrode for both electrolytes. A lot of the results were explained in terms of the impact of hydrogen evolution and the presence of various Cr complexes. Further work is needed in order to determine the exact nature of the Cr species present and their impact with regards to deposition.

TCCT was successfully replicated using lab scale conditions. The corrosion behaviour of the lab made samples, observed using the SVET, were similar to that of line-produced samples. In spite of this, overall the line-produced samples were superior with regards to their corrosion performance.

5.5. References

1. Wijenberg JHOJ, de Vooys ACA, Kortlever R, Koper MTM. Oxidation reactions in chromium(III) formate electrolytes at platinum and at a catalytic mixed metal oxide coating of iridium oxide and tantalum oxide. Electrochim Acta. 2016;213:194–200.
2. Wijenberg J. Method for manufacturing chromium oxide coated tinplate. WO 2020/173953 A1, 2020.
3. Giovanardi R, Orlando G. Chromium electrodeposition from Cr(III) aqueous solutions. Surf Coatings Technol. 2011;205(15):3947–55.
4. Wijenberg JHOJ, Steegh M, Aarnts MP, Lammers KR, Mol JMC. Electrodeposition of mixed chromium metal-carbide-oxide coatings from a trivalent chromium-formate electrolyte without a buffering agent. Electrochim Acta. 2015;173:819–26.

5. de Vooys ACA, Wijenberg JHOJ, Koper MTM. Cyclic voltammetry study of trivalent basic chromium sulphate electrolytes contaminated with sulphite. Electrochim Acta. 2018;269:700–5.

6. Bertero E, Manzano C V., Pellicer E, Sort J, Ulfig RM, Mischler S, et al. 'Green' Cr(iii)–glycine electrolyte for the production of FeCrNi coatings: electrodeposition mechanisms and role of by-products in terms of coating composition and microstructure. RSC Adv. 2019 Aug 8;9(44):25762.

7. Protsenko V, Danilov F. Kinetics and mechanism of chromium electrodeposition from formate and oxalate solutions of Cr(III) compounds. Electrochim Acta. 2009 Oct 1;54(24):5666–72.

8. Afzal M, Saleem M, Mahmood MT. Temperature and Concentration Dependence of Viscosity of Aqueous Electrolytes from 20 to 50 °C. Chlorides of Na+, K+, Mg2+, Ca2+, Ba2+, Sr2+, Co2+, Ni2+, Cu2+, and Cr3+. J Chem Eng Data. 1989;34(3):339–46.

9. Lambert S. The influence of temperature on the efficiency of electroplating from various ionic liquids. Circuit World. 2006;32(4):36–41.

6. The effect of thermal treatment on the composition and corrosion resistance (both atmospheric and aqueous) of Cr metal / Cr oxide coatings for steel used in packaging applications

6.1. Introduction

The results from earlier chapters in this thesis have led to the hypothesis that the Cr (III) oxide layer on the surface of TCCT plays a key role with regards to the material's corrosion performance. Determining whether the Cr (III) oxide coating weight and composition could be altered in other ways was hence investigated. It was proposed that thermal treatment may initiate chemical reactions and in turn provide a way of changing the chemical composition of the oxide layer. Subsequently, this may alter the corrosion performance of TCCT.

Furthermore, it has previously been suggested that thermal treatment of ECCS increases the adhesion of the lacquer on the surface (1). This in turn, may have a positive impact on improving corrosion that involves coating delamination such as FFC. Thus, in this chapter a systematic study into the effect of thermal treatment on the corrosion resistance properties of TCCT was conducted Initial experiments involved characterising the surface and chemical make-up of the thermally treated TCCT by means of SEM and XPS. The effect of this change in chemistry on both atmospheric and aqueous corrosion resistance, common within the packaging industry, was then investigated. This was achieved by means of FFC studies and use of the SVET.

Overall, the aims of this chapter were to investigate the effect of thermal treatment on the corrosion performance of TCCT.

6.2. Materials and methods

6.2.1. Materials

The samples used included those described in previous chapters; electroplated with a standard amount (100 $mg.m^{-2}$) of Cr metal but varying amounts of overlaying Cr (III) oxide. The sample used to investigate the effect of thermal treatment had an overlaying Cr (III) oxide coating weight of 7.5 $mg.m^{-2}$, as this was the threshold coating weight which lead to significantly improved corrosion resistance. In order to get a better understanding of the role of the oxide, as this is the layer that will be altered during thermal treatment, a sample consisting of blackplate electroplated with a single layer of Cr (III) oxide of 590 $mg.m^{-2}$ was also used.

These two samples were thermally treated at a range of temperatures(shown in Table 1) for a time of 15 minutes in an oven (1).

Table 6.1.Temperatures that the samples were heated at for 15 minutes.

Heat treatment / 15 mins
150˚c
200˚c
250˚c
300˚c
350˚c
400˚c

6.2.2. Methods

Samples were cut from a larger sheet and cleaned using IPA prior to thermal treatment. They were then characterised using XPS, SEM and to understand how the surface appearance and composition if affected by thermal treatment. The methods for conducting XPS and SEM were consistent with those carried out earlier in this thesis. In brief XPS spectra were recorded on a Kratos Axis Ultra using monochromated Al Kα X-rays of 1486.8 eV. The measured spot size was 700 μm x 300 μm. The XPS spectra was subsequently analysed in CasaXPS software with Shirley backgrounds.

Binding energies were calibrated to the main hydrocarbon peak at 284.8 eV (1). A ZEISS SEM was used with a EHT of 20.0 kV, a probe current of 500 pA and a working distance of 11.5 mm.

Raman spectroscopy was introduced to gain a better understanding of the structure of the coatings, since it is a well-known method for the characterization of both amorphous and crystalline materials. For Raman spectroscopy, 1cm x 1 cm samples were cut from a larger sheet. Measurements were performed using a Renishaw inViva Raman system. A 532nm laser and 50x objective were used. To reduce the amount of noise in the scan, a laser power of 150 mW and acquisition time of 10 s were used to measure a map of 40 different points, across a 800 µm x 500 µm area, which were averaged in a single spectrum. The peak positions were determined using Wire.4.4 software. The experimental methods for investigating FFC and SVET were consistent with those described earlier in this thesis.

6.3. Results

6.3.1. Material characterisation

The effect of thermal treatment on the surface of the sample was characterised using the Zeiss SEM. The SEM images showed that the steel substrate was heterogenous with evidence of varying rolling roughness. It was also observed that the Cr coating follows the structure of the substrate. The surfaces of the samples that were thermally treated appeared to have defected areas where the coating had ‘cracked’ which may be of concern for its corrosion protection performance.

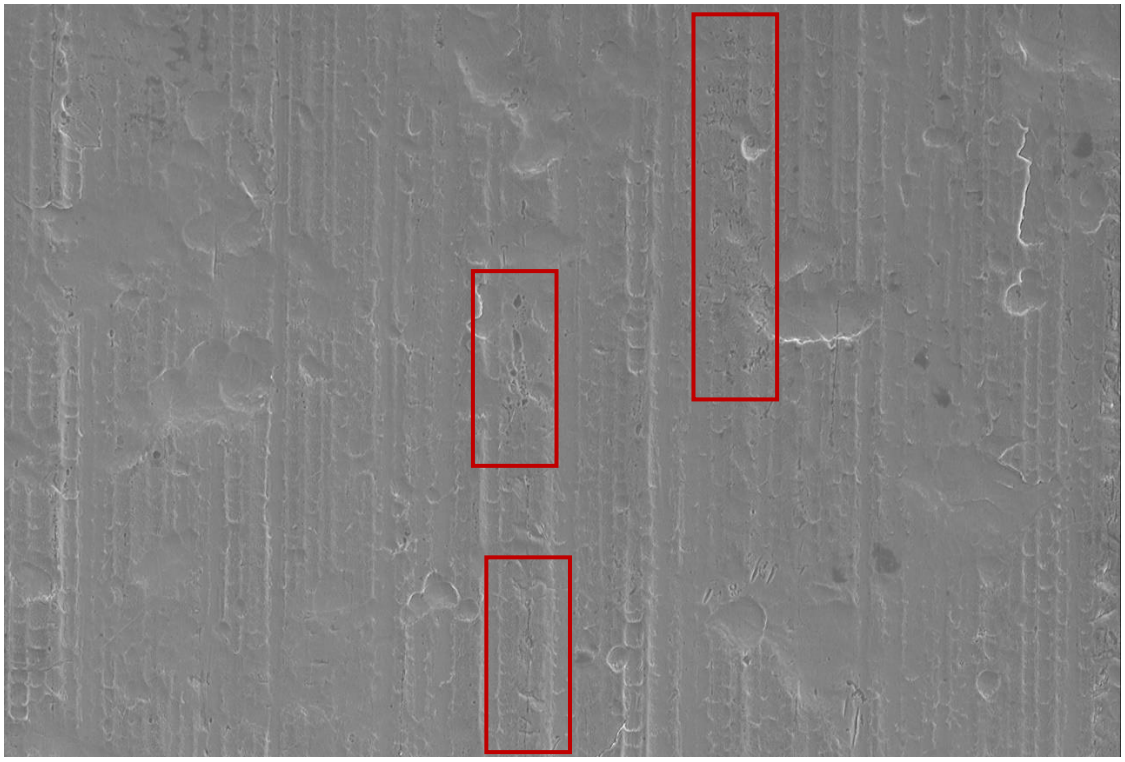

Figure 6.1. Example of defected areas in the thermally treated substrates.

XPS was used to compare differences in the surface chemistry of the outermost layer (define) of TCCT after it was subjected to various temperatures (Table 6.1) for 15 minutes. The changes to chemical composition as the temperature was increased (up to 400 °C) can be seen in the XPS surface scans shown in Figure 6.2. Figure 6.2 shows the fitted oxygen peaks for the thermally treated samples. The grey peak depicts the hydroxide peak, and orange the oxide. At room temperature the majority of the species present were in the form of Cr (III) hydroxide, as shown by the large orange peak. As the temperature was increased there was a reduction in the size of the orange, hydroxide peak and an increase in size of the grey, oxide peak, suggesting that the Cr (III) hydroxide was condensed (dehydrated) to Cr (III) oxide as the temperature was increased. On reaching 400 ˚C the size of the orange peak was considerably smaller than at room temperature and the presence of a single grey peak dominated, suggesting that almost all the hydroxide had been condensed and a restructuring into a stoichiometric oxide had occurred.

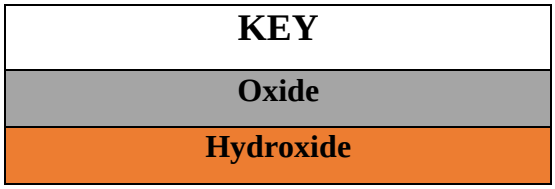

25 °C

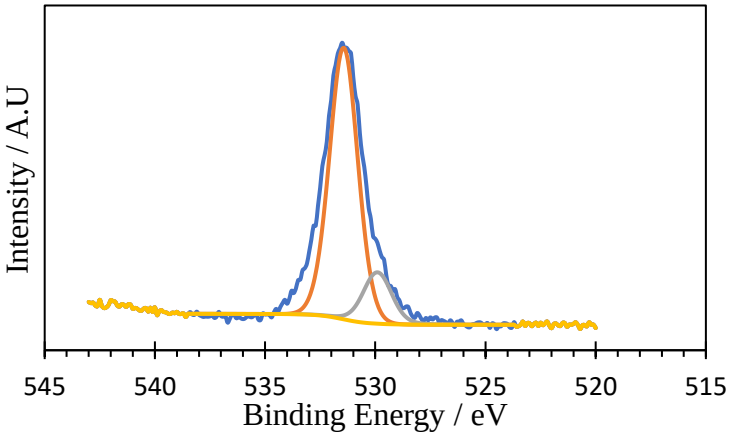

150 °C

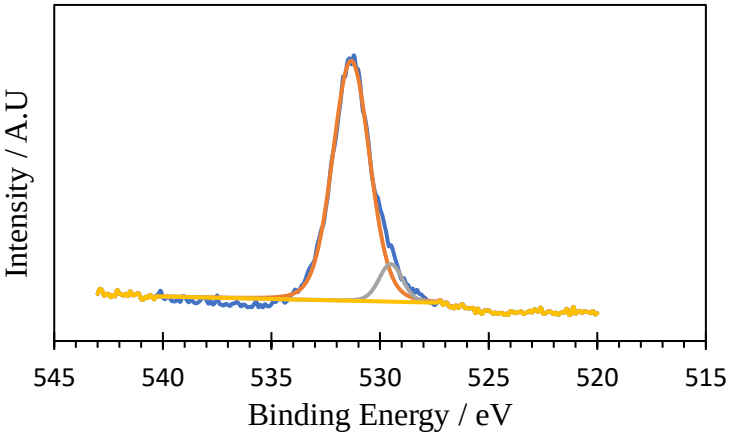

200 °C

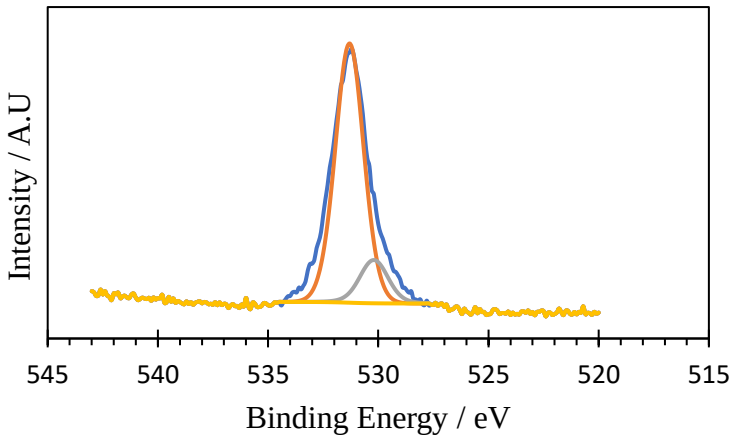

250 °C

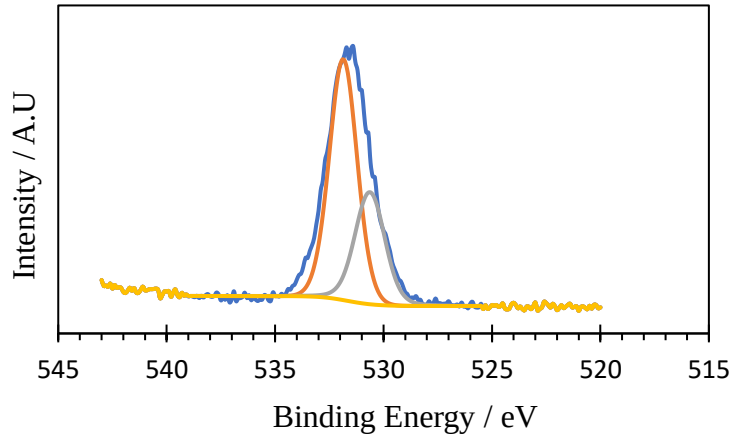

300 °C

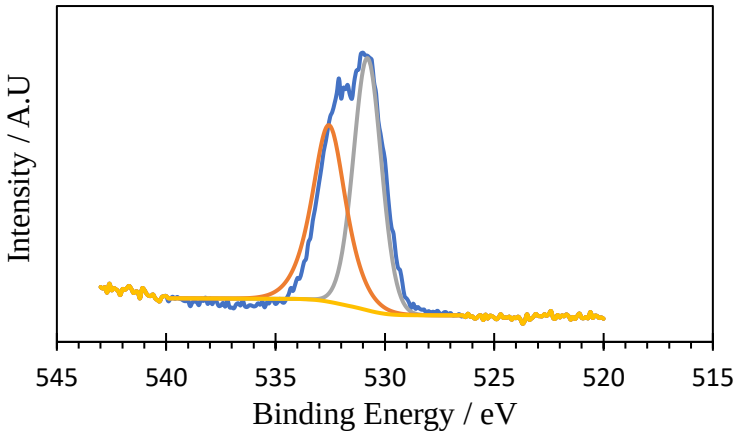

350 °C

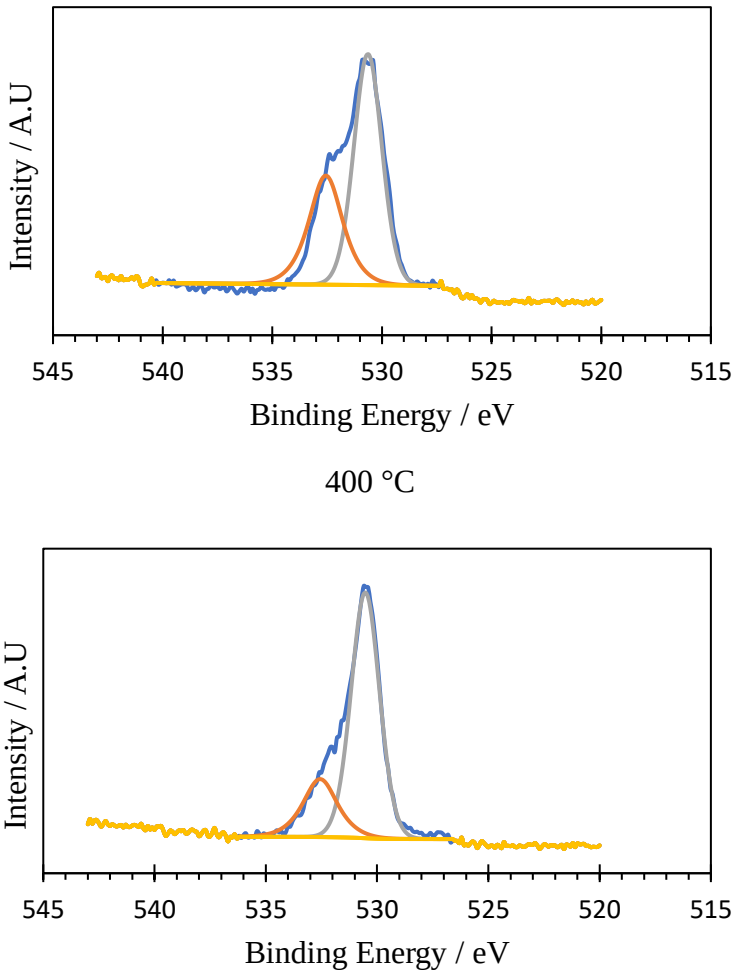

Figure 6.2. XPS curve fitting of the O1s peak from a surface scan of TCCT with a Cr (III) oxide coating weight of 7.5 mg.m^{-2} after heating to various temperatures.

Table 6.2 shows how the relative composition of oxide increased and hydroxide decreased as the temperature was increased from room temperature to 400 °C.

Table 6.2. The respective composition of oxide and hydroxide at increasing temperatures.

Temperature / °C	Oxide / %	Hydroxide / %
25	5	95
150	9	91
200	4	96
250	12	88
300	52	48
350	62	38
400	77	23

The percentage of Cr and Fe species present on the surface of the unheated sample and the sample heated at 400 °C can be seen in Figure 6.3. It was evident that the majority

of the Cr present in the unheated sample was in the form of $Cr(OH)_3$. Although at 400 ˚C there was still some $Cr(OH)_3$ present, the majority of it has been condensed to Cr_2O_3. The rate of hydroxide to oxide conversion is relatively low at temperatures below 200 °C but becomes rapid beyond 200 °C. With regards to iron, there was a fairly even mix of Fe and Fe oxide on the unheated sample. Heating the sample to 400 °C has caused iron to be oxidised meaning that Fe oxide is the predominant species present on the heated sample.

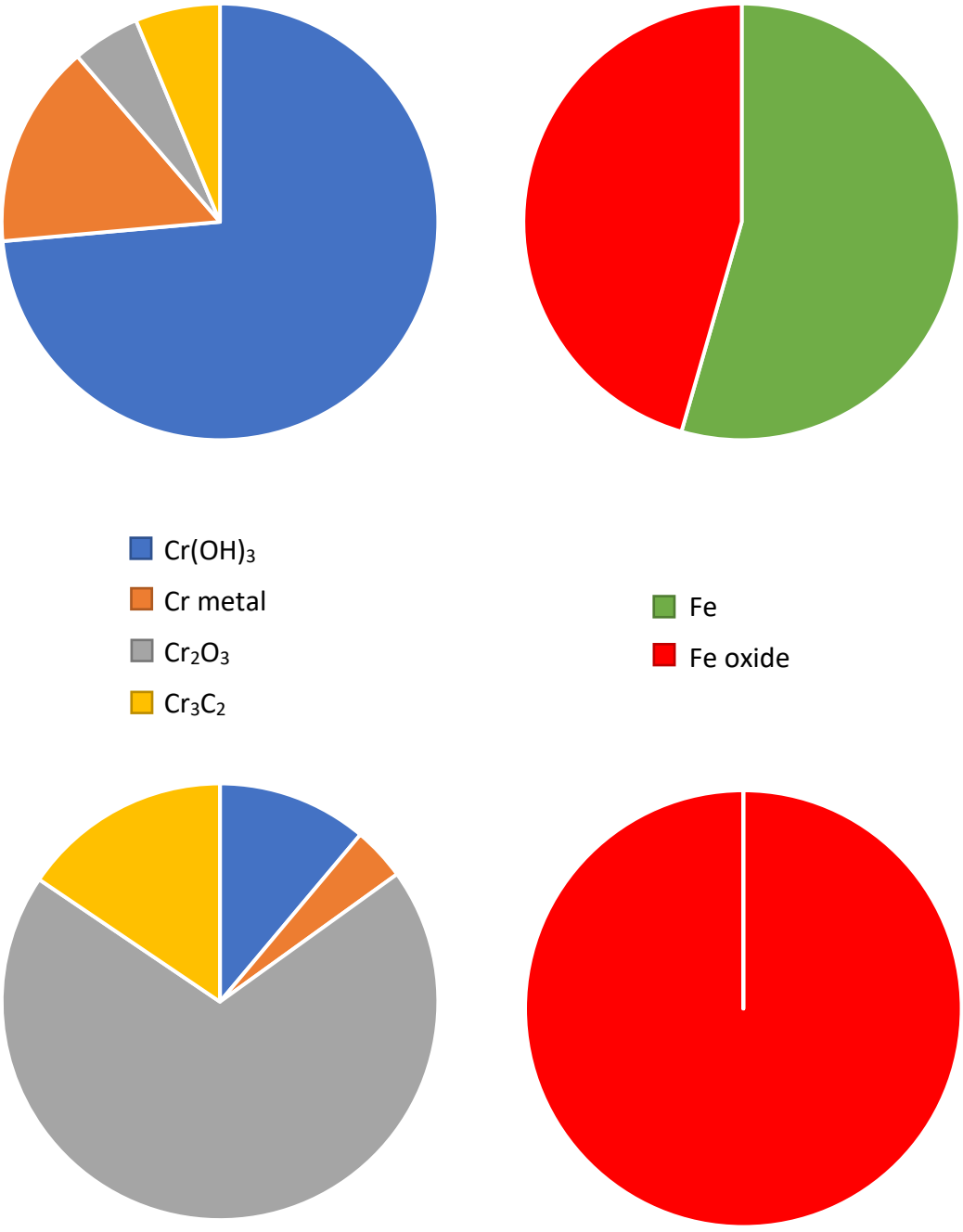

Figure 6.3. Percentage of Cr and Fe species present in the unheated (top) and 400 °C (bottom).

Table 6.3 shows how the Cr components changes as the temperature was increased from room temperature to 400 °C. Most notably heating caused the $Cr(OH)_3$ content to be significantly reduced and the Cr_2O_3 content to increase.

Table 6.3. Respective percentage of Cr components at room temperature and 400 °C.

Temperature / °C	$Cr(OH)_3$	Cr-metal	Cr_2O_3	Cr_3C_2
25	73	16	5	6
400	11	4	69	16

Since Raman spectroscopy is a well-known method for the characterization of both amorphous and crystalline materials it was employed gain a better understanding of the structure of the coatings.

Figure 6.4 shows the Raman spectra of the high (590 $mg.m^{-2}$) Cr (III) oxide sample unheated as well as following heat treatment at 400 ˚C. Raman shifts at 1315cm^{-1}, 658 cm^{-1}, 550 cm^{-1}, 348 cm^{-1}, and 303 cm^{-1} can be assigned to the Raman modes of Cr_2O_3 (2).

With an increase in temperature to 400 °C, the Raman peaks related to Cr_2O_3 Raman shifts increased significantly and the peaks became less broad indicating that the coatings transferred from an amorphous structure to a crystalline one (2).

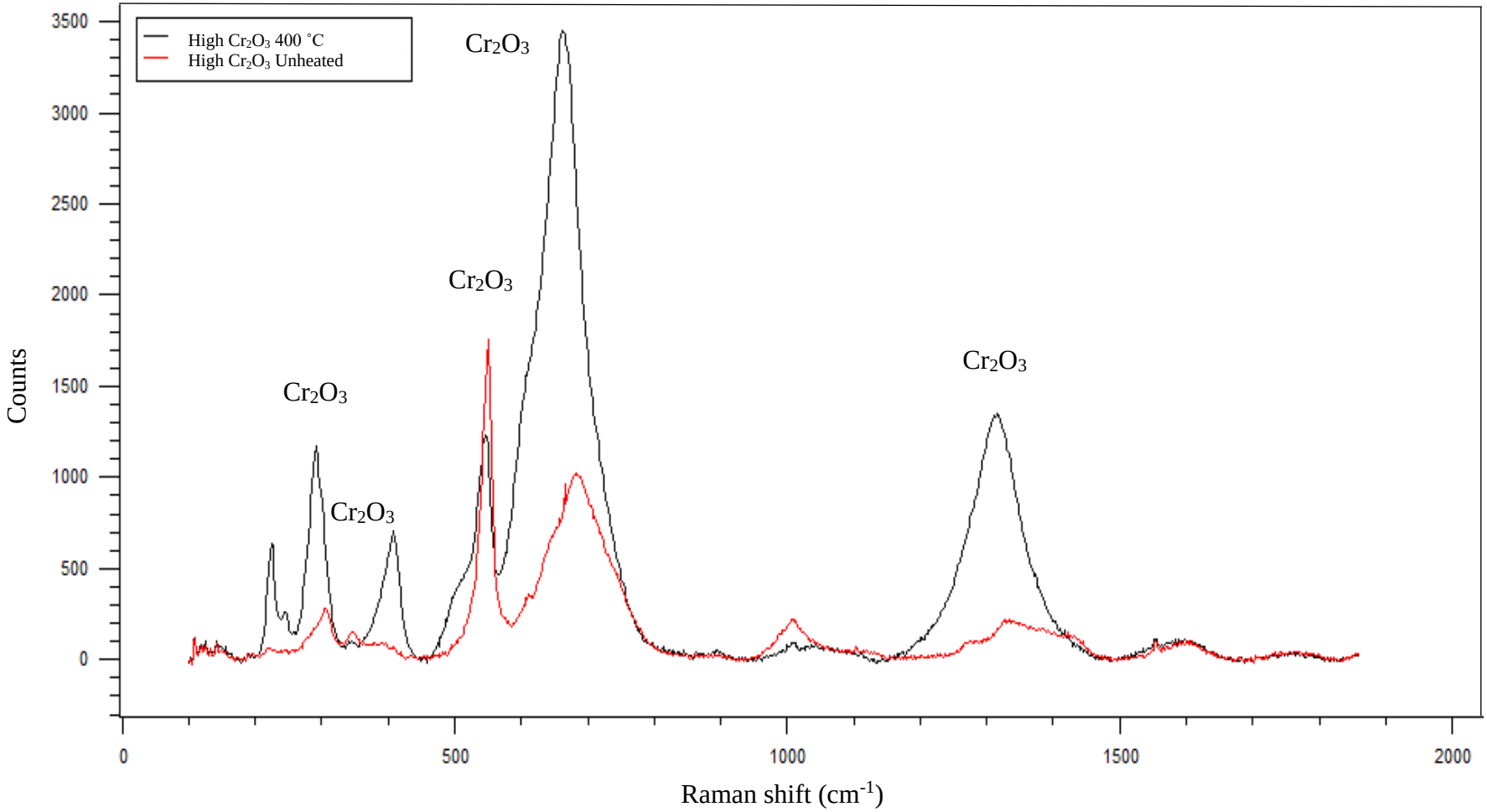

Figure 6.4. Raman spectra of a blackplate sample electroplated with 590 $mg.m^{-2}$ Cr_2O_3. The red line depicts the unheated sample and the black

line, the sample heated to 400 °C.

6.3.2. Effect of thermal treatment on corrosion resistance

Chemical characterisation of the surface of thermally treated samples concluded that increasing the temperature led to a change in the surface chemistry of the TCCT substrate. The composition of Cr_2O_3 increased with increasing temperature, from 25 °C to 400 °C, whilst the composition of $Cr(OH)_3$ decreased. The effect of this change in surface chemistry on corrosion performance was then investigated.

Potentiodynamic polarisation provided a measure of the expected corrosion performance of the thermally treated substrates. The potentiodynamic polarisation curves can be seen in Figure 6.5. Differences in both the cathodic and anodic branches of the polarization curves were observed on TCCT substrate heated to various temperatures. Most notably, the anodic currents were greater for the samples heated to higher temperatures. The cathodic currents were also slightly higher for the samples heated to greater temperatures. The OCP value was shifted slightly more negatively as the temperature that the substrate was heated to increased. Based on these observations, there is reason to suggest that increasing heating temperature leads to a decrease in corrosion performance, as observed by the increase in both anodic and cathodic currents at higher temperatures.

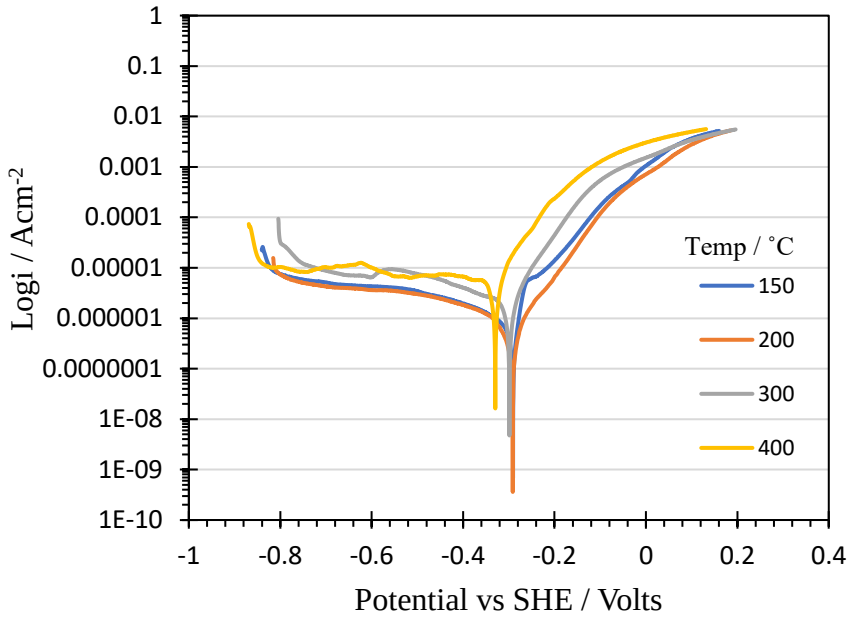

Figure 6.5. Current density as a function of potential for varying heating temperatures of a sample of TCCT with a Cr (III) oxide layer of 7.5 mg.m^{-2} measured in 1 wt. % NaCl with a potential sweep rate of 0.1667 mV.s^{-1}.

Icorr values were calculated. It can be seen in Figure 6.6 that the value of i_{corr} increased with increasing temperature implying a faster corrosion rate on the samples subjected to higher heating temperatures. At 400 °C i_{corr} was as high as 14 µA.cm^{-2}.

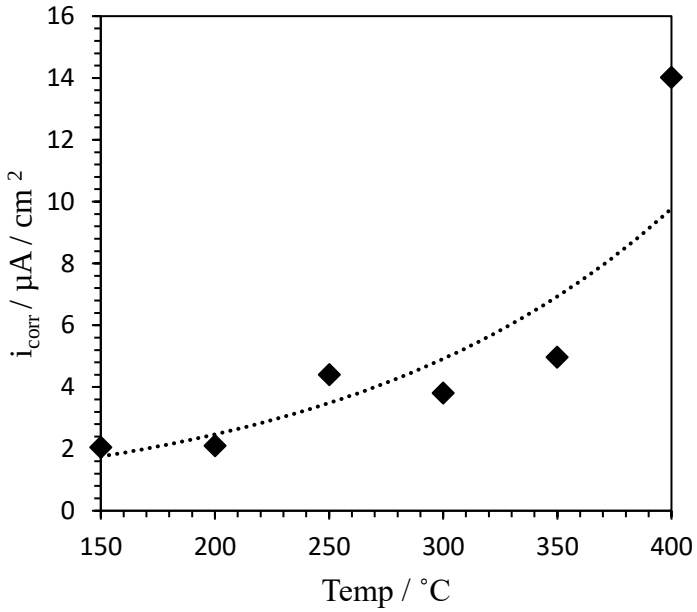

Figure 6.6. i_{corr} values as a function of heat treatment temperature.

Potentiodynamic polarisation measurements recorded greater anodic current values for higher heating temperature. As FFC is driven by the anodic reaction it was proposed that the samples heated to greater temperatures would be more susceptible to FFC than the lower heating temperatures. FFC experiments were conducted on the sample with a Cr (III) oxide coating weight of 7.5 $mg.m^{-2}$ that had been heated at various temperatures for 15 minutes. Figure 6.7 shows images taken 4 weeks after initiation with 0.005 M $FeCl_2$. A primary experiment and two repeats at each temperature were conducted. It appeared that the samples heated to a temperature of 250 °C and above, had an increase in the amount of FFC that occurred.

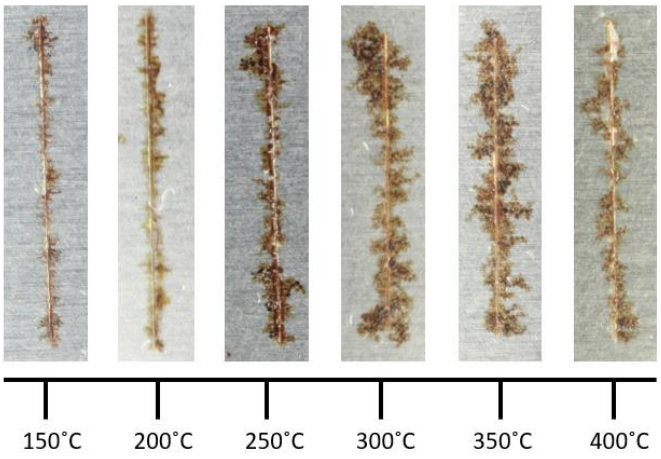

Figure 6.7. FFC on a sample with a Cr(III) oxide coating weight of 7.5mg.m^{-2}, 4 weeks after initiation with 0.005 M $FeCl_2$ for a range of heat treatments.

The composition of the Cr (III) oxide layer was shown to change with thermal treatment and, in turn, effect the corrosion resistance of the sample. To gain a better understanding of the role of the oxide, as well as the effect of the change in composition on aqueous corrosion, a blackplate sample consisting of just a layer of Cr (III) oxide with a coating weight of 590 $mg.m^{-2}$ was investigated further using the SVET.

The SVET can provide further data with regards to the electrochemical processes occurring on the surface of the substrate, by means of spatially resolving areas of dissimilar electrochemical activity and plotting this information into a current density map. This offers a visual representation of the location and intensity of anodic and

cathodic features, measured by the SVET tip. The colour change from red to blue is indicative of the shift from anodic to cathodic activity. Figure 6.8 shows the SVET measured current density maps of an unheated sample with just a single layer of Cr (III) oxide in 1 wt. % NaCl over a period of 24 hours.

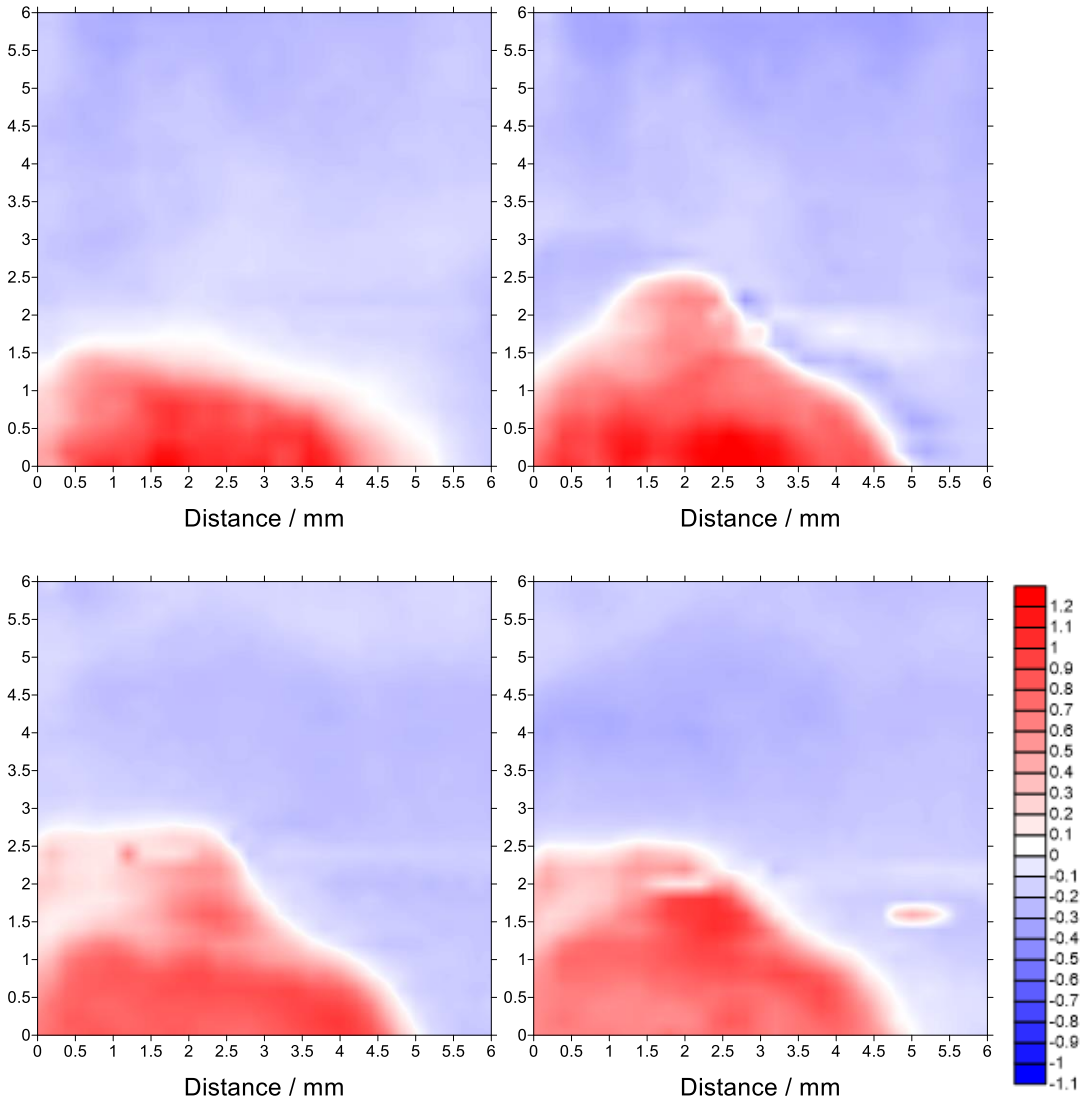

Figure 6.8. SVET-measured current density maps of blackplate with a layer of Cr (III) oxide (590 mg.m^{-2}) in 1 wt. % NaCl pH 7. Maps represented hours 1, 8, 16 and 24 respectively.

After one hour a single anode had formed in the bottom left corner. The anodic area increased in size until the end of the experiment, with the remainder of the surface was observed to be cathodic and relatively inert.

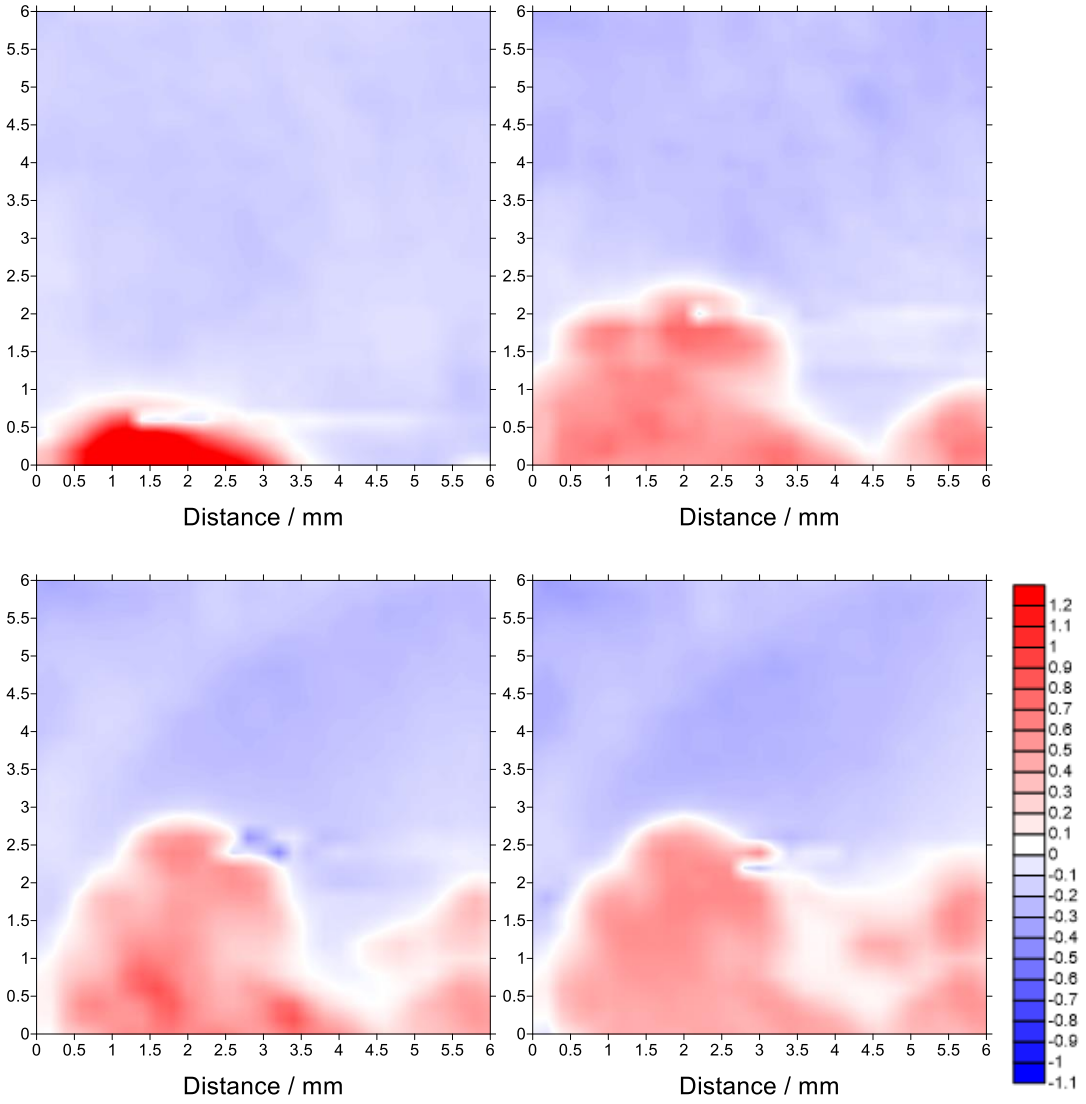

Figure 6.9. SVET-measured current density maps of blackplate with a layer of Cr (III) oxide (590 mg.m^{-2}) heated to 200 °C in 1 wt. % NaCl pH 7. Maps represented hours 1, 8, 16 and 24 respectively.

Figure 6.9 shows the SVET current density maps of a sample with a single layer of Cr (III) oxide heated to 200 °C. An anodic area which grew in size was again visible from the outset of the experiment. Current density values recorded were predominantly in the region of 0.5 A.dm^{-2}.

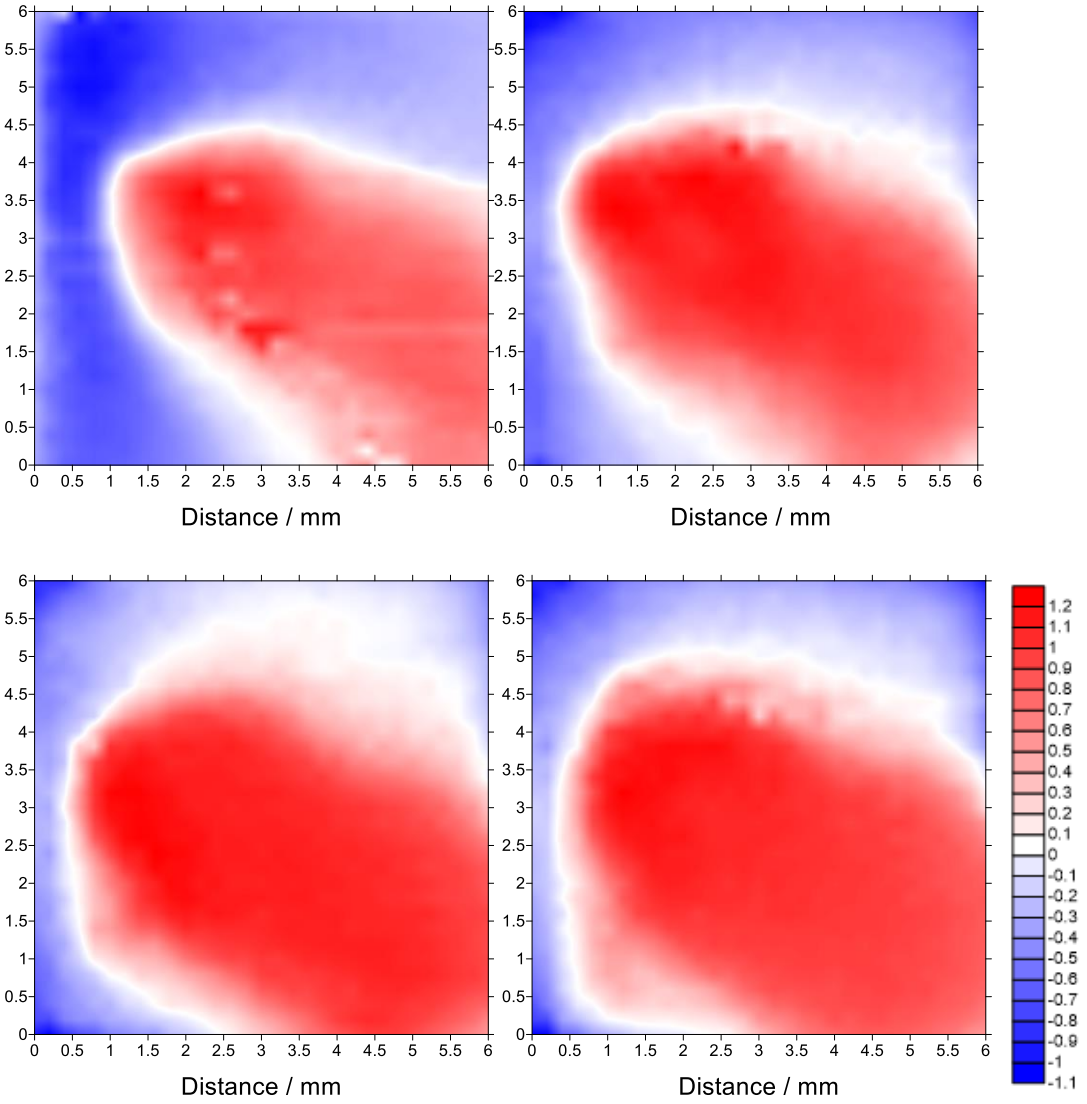

Figure 6.10. SVET-measured current density maps of blackplate with a layer of Cr (III) oxide (590 mg.m^{-2}) heated to 400 °C in 1 wt. % NaCl pH 7. Maps represented hours 1, 8, 16 and 24 respectively.

Figure 6.10 shows the SVET current density maps of a sample heated to 400 °C. In contrast to the previous samples, after one hour a large proportion of the surface acted as a net anode. The darker shade of red on the sample thermally heated to 400 °C is indicative of the enlarged anodic current density values (over 1 A.dm^{-2}) that were recorded on the surface of the substrate.

As iron is the less noble metal and thus, more likely to corrode, as well as the presence of red rust, this anodic activity was paired with Fe mass loss (equation 6.1).

$$Fe \rightarrow Fe^{2+} + 2e^{-} \qquad (6.1)$$

Figure 6.11 shows the difference in Fe mass loss between the unheated sample and the samples heated to 200 °C and 400 °C, respectively, over the course of 24 hours. The accumulated mass loss for the unheated sample and the sample heated to 200 °C were very similar at approximately 3.20 $g.m^{-2}$ and 3.4 $g.m^{-2}$ respectively, over the course of the experiment. Unsurprisingly, due to the increased anodic activity, a significant difference in mass loss was seen for the sample heated to 400 °C in comparison to the other two samples. An accumulated Fe mass loss of 8.3 $g.m^{-2}$ was recorded over the 24 hour period.

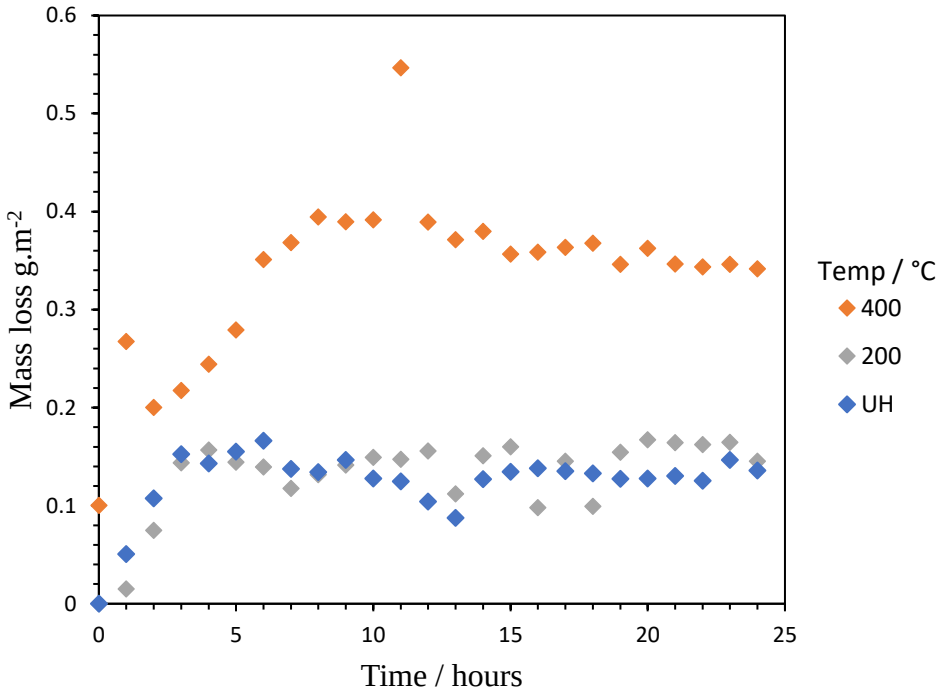

Figure 6.11. SVET derived mass loss data of blackplate with a Cr (III) oxide coating (590 $mg.m^{-2}$) immersed in 1 wt. % NaCl.

6.4. Discussion

The results showed that thermal treatment successfully worked as a way to alter the Cr (III) oxide layer without the use of wet chemistry. More specifically, it led to changes in the surface composition as demonstrated by XPS surface scans; a greater proportion of Cr was present on the samples subjected to lower temperatures. On exposure to the NaCl electrolyte some of the Cr may combine with oxygen to form chromium oxide. This passivation process will provide greater corrosion protection on these samples heated at lower temperatures and is proposed to be part of the reason

the lower temperature samples were less susceptible to aqueous corrosion. Increasing the temperature from room temperature to 400 °C caused Cr hydroxide to be condensed to Cr oxide and Fe to be oxidised to Fe oxide.

It has been reported that the structural hydroxide within the Cr hydroxide remains stable up to approximately 100 °C and then it decreases as the temperature is increased (1). In turn, the amount of surface oxide species increases. The water of hydration within the Cr structure is activated via thermal treatment. This allows for the creation of a coordinated –OH network on the surface of the material for subsequent bonding within a Cr network. This olation process at the surface is followed by an oxolation process, and leads to an increased formation of Cr_2O_3 species (1).

However, this change in surface composition was also shown to cause an overall decrease in the corrosion resistance of the sample. The corrosion performance, both aqueous and atmospheric, remained similar until the sample was heated over 250 °C, as demonstrated by potentiodynamic polarisation and FFC studies. The oxide content, as measured by XPS, was shown to be below 10 % for the unheated sample and the samples heated to 150 and 200 °C. Above these temperatures the oxide content rapidly increased, and hydroxide decreased, and the corrosion performance decreased. There was significantly more FFC on the samples subjected to temperatures of 250 °C and above. It was therefore proposed that $Cr(OH)_3$ provides more corrosion resistance in comparison to Cr_2O_3. Both $Cr(OH)_3$ and Cr_2O_3 offer impressive insulating characteristics due to their semiconductor properties. Cr_2O_3 has a wide band gap of around 3 eV indicating more energy is required to excite an electron compared with most transition metal-oxides (3). In comparison $Cr(OH)_3$ has a slightly lower band gap of 2.4 eV (4).

However, the decrease in coating thickness caused by heating, as the loss of water ligands due to the decomposition of $Cr(OH)_3$ means that the overall thickness of the layer is decreased. The density of chromium oxide is 5.22 $g.cm^{-3}$ whilst that of chromium hydroxide is 3.11 $g.cm^{-3}$. Thus, the decomposition of Cr hydroxide to Cr oxide will result in a denser and thinner coating (5). For example, a sample with a Cr (III) oxide coating weight of 7.5 $mg.m^{-2}$ will decrease in thickness from 2.4 nm to 1.4 nm if the layer is hypothetically made up of 100% $Cr(OH)_3$ and this is condensed to 100% Cr_2O_3. This thinner coating may provide less corrosion protection and thus, is

likely to be a reason for the increased corrosion on samples heated to a greater temperature. Furthermore, the amorphous nature of the coatings prior to heating may offer better insulating properties and thus block electron transfer to a greater degree compared to the crystalline nature of the thermally heated coatings. In turn, providing the unheated samples and samples heated to a lower temperature a greater degree of corrosion protection (6).

Electron transfer is associated with the cathodic oxygen reduction reaction towards the back of the FFC filament head. It is thus plausible the amorphous nature of the lower temperature coatings, act to block electron transfer during cathodic oxygen reduction, thus reducing the rate of the cathodic reaction. Hence, this explain the reduced amount of FFC on the samples subjected to lower temperatures.

There are some other proposed theories for the reduced amount of FFC observed on samples subjected to lower temperatures.

SEM analysis showed areas of the thermally treated coatings which appeared to have cracked leading to a greater number of defects present in the heated samples. Heating the sample may have caused oxide embrittlement creating pathways for oxygen to penetrate below the oxide layer. If there are more defects in the higher temperature samples this maybe the cause of the increased FFC area. The defects would allow easier access for the electrolyte to come into contact with the underlying iron, increasing the rate of metal dissolution, thus, increasing the rate of filiform corrosion.

Furthermore, potentiodynamic polarisation showed that the anodic currents were significantly higher for the samples heated to higher temperatures. This implies that these samples are more susceptible to the anodic reaction and again may be a cause for the increased FFC corroded area. During FFC, the separation of the organic coating from the substrate is linked to the anodic reaction. Thus, the samples which were heated to lower temperatures may have provided a degree of inhibition to the anodic reaction, reducing the rate at which FFC propagated. It is of note however, that the pH at which these measurements were taken (pH 7) were not directly comparable to the lower pH present during FFC (pH 2).

To get a better insight into the behaviour of purely the oxide layer, a sample consisting of blackplate electroplated with just Cr (III) oxide was studied using the SVET. The corrosion mechanism for all three samples (unheated, 200 °C and 400 °C) were

similar, in that a focal anode was formed and grew in size over time. However, a temperature of 400 °C was shown to drastically decrease the corrosion resistance of the sample. The anode was significantly larger, and a greater mass loss of Fe occurred over the course of the 24-hour study. These results again suggested that a greater heat treatment temperature led to a decrease in corrosion resistance. With this knowledge, it is plausible to suggest that the $Cr(OH)_3$ may act as a greater barrier to corrosion in comparison to Cr_2O_3.

6.5. Conclusion

A study into the effect of thermal treatment on the surface chemistry characteristics of TCCT was successfully carried out. Thermal treatment was shown to have an impact on the surface chemical characteristics of the substrate. Thermal heating caused the oxidation of $Cr(OH)_3$ and Fe into Cr_2O_3 and Fe_2O_3, respectively. This change in surface composition led to a decrease in corrosion performance of the TCCT substrates. Changes in substrate performance when thermally treated were also thought to be linked to the decrease in coating thickness caused by the change in surface species. Furthermore, the increased presence of defects on the thermally treated samples, thought to be caused by cracks in the coating, may also contribute towards the reduced corrosion performance.

6.6. References

1. Melvin C, Jewell E, Vooys A De, Lammers K, Mc N. Surface and Adhesion Characteristics of Current and Next Generation Steel Packaging Materials. J Packag Technol Res. 2018;2(2):93–103.

2. Mohammadtaheri M, Yang Q, Li Y, Corona-Gomez J. The effect of deposition parameters on the structure and mechanical properties of chromium oxide coatings deposited by reactive magnetron sputtering. Coatings. 2018;8(3):1–14.

3. Abdullah MM, Rajab FM, Al-abbas SM. Structural and optical characterization of Cr 2 O 3 nanostructures : Evaluation of its dielectric properties. 2014;027121:1–11.

4. Marchetti L, Perrin S, Wouters Y, Martin F, Pijolat M. Photoelectrochemical study of nickel base alloys oxide films formed at high temperature and high pressure water. Electrochim Acta. 2010;55(19):5384–92.

5. Wang L, Seyeux A, Marcus P. Thermal stability of the passive film formed on 316L stainless steel surface studied by ToF-SIMS. Corros Sci. 2020;165:1–15.

6. Zander D, Köster U. Corrosion of amorphous and nanocrystalline Zr-based alloys. Mater Sci Eng A. 2004 Jul 1;375–377(1–2 SPEC. ISS.):53–9.

7. Guo LQ, Qin SX, Yang BJ, Liang D, Qiao LJ. Effect of hydrogen on semiconductive properties of passive film on ferrite and austenite phases in a duplex stainless steel. Sci Rep. 2017;7(1):8–13.

7 The effectiveness of alanine as an inhibitor of aqueous iron corrosion

7.1 Introduction

Corrosion inhibitors act to reduce the rate of corrosion on a substrate, typically a metal. They work in a variety of ways; they may act to reduce the rate of the anodic reaction, the cathodic reaction or both (mixed type inhibitors). They can form a protective film over the metal to be protected or block sites susceptible to cathodic or anodic attack (1).

Hexavalent chromium based compounds are renowned as exceptional corrosion inhibitors (2). However, due to toxicity issues of chromate compounds mentioned in previous chapters, environmentally friendly corrosion inhibition systems have become of significant interest across numerous industrial sectors in recent years. Amino acids are non-toxic, environmentally friendly compounds that have shown to work effectively as corrosion inhibitors on a variety of metals including carbon steel, zinc and copper (1). Cysteine has previously been proven to work as a corrosion inhibitor on iron (3).

Amino acids contain two polar groups at opposite ends of the molecule, an amino group, and a carboxyl group. The nitrogen and oxygen atom of the carboxyl group enable amino acids to coordinate with metals and act as possible adsorption sites (1). Alanine is a hydrophobic amino acids with a similar chemical structure to cysteine, proven to inhibit corrosion on carbon steel (4). Alanine has a molecular weight of 89.09 $g.mol^{-1}$.

Computer modelling has previously been used to investigate the use of alanine as a corrosion inhibitor on iron as well as its mechanism of action (5). However, little work has been conducted into experimentally proving the inhibitory effects of alanine and this chapter will focus on their use as inhibitors of corrosion on iron.

It is well documented that in aqueous solutions, ionization of amino acids is pH dependent. Thus, it is of importance that the inhibitive effect of alanine is understood in electrolytes of varying pH.

The pKa values of alanine are 2.34 and 9.69, meaning it is predominantly in its zwitterion form in between the two values. Below a pH of 2.34 alanine will be in its protonated form and have a positive charge. Above a pH of 9.69 alanine will have a net negative charge (6).

In so doing, the effectiveness and mechanism of these amino acids was investigated by means of gravimetric weight loss studies, OCP measurements, and SVET. XPS, scanning electron microscopy (SEM) combined with energy-dispersive X-ray spectroscopy (EDS) was used for post-corrosion surface analysis.

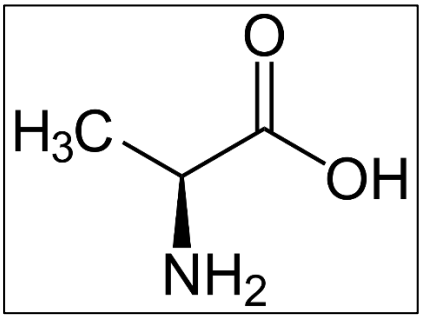

Figure 7.1. The chemical structure of alanine.

7.2 Materials and methods

7.2.1 Materials

A4 sheets of blackplate, a mild carbon steel (the substrate metal of TCCT®), were obtained from Tata Steel UK Trostre Steel Works and cut to the appropriate size using tin snips or a guillotine.

7.2.2 Methods

7.2.2.1 Gravimetric weight loss immersion studies

For gravimetric mass loss studies, blackplate was cut into 2 cm x 2.5 cm coupons and a small hole was made towards the top of the sample using a metal hole punch. This enabled the coupons to hang freely in the electrolyte with each side equally exposed in solution.

Initial studies involved immersion of blackplate in 1 wt. % NaCl, pH 7, with varying concentrations of alanine as shown in Table 7.1.

Table 7.1. Alanine concentration in 1L of electrolyte.

Alanine concentration / mol.dm^{-3}
10^{-2}
10^{-3}
10^{-4}

The blackplate coupons were weighed prior to, and after, the 24-hour immersion period and the inhibition efficiencies were calculated. To remove corrosion product from the blackplate coupons, the samples were placed into a sonicator with acetone for 1 minute and wiped clean with a swab.

7.2.2.2 Electrochemical measurements

Samples of size 2.5 cm x 2.5 cm were cut from a larger sheet and cleaned using isopropanol (IPA). A 0.8 cm^2 area of the blackplate sample was exposed to 250 ml of 1 wt. % NaCl electrolyte at specified pH values.

Open circuit potential (OCP) values were recorded at 20°C room temperature, using a Gamry interface 1000. A 2-electrode set up was used consisting of the working electrode (substrate) and a saturated calomel reference electrode.

Linear polarisation is an electrochemical technique, where the potential is increased or decreased with time in a linear way while the current is recorded. Linear polarisation

measurements were recorded at 20°C room temperature, using a Gamry interface 1000 and enabled the corrosion rate associated with the specimen to be determined. A 3-electrode set up was used consisting of the working electrode (substrate), saturated calomel reference electrode and platinum counter electrode. The linear polarisatino sweep was conducted between 0.015 V below and 0.015 V above the OCP. A sweep rate of 0.1667 $mV.s^{-1}$ was used, the ASTM standard scan rate (7).

7.2.2.3 Electrochemical impedance spectroscopy (EIS)

Electrochemical impedance spectroscopy (EIS) was performed using a Gamry interface 1000. A common three-electrode system was used consisting of blackplate as the working electrode, a saturated calomel electrode (SCE) reference electrode and a platinum counter electrode. The working electrode (sample) was polarized by ±10 mV around its OCP using sinusoidal perturbations with a range between 100 kHz and 10 mHz. Spectrums were taken every 2.5 hours.

7.2.2.4 Scanning vibrating electrode technique (SVET)

The SVET was used to visualise the electrochemical processes occurring on the surface of the sample. The SVET is able to spatially resolve areas of dissimilar electrochemical activity. Spatially resolved maps were produced on Golden Software's Surfer 10, a contouring and surface modelling software platform. Blackplate was immersed in 1 wt. % NaCl over a 24-hour period in the presence and absence of the inhibitor. The inhibitor was also dosed into the electrolyte after 2 hours (3 SVET scans) of the SVET experiment beginning to determine how it behaves after the sample has been corroded. Samples were scanned immediately after the addition of electrolyte and every hour onwards until the end of the 24-hour period.

7.2.2.5 SEM

Blackplate coupons that had been immersed in 1 wt. % NaCl both in the presence and absence of $x10^{-2}$ $mol.dm^{-3}$ alanine were analysed under the Hitachi TM3000 tabletop SEM with integrated EDS to provide an elemental map of the surface of the substrate after immersion. This was with the aim of providing a better understanding of the mechanism involved and how alanine attached to the surface of the metal.

7.2.2.6 XPS

Samples of size 1 cm x 1cm were cut from a blackplate coupon which had been immersed in 1 wt. % NaCl in the presence and absence of $x10^{-2}$ $mol.dm^{-3}$ alanine. XPS surface scans were run using a Kratos Axis Supra instrument. A monochromated 1486 eV Al Kα source was used and an analysis area of 300 µm x 800 µm was utilised. This technique provided a non-destructive analysis of the elemental composition of the surface of the material. In turn this may provide information on the attachment of alanine to the substrate.

7.3 Results

7.3.1 Gravimetric weight loss immersion studies

The visual appearance of the blackplate after 24 hours, following the removal of loose corrosion product, is shown in Figure 7.2. The results immediately highlighted that the presence of alanine in the electrolyte was altering the corrosion performance of blackplate. The samples immersed in the electrolyte in the presence of alanine (at any concentration) had corroded significantly less in comparison to the blackplate coupon in the absence of alanine. In particular, the sample immersed in the electrolyte with the presence of $x10^{-2}$ $mol.dm^{-3}$ alanine had obtained almost no visible corrosion damage. There was also significantly less visible loose corrosion product in solution for the sample immersed in electrolyte in the presence of $x10^{-2}$ $mol.dm^{-3}$.

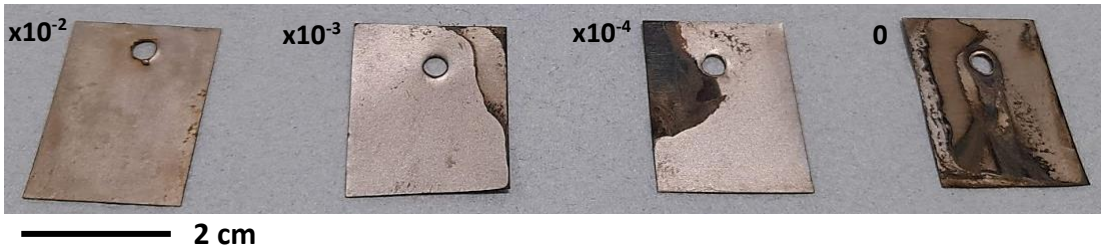

Figure 7.2. The visual appearance of blackplate coupons after being immersed in 1 wt. % NaCl with varying concentrations of alanine for 24-hours. The concentrations of alanine present in the electrolyte were $x10^{-2}$, $x10^{-3}$, $x10^{-4}$ and 0 $mol.dm^{-3}$ respectively. The scale bar can be seen in the bottom left of the image.

The surface of the samples after immersion were observed under the SEM and shown in Figure 7.3. SEM of the surfaces of blackplate prior to and after immersion in 1 wt. % NaCl in the presence and absence of $x10^{-2}$ $mol.dm^{-3}$ alanine. The SEM images reinforced the above findings.

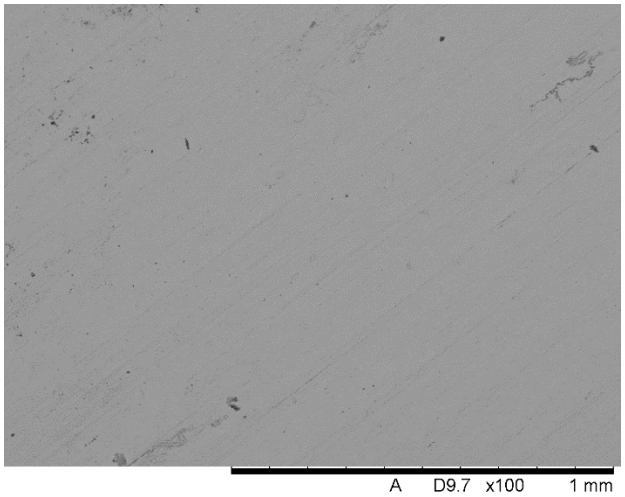

Blackplate prior to immersion in electrolyte.

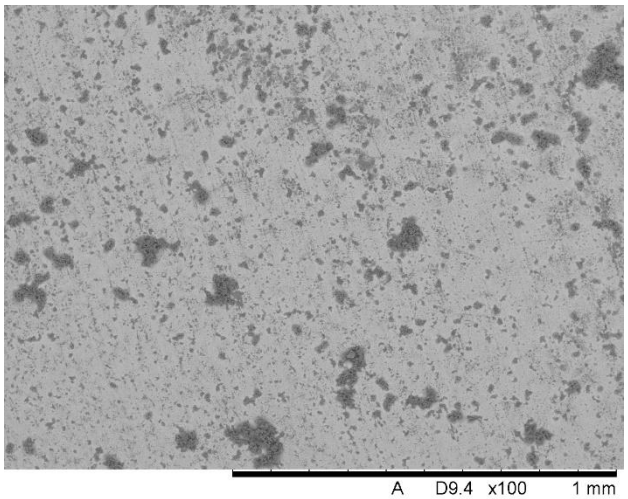

Blackplate after immersion in 1 wt. % NaCl electrolyte in the presence of $x10^{-2}$ $mol.dm^{-3}$ alanine.

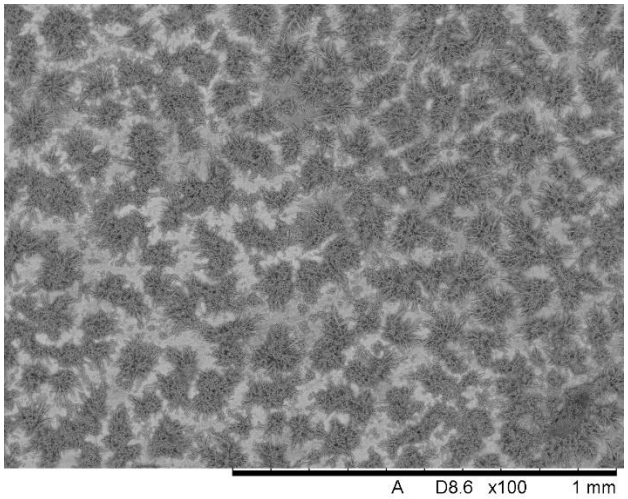

Blackplate after immersion in 1 wt. % NaCl electrolyte in the absence of $x10^{-2}$ $mol.dm^{-3}$ alanine.

Figure 7.3. SEM of the surfaces of blackplate prior to and after immersion in 1 wt. % NaCl in the presence and absence of $x10^{-2}$ $mol.dm^{-3}$ alanine.

From the gravimetric mass loss studies, the inhibition efficiency of alanine at various concentrations was determined. The results can be seen in Table 7.2. Three repeats

were conducted for each concentration of alanine. Inhibition efficiency was calculated using the following equation.

$$I.E\ \% = \frac{W_0 - W_1}{W_0} \times 100 \qquad (1)$$

Where W_0 is the weight loss of the coupon in the absence of inhibitor and W_1 is the weight loss of the coupon in the presence of inhibitor.

The highest inhibition efficiency (I.E) was provided by 1 x 10^{-2} mol.dm^{-3} alanine and the I.E decreased with alanine concentration. Although it is worth noting that the highest I.E was only 54%.

Table 7.2. The inhibition efficiency of varying concentrations of alanine calculated from mass loss after 24 hours immersion in 1 wt. % NaCl, pH 7.

Concentration of alanine added / mol.dm^{-2}	**Average mass loss after 24 hours / g**	**Inhibition Efficiency / %**
0	0.0055 ±0.0003	N/A
10^{-4}	0.0052 ±0.0003	5
10^{-3}	0.0043 ±0.0005	21
10^{-2}	0.0027 ±0.0007	51

Thus far, evidence suggests that alanine acts to inhibit corrosion of iron. To further understand the mechanism of inhibition further studies were completed. A sample of blackplate was initially placed into 1 wt. % NaCl in the presence of 1 x 10^{-2} mol.dm^{-3} alanine. After 24 hours the sample was removed and placed into electrolyte in the absence of alanine. If an alanine film was formed and stayed intact when transferred into the new electrolyte, it would be expected that little corrosion damage would be visible.

Figure 7.4 shows the appearance of the substrate 10 days after the initial immersion to determine if the film stayed intact after a prolonged time. Evidence of corrosion around the edges of the sample was noticed. The middle of the sample, however,

remained free from corrosion damage. It is hypothesised that the initial 24-hour immersion in electrolyte with alanine present had protected the middle of the sample from damage. However, the outer edge was covered in corrosion product perhaps due to its increased susceptibility to corrosion and thus alanine was less efficient at inhibiting these areas.

Figure 7.4. A blackplate coupon which was initially immersed for 24 hours in 1 wt. % NaCl in the presence of $\times 10^{-2}$ mol.dm^{-3} alanine followed by 9 days immersion in 1 wt. % NaCl in the absence of $\times 10^{-2}$ mol.dm^{-3} alanine.

To further investigate the inhibitive effects of alanine in the case that the pH was less than pKa_1, or more than pKa_2 gravimetric weight loss experiments were repeated in electrolytes of low (pH 2 and thus, alanine will have a net positive charge) and high (pH 11 and thus, alanine will have a net negative charge) pH. At pH 7 the strongest inhibitory effects were observed when alanine was added at a concentration of $x10^{-2}$ mol.dm^{-3}. Thus, mass loss experiments for these new low and high pH electrolytes were conducted in the presence and absence of $x10^{-2}$ mol.dm^{-3} alanine.

Table 3. The inhibition efficiency of varying concentrations of alanine calculated from mass loss after 24 hours immersion in 1 wt. % NaCl, pH 2 and pH 11.

Concentration of alanine added / mol.dm^{-2}	**Average mass loss after 24 hours / g**	**Inhibition Efficiency / %**
0 – pH 2	0.0066 ±0.0011	N/A
10^{-2} – pH 2	0.0042 ±0.001	37
0 – pH 11	0.0050 ±0.0008	N/A
10^{-2} – pH 11	0.0013 ±0.0001	74

The addition of x10^{-2} mol.dm^{-3} alanine provided a degree of inhibition of iron corrosion in 1 wt. % NaCl at both pH 2 and pH 11. A significantly higher inhibition efficiency was seen at pH 11, where alanine will have a net negative charge, in comparison with pH 2, where alanine will have a net positive charge. Furthermore, there was an improvement in the inhibition efficiency recorded at pH 11 compared with pH 7, with pH 2 offering the least inhibition efficiency. Also of note was the limited corrosion product in solution of the electrolyte at pH 2 both in the absence and presence of alanine. Thus, even in the absence of the inhibitor, an electrolyte with a pH of 2 leads to a reduced amount of corrosion product being released into solution.

7.3.2 Electrochemical measurements

Linear polarisation was conducted in order to get a better understanding of how the rate of corrosion changed throughout the duration of the experiment. Figure 7.5 shows the corrosion rate over a 24-hour period for blackplate in 1 wt. % NaCl in the absence and presence of x10^{-2} mol.dm^{-3} alanine. The corrosion rate observed on blackplate when alanine is present is significantly less (over half) compared with the corrosion rate when alanine is absent. Overtime the corrosion rate of both samples gradually decreases from approximately 11 to 9 mpy in the absence of alanine and approximately 6 to 3 mpy in the presence of alanine. Towards the end of the 24-hour period (after approximately 20 hours) a slight increase in corrosion rate is observed on the sample in the presence of alanine.

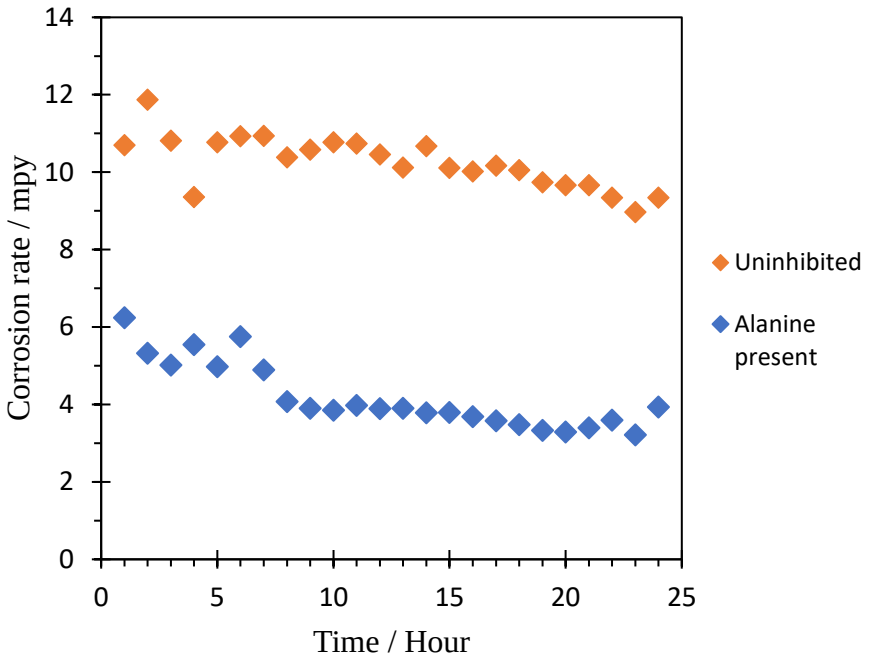

Figure 7.5. Corrosion rate, as calculated from linear polarisation measurements, for blackplate in 1 % NaCl in the absence and presence of $\times 10^{-2}$ mol.dm^{-3} alanine.

OCP measurements were conducted to determine the corrosion potential associated with blackplate immersed in 1 wt. % NaCl, pH 7, in the presence and absence of 1 x 10^{-2} mol.dm^{-3} alanine. Blackplate samples were immersed in the relevant electrolyte for 24 hours where they were free to corrode. The results are shown in Figure 7.6.

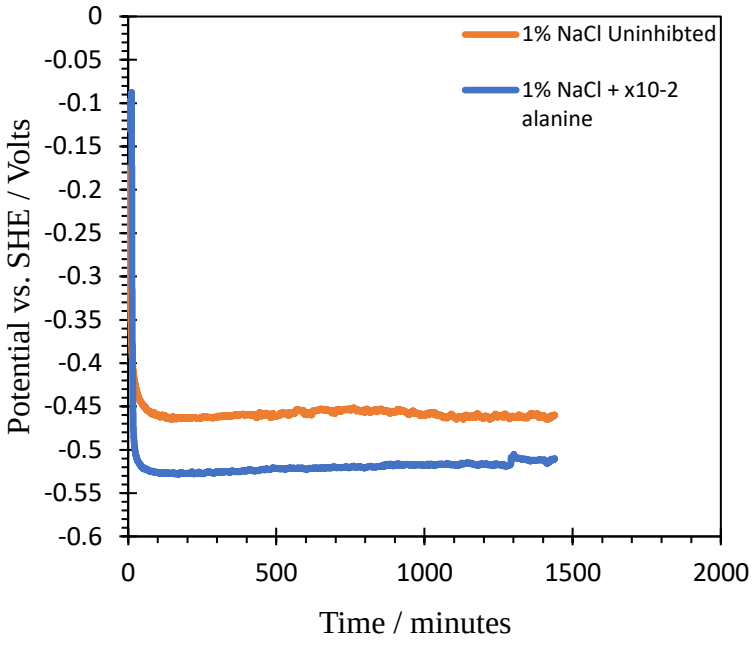

Figure 7.6.Open circuit potential (OCP) for blackplate in 1% NaCl in the absence and presence of ×10^{-2} mol.dm^{-3} alanine.

In both cases, the OCP becomes very stable (the voltage is negligibly changing) after approximately 1 hour of immersion. Unsurprisingly, the OCP for blackplate is ~ 0.45 V vs. SHE. The addition of alanine shifts the OCP to a more negative value of ~ 0.52 V vs. SHE, this being approximately 70 mV lower than that recorded in the absence of alanine. This finding is indicative of alanine behaving as a cathodic inhibitor at this pH. At pH 7 alanine will exist as a zwitterion. Hence, the adsorption of the zwitterion may be directly to the metal surface or via Cl^- ions. In turn it is plausible that it acts to block cathodic sites, retarding corrosion.

A different experiment was then conducted to determine the effect that the addition of 1 x 10^{-2} mol.dm^{-3} alanine had on the OCP when added to 1 wt. % NaCl after allowing the blackplate to freely corrode for 2 hours. The results can be seen in Figure 7.7. Once stabilised, the OCP values, both in the absence and presence of alanine, were unchanged from those in Figure 7.6; alanine still lowered the OCP by the same amount (approximately 70 mV) when it was added 2 hours after the blackplate was immersed in the electrolyte.

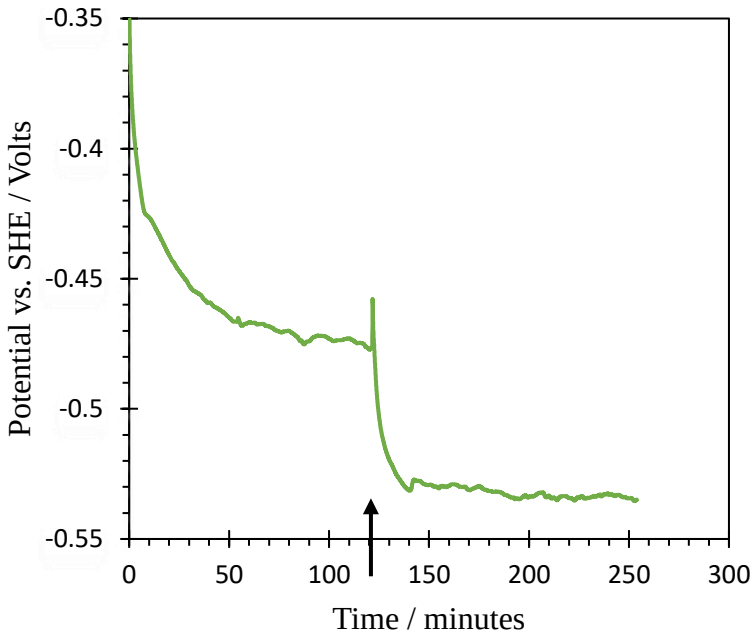

Figure 7.7. Open circuit potential (OCP) for blackplate in 1 wt. % NaCl with the addition of $\times 10^{-2}$ mol.dm^{-3} alanine halfway through, indicated by the arrow.

To further investigate the inhibitive effects of alanine in the case that pH is less than pKa_1 (alanine will have a positive charge), or more than pKa_2 (alanine will have a negative charge) OCP measurements were repeated in electrolytes of varying pH. Figure 7.8 shows the OCP for blackplate in 1 % NaCl pH 11 in the absence and presence of alanine. The OCP measurement in the absence of alanine was similar to that at pH 7, approximately 0.45 V vs. SHE. However, in contrast to the behaviour observed at pH 7, at pH 11 the presence of alanine shifted the OCP (by approximately 50 mV) to a more positive value. At a pH of 11 alanine will have a net negative charge and thus may form a complex with Fe^{2+}, inhibiting the anodic reaction and thus explain the increase in OCP. Figure 7.9 shows the OCP for blackplate in 1 % NaCl pH 2 in the absence and presence of alanine. The OCP measurement in the absence of alanine slightly shifted in the positive direction compared to that of pH 7 and pH 11 and was recorded to be approximately 0.38 V vs. SHE. The presence of alanine slightly shifted the OCP (by approximately 30 mV) to a more positive value. At a pH of 2 alanine would have a net positive charge and thus, may bind to the surface via halide ions and block active sites for anodic dissolution, hence increasing the OCP.

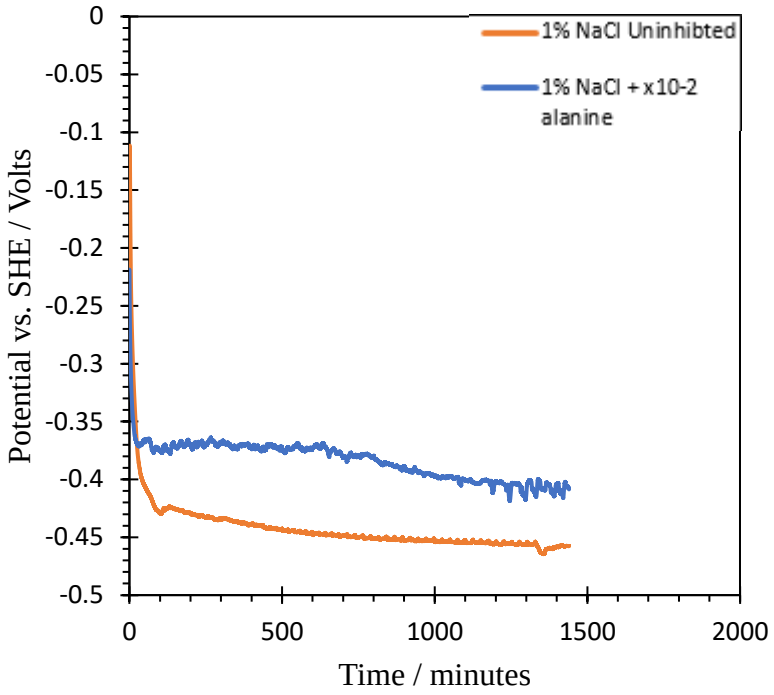

Figure 7.8. Open circuit potential (OCP) for blackplate in 1 wt. % NaCl, pH 11, in the absence and presence of $\times 10^{-2}$ mol.dm^{-3} alanine.

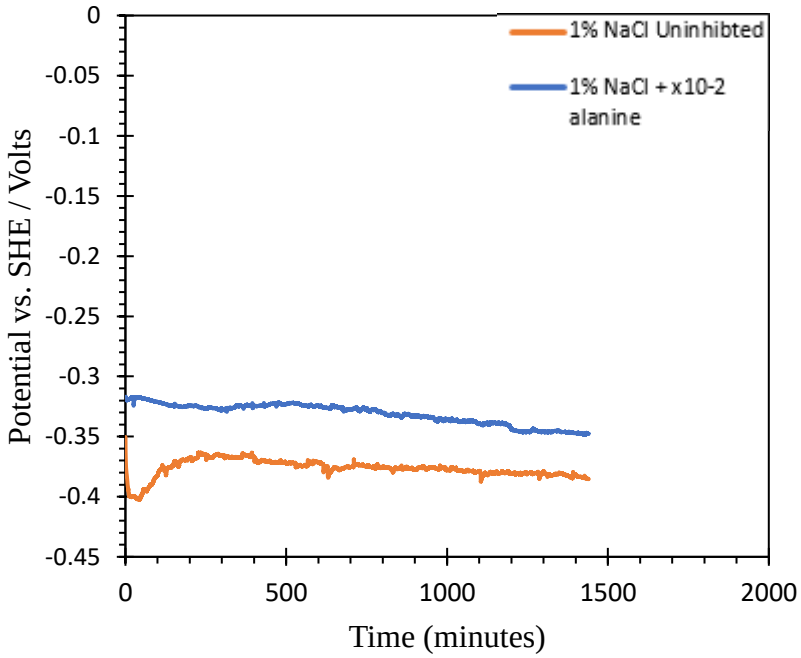

Figure 7.9. Open circuit potential (OCP) for blackplate in 1 wt. % NaCl, pH 2, in the absence and presence of $\times 10^{-2}$ mol.dm^{-3} alanine.

7.3.3 FTIR analysis

FTIR was conducted on a sample immersed in $x10^{-2}$ $mol.dm^{-3}$ alanine for 24 hours. A comparison spectrum of pure alanine in powder form is also shown. Figure 7.10 and Figure 7.11 show the spectra collected. The spectrum of pure alanine contained a broad $-NH_3^+$ stretching band in the region of 3100 cm^{-1}. However, in the spectra with blackplate immersed in the amino acid solution this was replaced by several sharp bands suggestive of deprotonation and coordination of the $-NH_2$ groups (8). Furthermore, the characteristic NH_3^+ groups, present in the pure alanine sample were absent in the spectra for of the immersed blackplate in amino acid solution.

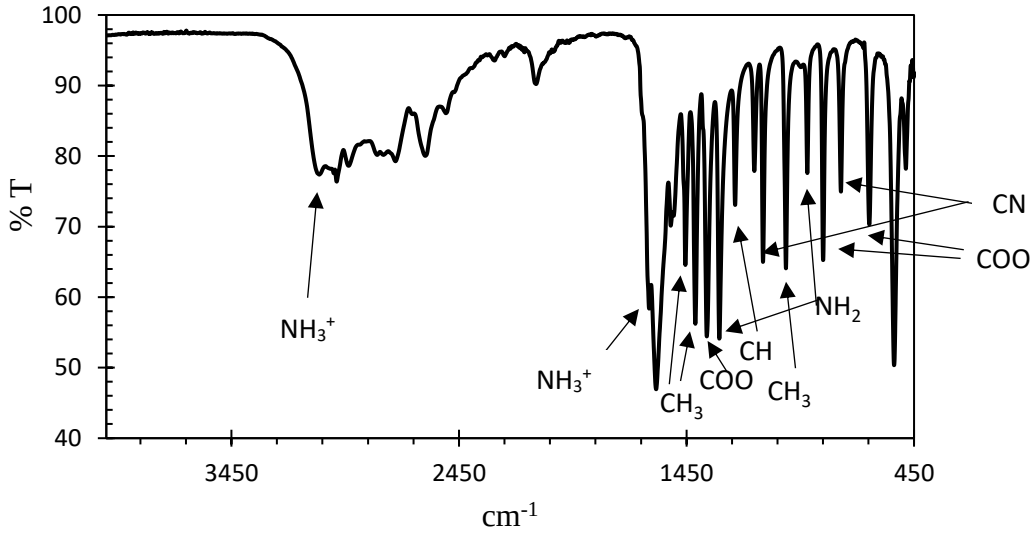

Figure 7.10. FTIR spectrum of pure alanine.

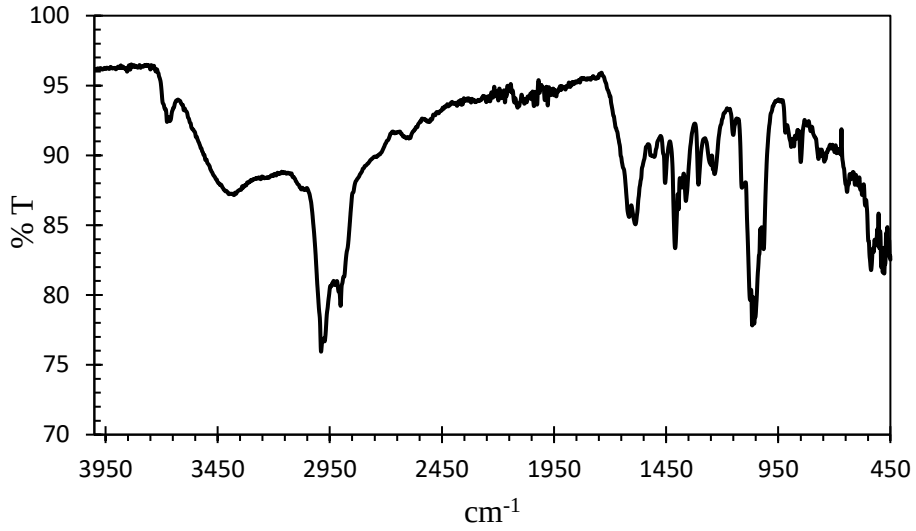

Figure 7.11. FTIR spectrum of blackplate immersed in 1 wt. % NaCl in the presence of alanine.

7.3.4 Studies into the effectiveness of amino acids as corrosion inhibitors using the SVET

SVET derived surface plots of the current density above the freely corroding samples in pH 2, 7 and 11 1 wt. % NaCl electrolytes are shown below. The SVET was used to greater understand the mechanistic differences in the inhibitory effect of alanine on the iron surface at varying pH concentrations. This offers a visual representation of the location and intensity of anodic and cathodic features, measured by the SVET tip. Scans took place every hour for 24 hours. The plots shown were obtained after varying times of electrolyte immersion and were chosen to best represent the mechanistic differences observed at varying pHs.

Figure 7.12 shows the current density maps for the control at pH 7. The colour change from red to blue, observed on the SVET maps, is indicative of the shift from anodic to cathodic activity. Initially corrosion was highly localised with numerous focal anodes present across the surface after 1 hour of immersion. By hour 4, a significant portion of the surface was anodically active, and this anode grew in size with time. By the end of the 24 hours almost the entire surface was made up of anodic activity and corrosion product was observed across this entire region.

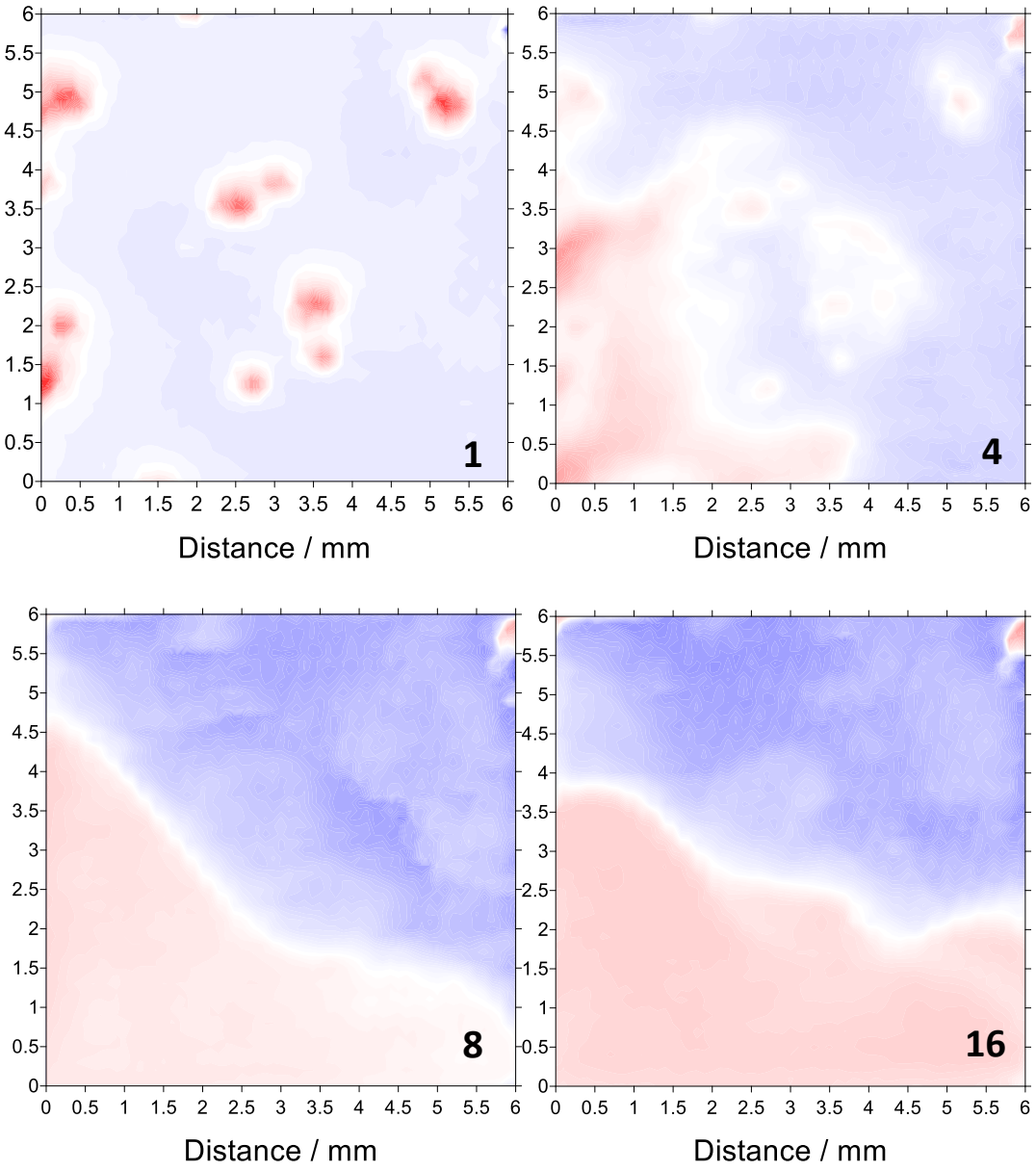
1
4
8
16
Distance / mm
Distance / mm
Distance / mm
Distance / mm

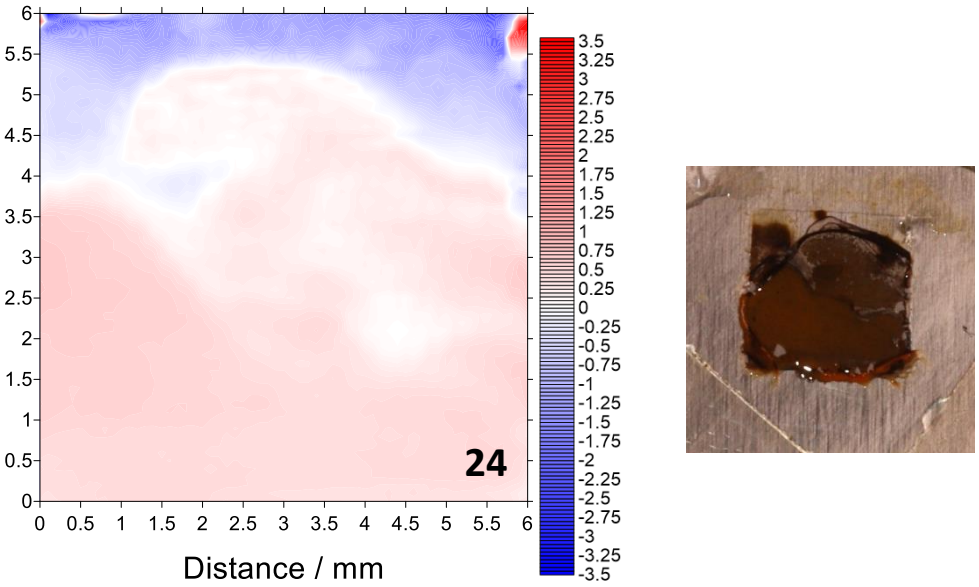

Figure 7.12. SVET-measured current density maps of blackplate in 1 wt. % NaCl pH 7. Numbers in the bottom right dictate the respective hours at which the plot was taken from.

Figure 7.13 shows the current density maps for blackplate immersed in 1 wt. % NaCl at pH 7, in the presence of $x10^{-2}$ $mol.dm^{-3}$ alanine. At this pH alanine acts as a zwitterion and has a zero net charge. There was little evidence of significant activity up to 12 hours. Following this, a region of anodic activity occupied the surface except for the edges. Of note was the appearance of the sample after the 24-hour immersion, which seemed to show little evidence of corrosion.

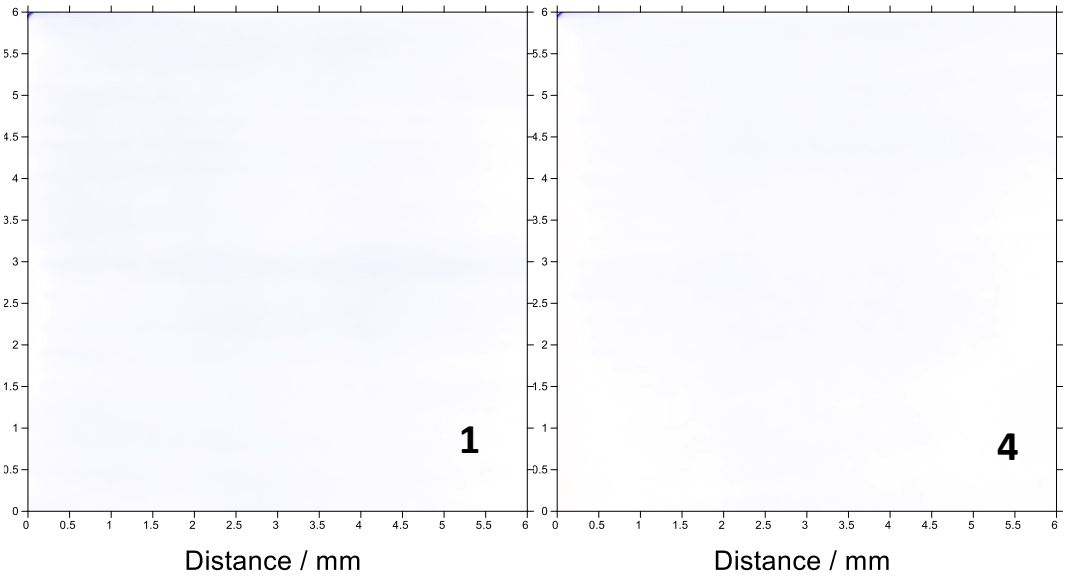

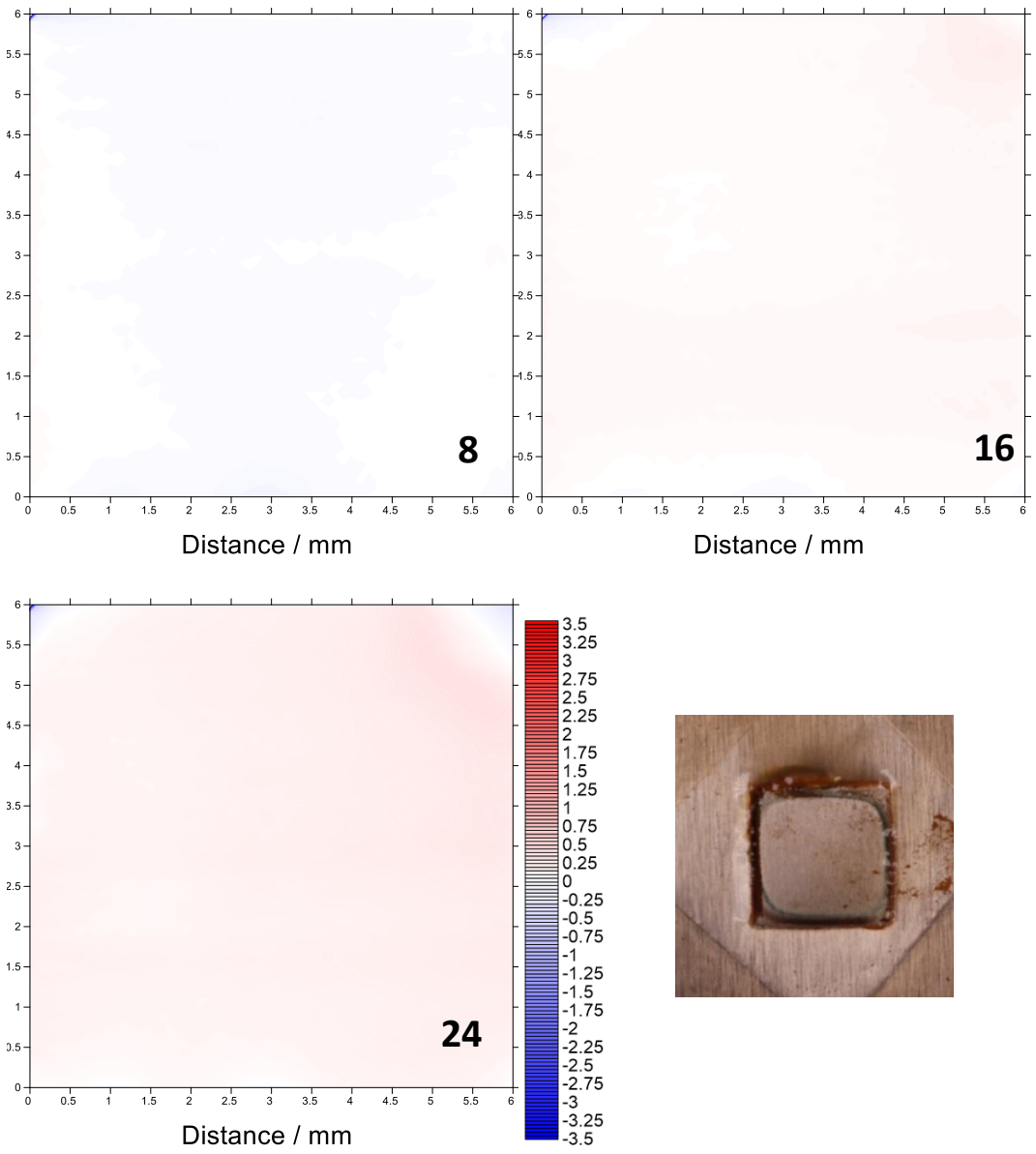

Figure 7.13. SVET-measured current density maps of blackplate in 1 wt. % NaCl pH 7 in the presence of $\times 10^{-2}$ alanine. Numbers in the bottom right dictate the respective hours at which the plot was taken from.

The area averaged anodic and cathodic current density values observed over the 24-hour time period for the pH 7 electrolyte in the absence and presence of x 10^{-2} mol.dm^{-3} alanine are shown in Figure 7.14. It was clear that alanine had a big influence on the corrosion processes occurring on the sample surface. The anodic current densities were significantly lower towards the start of the experiment when alanine was present, and little activity was observed on the surface of the substrate. Over the course of the experiment, in the presence of alanine, the surface being more active with the presence

of a faint anodic region dominating the square. Little corrosion was observed on the surface of the substrate after the experiment was finished.

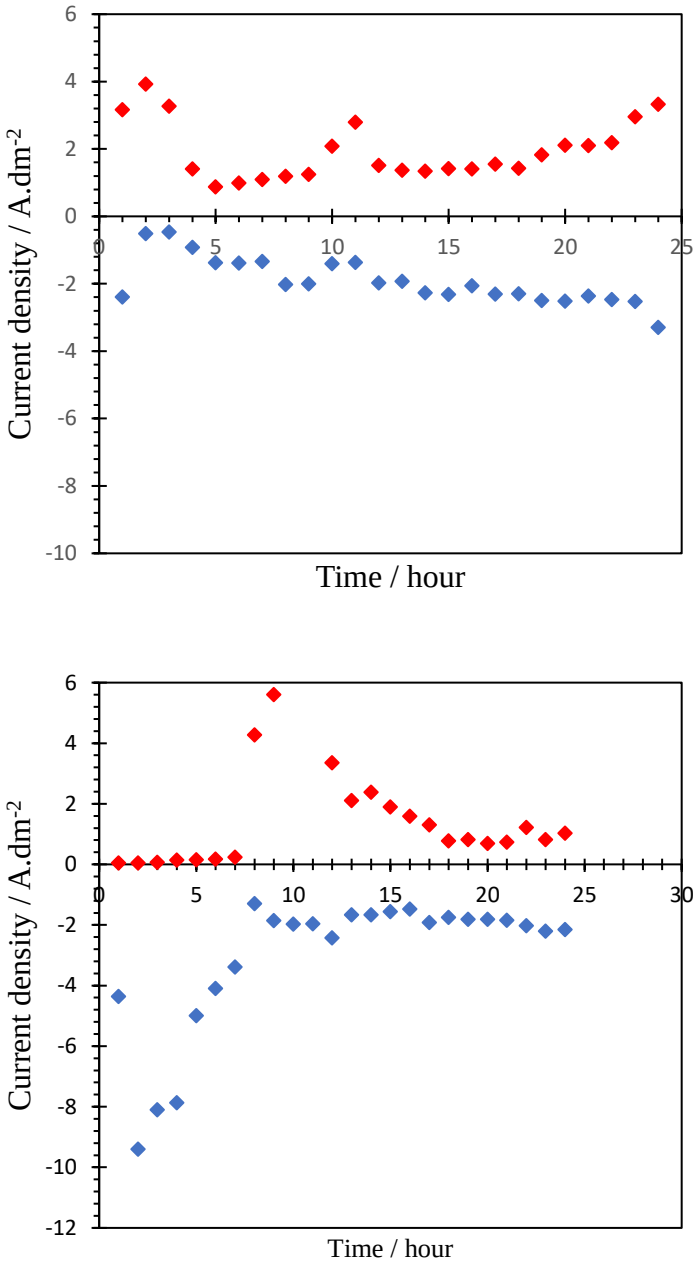

Figure 7.14. The area averaged anodic and cathodic current density values observed on the surface of the sample as a function of time for blackplate in 1 wt. % NaCl pH 7. The graphs show the data in the absence and presence of $\times 10^{-2}$ mol.dm^{-3}alanine respectively.

In order to gain more insight into the mechanism of alanine as a corrosion inhibitor, SVET scans were repeated but alanine was added part way through the experiment. Figure 7.15 shows the SVET measured current density maps of blackplate in 1 wt. %

NaCl over a period of 24 hours. Alanine was added after the 2-hour scan had taken place. In the absence of the inhibitor a large, focal anodic site was present the top right-hand corner of the sample and grew in size up to the addition of alanine. Initially both the anodic and cathodic currents observed on the sample were relatively large, at 3.2 and -1.7 $A.m^{-2}$ respectively. After the addition of alanine (after hour 2), both the anodic and cathodic current densities tended towards 0 $A.dm^{-2}$ and there was very little activity on the surface. By hour 16 a large but weak anodic site was present which continued to progress outwardly until the end of the experiment. By hour 24 a large proportion of the surface was occupied by anodic activity. This larger anode possessed a reduced intensity relative to the initial focal anode.

The appearance of the sample after 24 hours of immersion can be seen in Figure 7.15. Little evidence of corrosion was present on the surface of the material. A faint line was also present around the edge of the exposed area.

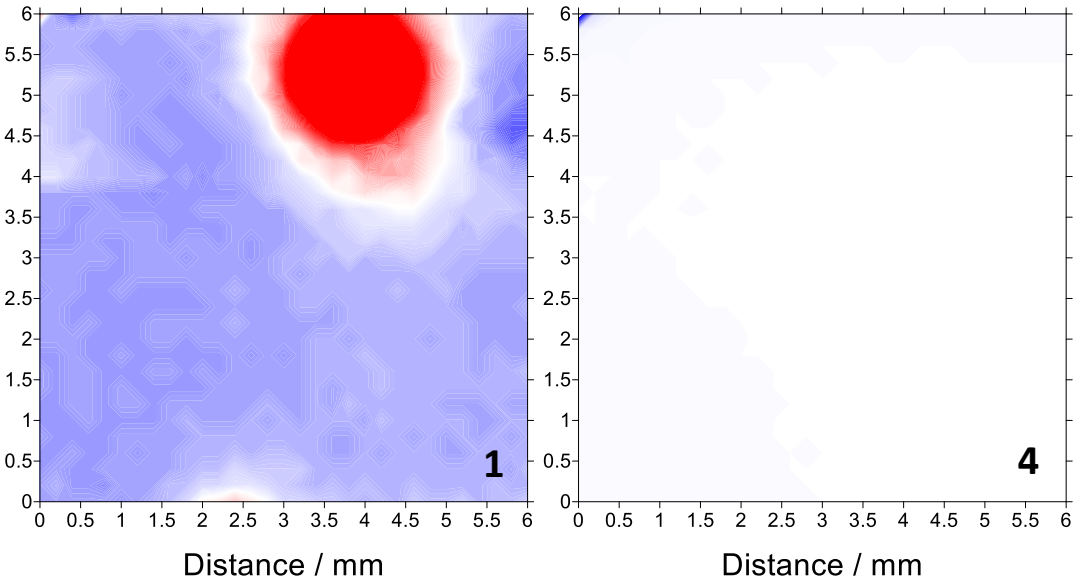

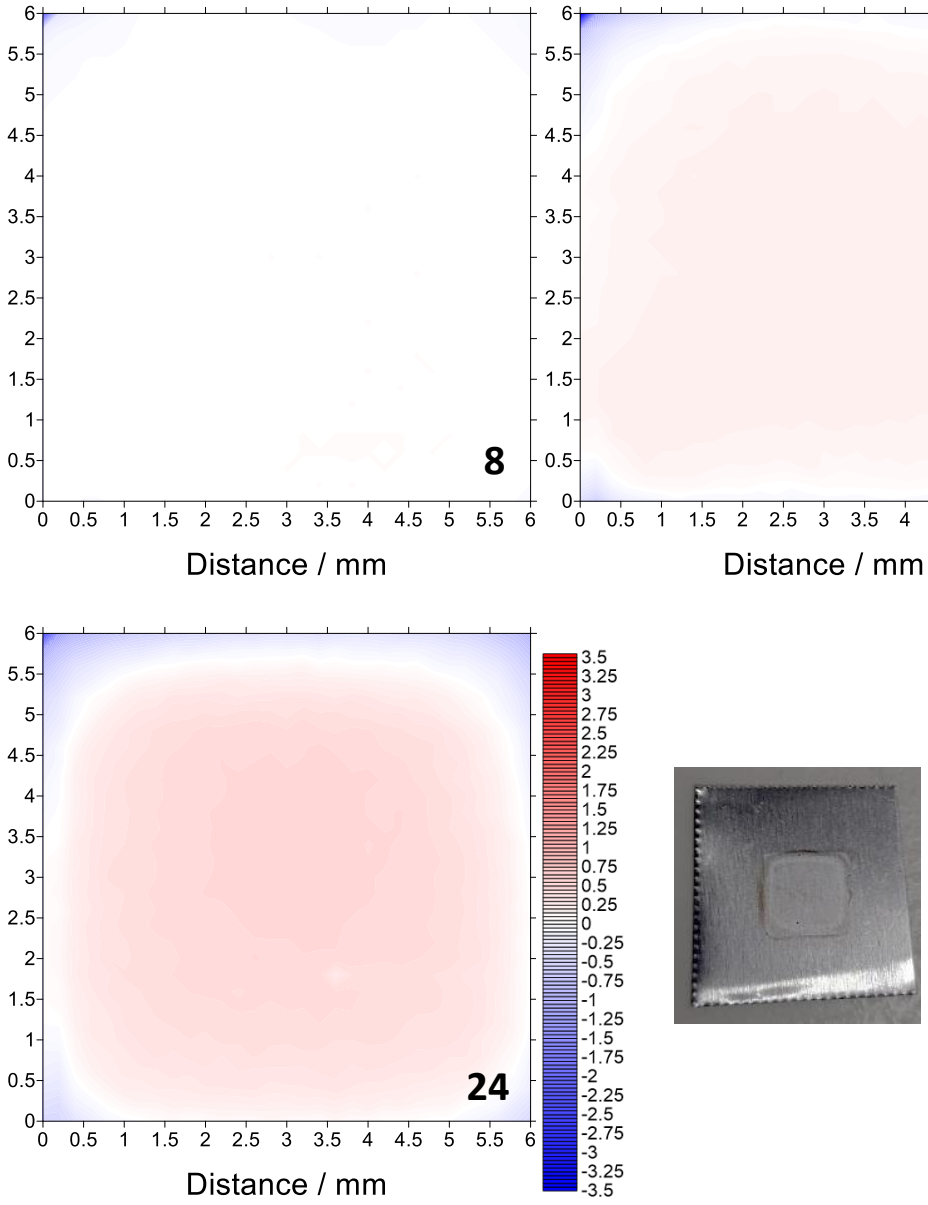

Figure 7.15. SVET-measured current density maps of blackplate in 1 wt. % NaCl pH 7 with the addition of $\times 10^{-2}$ alanine after 2 hours of immersion. Numbers in the bottom right dictate the respective hours at which the plot was taken from.

The SVET can also provide a value of semi-quantitative metal loss (Fe in this case), as calculated using SVET derived anodic j_z values, during the 24-hour period. The results from this can be seen in Figure 7.16. During the initial 2 hours, in the absence of alanine, the mass loss of Fe was increasing significantly with an estimated ~1 $g.m^{-2}$ mass loss in just 1 hour. After the addition of alanine, a significant reduction in mass loss was observed. After approximately 12 hours the mass loss gradually increased but

remained lower than that observed in the initial hours of the experiment, in the absence of alanine.

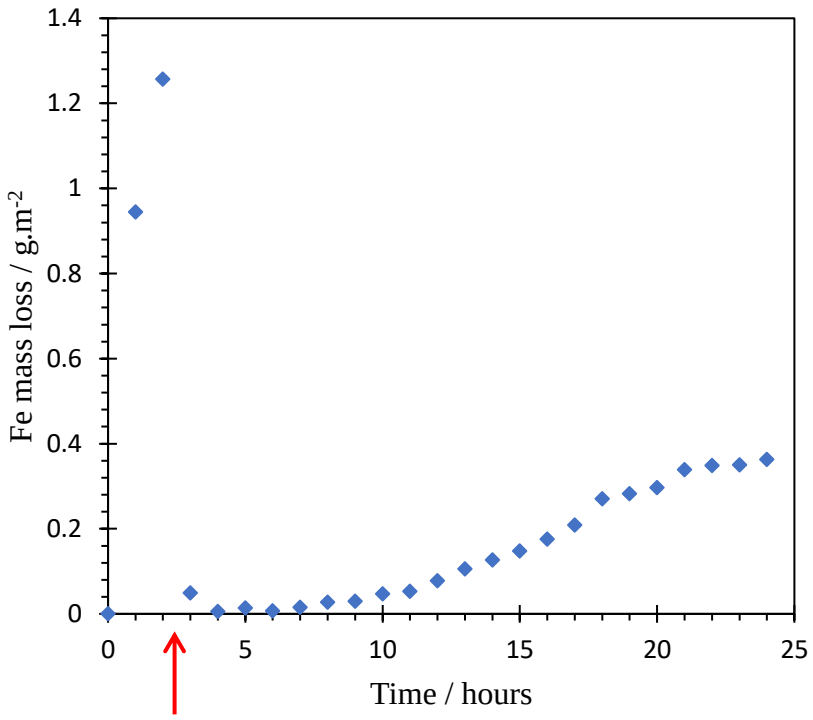

Figure 7.16. SVET derived mass loss data of blackplate immersed in 1 wt. % NaCl with the addition of $\times 10^{-2}$ mol.dm^{-3} alanine after 2 hours indicated by the red arrow.

The SVET experiments were then repeated for x 10^{-2} mol.dm^{-3} alanine at pH 2 and 11. Alanine is in its cationic and anionic form respectively, at these pHs. Figure 7.17, Figure 7.18 and Figure 7.19 show the SVET current density maps for blackplate immersed in a 1 wt. % NaCl solution, pH 2, in the absence and presence of alanine, and in the case that alanine is added after 2 hours of immersion in NaCl. All three sets of current density maps appear so be similar in appearance. A region of anodic activity occupied the edges of the square whilst cathodic activity dominated in the middle.

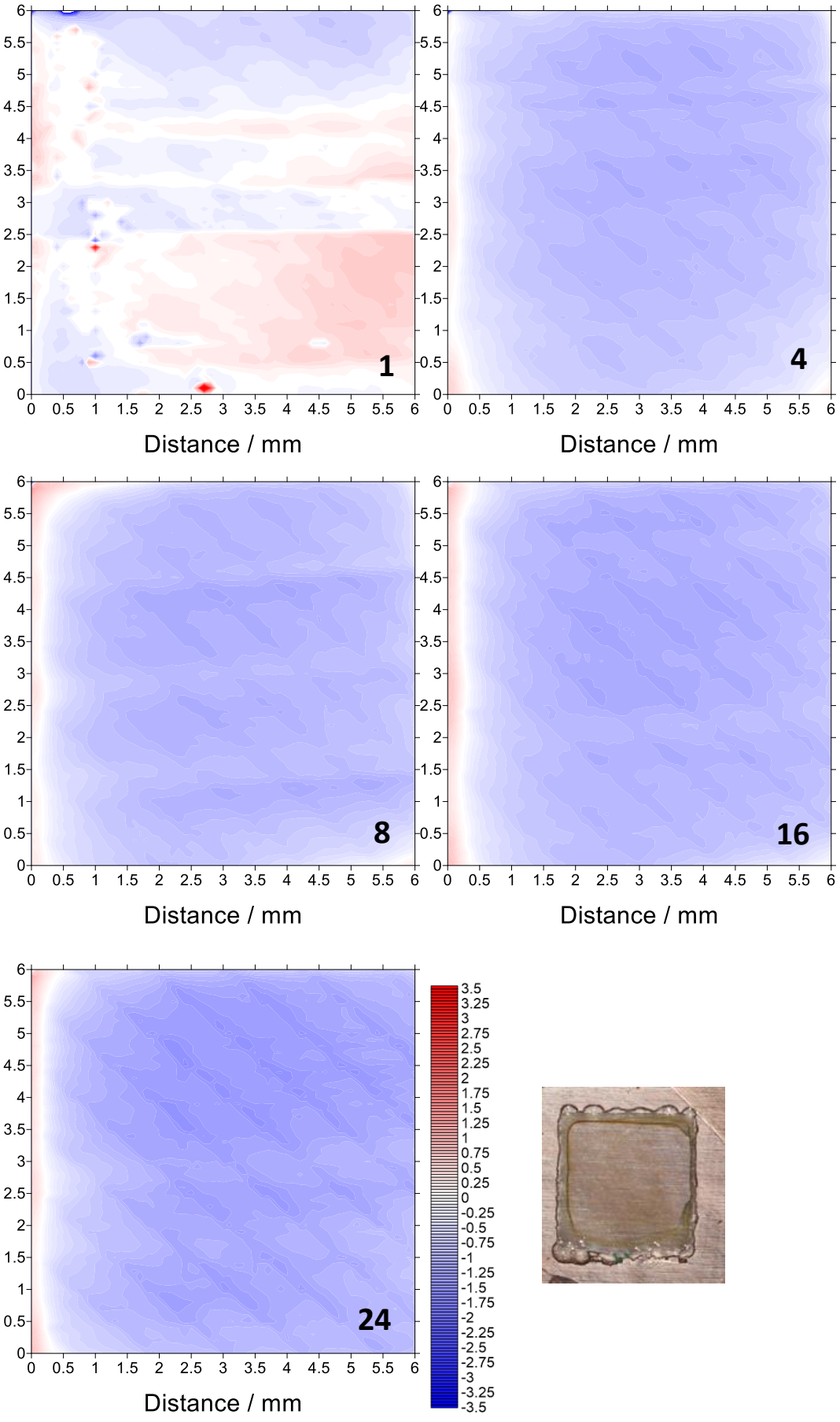
1
4
8
16
24
Distance / mm
3.5
3.25
3
2.75
2.5
2.25
2
1.75
1.5
1.25
1
0.75
0.5
0.25
0
-0.25
-0.5
-0.75
-1
-1.25
-1.5
-1.75
-2
-2.25
-2.5
-2.75
-3
-3.25
-3.5

Figure 7.17. SVET-measured current density maps of blackplate in 1 wt. % NaCl pH 2. Numbers in the bottom right dictate the respective hours at which the plot was taken from.

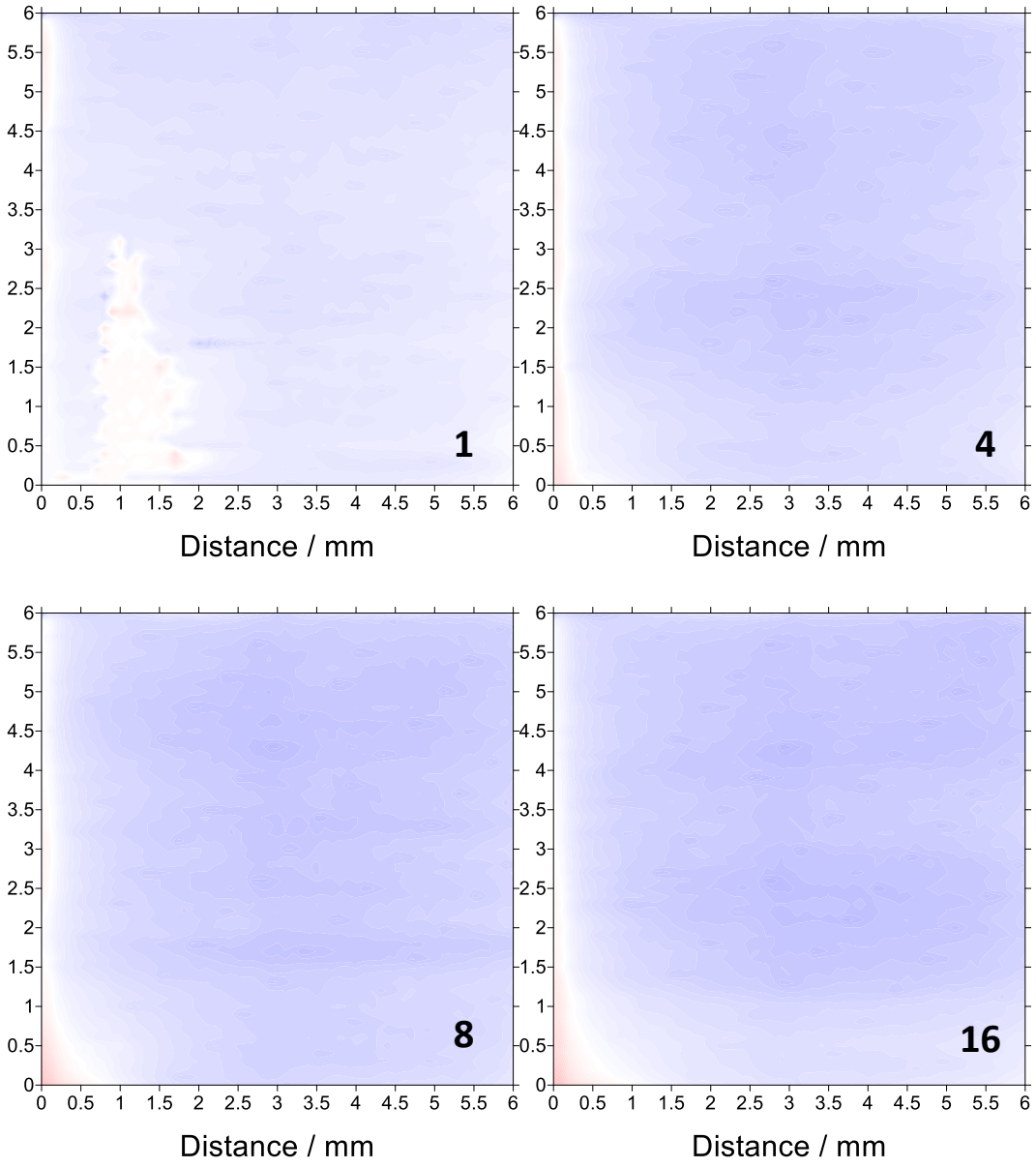

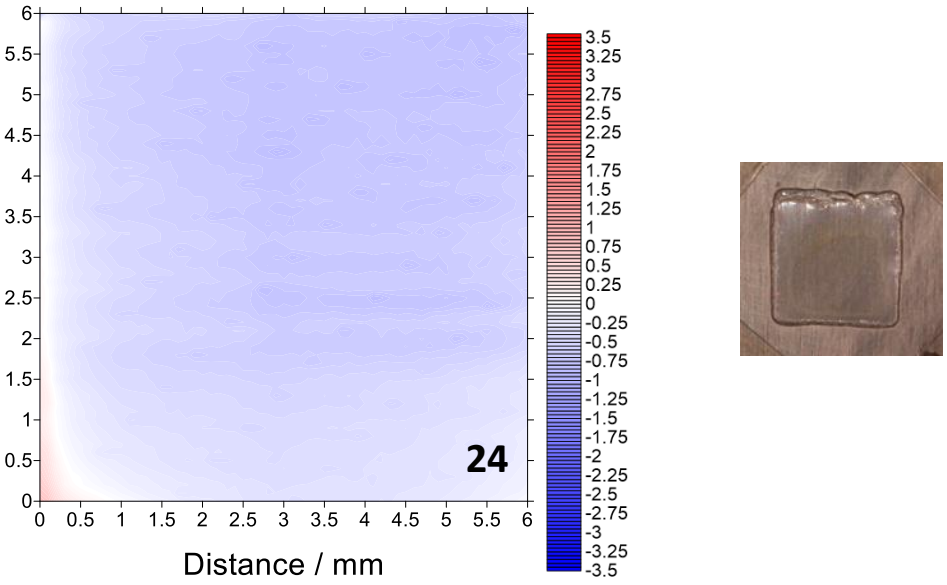

Figure 7.18. SVET-measured current density maps of blackplate in 1 wt. % NaCl pH 2 with the addition of $\times 10^{-2}$ mol.dm^{-3} alanine. Numbers in the bottom right dictate the respective hours at which the plot was taken from.

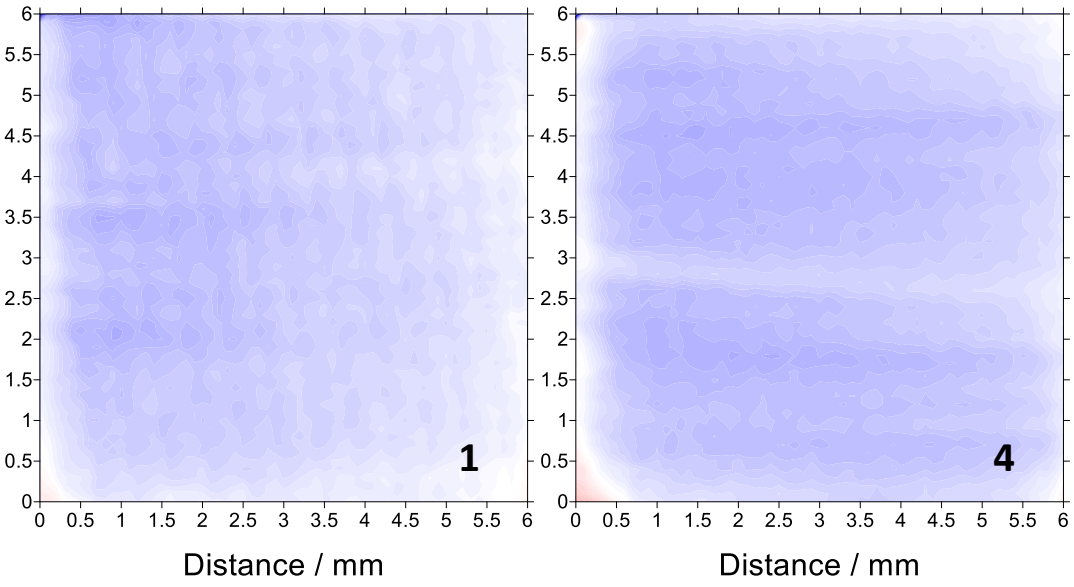

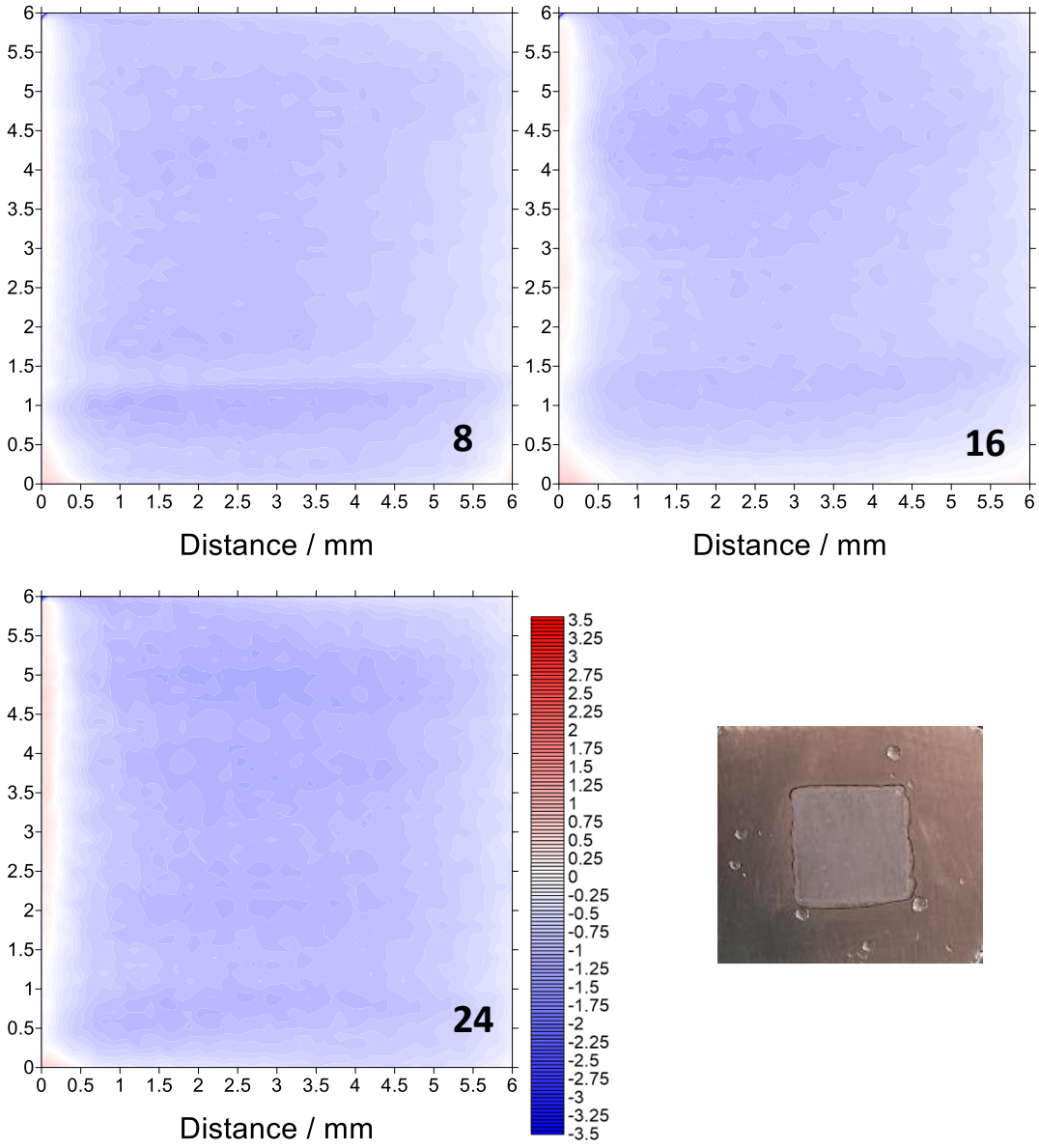

Figure 7.19. SVET-measured current density maps of blackplate in 1 wt. % NaCl pH 2 with the addition of $\times 10^{-2}$ mol.dm^{-3} alanine after 2 hours of immersion. Numbers in the bottom right dictate the respective hours at which the plot was taken from.

The area averaged anodic and cathodic current density values observed over the 24-hour time period for the pH 2 electrolyte in the absence and presence of x 10^{-2} mol.dm^{-3} alanine are shown in Figure 7.20. The current density values observed on iron in the absence of alanine are initially slightly higher and then decrease to a value very similar to those observed on the surface of iron in the presence of alanine.

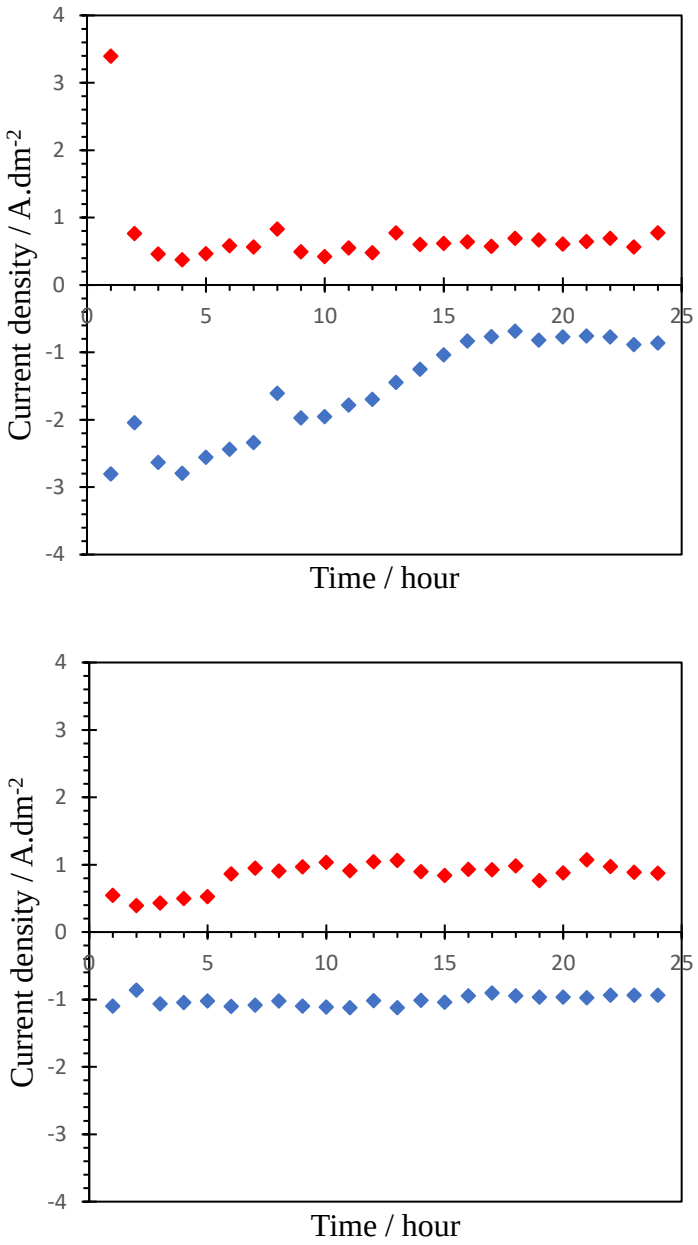

Figure 7.20. The area averaged anodic and cathodic current density values observed on the surface of the sample as a function of time for blackplate in 1 wt. % NaCl pH 2. The graphs show the data in the absence and presence of $\times 10^{-2}$ mol.dm^{-3} alanine respectively.

The SVET scans for pH 11 are shown below in Figure 7.21, Figure 7.22 and Figure 7.23. In the absence of alanine, a single anode was initially observed, the adjacent area being cathodic. In time, regions of anodic activity were observed to migrate across the surface of the sample. By the end of the 24-hour experiment almost the entire surface was covered in corrosion product. Putting into context what is known about iron

corrosion at pH 11 using the Pourbaix diagram, the surface of the metal will be covered in Fe_2O_3. Although it is of note that at the start of the experiment the surface is removed of oxide and thus it will take a bit of time for the oxide layer to develop.

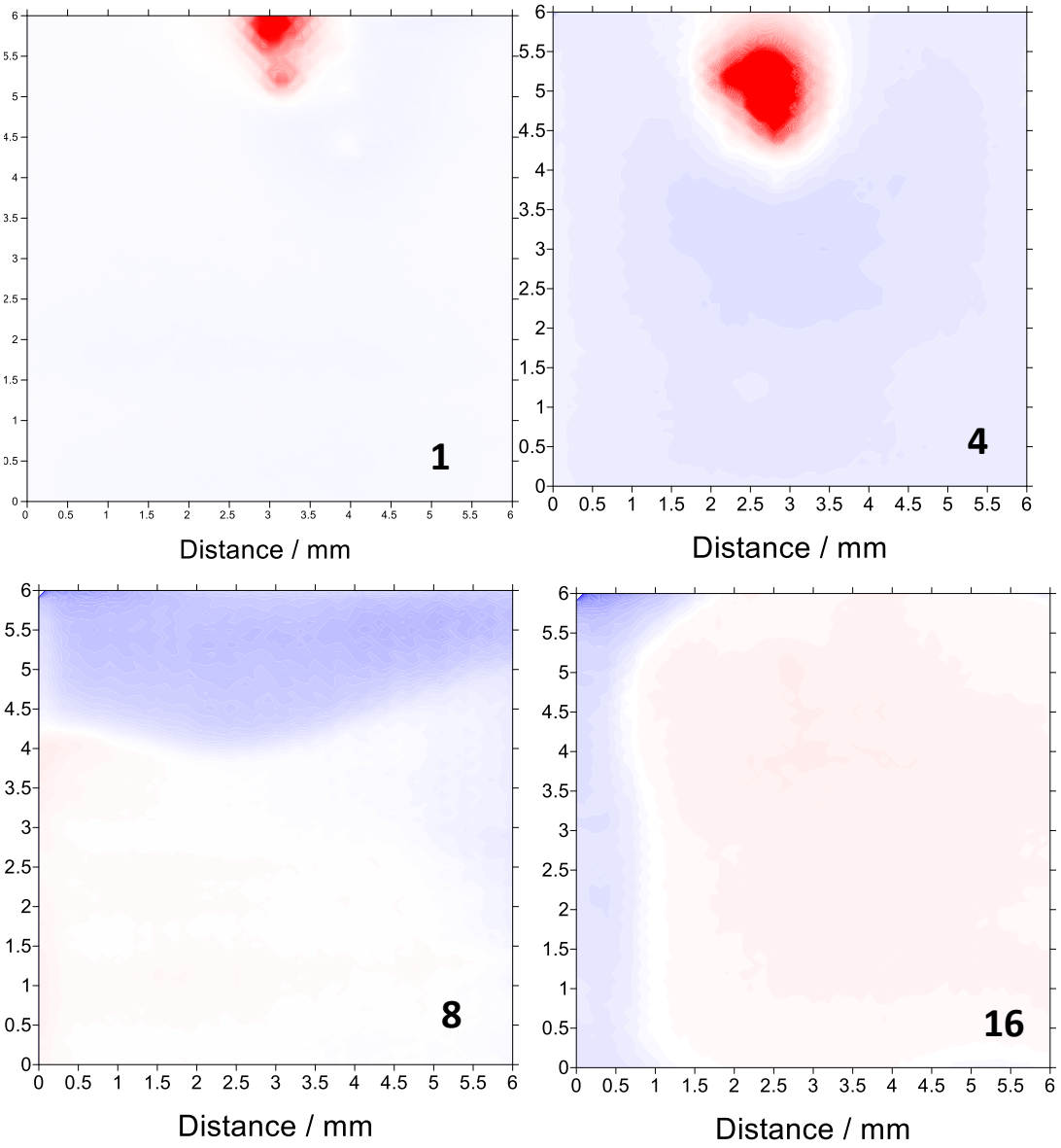

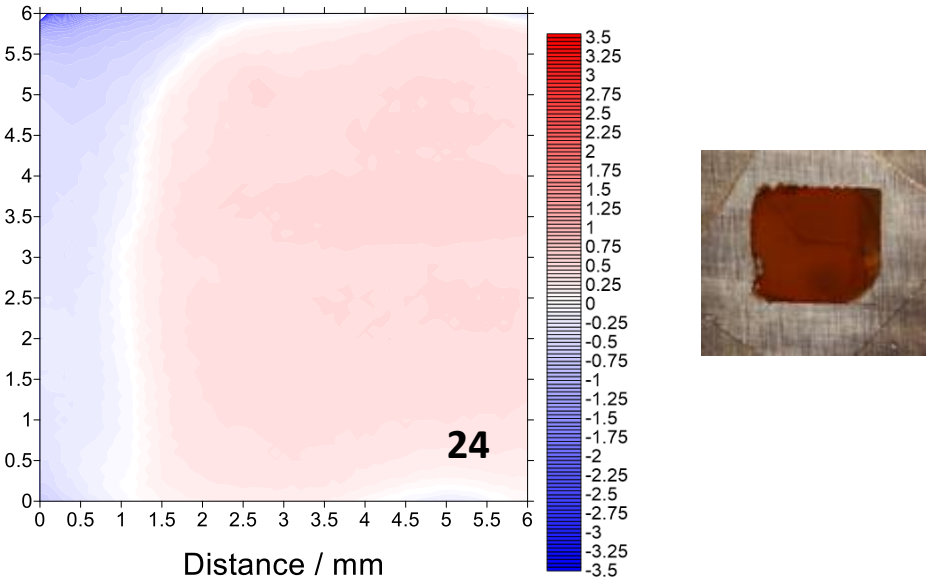

Figure 7.21. SVET-measured current density maps of blackplate in 1 wt. % NaCl pH 11. Numbers in the bottom right dictate the respective hours at which the plot was taken from.

The presence of alanine at pH 11 significantly changed the appearance of the SVET current density maps. This can be seen in Figure 7.22. Very little activity was observed on the surface of blackplate for the duration of the experiment. No corrosion product was visible on the sample after 24 hours.

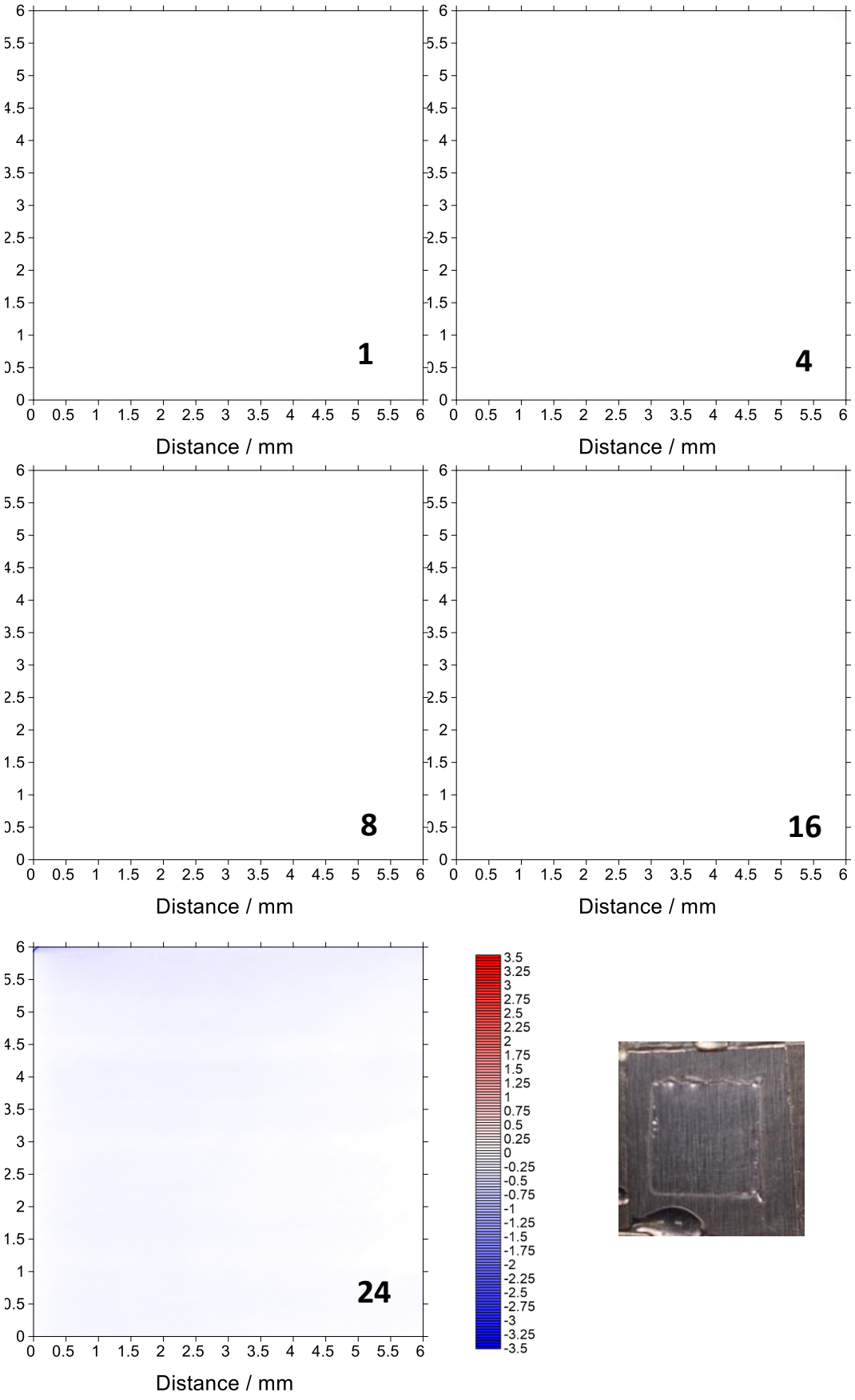
1
4
8
16
24
Distance / mm
3.5
3.25
3
2.75
2.5
2.25
2
1.75
1.5
1.25
1
0.75
0.5
0.25
0
-0.25
-0.5
-0.75
-1
-1.25
-1.5
-1.75
-2
-2.25
-2.5
-2.75
-3
-3.25
-3.5

Figure 7.22. SVET-measured current density maps of blackplate in 1 wt. % NaCl pH 11 with the addition of $\times 10^{-2}$ mol.dm^{-3} alanine. Numbers in the bottom right dictate the respective hours at which the plot was taken from.

The addition of alanine after 2 hours meant that although a region of anodic activity was observed to migrate across the surface, it took longer for this to occur. Prior to this, little activity was observed on the surface of blackplate.

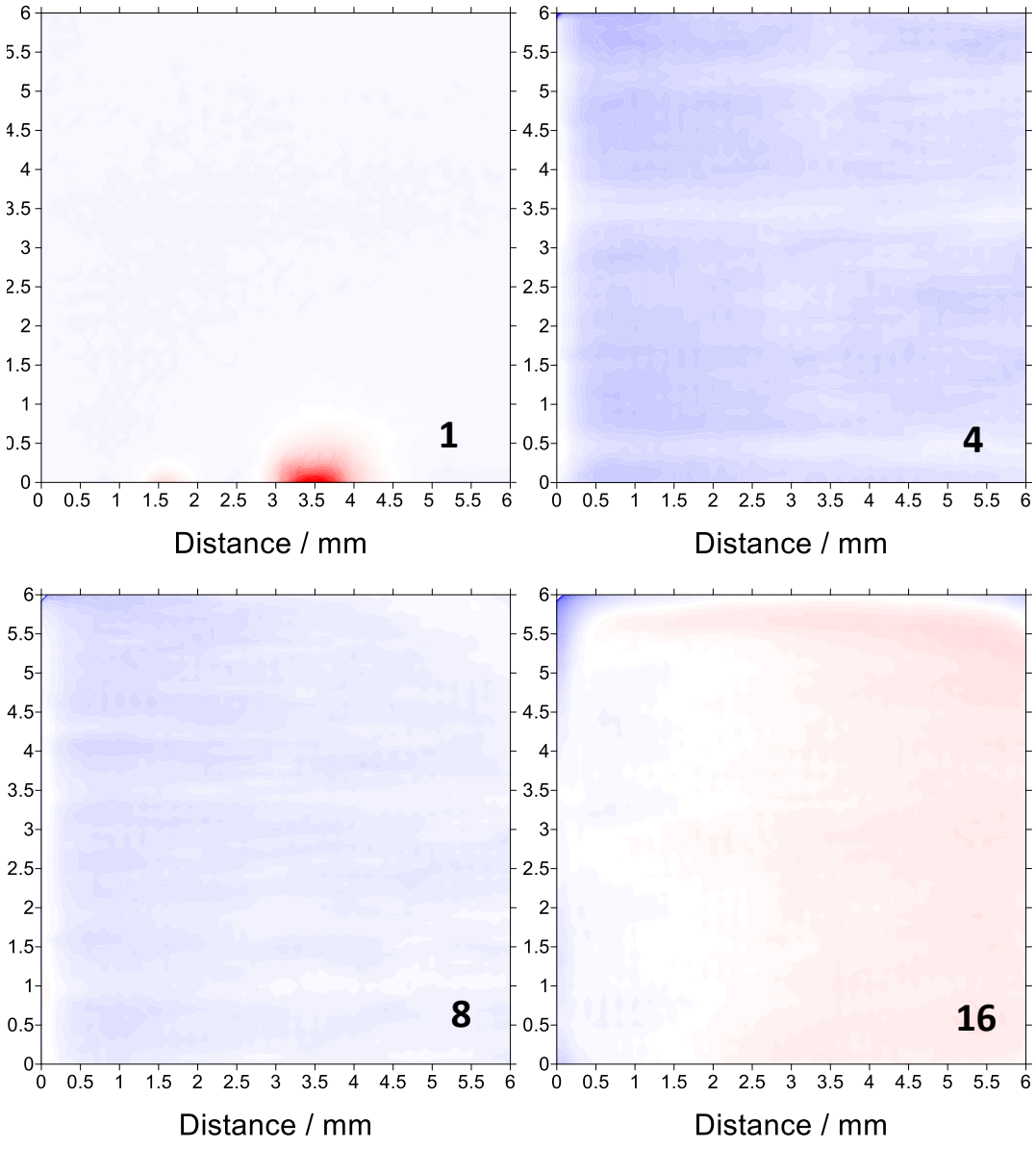

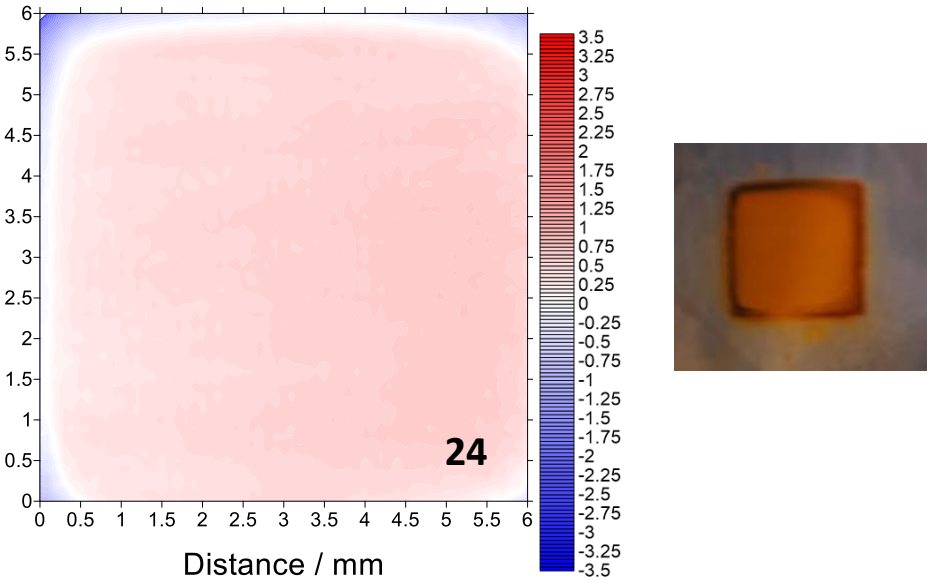

Figure 7.23. SVET-measured current density maps of blackplate in 1 wt. % NaCl pH 11 with the addition of $\times 10^{-2}$ mol.dm^{-3} alanine after 2 hours of immersion. Numbers in the bottom right dictate the respective hours at which the plot was taken from.

The area averaged anodic and cathodic current density values observed over the 24-hour time period in the presence of alanine are shown in Figure 7.24. It highlights the effectiveness of alanine in reducing both anodic and cathodic current density values present on the iron surface at pH 11. In the presence of alanine there is extremely little activity, anodic or cathodic, occurring on the surface of iron.

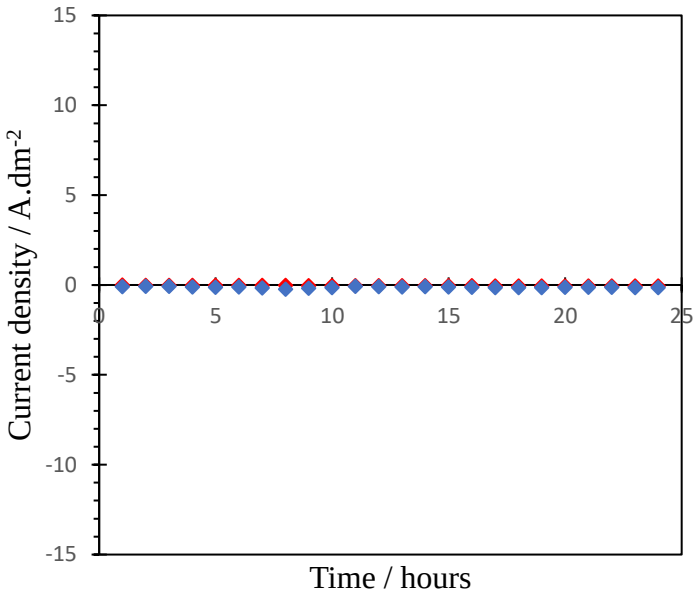

Figure 7.24. The area averaged anodic and cathodic current density values observed on the surface of the sample as a function of time for blackplate in 1 wt. % NaCl pH 11 in the presence of $\times 10^{-2}$ mol.dm^{-3} alanine.

Table 4 shows the SVET derived mass loss values and the respective inhibition efficiencies at varying pHs for blackplate immersed in 1 wt. % NaCl in the presence and absence of alanine. The inhibition efficiencies extrapolated from the mass loss values obtained from the SVET were similar to those derived from the physical mass loss experiments, providing validity of the SVET data.

Table 4. SVET derived mass loss values calculated for a blackplate sample freely corroding in pH 2, pH 7 and pH 11, 1 wt. % NaCl with 0 and $\times 10^{-2}$ alanine additions for 24 hours.

pH	Control (g/m^2)	X10^{-2} alanine (g/m^2)	I.E %
2	0.24	0.149	37.9
7	4.5	1.84	59
11	2.4	0.028	99

7.3.5 EIS studies into the mechanism of inhibition

Previously electrical impedance spectra have been used to confirm the formation of a protective film on a surface (9). Thus, in order to gain a better insight into the mechanism of the inhibitor, and hopefully compliment the data obtained from the

SVET, EIS studies were undertaken in the frequency range of 1mHz to 100 kHz. The amplitude of the excitation signal was set to 10 mV relative to the OCP. EIS was used to determine corrosion related electrochemical parameters and investigate how these changed over time. The figures below show EIS Bode plots for blackplate in 1 wt. % NaCl in the absence and presence of $x10^{-2}$ M alanine respectively. The scans took place every 2 and a half hours starting from 1 hour after immersion. This is represented by the colour of the marker becoming increasingly lighter with time. Looking at the data from the SVET this time was perceived to be sufficient to gain enough information on what was occurring at the surface of the substrate.

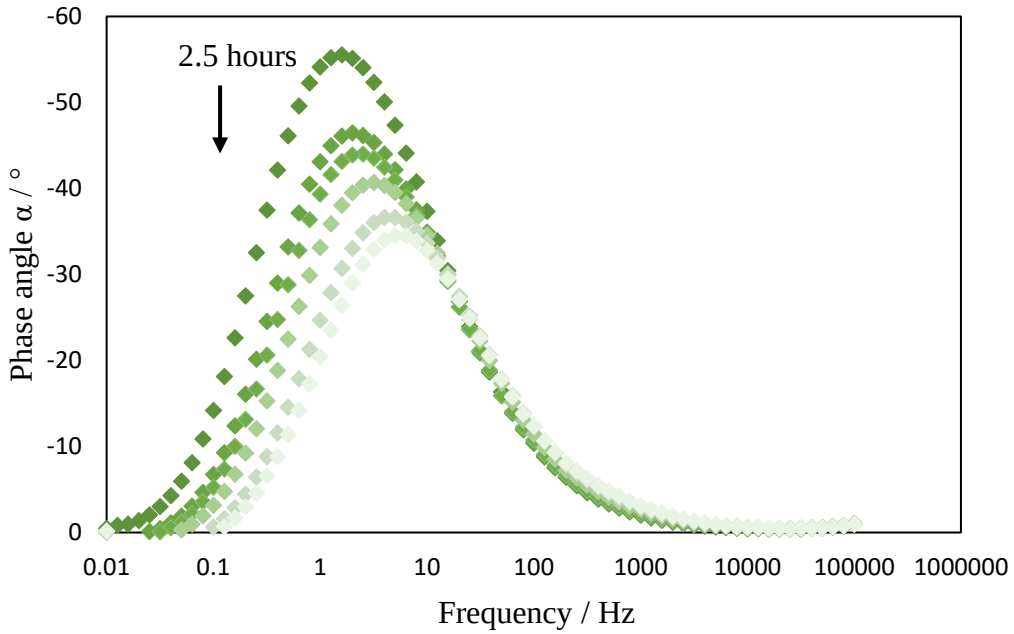

Figure 7.25. EIS Bode phase plot for blackplate in 1 wt. % NaCl in the absence of $\times 10^{-2}$ mol.dm^{-3} alanine.

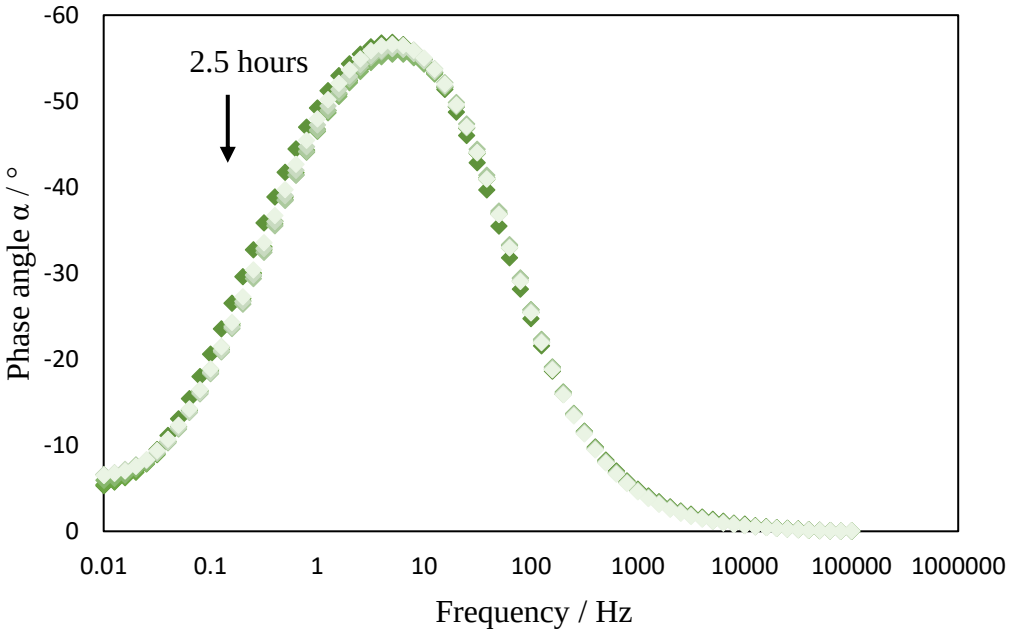

Figure 7.26. EIS Bode phase plot for blackplate in 1 wt. % NaCl in the presence of ×10^{-2} mol.dm^{-3} alanine.

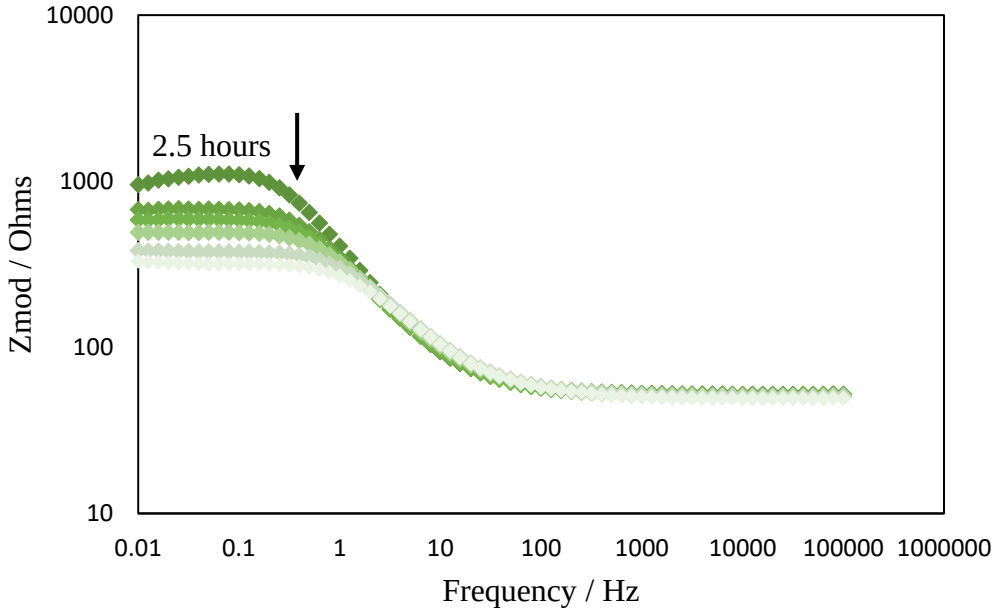

Figure 7.27. EIS Bode magnitude plot for blackplate in 1 wt. % NaCl in the absence of ×10^{-2} mol.dm^{-3} alanine.

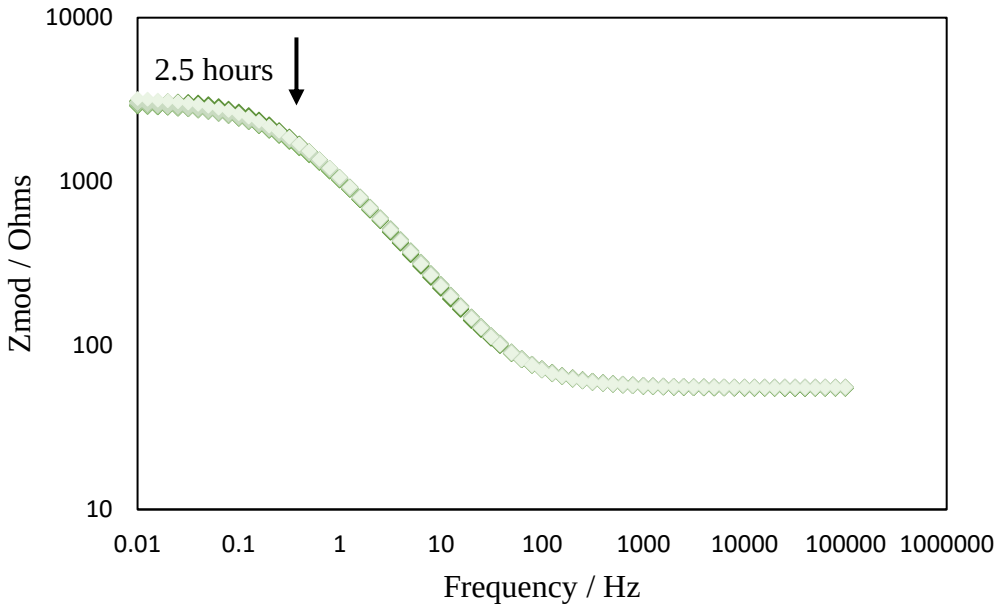

Figure 7.28. EIS Bode magnitude plot for blackplate in 1 wt. % NaCl in the presence of $\times 10^{-2}$ mol.dm^{-3} alanine.

Figures 7.20-23 show the EIS Bode phase and magnitude plots for blackplate in the absence and presence of alanine respectively.

In Figure 7.25 and Figure 7.26 the single phase angle peak, present in both the absence and presence of the inhibitor, relates to the charge-transfer controlled corrosion processes. The phase angle response shows which behaviour of RC electrical component the system best resembles. For example, a phase shift of 0° corresponds to resistor like behaviour, -90° a capacitor and 90° an inductor. The phase angle, in both the presence and absence of alanine, was approximately -55° suggesting that in the present analysis, blackplate did not behave as an ideal capacitor. The deviation from the ideal capacitive response can be attributed to surface roughness (10). With alanine present, the large phase angle signal provides information on a strong adsorption process over the substrate (11). The size of the phase angle was greater with the addition of alanine indicating its inhibition activity and increased surface coverage of a superior protection layer (12). The phase angle does not change with immersion time when alanine was present suggesting it is providing strong corrosion protection. However, in alanine's absence the phase angle decreased significantly with time indicative of corrosion processes and a reduced capacitive response (11).

The Bode magnitude plot, displayed in Figure 7.27, shows that at low frequencies, in the absence of alanine, impedance decreased with increased immersion time. This is indicative of the iron corroding. In comparison, Figure 7.28 shows that in the presence of alanine, at low frequencies, the initial impedance value was higher to start with indicating reduced corrosion rate. Furthermore, throughout the experiment the value of impedance did not decrease again highlighting the impressive inhibition activity of alanine.

It is worth noting that the presence of alanine in solution does not substantially change the shape of the plots but increases the impedance. This observation strongly suggests that alanine does not alter the mechanism of corrosion reaction but instead inhibits corrosion through the formation of a barrier film which retards charge-transfer (13).

To show more clearly how R_{CT} changes with immersion time, in the presence and absence of alanine, Figure 7.29 and Figure 7.30 show the EIS Nyquist plots, where the diameter of the semicircle corresponds to R_{CT}. It can clearly be seen that in the absence of alanine the diameter of the semi-circle decreases with time. However, with alanine present, the diameter of the semi-circle stays more or less constant.

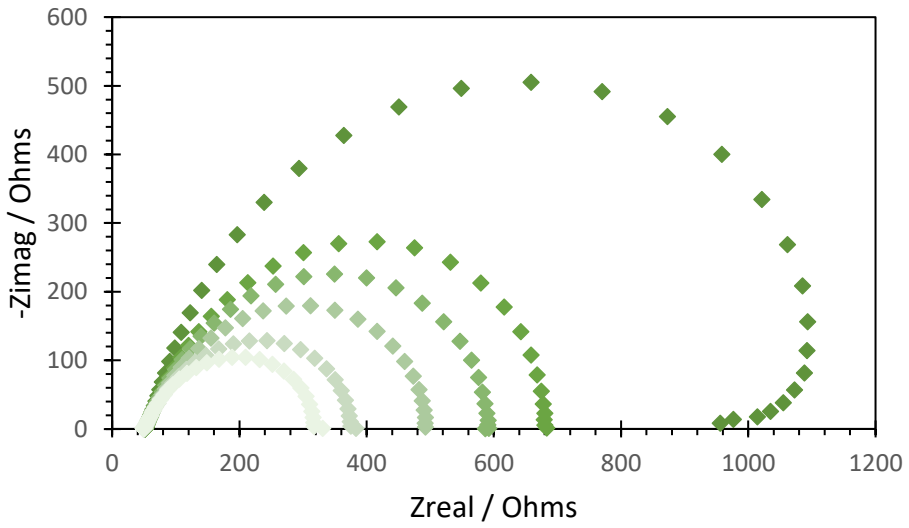

Figure 7.29. EIS Nyquist plot for blackplate in 1 wt. % NaCl in the absence of $\times 10^{-2}$ mol.dm^{-3} alanine.

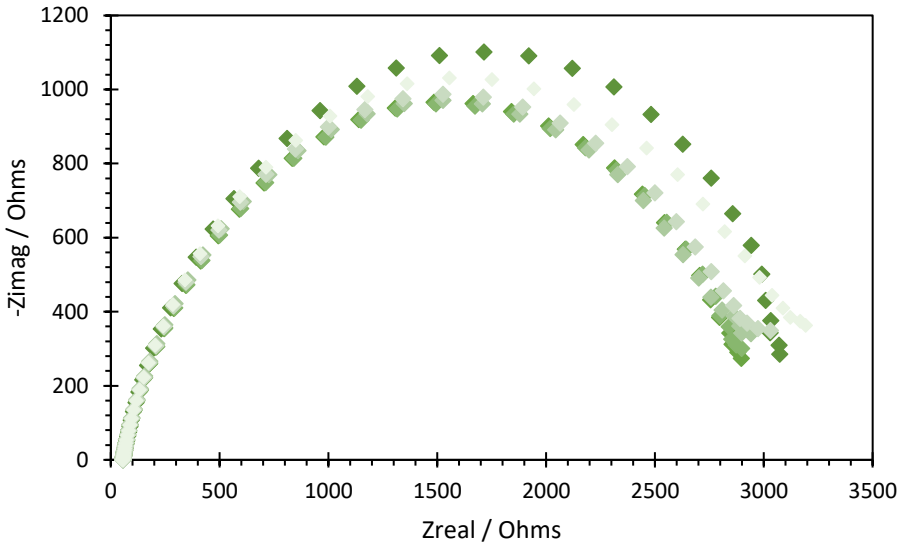

Figure 7.30. EIS Nyquist plot for blackplate in 1 wt. % NaCl in the presence of $\times 10^{-2}$ mol.dm^{-3} alanine.

To interpret the EIS data, an equivalent circuit model was created as shown in Figure 7.31. R_S represents the solution resistance corresponding to the resistance of the solution between the working electrode and the counter electrode. R_{CT} represents the charge transfer resistance, corresponding to the corrosion reaction at the metal substrate/solution interface. The CPE represents the constant phase element and is used in place of a capacitor.

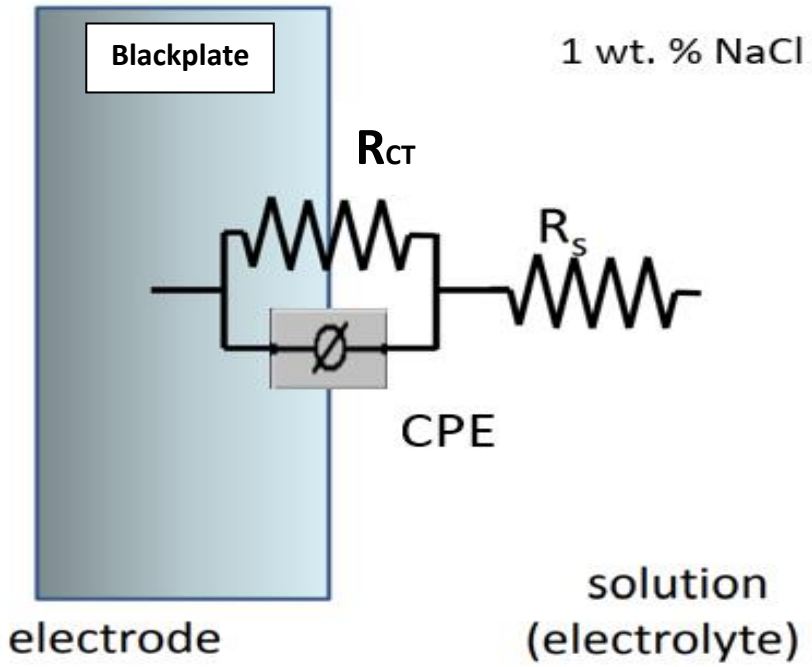

Figure 7.31. Equivalent circuit model for analysis of impedance spectra.

R_S remains constant at around 54 Ohms throughout the duration of the experiment as demonstrated by the value furthest to the right on the Bode magnitude plots shown in Figure 7.27 and Figure 7.28.

Figure 7.32 shows how the addition of alanine effects the values obtained for polarisation resistance (in this case charge transfer resistance). R_P was significantly higher when alanine was present in solution. This suggests that the addition of alanine acts to reduce corrosion processes occurring on the substrate. Over time R_P gradually increased for blackplate immersed in a solution containing 1 wt. % NaCl in the

presence of $x10^{-2}$ mol.dm^{-3} alanine. Without alanine, R_P rapidly decreased with time indicative of the blackplate corroding.

An increase in R_P suggests that the mass and electron transfer between the metal/electrolyte interface becomes difficult, in turn resulting in a reduction of corrosion processes (14).

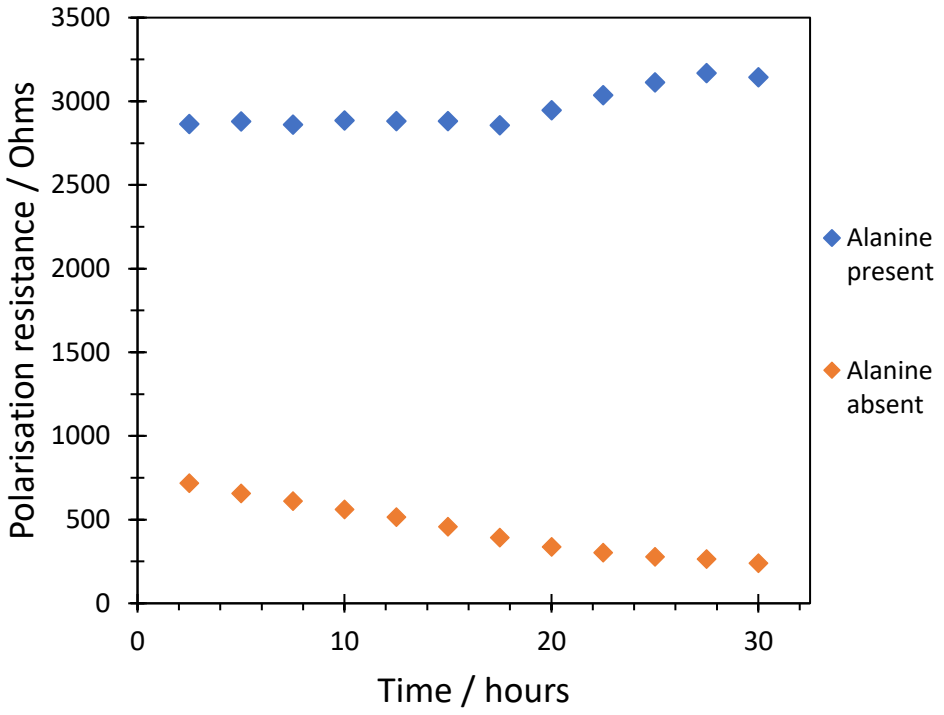

Figure 7.32. Polarisation resistance as a function of time extrapolated from EIS measurements for blackplate immersed in 1 wt. % NaCl in the presence and absence of $\times 10^{-2}$ mol.dm^{-3} alanine.

Also, the decrease in the value of CPE_{dl} implies that amino acids would successfully adsorb on the steel surface by replacing pre-adsorbed water molecules

The inhibition efficiency of the inhibitor was, then, calculated using the following equation (15):

$$IE\% = \left(1 - \left[\frac{Rp^{(b)}}{Rp^{(in)}}\right]\right) \times 100 \qquad (2)$$

where $Rp^{(b)}$ and $Rp^{(in)}$ are the polarization resistances in the absence and presence of the inhibitor, respectively.

Using this equation, the inhibition efficiency was calculated to be 92.4 % after 30 hours of immersion in NaCl in the presence of alanine.

7.3.6 Surface analysis

XPS spectra of nitrogen and oxygen peaks from an XPS surface scan of blackplate immersed in 1 wt. % NaCl in the absence and presence of alanine can be seen in Figure 7.33 and Figure 7.34 respectively. A distinct peak at 400 eV corresponding to the amide peak can be observed in the N1s spectra obtained from a sample immersed in NaCl in the presence of alanine (16). In the case that alanine was absent, no peak was observed in the N1s spectra. Along with EDS data, this provided strong evidence that an alanine film was indeed formed on the surface of the blackplate.

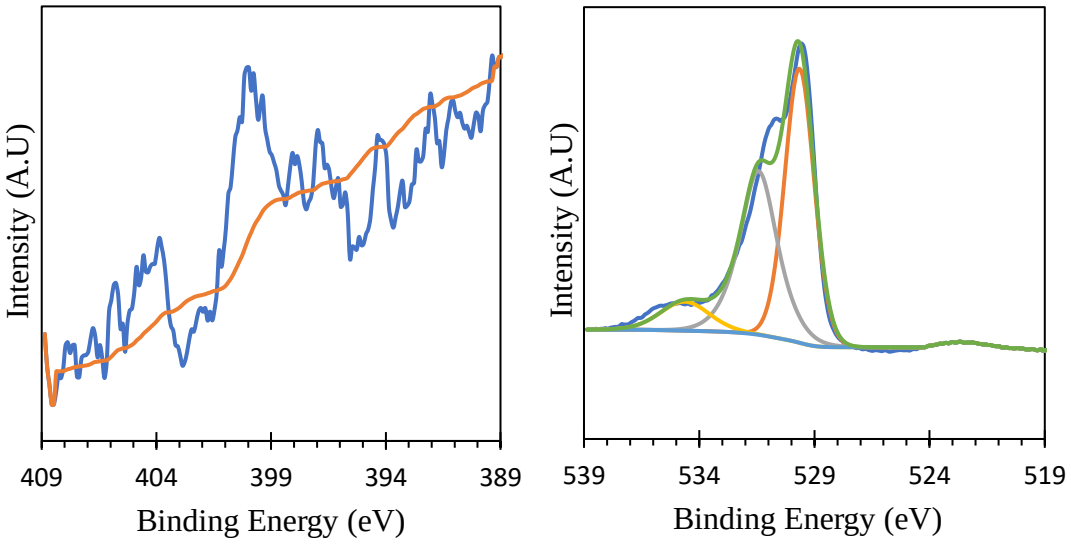

Figure 7.33. XPS spectra of nitrogen (left) and oxygen (right) for blackplate immersed in 1% NaCl.

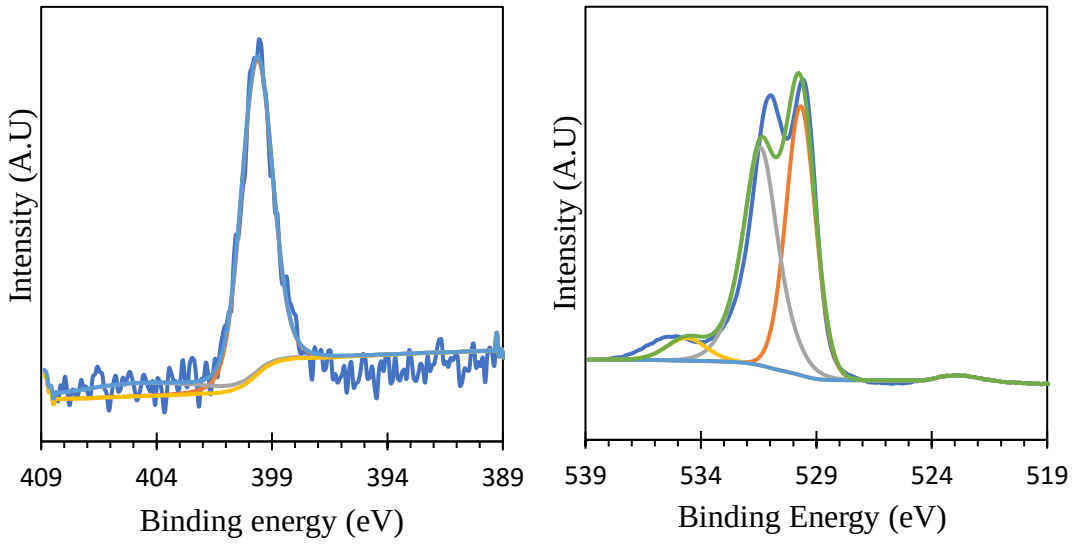

Figure 7.34. Figure 7.27. XPS spectra of nitrogen (left) and oxygen (right) for blackplate immersed in 1% NaCl + ×10^{-2} mol.dm^{-3} alanine.

7.4 Discussion

The results suggest that alanine acts to inhibit corrosion on iron. The exact nature of the inhibited surface has yet to be discerned. However, it is suggested that alanine offers initial protection to the iron substrate via a film forming adsorption mechanism.

The results from the gravimetric weight-loss study highlighted that alanine provided a degree of inhibition efficiency (I.E) for blackplate in 1 wt. % NaCl. A concentration of x10^{-2} mol.dm^{-3} alanine acted to inhibit corrosion to the greatest extent and was thus, studied further. The extent of corrosion inhibition was also affected by the pH of the electrolyte.

Gravimetric weight loss studies showed that alanine offered, to some extent, corrosion protection, irrespective of pH. Although, when alanine was immersed at higher pHs, a much greater extent of inhibition was seen. When the electrolyte was at a pH of 11, alanine offered the greatest I.E of 74%.

Visual observations of the samples from the gravimetric weight loss studies, as well as SEM images of samples after immersion, indicate that in the presence of inhibitor the rate of corrosion is suppressed. The studies showed how the metal surface was almost free from corrosion in the presence of alanine. Again, this highlighted the

effectiveness of alanine as a corrosion inhibitor on iron. As aformentioned impedance spectra has been used in previous work to confirm the presence of aprotective film a the surface of a metal. The change in impedance parameters including the increase in charge transfer resistance and deccrease in capacitance, in the presence of alanine, led to the conclusion that a protective film is indeed formed on the surface of blackplate (9). This supported the idea that a film forming adsorption mechanism was indeed occuring.

OCP measurements were recorded to gain a better insight into the mechanism of inhibition. When the electrolyte was at a pH of 7, the OCP measurements were significantly more negative when the inhibitors were present in the electrolyte suggesting that they were suppressing the cathodic reaction and ultimately acting acted as cathodic inhibitors. This decrease in OCP indicated that the inhibitor was interacting with the system and may be correlated to the adsorption of an Fe-alanine complex onto the surface of the blackplate sample. Hence, the increased surface concentration of Fe may cause the negative shift in potential.

At pH 7 alanine exists in its zwitter ionic form. What's more, the iron surface is forecast to be covered in iron oxide, which has an isoelectric point greater than pH 7. Hence, the surface will be positively charged at this pH. It is hypothesised that anionic alanine adsorbs directly onto the iron surface whilst the cationic form adsorbs via Cl^-; halide ions have previously been shown to adsorb ion the surface of metals by creating orientated dipoles (17). SVET studies concurred with this hypothesis. At pH 7, in the presence of inhibitor a faintly anodic region was observe over the surface of the metal after the 24-hour period, however, little corrosion was visually observed on the surface. This provides evidence for the formation of an Fe-alanine complex as the presence of an Fe species on the surface may have caused the faint anodic current to be observed.

When the pH of the electrolyte was at pH 2 and pH 11 respectively, the addition of alanine caused the OCP value to be shifted in the positive direction. This shift in OCP suggest that the inhibitor may be acting to supress the anodic reaction and act as an anodic inhibitor.

At pH 11, the protonated amino group would lose its proton and alanine would behave as an anion. There is potential for the formation of an Fe-alanine complex. This

concurs with the findings from the SVET work. In the absence of inhibitor, the sample corrodes, initially via individually anodes, and then more generalised corrosion. In the presence of alanine, the sample remains inert for the duration of the experiment. However, of interest is the addition of alanine after 2 hours. The initial anodic activity had been replaced by cathodic activity where it was proposed the anionic alanine had absorbed onto the surface, providing protection. Overtime, the surface of iron is expected to be covered in greater amounts of Fe oxide and have a negative charge. In turn, it was proposed that as the alanine film was broken down, the negatively charged alanine would be unable to adsorb to the surface and explain why it did not provide corrosion protection for the duration of the experiment.

At pH 2 the carboxyl group is protonated, and alanine behaves as a cation with a net positive charge. It is proposed that the protonated alanine would be able to adsorb onto the surface of iron via Cl^-. SVET studies offered more insight into how the inhibitor was interacting with the system to inhibit corrosion. Surprisingly, even in the absence of alanine, little corrosion was evident on the surface of blackplate. In the presence of alanine, a slight reduction in the anodic values was observed, concurring with the proposal of alanine acting as an anodic inhibitor at this pH.

The results provide good evidence to suggest that alanine acts as a mixed-type inhibitor at pH 7, and an anodic inhibitor at pH 2 and 11. The following mechanism of corrosion inhibition is proposed. An Fe^{2+} - alanine complex is formed across the surface of the metal thus, blocking the anodic and cathodic sites and retarding corrosion processes (pH dependent). The following reactions are suppressed:

pH 2, 7 and 11: $Fe \rightarrow Fe^{2+} + 2e^-$

pH 7: $O_2 + 2H_2O + 4e^- \rightarrow 4OH^-$

thus slowing down the rate of corrosion.

Alanine adsorbs onto the Fe surface, blocking active corrosion sites, by means of its nitrogen and oxygen atoms with the lone pair electrons in its molecule. Results obtained from EDS, FTIR and XPS supported this hypothesis. Results from EIS supported this hypothesis by showing how alanine does not alter the mechanism of corrosion reaction but inhibits corrosion through the formation of a barrier film which retards charge-transfer.

7.5 Conclusion

A systematic study into the effect of alanine on the corrosion inhibition of commercially produced blackplate was conducted. The results showed that alanine acted to inhibit corrosion on blackplate.

Inhibition efficiency increased as the pH of the electrolyte was increased. Immersion studies showed that a greater concentration of these amino acids offered enhanced corrosion resistance with a concentration of $x10^{-2}$ $mol.dm^{-3}$ providing the highest corrosion resistance levels.

It is hypothesised that inhibition occurs via adsorption of the inhibitor molecules and the formation of a protective film on the metal surface.

EIS and SVET measurements revealed the high inhibition power of these amino acids. EIS shows that the corrosion of Fe in NaCl is controlled by charge transfer and the addition of alanine to solution inhibits corrosion without modifying the mechanism of corrosion.

The adsorption of alanine onto the surface of iron, by means of its nitrogen and oxygen atoms, was demonstrated by EDS, FTIR and XPS surface scans. This mechanism of adsorption decreases the accessable surface area of exposed iron and blocks active corrosion sites, ultimately providing good corrosion protection.

The results demonstrate the potential use of the amino acid alanine as an environmentally friendly corrosion inhibitor for iron. Although it should also be highlighted that pH 11 has a significant effect with regards to inhibition efficiency.

7.6 References

1. Gowri S, Sathiyabama J, Rajendran S. Corrosion inhibiiton by amino acids - an over review. Eur Chem Bull. 2012;1(11):470–6.

2. Gharbi O, Thomas S, Smith C, Birbilis N. Chromate replacement : what does the future hold ? Mater Degrad. 2018;2(12):23–5.

3. El-Deab MS. Interaction of cysteine and copper ions on the surface of iron: EIS, polarization and XPS study. Mater Chem Phys. 2011;129(1–2):223–7.

4. Raja A., Venkatesan R, Sonisheeba R, Paul raj J., Sivakumar S, Angel P, et al. Corrosion Inhibition by Cysteine - An Over View. Int J Adv Res Chem Sci. 2014;1(1):101–9.

5. Khaled K., Abdelshafi N., El-Maghraby A., Aouniti A, Al-Mobarak N, Hammouti B. Alanine as Corrosion Inhibitor in Acid Medium: A Molecular Level Study. Electrochem Sci. 2012;7:12706–19.

6. PubChem. Alanine [Internet]. Available from: https://pubchem.ncbi.nlm.nih.gov/compound/Alanine#section=Dissociation-Constants

7. Potentiodynamic Scan/Cyclic Polarization Gamry Instruments [Internet]. [cited 2023 Mar 9]. Available from: https://www.gamry.com/application-notes/corrosion-coatings/potentiodynamic-cyclic-polarization/

8. Seo J, Hoffmann W, Malerz S, Warnke S, Bowers MT, Pagel K, et al. Side-chain effects on the structures of protonated amino acid dimers: A gas-phase infrared spectroscopy study. Int J Mass Spectrom. 2018;429:115–20.

9. Gowrani T, Manjula P, Baby N, Manonmani K., Sudha R, Vennila T. Int. Int J Nano Corr Sci Engg. 2015;2(1):12–21.

10. Verma C, Quraishi MA, Ebenso EE, Obot IB, El Assyry A. 3-Amino alkylated indoles as corrosion inhibitors for mild steel in 1M HCl: Experimental and theoretical studies. J Mol Liq. 2016;219:647–60.

11. Zhang Z, Tian N, Zhang W, Huang X, Ruan L, Wu L. Inhibition of carbon steel corrosion in phase-change-materials solution by methionine and proline. Corros Sci. 2016;111:675–89.

12. Yildiz R. An electrochemical and theoretical evaluation of 4,6-diamino-2-pyrimidinethiol as a corrosion inhibitor for mild steel in HCl solutions. Corros Sci. 2015;90:544–53.

13. Hamed E, Abd El-Rehim SS, El-Shahat MF, Shaltot AM. Corrosion inhibition of nickel in H 2SO 4 solution by alanine. Mater Sci Eng B Solid-State Mater

Adv Technol. 2012;177(5):441–8.

14. Singh RK, Devivaraprasad R, Kar T, Chakraborty A, Neergat M. Electrochemical Impedance Spectroscopy of Oxygen Reduction Reaction (ORR) in a Rotating Disk Electrode Configuration: Effect of Ionomer Content and Carbon-Support. J Electrochem Soc. 2015;162(6):F489–98.

15. Ibrahim MAM, Messali M, Moussa Z, Alzahrani AY, Alamry SN, Hammouti B. Corrosion inhibition of carbon steel by imidazolium and pyridinium cations ionic liquids in acidic environment. Port Electrochim Acta. 2011;29(6):375–89.

16. Puerto MA, Costa TMH, Jornada JAH, Balzaretti NM. Pyrolisys of α-aminoacids under high-pressure investigated by XPS, Raman and infrared spectroscopy. Mater Chem Phys. 2018;211:107–16.

17. Lorenz W. Z. Phys. Chem., 65, 244 (1970). Z Phys Chem. 1970;65(244).

8 Conclusions and future work

8.1 Conclusions

In this thesis, a novel Cr (III) bilayer coated steel called Trivalent Chromium Coated Technology (TCCT) was investigated, focusing on its resistance to corrosion-driven coating failure of a model Poly (vinyl) butyral organic coating. The two mechanisms of corrosion-driven organic coating failure studied in depth were filiform corrosion and corrosion-driven cathodic coating delamination. SEM characterisation of the TCCT steel surface revealed numerous imperfections such as defects in the lower Cr (III) oxide coating weights. The presence of these defects on the lower Cr (III) oxide coating weights, as well as the impressive insulating properties of Cr (III) oxide, were thought to be contributing factors to the improved corrosion resistance observed with increasing coating weight. A Cr (III) oxide coating weight of approximately 7 $mg.m^{-2}$ was deemed significant in terms of offering impressive corrosion resistance, comparable to that of the current standard, ECCS.

In chapter 3, it was found that the extent of corrosion-driven disbondment of a model PVB coating adhered to TCCT decreased with increasing chromium (III) oxide coating weight. The mechanism of cathodic coating delamination was found to be dependent on the TCCT coating weight. The kinetics of cathodic disbondment on iron and low coating weight TCCT were rate-limited by the migration of Na^+ cations and hence, parabolic in nature. The kinetics changed from parabolic to linear, whereby electron transfer was rate-limiting, as the coating weight was increased. In addition, diminished electrocatalytic activity for ORR, as measured from cathodic polarisation measurements, were found to correlate with diminished delamination kinetics. A TCCT Cr (III) oxide coating weight of 7.5 $mg.m^{-2}$ was sufficient enough to provide resistance to corrosion-driven organic coating delamination altogether, such that it provided similar performance to ECCS.

In chapter 4, it was found that the extent of FFC increased with decreasing Cr (III) oxide coating weight. A coating weight of approximately 6.5 $mg.m^{-2}$ was deemed significant with regards to reducing the amount of FFC corroded area. Time-lapse videos of FFC propagation over the TCCT surface revealed that FFC appeared to

advance as a continuous chain of pit-like features, especially on the lower oxide coating weights. SEM characterisation of the FFC filaments on the TCCT surface showed that the filament head advances as a series of pit-like features, in agreement with the time-lapse video observations. From visual characterisation of FFC on TCCT steel, by optical and electron microscopy, it is proposed that the filiform advances by a successive-pitting mechanism, by which the head advances forward by 'jumping' to the next available defect in the TCCT coating and/or by undermining of the TCCT coating.

Chapter 5 described how a lab scale TCCT electroplating line was successfully replicated in the labs in Swansea. The electrodeposition of Cr metal and Cr (III) oxide coatings on low carbon mild steel from a trivalent chromium electrolyte was thus, made possible. The amount of both Cr metal and Cr (III) oxide deposition was found to be strongly affected by the applied current density, temperature, pH as well as plating time. Hydrogen evolution was found to be a major issue with regards to the blocking of Cr deposition onto the substrate, and hence providing greater areas of iron exposure. SEM characterisation of the lab produced samples indicated a higher population of defects (pores and pinholes) in the Cr coating, compared to line produced samples. The corrosion performance trends recorded were similar for both lab-made and line produced samples, although the overall corrosion performance was lower for that of the lab-made samples.

Chapter 6 evaluated the effect of thermal treatment on the chemical composition of TCCT samples. It was shown that increasing the temperature from room temperature to 400 °C caused the $Cr(OH)_3$ to be condensed into Cr_2O_3. In turn, this led to a reduction in corrosion performance of the substrate, thought to be linked to the decrease in coating thickness as well as nature of the coating, as a result of the change in surface species.

Chapter 7 investigated the use of the amino acid alanine as a potential 'green' corrosion inhibitor. A greater concentration alanine offered enhanced corrosion resistance with a concentration of $x10^{-2}$ $mol.dm^{-3}$ providing impressive corrosion resistance levels. It was hypothesised that inhibition occurred via adsorption of the inhibitor molecules and the formation of a protective film on the metal surface. The results demonstrated the potential use of the amino acid alanine as an environmentally friendly corrosion

inhibitor for iron. Although it should also be highlighted that pH has a significant effect with regards to inhibition efficiency.

8.2 Future work

1. Characterise the cross-section of filiform filaments using FEG-SEM and/or FEG-TEM to gain further insight as to how FFC affects the TCCT coating. This would aid in the conformation as to whether the Cr coating stays intact following filiform propagation.

2. Carry out mechanical deformation of the TCCT steels using a robust and repeatable procedure that is closely linked to the can making process used in industry.

3. Assess the resistance of mechanically deformed TCCT steels to both filiform corrosion and corrosion-driven cathodic coating delamination. Using the same methodology as that used in this thesis would serve as a good comparison between samples that has been mechanically deformed and those that had not.

4. Determine the corrosion mechanism of such coating failure mechanisms applicable to mechanically deformed organic coated TCCT steel.

5. Explore further the comparability of lab-based and line-produced samples and investigate how the lab-based process can be improved. Using a rotating cylinder electrode would simulate the hydrodynamics of the line electroplating bath more accurately.

6. Use the lab scale electroplating line to identify the optimal plating conditions for coating deposition as well as corrosion resistance. Altering more than one parameter at once may aid in determining the ideal plating parameters.

7. Identify methods to reduce hydrogen evolution at the surface of the cathode. For example, reducing the applied current density would assist in reducing hydrogen evolution.

8. Identify complexes present in the TCCT electrolytes, using UV-Vis and other techniques. In turn, the results from this work could assist in suggestions for changes to electrolyte compositions.

9. The exact nature of the inhibitive film formed by alanine is not yet fully understood and, given the effectiveness of alanine as a corrosion inhibitor at pH 11, it should be the subject of further work. The stability of the inhibitive effect is also a potential area of future research.